

**The use of remote sensing imagery  
for groundwater risk intensity mapping  
in the Wadi Shueib, Jordan**

Zur Erlangung des akademischen Grades eines  
Doktors der Naturwissenschaften  
an der Fakultät für Bauingenieur-,  
Geo- und Umweltwissenschaften  
der  
Universität Karlsruhe  
genehmigte  
Dissertation

Von  
Heike Werz  
aus Stuttgart

Karlsruhe 2006

Tag der mündlichen Prüfung: 24.02.06  
Referent: Prof. Dr. H. Hötzl (Karlsruhe)  
Korreferent: Prof. Dr. H.-P. Bähr



## KURZFASSUNG

### Der Nutzen von Fernerkundungsdaten für die Kartierung der Grundwasser-Risiko-Intensität im Wadi Shueib, Jordanien

Das übergeordnete Ziel der vorliegenden Arbeit war die Einschätzung der Grundwasserrisikointensität gegenüber Schadstoffen in einem, von verkarsteten Kalksteinen dominierten, Arbeitsgebiet in Jordanien. Dafür wurden Karten im regionalen Maßstab erzeugt, welche die Grundwasservulnerabilität (Verletzlichkeit), die potentielle Grundwassergefährdung durch Schadstoffe (Grundwasserhazards) und die Grundwasserrisikointensität darstellen. Für die Erstellung dieser Karten wurde ein kombinierter Ansatz aus der Anwendung von Fernerkundungsdaten und GIS gewählt, der es ermöglicht, eine große Anzahl digitaler aktueller thematischer Karten anzufertigen und miteinander zu kombinieren.

Nach einer kurzen Zusammenfassung über bestehende Anwendungen von Fernerkundungsdaten in der Hydrogeologie und für die Einschätzung der Grundwasservulnerabilität und der Grundwasserhazards folgt eine Beschreibung der Techniken und Methoden, die für die Bearbeitung der Fernerkundungsdaten und deren Nachbearbeitung mit GIS angewendet wurden. In diesem Zusammenhang wird diskutiert, in welchem Maße konventionelle Kartiermethoden und Techniken zur Datenerfassung für die Einschätzung der Grundwasserrisikointensität in Gebieten mit spärlicher oder unzureichender Datengrundlage, durch Fernerkundungsdaten verbessert oder ersetzt werden können. Weiterhin wird diskutiert, ob und wie sich Richtlinien und Methoden zur Grundwasservulnerabilität und Risikointensitätsabschätzung, die für europäische (Karst-) Gebiete im Rahmen der COST Action 620 entwickelt wurden (Zwahlen et al., 2004), in semi-aride Klimabereiche übertragen lassen.

Innerhalb der Studie standen drei Fernerkundungsdatensätze zur Verfügung: LANDSAT ETM<sup>+</sup> Daten, digitale Farbluftbilder (1:10,000) und analoge schwarz-weiß Luftbilder (1:30,000). Die Auswertung der Daten erfolgte mittels unüberwachter und überwachter Klassifikation, Ratiobildung und visueller Interpretation. Neben Landbedeckungs- und Landnutzungskarten wurden zahlreiche andere thematische Karten aus den Fernerkundungsdaten erstellt. Für einen Teil des Arbeitsgebietes wurde an Hand hochauflösender digitaler Luftbilder der Grad der Verkarstung visuell bestimmt und die Lage von punktuellen Schadstoffquellen ausgewiesen.

Da nicht alle benötigten Informationen aus den Fernerkundungsdatensätzen abgeleitet werden konnten, wurden für das Arbeitsgebiet zusätzliche thematische GIS-Karten aus räumlichen und nicht-räumlichen Daten erstellt, die auf Gelände- und Laboruntersuchungen oder Literaturstudien beruhen. Die erstellten Karten beinhalten u.a. (hydro-)geologische Eigenschaften, Bodendaten und Höheninformationen. Ein Schwerpunkt lag hierbei auf der Kartierung und Charakterisierung der Böden im Arbeitsgebiet als thematische Eingangskarte für die Grundwasservulnerabilität- und Grundwasserhasardkarte.

Die Ergebnisse zeigen, dass sich die Verwendung von Orthophotos kombiniert mit GIS für die Größe des Arbeitsgebietes (185 km<sup>2</sup>), für den gewählten Kartenmaßstab von 1:50,000 und für die zu erfassenden Daten als am effizientesten erweist. Die höhere räumliche Auflösung ermöglicht eine Interpretation des Verkarstungsgrades der Kalksteine und eine Detailkartierung

von potentiellen Grundwassergefährdungen, die mit den LANDSAT ETM<sup>+</sup> Daten nicht erfasst werden können. Durch die räumliche Auflösung der multispektralen LANDSAT ETM<sup>+</sup> Daten von 30 m ist der Informationsgehalt im Vergleich zu Luftbildern auf generalisierte Aussagen beschränkt. So waren beispielsweise kleinparzellige landwirtschaftliche Flächen und Straßen auf den Satellitenbildern nicht eindeutig zu identifizieren.

Resultierend aus der Kombination der Vulnerabilitätskarte und der Hazardkarte weist die Grundwasserrisikointensitätskarte die Vulnerabilität der Grundwasserleiter und die potentielle Schadstoffgefährdung im Arbeitsgebiet aus. Eine hohe Risikointensität existiert in den Stadt- und Siedlungsgebieten, da sich dort einzelne Gefahrenquellen überlagern und teilweise aufsummieren. Die größte Gefährdung im Arbeitsgebiet entsteht durch punktuelle Einträge beispielsweise aus fehlenden Abwasseranschlüssen, Sickergruben ohne abdichtende Wände oder Autowerkstätten und illegalen Mülldeponien. Potentielle flächenhafte Schadstoffeinträge entstehen vor allem durch Düngung. Sind diese Gefährdungen mit einer hohen oder extrem hohen Vulnerabilität des obersten Grundwasserleiters verbunden, resultiert daraus eine sehr hohe Grundwasserrisikointensität. Hohe Vulnerabilitäten im Arbeitsgebiet entstehen vor allem durch fehlende oder lückenhafte Bodenbedeckung, fehlende Deckschichten über den Grundwasserleitern und starke Verkarstung der anstehenden Kalksteine.

Grundwasserrisikointensitätskarten tragen zur langfristigen Planung von Grundwasserschutzmaßnahmen bei. Die angewendeten Techniken können auf andere (semi-)aride Gebiete mit ähnlicher Landbedeckung übertragen werden. Obwohl die Auswertung von Fernerkundungsdaten keine Technik zur Erfassung der Grundwasserrisikointensität sein kann, die konventionelle Kartierungen und Datenerfassungsmethoden vollständig ersetzt, zeigen die Ergebnisse, dass die kombinierte Nutzung von Fernerkundungsdaten und GIS ein leistungsfähiges und effektives Hilfsmittel ist. Die große Menge an abgeleiteten aktuellen Informationen über die Landnutzung, Vegetationsbedeckung, Infrastruktur und Verstädterung, Lage und Ausdehnung bestimmter Schadstoffquellen eröffnet neue Perspektiven für eine großräumige, effektive, preiswerte Kartierung der Grundwasservulnerabilität, der Grundwasserhazards und letztlich der Grundwasserrisikointensität. Darüber hinaus liefern die erhaltenen Informationen einen wertvollen Ansatz für die Landnutzungsplanung und das Grundwassermanagement in Bereichen mit gefährdetem Grundwasser.

## ABSTRACT

The main goal of this study was the generation of groundwater vulnerability, hazard and groundwater risk intensity maps, using existing European guidelines for groundwater risk intensity maps and groundwater vulnerability and adopt them in a test area in Jordan under (semi)arid climate conditions.

Hereby the application of remote sensing imagery for data acquisition, the testing of the usage of information derived from the imagery and the production of digital thematic information were important objectives. Following a rough overview of existing approaches, that use remote sensing technique in hydrogeology and for groundwater vulnerability and hazard mapping, a review of the techniques is given that have been applied and demonstrated in this work for processing and analysing the imagery including classification schemes, construction of orthophotos and post-processing procedures using GIS. Consequently it was investigated to what extent conventional procedures of data acquisition for groundwater vulnerability and hazard mapping can be enhanced by remote sensing imagery in areas where only sparse and insufficient observed and measured data is available.

Data acquired by three passive sensors was incorporated using visual image interpretation and digital image processing: a LANDSAT ETM<sup>+</sup> image, colour digital aerial photographs (1:10,000) and analogue panchromatic aerial photographs (1:30,000). Land cover, land use maps and various thematic maps including roads, urban areas, location and size of groundwater hazards were prepared using the generated orthophotos and Landsat ETM<sup>+</sup> data. In one section of the test area high-resolution digital aerial photographs were used for the assessment of the degree of karstification and for the identification, location and extension of point-source hazards.

In addition, thematic layers of auxiliary spatial and non-spatial data were generated by a GIS based on field and laboratory investigations. The thematic layers included hydrogeological characteristics, geological information, soil properties, and digital terrain information. In this context the intensive mapping of soils and their characteristics as well as detailed field and laboratory soil investigations as a basis for the groundwater vulnerability and hazards was an important issue.

The results indicate that the use of orthophotos combined with GIS appeared to be the most accurate and effective combination in test area. In contrast to the LANDSAT ETM<sup>+</sup> data, the higher spatial resolution of the orthophotos allowed a detailed interpretation of small features (e.g. karst features and agricultural areas with minor extension) that were important for the risk assessment.

The groundwater risk intensity map clearly indicates the vulnerable areas and the “hot spots” of potential contamination in the test area resulting from the combination of the groundwater vulnerability and hazard map. In urban areas the highest risk intensity occurs, since concentrations of different hazard types interfere with each other. Additionally the urban areas in the test area are often in karstified limestones that miss auxiliary sediment or soil cover and are therefore highly vulnerable. The main hazards in the test area are point source hazards caused by missing or leaking sewer systems, factor farms, manure heap, septic tanks and car service stations without unpaved floors and illegal waste dump.

The groundwater risk intensity results can contribute to a long-term planning of protective measurements for the groundwater, and the techniques can be transferred to other areas with similar climatic and land cover conditions. Though the processing and interpretation of remote sensing data will never be a stand-alone technique that can be applied to replace conventional data acquisition, the results show that the integrated use of GIS and remote sensing technique is a powerful tool for the assessment of the groundwater risk intensity. The large amount of information derived from digital images offers new opportunities for vulnerability and hazard assessment, particularly those parameters related to land use, vegetation coverage, urbanisation and infrastructure making this approach valuable for the evaluation of endangered groundwater bodies.

## الخلاصة

### أستخدام تقنية الصور بالاستشعار عن بعد لترسيم خرائط شدة مخاطر الملوثات على المياه الجوفية في منطقة وادي شعيب, الأردن

الهدف الرئيسي من هذه الدراسة هو استنباط خريطة موضحة لدرجة حساسية المياه الجوفية للملوثات و شدة المخاطر اللتي قد تتعرض لها هذه المياه باستخدام معايير خرائط حساسية المياه الجوفية الاوروبية، وتطبيقها على منطقة الدراسة في الاردن تحت الظروف المناخية شبه القاحلة.

وهنا فإن تطبيق تقنية التحسس عن بعد على المعطيات المأخوذة، و فحص استخدام المعلومات المشتقة من الصور والمعلومات الرقمية شكلت هدفا هاما لهذه الدراسة. تبعا للاطلاع السطحي على الالية الموجودة والمتمثلة في استخدام تقنية الاستشعار عن بعد في الهيدروجيولوجيا ورسم حساسية المياه الجوفية للملوثات، فإن هذه التقنية والتي تم تطبيقها وتوضيحها في هذا العمل قد استخدمت لتحليل الصور وتصنيفها، بالإضافة الى انشاء صور متعامدة في التحليل والمعاملة باستخدام تقنية مسح المعلومات الجيولوجية. بالتالي فقد تم فحص مدى فعالية هذه العملية لمعالجة المعلومات المعطاة لحساسية المياه الجوفية ورسم المخاطر بواسطة الاستشعار الصوري عن بعد في المناطق التي لا يوجد فيها معلومات كافية أو قياسات عن حجم المخاطر أو الملوثات التي تتعرض لها هذه المياه.

إن المعلومات المتوفرة من ثلاث لواقط استشعار ادخلت باستخدام تقنيات تفسير الصور المرئية ومعالجة الصور المرئية: الصور الفضائية للأرض LANDSAT ETM<sup>+</sup>، الصور الرقمية الهوائية الملونة (1:10.000)، والصور الورقية الهوائية غير الملونة (1:30.000).

خرائط الغطاء الأرضي، وخرائط استخدام الأراضي من الخرائط ذات الدلالة بما فيها خرائط الطرق والمناطق السكنية بالإضافة الى حجم ومواقع ملوثات المياه الجوفية كانت قد اعدت باستخدام الصور المتعامدة و التصوير الفضائي للأرض بواسطة LANDSAT ETM<sup>+</sup>.

في جزء من المنطقة استخدمت صور رقمية هوائية عالية التحليل لتقييم درجة التجوية للصخور ومواقع وامتداد الملوثات ذات المصدر المحدد.

بالإضافة الى ذلك، فإن الطبقات المجسمة من معطيات الخرائط المحورية قد تم انتاجه باستخدام GIS اعتمادا على الدراسات الحقلية والمخبرية. هذه الطبقات تحتوي ايضا على معلومات عن الخصائص الهيدروجيولوجية، المعلومات الجيولوجية، خصائص التربة، ومعلومات رقمية عن مستويات الارتفاعات السطحية. في هذا السياق فان الرسم الخرائطي المكثف للتربة وخصائصها بالإضافة الى الدراسات التفصيلية الحقلية للتربة كالمحيط الاساسي لحساسية المياه للملوثات كان على درجة كبيرة من الاهمية.

أظهرت النتائج بأن استخدام الصور التعامدية بالإضافة الى GIS هي أكثر الطرق المترافقة دقة وصحة وفعالية في المنطقة المدروسة، مقارنة مع نتائج LANDSAT ETM<sup>+</sup> فقد سمحت الصور المتقابلة عالية التحليل بالتفسير الدقيق للخواص الدقيقة، فعلى سبيل المثال إبراز خاصية التجوية Karstification للصخور والمناطق الزراعية مع امتدادات صغيرة، والتي كانت من الاهمية بمكان لتقييم المخاطر على المياه الجوفية.

أظهرت خريطة شدة المخاطر على المياه الجوفية بوضوح المناطق الحساسة للتلوث و " النقط الساخنة" للملوثات الكامنة في منطقة الدراسة والمأخوذة من خريطتي حساسية المياه الجوفية و المخاطر الكامنة. ففي

المناطق العمرانية المأهولة فإن شدة المخاطر تكون أعلى بسبب وجود العديد من الملوثات المتداخلة مع بعضها. بالإضافة الى المنطقة العمرانية في منطقة الدراسة فإن سخور الحجر الجيري المجوية والفاقدة للرسوبيات أو غطاء التربة هي أيضا مناطق ذات حساسية عالية للملوثات. إن الخطر الملوث الاساسي في المنطقة المفحوصة هي ذات نوع محدد المصدر والنتاج عن التسريب من شبكات المياه العادمة، الري، مخلفات الحيوانات، الحفر الامتصاصية و محطات كراجات السيارات والتي لا تأخذ بعين الاعتبار الأراضي الغير عازلة ومكبات النفايات غير القانونية.

يمكن للنتائج المأخوذة من هذه الدراسة لشدة مخاطر الملوثات على المياه الجوفية أن يكون لها دور كبير في عملية التخطيط طويل الأمد حول إجراءات الحماية والتقليل من مخاطر هذه الملوثات على المياه الجوفية، كما ويمكن نقل هذه التقنية إلى منطقة أخرى لها نفس الظروف المناخية والغطاء الأرضي. لذلك فإن معالجة وتفسير نتائج الاستشعار عن بعد سوف لن تكون التقنية الوحيدة الممكنة لتطبيقها لاستبدال عملية الحصول على المعلومات بشكل تقليدي، فقد أظهرت النتائج أن الإستخدام المتكامل لبرنامج GIS وتقنية الإستشعار عن بعد هي الإداة القوية والفعالة لتقييم شدة مخاطر الملوثات على المياه الجوفية. إن الكمية الكبيرة للمعلومات المشتقة من الصور الرقمية وفرت فرصة جديدة لتقييم حساسية المنطقة للملوثات والمخاطر البيئية، وخصوصا تلك المعايير ذات العلاقة باستخدام الأراضي، الغطاء النباتي، والنشاط العمراني والبنية التحتية والتي جعلت هذه الطريقة ذات قيمة ومغزى لعملية التقييم للأجسام المائية المهددة.



## תקציר

### שימוש בהדמיית חישה מרחוק לשם מיפוי צפיפות סיכוני מי תהום, באזור וואדי שוהיב, ירדן

מטרתו העיקרית של המחקר המוצג הינה הפקת מפות רגישות מי תהום, מפות סיכוני מי תהום, ומפות צפיפות סיכוני מי תהום. העבודה מתבססת על קיום מנחים אירופאים קיימים, למפות רגישות וצפיפות סיכוני מי תהום, תוך התאמתם לתנאים הסמי – ארדיים של אזור הניסוי בירדן. בתוך כך, ישום רכישת נתוני הדמיות חישה מרחוק, ובדיקת הישימות של נתונים אלו להפקת מידע תמאטי דיגיטאלי הוו מטרות עיקריות. לאחר סקירה כללית של תפישות קיימות לשימוש בחישה מרחוק ליישומים הידרוגאולוגיים בכלל, ולמיפוי רגישות וסיכוני מי תהום בפרט. נבחרו מספר שיטות מתוך השיטות שנלמדו, השיטות ששימשו במחקר זה מתוארות להלן. בנוסף, להדגמת השיטות באמצעות תוצאות העיבוד וניתוח נתוני החישה מרחוק, ובכלל כך, שיטת המיון, הכנת תמונות אורטופוטו, ושימוש בשיטות GIS לאחר שלבי העיבוד הראשוניים. לבסוף, לשם הכנת מפות רגישות וצפיפות סיכונים למי התהום הוערכה מידת היעילות של שימוש בשיטות איסוף מידע קלאסיות באזור בו כמות הנתונים ואפשרות איסוף הנתונים הינם מוגבלים, תוך הסתייעות בנתוני חישה מרחוק למילוי החסר.

המידע התקבל על ידי שלושה חיישנים סבילים, בשילוב עם ניתוח הדמיות ויזואליות, ועיבוד תמונה דיגיטאלי, ובכלל כך הדמיות Landsat ETM<sup>+</sup>, צילומי אויר דיגיטאליים צבעוניים (1:10,000) וצילומי אויר פנכרומאטיים אנלוגיים (1:30,000). מפות כיסוי ושימושי קרקע, לצד מפות תמאטיות כדוגמת מפות דרכים, אזורי ישוב, מיקום ומימדי סיכוני מי תהום, הוכנו בעזרת תמונות האורטופוטו ונתוני ה Landsat ETM<sup>+</sup>. בחתך אחד של אזור העבודה נעשה שימוש בתצלומי אויר בהפרדה גבוהה על מנת להעריך את מידת הקרסטטיפיקציה, ולזיהוי ומיקום מקורות סיכום נקודתיים.

בנוסף, שכבות תמאטיות של נתוני מרחביים ולא מרחביים שמשו לעזר באמצעות שילוב בפלטפורמת GIS ובהתבסס על מחקר השדה ועבודת המעבדה. השכבות התמאטיות כללו מאפיינים הידרוגיאולוגיים, מידע גיאולוגי, תכונות הקרקע ו DEM. בהקשר זה המיפוי האינטנסיבי של קרקעות ותכונותיהן, בנוסף לעבודות מעבדה ושדה מקיפות שלמדו את תכונות הקרקעות הוו בסיס ראשון במעלה ליצירת מפתח להערכת רגישות וצפיפות סיכוני מי התהום. התוצאות מלמדות כי שימוש משולב בתמונות אורטופוטו עם GIS הינו השילוב המדויק, היעיל והמתאים ביותר לאזור המחקר. בניגוד לנתוני ה Landsat ETM<sup>+</sup> ההפרדה המרחבית הגבוהה של תמונות האורטופוטו מאפשרת פענוח מפורט של מאפיינים קטנים (כדוגמת: מאפיינים קרסטיים ומאפייני אזוריים חקלאיים מקומיים), אשר להם חשיבות בהערכת סיכונים.

מפת עוצמות סיכוני מי התהום מלמדת בבירור כי אזורי הרגישות וה "נקודות החמות" של פוטנציאל הזיהום באזור המחקר, נובעים משילוב של בין מיפוי אזורי מקורות הזיהום ואזורי רגישות מי התהום. עוצמת הסיכון הגבוהה ביותר אופיינה באזורים עירוניים, שכן, באזורים אלו קיים שילוב של מקורות זיהום מגוונים, לצד תשתית קרבונאטית קרסטית חשופה ולפיכך בעלת מקדם רגישות גבוה ביותר, אשר מאפיינת את מרבית האזורים העירוניים באזור המחקר. מקורות הסיכון העיקריים הם מקורות נקודתיים כדוגמת מערכות ניקוז עירוניות לקויות או חסרות, חוות, ערימות זבל, בורות סופגים, אזורי שירות לכלי רכב חסרי חיפוי, ניקוז וטיפול וגם אתרי סילוק פסולת פיראטיים.

הפעלת מיפוי עוצמות הזיהום בתכנון אזורי הינה בעל חשיבות להשמת אמצעי מיגון למי התהום ולמימוש שיטות אלו גם באזורים נוספים בעלי תנאים אקלימיים וגיאומורפולוגיים דומים. שימוש בעיבוד וניתוח של נתוני חישה מרחוק אינו יכול להחליף שיטות איסוף מידע קלאסיות, התוצאות מלמדות כי שימוש משולב ב GIS עם שיטות חישה מרחוק הוא כלי חזק להערכת עוצמות סיכוני זיהום מי תהום. כמות המידע הגדולה שמושגת מהמידע הדיגיטאלי מציעה אפשרויות חדשות להערכת סיכוני ורגישות מי תהום, ובייחוד במשתנים הקשורים בשימושי קרקע, כיסוי צמחיה ובנוסף תהליכי איור ופיתוח תשתיות אשר גורמים לגישה זו לקבל משנה חשיבות להערכת רמות הסיכון לגופי מי התהום.

## ACKNOWLEDGEMENTS

This thesis was prepared at the Department of Applied Geology at the University of Karlsruhe and supervised by Prof. Dr. H. Hötzl. First of all I would like to thank him for the possibility to accomplish my PhD thesis within the framework of an international research project and for supporting me in completing this thesis with valuable suggestions and discussions. My sincere gratitude is also to Prof. Dr. H.P. Bähr from the Institute of Photogrammetry and Remote Sensing for correcting this thesis and being my co-referee.

I am grateful to Dr. Manfred Sties for the introduction to the field of remote sensing, for his continuous support and interest in my studies, for inspiring discussion, helpful comments and corrections.

Many thanks to all the colleagues from Germany, Israel, Jordan and Palestine of the multilateral project "Water Resources Evaluation for a Sustainable Development in the Jordan Rift Basin" for the motivating discussions and their support during the last years of scientific cooperation and friendship.

I would like to thank Prof. Dr. Elias Salameh and his staff from the Geological Department of the Jordan University for his friendliness and his support during my fieldwork in Jordan. I am also thankful for the support I received from the Ministry of Water, the Jordan Valley Authority, the Water Authority of Jordan, and the Natural Resources Authority in Amman.

I am grateful to Dr. Wasim Ali for translation help and for his introduction in the Arabic culture and to William Al-Khoury and his family from Fuhays, Jordan. I will never forget the kindness and hospitality they offered me in Jordan.

Many thanks to Prof. Akiva Flexer and Dr. Annat Yellin-Dror and from Tel Aviv University in Israel for their support and corrections of parts of my thesis.

I would like to thank my diploma students for their field- and laboratory work that contributed partly to this thesis

I am grateful to Oliver Sonnentag and Jennifer Striebel and Claus Heske for language review, corrections and technical support. My appreciation goes to all my colleagues at the University of Karlsruhe for the good time, and excellent cooperation.

I would like to thank all other people that deserved acknowledgements for their help, great support and assistance in the last few years.

Finally I would like to express my gratitude to my parents for their support and to Christoph for his understanding, serenity and his continuous kindly encouragement.



## CONTENTS

Kurzfassung .....	III	
Abstract .....	V	
الخلاصة .....	VII	
תקציר .....	IX	
Acknowledgements .....	XI	
Contents .....	XIII	
List of Figures .....	XV	
List of Tables .....	XVIII	
<b>1</b>	<b>Introduction .....</b>	<b>1</b>
1.1	Overview and objectives .....	1
1.2	Research and cooperation .....	3
1.3	The role of groundwater in Jordan .....	3
<b>2</b>	<b>Test Area .....</b>	<b>5</b>
2.1	Topography, climate and general characteristics .....	5
2.2	Vegetation .....	7
2.3	Geological framework .....	7
2.4	Stratigraphy .....	13
2.5	Tectonics .....	16
2.6	Hydrogeology .....	20
<b>3</b>	<b>Theoretical Aspects of Groundwater Vulnerability, Hazards and Risk</b>	
	<b>Intensity .....</b>	<b>27</b>
3.1	Groundwater vulnerability .....	27
3.2	Groundwater hazards .....	28
3.3	Groundwater risk intensity .....	30
<b>4</b>	<b>Theoretical Aspects of Remote Sensing .....</b>	<b>31</b>
4.1	Physical principles of remote sensing .....	31
4.2	LANDSAT ETM <sup>+</sup> .....	32
4.3	Satellite image classification .....	34
4.4	Normalized Difference Vegetation Index (NDVI) .....	35
4.5	Orthophotos .....	36
<b>5</b>	<b>Remote Sensing in Hydro(geo)logy, Groundwater Vulnerability and</b>	
	<b>Hazard Mapping .....</b>	<b>37</b>
5.1	Introduction .....	37
5.2	Applications in the field of hydrogeology .....	39
5.3	Applications for groundwater vulnerability and hazard mapping .....	42
<b>6</b>	<b>Data Sets and Methodology .....</b>	<b>45</b>
6.1	Introduction .....	45
6.2	LANDSAT ETM <sup>+</sup> data .....	46
6.3	Analogues black and white photographs (1:30,000) .....	64
6.4	Digital colour photographs .....	69
6.5	LANDSAT ETM <sup>+</sup> image contra orthophotos .....	74
6.6	Soil investigations .....	76
6.7	Additional spatial and non-spatial data .....	85

<b>7</b>	<b>Groundwater Vulnerability in the Test Area .....</b>	<b>87</b>
7.1	Protective cover (P-factor).....	87
7.2	Infiltration conditions (I-factor).....	89
7.3	Results .....	91
7.4	Error discussion.....	94
<b>8</b>	<b>Groundwater Hazards in the Test Area .....</b>	<b>97</b>
8.1	Introduction.....	97
8.2	Compilation of the hazard map .....	98
8.3	Results .....	101
8.4	Error discussion & conclusions .....	106
8.5	Applicability of the COST Action 620 in the test area.....	107
<b>9</b>	<b>Groundwater Risk Intensity in the Test Area.....</b>	<b>111</b>
9.1	Introduction.....	111
9.2	Results .....	112
9.3	Use of the risk intensity map for groundwater management.....	113
<b>10</b>	<b>Usefulness of Remote Sensing Data for Groundwater Risk Intensity</b>	
	<b>Mapping.....</b>	<b>115</b>
10.1	Overview .....	115
10.2	Lessons learned.....	116
<b>11</b>	<b>Recommendations .....</b>	<b>121</b>
11.1	Choice of the remote sensing data.....	121
11.2	Choice of the image analysing software.....	121
11.3	Validation of the results .....	122
11.4	Delineation of groundwater protection zones .....	122
11.5	Groundwater management in the test area.....	122
<b>12</b>	<b>References .....</b>	<b>125</b>
<b>13</b>	<b>Appendix.....</b>	<b>137</b>

## LIST OF FIGURES

Fig. 1.1:	Circle irrigation (24 h/d) of potatoes growing in the middle of the southern desert in the Wadi Disi (photograph taken October 2001).....	4
Fig. 1.2:	Section of a Landsat scene (bands 5/4/3 merged with panchromatic band) of the southern desert of Jordan. Coloured circles show irrigated fields. ( <a href="http://www.eurimage.com/gallery/webfiles/ls_deserts.html">http://www.eurimage.com/gallery/webfiles/ls_deserts.html</a> ).....	4
Fig. 2.1:	a) Location of the test area in Jordan, b) Location and extent of the Middle East ( <a href="http://www.wikipedia.de">www.wikipedia.de</a> ), c) Test area with major towns and streets.....	5
Fig. 2.2:	Characteristic land cover types of the test area: a) In the southwestern part (below sea level) agriculture and dense vegetation is limited to the existence of continuous soil cover which mainly exists on the valley floors. b) In the northern part pasture and agricultural areas dominate (photographs taken April 2002). .....	6
Fig. 2.3:	Mean monthly precipitation values (1971-1991) at four gauging stations in the test area.....	6
Fig. 2.4:	Tectonic plate boundaries in the Near East and location of Jordan (modified after Johnson, 1998).....	8
Fig. 2.5:	Lithofacies belts Cretaceous times: a) Early Cretaceous facies belts: (1) mostly continental sandstone, (2) sandstones-shale-limestone facies, (3) thick marine shaley sequence and volcanism; b) Mid-Cretaceous (Aptian-Turonian) lithofacies: (1) thin carbonate sequence, interbedded with sandstone, (2) mostly carbonates (limestones and dolomites), (3) mostly calcilutite facies; c) Senonian lithofacies belts: (1) sand, flint and chalk, (2) chalk marl and flint (3) mostly chalk, sparse flint (modified after Flexer, 2001).....	10
Fig. 2.6:	Regional setting Dead Sea Tranform. A=Arava valley; B=Beer sheva valley; G=Galilei; J=Jericho; L=Lebanon; T=Lake Tiberias; Y=Yizreel valley, (Garfunkel & Ben-Avraham, 1996). .....	12
Fig. 2.7:	Sequence of the Ajloun Group and indicated boundaries of the A3, A5/6 and A7 formations, (image width: 600 m photograph taken 11.09.2002). .....	14
Fig. 2.8:	Cavernous Hummar Formation showing prominent, massive cliffs in the upper part (image width: ~ 25m, photograph taken 02.05.2005).....	15
Fig. 2.9:	Location of the Wadi Shueib Structure (modified after Qassem, 1997).....	18
Fig. 2.10:	Normal fault; showing a dip-slip displacement of approximately 50 m of the massive limestones of the Hummar Formation (photograph taken 03.05.2005).....	18
Fig. 2.11:	Geological Map of the test area (modified after Shawabkeh, 2001; Moh'd & Muneizel, 1998; MacDonald & Partners, 1963; Sawarieh & Barjous, 1993).....	19
Fig. 2.12:	Geological cross section of the test area (modified after Shawabkeh, 2001). The location of the cross section is indicated in Fig. 2.11. ....	19
Fig. 2.13:	Wadi Sir Formation showing typical microkarst relief, cave systems and a "blocky" appearance of the landscape (photographs taken 03.05.2003).....	21

Fig. 2.14:	Location and aquifer system of the main springs in the test area and the wadi courses on top of a DEM (spatial resolution 15 m). .....	22
Fig. 4.1:	Spectral characteristics of (a) energy sources, (b) atmospheric transmittance, and (c) common remote sensing systems (Lillesand & Kiefer, 2004). .....	31
Fig. 4.2:	Typical spectral reflectance curves for vegetation, soil, and water (Lillesand & Kiefer, 2004). .....	32
Fig. 5.1:	Applications of remote sensing in hydrology, hydrogeology and groundwater management (text modified and supplemented after Hochschild, 1998, image: NASA.).....	38
Fig. 5.2:	Infiltration rate image of research area, as generated on the basis of soil reflectance information. A low infiltration rate area is marked as A on the image, high infiltration areas are marked as B,C, D (Ben-Dor et al. 2004). .....	40
Fig. 6.1:	Processing steps and data types of the present study.....	45
Fig. 6.2:	Characteristic examples of the NDVI cover classes. Type a) is dominating on elevations below sea level in bad lands with sparse soil and vegetation cover, quarries and urban areas. Type b) is dominating in elevations above sea level above limestones with patchy soil cover or mature yellow or harvested crops. Type c) is dominating in areas with agricultural fields with green crops, orchards, oaks and pine trees with intervals of several meters between the trees. Type d) is dominating over dense orchards and pine or oak trees, in the majority of cases located close to a wadi course or well irrigated agricultural fields. ....	48
Fig. 6.3:	Unsupervised classification result of the LANDSAT ETM <sup>+</sup> data of the test area. ....	52
Fig. 6.4:	Class area percentage of the unsupervised classification of the LANDSAT ETM <sup>+</sup> data.....	53
Fig. 6.5:	Mean grey values of the training areas of the used bands of the LANDSAT ETM <sup>+</sup> image.....	57
Fig. 6.6:	Supervised classification results of the LANDSAT ETM <sup>+</sup> data of the test area. ....	59
Fig. 6.7:	Class area percentage of the supervised classification of the LANDSAT ETM <sup>+</sup> data.....	59
Fig. 6.8:	a) Aerial photograph with displayed Ground Control Points (P) and collected Tie points, partly manual (Tk) and automatically collected (AT). b) Orthophoto derived after rectification process of the aerial photograph.....	65
Fig. 6.9:	Orthophoto defects in the test area: a) heavy distortions lead to a curved border of an originally straight acre boundary, b) tonal differences between two orthophotos.....	66
Fig. 6.10:	Examples of thematic maps derived by on-screen digitising the orthophoto-mosaic of the black & white aerial photographs 1:30,000. ....	68
Fig. 6.11:	Digital orthophotos (1:10,000) overlaid by the geology (70 % transparent) and digitised thematic layer showing three levels of karstification. The grey box indicates the coverage of the digital colour orthophotos in the study area. ....	71



Fig. 6.12:	Section of the automatic supervised classification result of the digital aerial colour photographs after merging of informational classes. ....	72
Fig. 6.13:	Supervised classification results of the LANDSAT ETM <sup>+</sup> data overlaid by the thematic maps of the orthophotos generated within ArcGIS.....	74
Fig. 6.14:	Soil map of the test area including soil coring and soil locations (Werz et al., 2006).....	77
Fig. 6.15:	Lithic Leptosol fills and seals karst cavity. (Photograph taken May 2003.) .....	79
Fig. 6.16:	Hydraulic conductivities of representative soil locations (modified after Werz et al., 2006).....	82
Fig. 6.17:	Granulometric parameters: unconformity and gradation of representative soil locations (modified after Werz et al., 2006). ....	82
Fig. 6.18:	Soil thickness of representative soil locations (modified after Werz et al., 2006).....	83
Fig. 6.19:	CEC, eFC and pH values of representative soil locations (modified after Werz et al. 2006).....	83
Fig. 7.1:	Determination of the P-factor (Goldscheider, 2002). ....	87
Fig. 7.2:	Annual precipitation in the test area and surroundings based on modelling results from Orthofer (2001). Cell size 850 m.....	88
Fig. 7.3:	Determination of the I-factor (Goldscheider, 2002).....	90
Fig. 7.4:	Determination of the dominant flow process (after Goldscheider, 2002).....	90
Fig. 7.5:	a) P-Factor map showing the protective cover effectiveness, b) I-Factor map showing the infiltration conditions expressed as degree of bypassing. ....	92
Fig. 7.6:	Groundwater vulnerability map of the test area. ....	93
Fig. 7.7:	a) Area percentage of the assigned topsoil values for the protective cover; b) area percentage of the existing vulnerability classes. ....	94
Fig. 8.1:	Schematic illustration of the main hazards in the test area (Werz & Hötzl., 2005).....	97
Fig. 8.2:	Hazard types, weighting value (H) and number of occurrence of the hazard types in the test area; n.n. indicates that there are no numbers for the hazards are existing.....	99
Fig. 8.3:	Unclassified hazard map of the test area (modified after Storz, 2004).....	102
Fig. 8.4:	Occurrence of a) industrial hazards, b) municipal hazards, c) agricultural hazards. ....	103
Fig. 8.5:	Classified Hazard map of the test area (modified after Storz, 2004). ....	105
Fig. 8.6:	Leaking oil pump in the test area causing a significant point hazard.....	107
Fig. 9.1:	Diagram of risk intensity index calculated after equation (9.1). Five classes were assigned to build risk classes (after Hötzl et al., 2004).....	111
Fig. 9.2:	Risk intensity map of the test area (Werz & Hötzl, 2005). ....	112
Fig. 10.1:	Effect of ground resolution cell size of different remote sensing images used in this work (illustration modified after Lillesand & Kiefer, 2000). ....	117

## LIST OF TABLES

Tab. 2.1:	Stratigraphy in the Wadi Shueib catchment area (modified after Powell, 1989). The numbers (Z1, ..., B2) indicate the common used shortcuts for the geological units.....	13
Tab. 2.2:	Location and discharge of the major springs in the test area.....	23
Tab. 2.3:	Results of hydrochemical analysis of the major cations and anions in the three major springs of the test area (source: Analysis of the Geological Department, University of Amman). ....	24
Tab. 2.4:	Results of hydrochemical analysis heavy metals in the three major springs of the test area (source: Analysis of the Geological Department, University of Amman).....	24
Tab. 2.5:	Microbiological analysis of the three main springs in the test area. ....	25
Tab. 3.1:	Three levels of hazard classification. The example of municipal waste shows the level III hazard type classification (modified after De Ketelaere et al., 2004). ....	29
Tab. 4.1:	Spectral bands of the LANDSAT ETM+ sensor (grey: band not used in this work).....	33
Tab. 6.1:	Projection parameters of the used remote sensing images and thematic data layers.....	46
Tab. 6.2:	Parameterisation (given in PCI Geomatics terminology) for the ISODATA clustering algorithm. ....	51
Tab. 6.3:	Separability of the spectral classes using Bhattacharya distance.....	60
Tab. 6.4:	Confusions matrix of the supervised classification of the LANDSAT ETM+ data. ....	61
Tab. 6.5:	Vegetation classes according to specific NDVI value ranges. ....	48
Tab. 6.6:	Degree of karstification / fracturing (F) used for the calculation of the vulnerability after the PI-method, Goldscheider (2002). ....	69
Tab. 6.7:	Interpretation key used for the classification of the three levels of karstification following the PI-method after Goldscheider (2002). ....	70
Tab. 6.8:	Comparison of the percentages of agricultural areas in the study area based on the information derived from different remote sensing data sources and processing steps. ....	75
Tab. 6.9:	Soil map units in the test area based on reference soil types and added qualifiers of the WRB (modified after Kuntz, 2003). ....	78
Tab. 6.10:	Analysed soil parameters and implemented soil tests in the test area. For detailed descriptions of the individual tests refer to Kuntz, 2003. ....	80
Tab. 6.11:	Typical saturated infiltration rates for specific soil textures. ....	81
Tab. 6.12:	Saturated infiltration rates in the test area.....	81
Tab. 7.1:	Legend of vulnerability, P-factor and I-factor map (after Goldschneider, 2002). ....	93

Tab. 8.1:	Evaluated hazard index of the urbanisation in relation to the percentage of connected houses to the sewer system (modified after Storz, 2004). .....	100
Tab. 8.2:	Distribution and proportion of the hazard index (HI) classes in the test area. ....	105
Tab. 10.1:	Thematic layers used for the groundwater vulnerability (dark grey shaded) and hazard assessment (light grey shaded) based on information from remote sensing imagery. ....	115



# 1 INTRODUCTION

## 1.1 Overview and objectives

At present, Jordan as well as many other Middle-East countries is over-using all of its annual renewable freshwater resources. The growing demand for water supply is a result of the fast socio-economic development of Jordan and causes serious problems related to the availability of water resources, resources depletion, and excessive exploitation. The over-extraction of groundwater resources has degraded water quality, resulted in the abandonment of many water wells (Chebaane et al., 2004; Al-Kharabsheh-Atef, 1999) and endanger a future use of the limited groundwater resources (Dottridge & Abu-Nizar, 1999; Salameh, 1996; Jiries, 1999). Furthermore, water quality is also at risk by groundwater hazards. Increased salinity, pollution from coliforms and nitrogenous wastes, contamination from agro-chemicals, such as pesticides, pathogens, toxic and heavy metals are the major quality degradation indicators. Especially the groundwater of the Cretaceous karst aquifers in Jordan is highly vulnerable due to its inherent characteristics namely high flow velocities, short residence time and fast hydraulic reactions.

The contamination of the aquifers depends on the impact from domestic pollution, solid waste, from industry and fertilizer application by agriculture. The sources of domestic pollution are wastewater leakage in built-up areas, effluents and leakage from dumping sites, and leakage from sewer systems. An assessment of the aquifer situation and more efficient management strategies are required in order to improve the environmental situation in Jordan and the neighbouring states including the establishment of groundwater protection areas for source and resource protection of groundwater based on the implementation of groundwater protection concepts.

Until now, Middle East countries like Jordan miss a consistent approach for groundwater protection and sustainable management strategies, therefore in my PhD research an existing European concept was tested with respect to its transferability on a test area in Jordan. The applied European concept was developed by the COST Action 620 focusing in an improved and consistent approach for the protection of karst groundwater on a European level given impetus by the European Water Framework Directive, which provides a common framework for water resource policy and management (Zwahlen et al., 2004). COST is the acronym for "European Cooperation in the field of Scientific and Technical Research" and is a framework for international research and development cooperation supported by the European Union that covers a wide range of scientific topics organized in so-called COST actions. The COST Action 620 "Vulnerability and risk mapping for the protection of carbonate (karst) aquifers" was established to develop an approach for the protection of karst aquifers. The COST Action 620 approach focuses on the assessment of the groundwater vulnerability, the potential groundwater hazards and the groundwater risk intensity of an aquifer as a basis for protection strategies. In this context the term groundwater vulnerability is used to define the sensitivity of the geological sequence that contaminants can pass through. Groundwater hazards are defined as potential sources of contamination resulting from human activities taking place mainly at the land surface (Hötzl et al., 2004). And finally the risk intensity map reflects the probability of groundwater to be actually contaminated by human activities showing that the highest risk of contamination exists where a dangerous hazard is located in zones that are characterized by highly vulnerable aquifers.

In Middle East countries a major challenge for the mapping of groundwater vulnerability and potential groundwater hazard is the sparse, non-suitable or even non-available topographical, hydrological or hydrogeological database. Besides data gained by conventional field investigations remote sensing imagery can be used to fill partly the lack of data and can provide additional information that is not available on topographic maps. The main advantage of remotely sensed imagery compared to conventional techniques is that it allows for a fast and complete collecting of regional spatial data, especially in inaccessible areas missing topographic data. The large amount of information derived from digital images offers new opportunities for groundwater vulnerability and hazard assessment, particularly those parameters related to land use and vegetation coverage (Werz & Hötzl, 2005). During the last years the number of satellite and airborne platforms has multiplied and their spatial resolution, global coverage, and orbital frequency have increased. The generation of digital orthophotos on desktop systems has to be considered as state-of-the-art and provides an important tool for visualizing information (Krupnik, 2003). Imagery, either from satellites or aerial photography, is widely used for updating or completing GIS data sets from base maps to thematic overlay (Williams, 2001). Within a GIS environment display, manipulation and combination of the information derived from remote sensing imagery with data from field investigations, and the analysis of the relevant data in an associated database can be performed. The three major goals of this thesis can be summarized as:

- to apply and transfer the European concept for hazard and risk intensity mapping developed by the COST Action 620 (Zwahlen et al., 2004), and the vulnerability concept developed by Goldscheider (2002) to a test area in Jordan that is considered as a developing country under (semi)-arid climatic conditions;
- to develop and test the integrated use of a GIS data and remote sensing imagery for the assessment and the mapping of groundwater vulnerability, groundwater hazards and groundwater risk intensity to improve the data situation in the test area and to investigate to what extent conventional procedures of data acquisition can be enhanced by information extracted from remote sensing imagery;
- to accomplish detailed field- and laboratory investigations, to collect and generate auxiliary data of the test area that could not be derived from remote sensing imagery such as information about the protective potential of the soils, digital terrain data and specific hazard characteristics that are needed for European approaches.

The thesis is organized into 11 sections. Following the Introduction Chapter 2 gives a detailed description of the geographical, climate, hydro(geo)logical and geological characteristics of the test area. Chapter 3 gives an overview of the theoretical aspects of groundwater vulnerability, hazard- and risk intensity mapping. Chapter 4 delineates the basic principles of remote sensing and photogrammetry. Chapter 5 provides background information on existing methods for the integration of remote sensing data in the field hydrogeology and in the field of groundwater vulnerability and hazard mapping. The data set and methodology part in chapter 6 gives a detailed outline with the purpose to introduce the computational environment, present the remote sensing data processing that was applied and the obtained results, and the field and laboratory

investigations. Chapter 7-9 describe the generation of groundwater vulnerability, hazard and risk intensity maps of the test area using the thematic layers derived from remote sensing imagery and the results of the field- and laboratory work and additional collected or processed data of the test area. The thesis closes with a discussion of the significance and usefulness of the used remote sensing data for groundwater risk intensity in chapter 10, followed by recommendations and conclusions in chapter 11.

## 1.2 Research and cooperation

The study was accomplished within the framework of the multilateral project: “*Water Resources Evaluation for a Sustainable Development in the Jordan Rift Basin, a German –Israeli-Jordanian –Palestinian Joint Research Program*” (GIJP project) funded and supported by the German Ministry of Education and Research (BMBF 02WT0160) and the Israeli Ministry of Science (MOS). The main goal of this project was the investigation and evaluation of the freshwater resources in the Jordan Valley and its surroundings.

Two diploma theses were carried out and supervised within the framework of this thesis focusing on soils and groundwater-hazards in the test area (Kuntz, 2003; Storz, 2004).

## 1.3 The role of groundwater in Jordan

Jordan is known to be one of the most water scarce countries in the world, where it is a challenge to find a compromise between water demands and water resources management (Ministry of Water and Irrigation (MWI), National Water Master Plan Jordan, 2004).

More than 80 % percent of the area of Jordan consist of desert receiving rainfall of less than 100 mm/a. About 90 % of the annual rainfall is lost to evaporation. Intensive groundwater abstractions often lead to salt-water intrusions and depletion of the aquifers. With a share of 64 % (2001), irrigated agriculture is the major consumer of water in Jordan (Ministry of Water and Irrigation (MWI), National Water Master Plan Jordan, 2004).

There are still many problems to find compromises between the agriculture water demand and a sustainable groundwater management. For example, overexploitation of the Wadi Disi aquifer in the S of Jordan non-renewable fossil groundwater resources for irrigating plants 24 h/d leads to a severe decline in the groundwater levels of the Disi aquifer (Fig. 1.1, Fig. 1.2). In 2003 the Ministry of Water and Irrigation started to charge groundwater abstractions for commercial purposes (Elias Salameh, *personal communication*, 2005) introducing a more efficient and effective management.

During the last years the Jordanian government has built several dams at wadi outflows to prevent freshwater from flowing into the main receiving stream of the Jordan River and finally the Dead Sea, where the water is considered to be lost when mixing with the salt water. The collected dam water is mainly used for agricultural purposes. Besides the salinisation processes caused by the Dead Sea water, salinity of major concern originates from different sources such as salt domes or evaporate layers buried within the Jordan Valley sediments. Furthermore, within

the last years the Jordanian government has put some emphasis on the development of water management strategies (Chebaane et al., 2004). There are several water management options to improve the present groundwater situation in Jordan. Water loss reduction programs, irrigation savings using more effective irrigation methods, changes in cropping pattern and upgrading the non-conventional groundwater resources are some possibilities.



Fig. 1.1: Circle irrigation (24 h/d) of potatoes growing in the middle of the southern desert in the Wadi Disi (photograph taken October 2001).

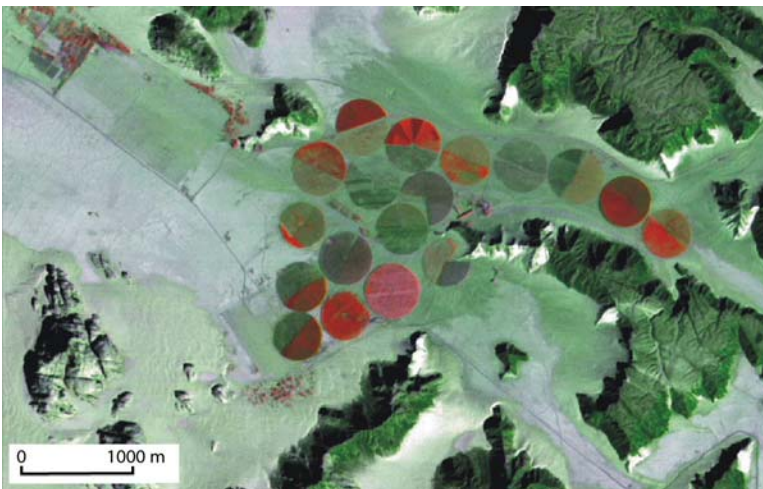


Fig. 1.2: Section of a Landsat scene (bands 5/4/3 merged with panchromatic band) of the southern desert of Jordan. Coloured circles show irrigated fields. ([http://www.eurimage.com/gallery/webfiles/l\\_s\\_deserts.html](http://www.eurimage.com/gallery/webfiles/l_s_deserts.html)).

As non-conventional groundwater resources Jordan started to use treated wastewater, brackish and desalinated water (Abu Shams, 2004; Al-Hadidi et al., 2004; Hardisty et al., 2004; Japan International Cooperation Agency, 1995) to overcome the water shortage. Even though the use of treated waste water affects the marketability and causes limitations for the export and increases the soil pollution farmers would generally accept it in case there would be effective quality control (ECO Consult, Rowena Lee, *personal communication*, 2005).

Pursuant to the Jordanian-Israeli peace treaty the two countries have regulations for sharing the water of the Yarmuk and Jordan river. The import of freshwater from other regions seems rather unfeasible, since the neighbouring countries also suffer from severe hydrologic deficits.



## 2 TEST AREA

### 2.1 Topography, climate and general characteristics

The test area is located in Jordan at 32°00' N and 35°45' E (centre) at the western slopes of the eastern highlands of the Jordan Rift Valley, about 20 km northeast of the Dead Sea (Fig. 2.1). The geographical borders of the test area coincide with the surface catchment of the Wadi Shueib. The total area of the test area is about 185 km<sup>2</sup>. The area is topographically complex, characterized by a steep relief with elevations ranging from -200 m in the southwest up to 1240 m in the northeast.

Land cover and land use of the area present a discrepancy due to small scale variations in climate and relief. The middle and northern parts are dominated by agriculture. Built-up areas are mainly located in the N and the northeastern areas and are characterized by a high population density, which is contrary to the sparsely low populated southern parts of the test area.

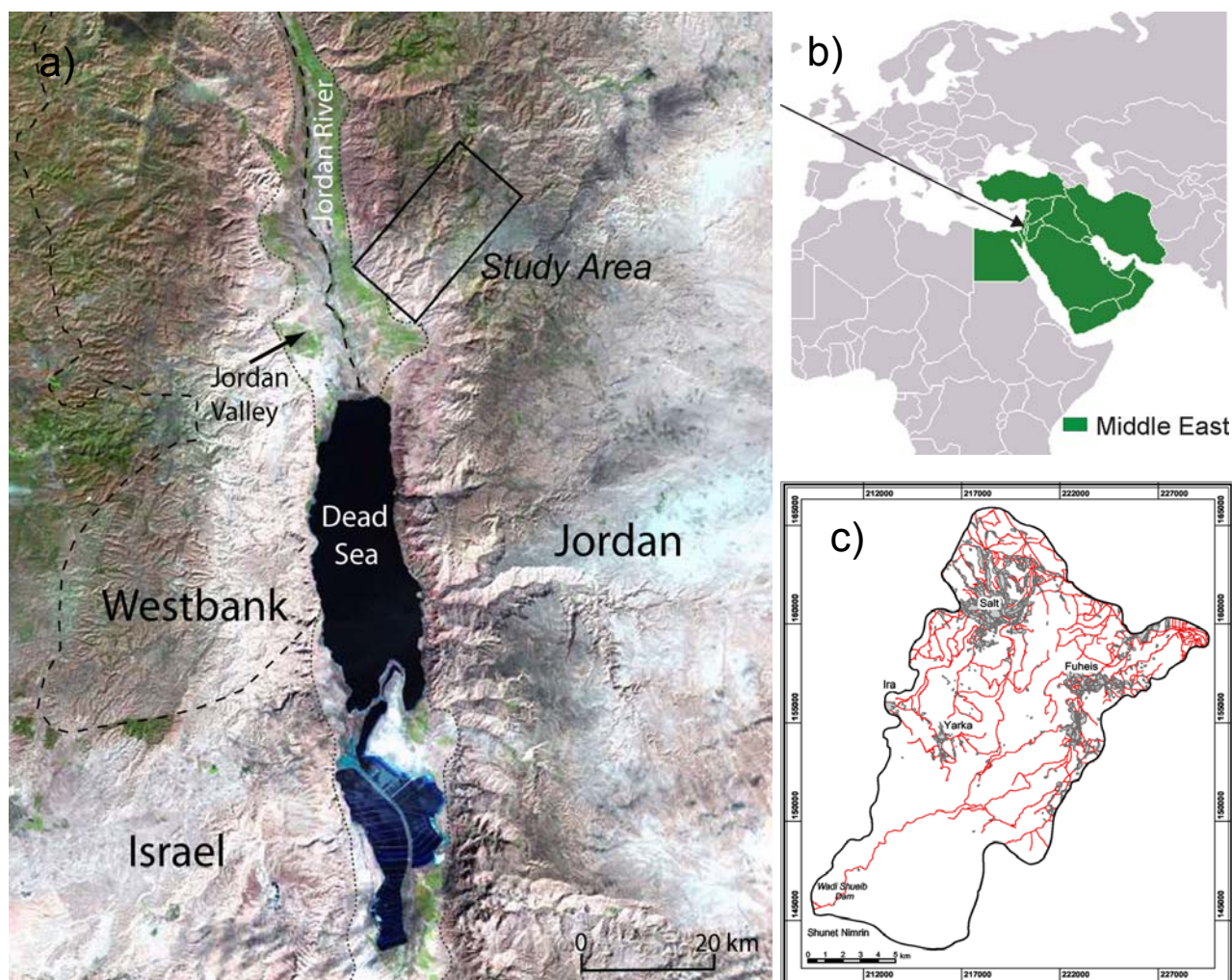


Fig. 2.1: a) Location of the test area in Jordan, b) Location and extent of the Middle East ([www.wikipedia.de](http://www.wikipedia.de)), c) Test area with major towns and streets.

Agriculture in the southern parts is limited to the existence of continuous soil cover which mainly exists on the valley floors. The SW border of the test area lies in the transition zone of the Jordan Rift Valley and the eastern highlands. The area is dominated by limestone rocks, partly highly karstified and often barely covered by soils. The vegetation cover is limited in the southern parts to vicinity of wadi courses, in the middle part and in the N to often patchy accumulations of soils mainly at valley floors or small depressions (Fig. 2.2).

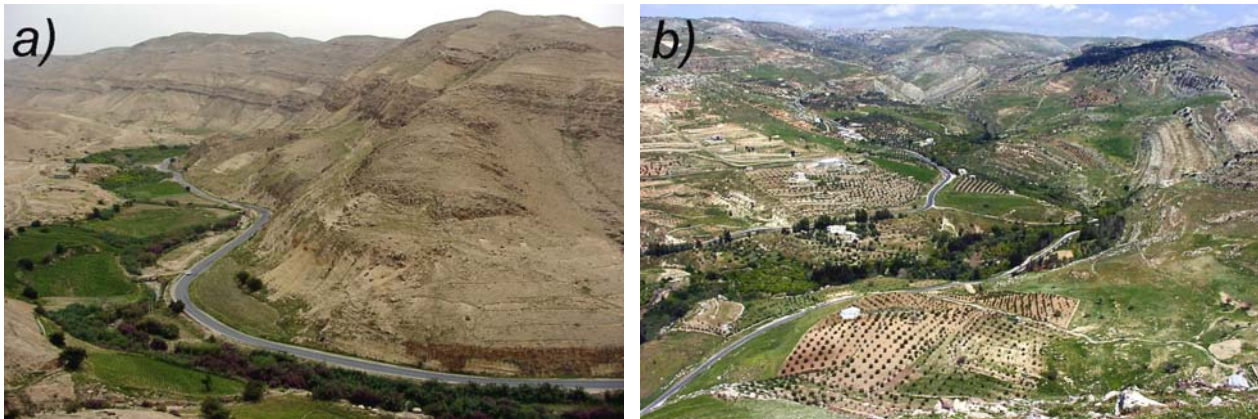


Fig. 2.2: Characteristic land cover types of the test area: a) In the southwestern part (below sea level) agriculture and dense vegetation is limited to the existence of continuous soil cover which mainly exists on the valley floors. b) In the northern part pasture and agricultural areas dominate (photographs taken April 2002).

The climate of the test area is semi-arid and belongs to the Mediterranean climate zone with large seasonal and daily temperature variations (Bender, 1968a). Four rainfall gauging stations are situated within the test area: Salt, Hummar, Wadi Shueib and South Shunet station at elevations of 769 m, 925 m, 300 m, and -160 m. A direct relation exists between the elevation of the gauging station and the precipitation amount (Fig. 2.3).

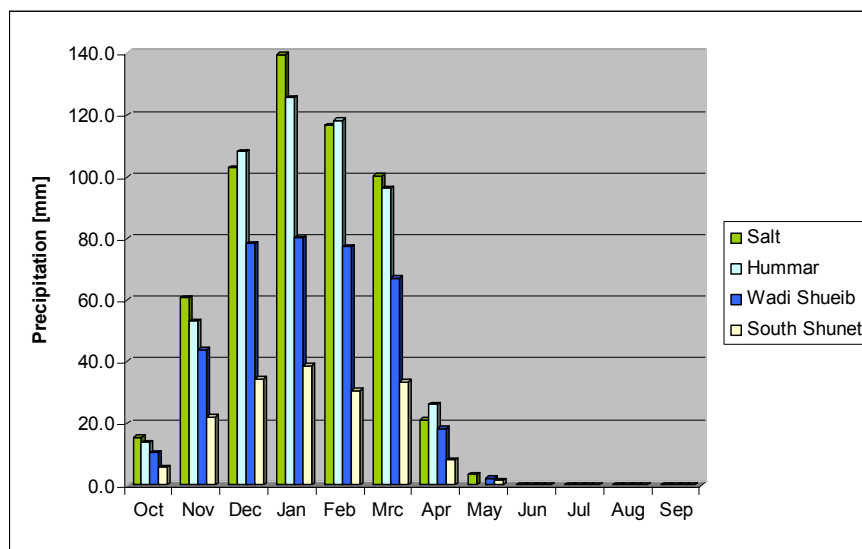


Fig. 2.3: Mean monthly precipitation values (1971-1991) at four gauging stations in the test area.

At South Shunet gauging station, in the south of the test area, the absolute daily temperatures range from a maximum of 47 C° (June 1965) to -4 C° (January 1982), whereas the average annual maximum temperature is 30°C, the annual minimum temperature is 19°C (Ta'any, 1992). Due to the high temperatures and the high evaporation rates only approximately 12 % of the precipitation infiltrates into the aquifer and contributes to groundwater recharge (Ta'any, 1992). Precipitation varies in the test area due to terrain complexity. Annual rainfall decreases rapidly westwards from over 600 mm at the town of Salt to less than 400 mm in the centre of the catchment area and to less than 20 mm in the extreme S at South Shunet (Taa' ny, 1992).

The mean monthly precipitation (1971-1991) in the elevated parts in the N and NE (Salt) of the test area is higher than in the lower parts (South Shunet). The mean annual precipitation (1971-1991) shows therefore a maximum of 560.6 mm at the gauging station in Salt and a minimum of 175.1 mm at the gauging station of South Shunet with a maximum of rainfall between December and March and a minimum in the months June until September.

## **2.2 Vegetation**

In the test area in Jordan the vegetation develops significantly during February and May, depending on the characteristics of the winter and the amount of precipitation. Normally not later than the beginning of June (in dry years even from May) the natural vegetation dries up. In the Jordan Valley due to intensive irrigation agriculture is possible during summer, whereas in the grabenshoulders where the test area is located principally rain-fed agriculture is existing. In the most cases, after one harvest of crops or legumes in June, the agricultural crop lands lie fallow.

Due to the fact that the Wadi Shueib water course itself has water all the year supplied by the outflow of the water treatment plant of Salt, some parts of the Wadi Shueib catchment area have special crop situations. In the flood plain of the wadi downriver of the treatment plant, there are many small agricultural crop lands used for more than one harvest cycle. Also in the area of Yarka and in the surroundings of Salt agriculture is possible during the most time of a year. Above the waste water treatment plant and in the lateral valleys of the Wadi Shueib mainly orchards are existing. On flat areas onto the slopes few agricultural areas, mainly crops exist. In the underflow areas of the Wadi Shueib below the sea water level and at heights slightly above sea level it is too steep and dry for agricultural activities.

## **2.3 Geological framework**

### **2.3.1 Geodynamics**

Jordan is part of the Middle East and is situated at the NW rim of the Arabian plate on the boundary opposite to the Sinai plate (Fig. 2.4). Three ongoing tectonic processes characterize the area of the Middle East: spreading occurs along the Red Sea, convergence is documented along the Cyprian Arc, the Taurus mountain range (in the N of Syria and S of Turkey), the Bitlis Suture and the Zagros thrust zone, whereas sinistral strike-slip movement characterizes the activity along the Dead Sea Transform (DST), also called Akaba-Levante Transform (Eisbacher, 1996), Jordan Rift Valley or Levantine Rift Valley (Horowitz, 2001), Dead Sea Fault Zone (Hall et

al, 2005) or Dead Sea Rift (Quassem, 1997). The processes along the Red Sea show a good example for a modern transition stage between rift development and subsidence of a passive continental margin (Eisbacher, 1996).

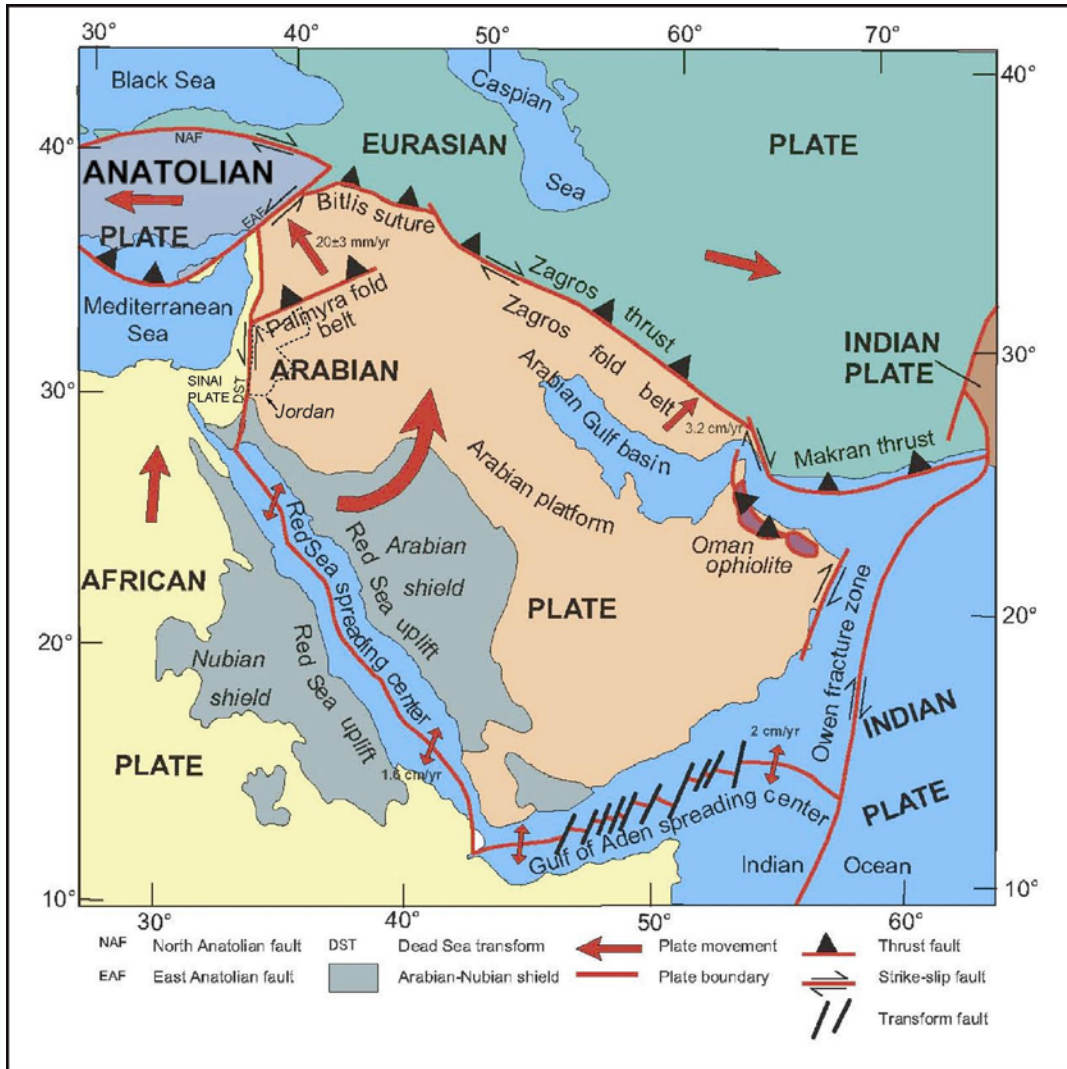


Fig. 2.4: Tectonic plate boundaries in the Near East and location of Jordan (modified after Johnson, 1998).

After following a series of orogenic phases in Late Proterozoic time, in the Infracambrian to Early Cambrian time the Arabian area entered an extensional phase which was characterized by intra-continental denudation, peneplanisation, rifting and wrenching (Husseini & Husseini, 1990). During Cambrian to Silurian times Jordan was situated near the southern border of the Paleotethys Ocean on the northern margin of the Gondwana Continent, showing little evidence of tectonic activity acting and acted as a relatively stable, passive continental margin, over which terrestrial and shallow marine sediments had accumulated (Flexer, 2001). Clastic Sediments were continuously supplied by the Arabian Nubian Shield northwards and marine influences characterized the northern part of Jordan. The material was deposited on a subsiding passive margin shelf area which was affected by worldwide eustatic sea level changes, resulting in a series of transgressions and regressions over the area (Andrews, 1991). Subsidence was

greatest in the NE of Jordan, close to the Tethys Ocean where about 800 m of clastic sediments were deposited. Nevertheless, Core Lab (1987) and National Resource Authority (NRA) (NRA/PCIAC, 1989) identified a period of tectonic activity during Early Cambrian-Ordovician including an extensional wrench regime with folding and high angle faulting.

From the Devonian to possibly the Early Carboniferous, the Arabian and adjacent plates were structurally affected by a regional Variscan tectonic event. This tectonic event is interpreted to be the crustal response to regional compression caused by the initiation of subduction of the Palaeo-Tethyan oceanic crust near the margin of Gondwana along Turkey and Iran (Husseini, 1992). The uplifted areas associated with this tectonic event were largely eroded during the Late Carboniferous and Early Permian when glacio-fluviatile and marginal marine conditions prevailed, leading regionally to a complete removal of up to thousand meters of lower Paleozoic rocks (Husseini, 1992). The Palaeozoic era closed in the Late Permian with a major transgression which deposited massive carbonates over most of a peneplaned Arabian plate. Also in Late Permian as well as in Triassic, active rifting along the Zagros suture projected extensional stresses across the Arabian plate causing substantial extensional movements along most major basement-controlled fault systems. Triassic transgression reached big parts of Jordan, depositing marine sediments. Uprising, combined with erosion preceded the deposition of lower Cretaceous sandstones (Kurnub Sandstone).

The Late Jurassic-Early Cretaceous erosion, which took place primarily due to the tilting of the Arabian platform, has progressively removed the entire Jurassic, Triassic and marine Upper Paleozoic from NW to SE (Hirsch, 1984). During Upper Cretaceous time Jordan, acting as continental shelf, underwent major marine transgressions (Abed, 1984). A regional transgression began in Mid Cretaceous (Aptian-Turonian) on the continental areas of northern and central Jordan. During Late Cretaceous (Senonian) the transgression advanced gradually further to the east and SE. Thickness and facies of the marine, chiefly carbonatic sediments deposited during the latter part of the Late Cretaceous and Early Tertiary indicate the development of swells and basins in marine shallow water areas (Bender, 1982). Flexer (2001) indicates that within the Cretaceous time three regional unconformities can be identified in the southern Levant area (including Jordan, Israel and the Palestine areas), subdividing the Cretaceous into three lithostratigraphic units (Fig. 2.5).

The first lithostratigraphic unit (Neocomian) is marked by a tectonic, volcanic and erosional activity. Jordan and the adjacent countries were covered by a considerable thickness of eolian-fluviatile sands, silts and shales, comprising the Nubian Sandstone of the Kurnub Group accumulated on the platform (Fig. 2.5a). During the second cycle (Aptian-Turonian) a differentiation into platform and off-shelf domain (basin) began. The platform accumulated shallow marine limestones and dolomites whereas in the basin calcilutite prevails (Fig. 2.5b). The continental arenaceous facies receded to the Nubo-Arabian shield in the southeast and was replaced progressively by marine limestones of the Ajloun Group. Tropic humid vegetation at that time allowed mobilisation of significant amounts of silica acid, which precipitated again in the marine shelf as chert layers (Bender, 1968).

The Turonian-Senonian boundary is characterized by a global eustatic fall, leading to vadose-karstic dissolution of top of the then youngest carbonatic formations and to a regional

unconformity (Flexer, 2001). The third sedimentary cycle begins with remarkable high sea level leading to carbonate (mostly chalk) sequences in various thickness (Fig. 2.5c) and is characterized by open sea conditions being controlled by the incipient folding of the Syrian Arc (= Palmyra fold belt) (Flexer, 1968 - 1971; Flexer & Honigstein, 1984) (Fig. 2.6). The mild compressional forces of the Syrian Arc phase echoed the closure of the neighbouring part of the Neo-Thetys that began in the Late Cretaceous (Garfunkel & Ben-Avraham) and continued into the Miocene. The closure of the Neotethyan Ocean during the Late Cretaceous-Palaeogene converted the long-lived passive margins of the Arabian Platform into active ones. In pre-Neogene times Jordan was then situated between two major tectonic units: the Nubo-Arabian massif to the south and the Alpine mobile orogenic belt to the north (Flexer, 2001).

The Palaeogene period started with a wide, extensive transgression, continued from the Cretaceous times leading to depositions of mainly marl, shale, chalk and flint and terminated with folding, uplift, faulting and volcanism due to the orogenic movements in the Alpine-Tauride (Zagros fold belt) system, reflecting probably the resumption of compression between the African and European plates (Dewey et al., 1973).

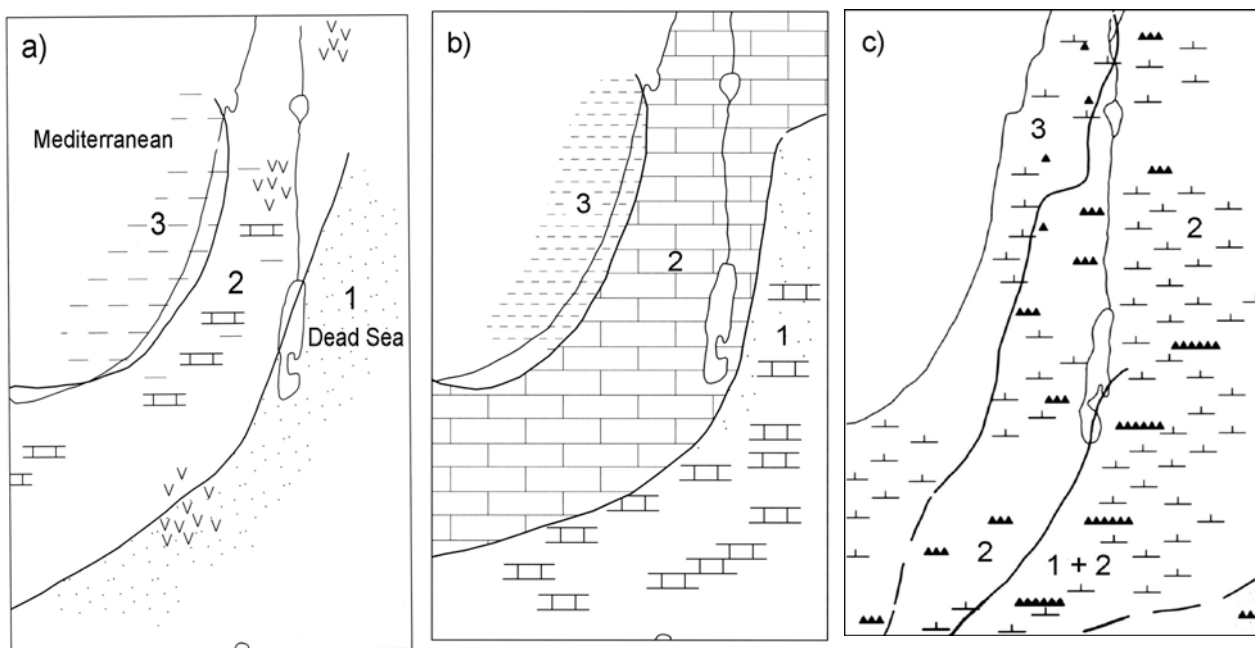


Fig. 2.5: Lithofacies belts Cretaceous times: a) Early Cretaceous facies belts: (1) mostly continental sandstone, (2) sandstones-shale-limestone facies, (3) thick marine shaly sequence and volcanism; b) Mid-Cretaceous (Aptian-Turonian) lithofacies: (1) thin carbonate sequence, interbedded with sandstone, (2) mostly carbonates (limestones and dolomites), (3) mostly calcilutite facies; c) Senonian lithofacies belts: (1) sand, flint and chalk, (2) chalk marl and flint (3) mostly chalk, sparse flint (modified after Flexer, 2001).

The major tectonic element that controls and determines the general structural features of Jordan is the Dead Sea Transform. The approximately 1000 km long Dead Sea Transform is an active plate boundary between the Sinai microplate and the Arabian plate that connects the divergent plate boundary along the Red Sea with the convergence zone along the Alpine orogenic belt in Turkey (Garfunkel et al., 1981) (Fig. 2.6). The transform formed as a result of the Mid-Cenozoic

breakaway of Arabia from Africa, which until then were parts of a continuous continent (Garfunkel & Ben-Avraham, 1996). The separation of the Arabia and Africa created the Red Sea where incipient seafloor spreading takes place (Coleman, 1984). Garfunkel et al. (1981) regard the Dead Sea Transform as major fault of the Red Sea mid-ocean opening.

After Horowitz (2001) the Dead Sea Transform is the direct continuation of the Syrian-African Rift connecting the active sea-floor spreading centre of the Red Sea in the south to Turkey in the N (Moh'd & Muneizel, 1998) (Fig. 2.4). An estimated 105 km of cumulative left-lateral, strike-slip offset has been measured across the transform that connects the spreading center of the Red Sea with the continental collision of the Taurus-Zagros mountain portion of the Alpine Orogenic belt in Turkey (Fig. 2.4) (Flexur et al., 2006). The accumulative lateral displacement of 105 km was estimated since the time of the rift initiation near the Oligocene-Miocene boundary (Cochran, 1983). The amount of motion was measured by matching the lineaments of both sides of the Dead Sea transform that correlate exactly with the assumed lateral displacement (Quennel, 1959). An independent estimation of a motion of about 100 km is obtained from the regional plate kinematics based on offset data from the Gulf of Aden and Red Sea.

Bayer & Hötzi (1988) explain the tectonics on the Arabian Red Sea margin and the evolution of the Dead Sea Transform interrelated with the different rifting stages of the Red Sea related to the Gulf of Suez, the Gulf of Aden and the Gulf of Aqaba. In Early Oligocene to the Middle Miocene times active continental rifting in the Red Sea with continuation in the Gulf of Suez took place whereas the early stage of the graben development was characterised by normal faults due to extensional forces. The asymmetric graben development were followed by the first marine ingression in the Gulf of Suez and northern Red Sea area proceeding from N to S. In Lower Miocene the Red Sea graben underwent increasing extension and subsidence accompanied by uplift of the graben shoulders.

From Late Miocene to Recent, the kinematics of the Red Sea has changed from active to passive rifting with extension to the sinistral shear along the Dead Sea Transform and accompanying passive opening of the Red Sea due to the oblique strike-slip movement of the Arabian Plate. This rearrangement led to a stagnation of the extension and subsidence in the Gulf of Suez and created a new plate boundary, the Dead Sea Transform. These changes are assumed to have been triggered by the seafloor spreading at the Gulf of Aden that started 10 to 12 Ma years ago, and resulted in a northward drift of the Arabian plate and therewith initiated the strike-slip motion along the Dead Sea Transform (Bayer & Hötzi, 1988) (Fig. 2.4). In contrast to the Gulf of Suez, which was decoupled from the main graben since this time, the Red Sea proceeded in a more or less continuous opening. The convergence zone at the northern part of the Arabian plate (Fig. 2.4) and in the Anatolian chains were connected over the Dead Sea Transform to the tensional setting of the Red Sea.

Due to continuous north drift of the Arabian plate, in Pliocene to Pleistocene times the residuals of the former Biblis ocean (today's North Syria and North Iraq) collided with the east Anatolian chains. Caused by the compressional stress due to the oblique abutment of east Anatolia extension along the Dead Sea Transform and thus parallel normal faulting occurred (Bayer, 1988). Internal shear movements in the Anatolian plate released parts of the compressive stress in the northern part of the Arabian plate (Bayer et al, 1988). However, a high amount of

compressive stresses in northern Arabian plate resulted in a compressive overprint of former fault systems in Jordan and Syria accompanied by folding. In the Amman area continuous compressional superimposition of former E-W trending normal faults determine the tectonic since the Late Pleistocene time (Bayer et al., 1988, Bayer et al., 1989).

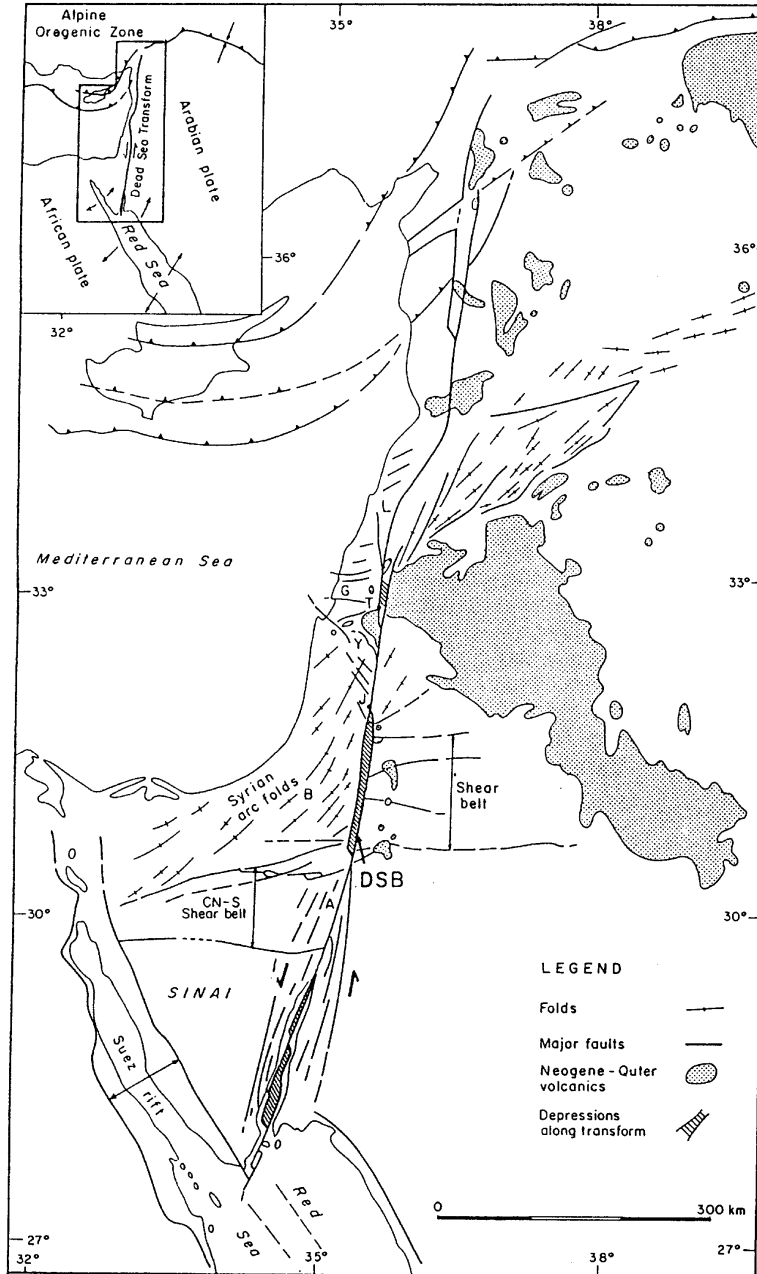


Fig. 2.6: Regional setting Dead Sea Transform. A=Arava valley; B=Beer sheva valley; G=Galilei; J=Jericho; L=Lebanon; T=Lake Tiberias; Y=Yizreel valley, (Garfunkel & Ben-Avraham, 1996).

The Neogene Dead Sea Transform is characterized by a string of deep pull-apart basins along its trace such as the Dead Sea and Sea of Galilee basins. These pull-apart basins formed between left-stepping master strike-slip faults, but the deep troughs are commonly bordered by marginal



normal faults (Flexur et al., 2006). Uplifted highlands bordering deep depressions filled with young sediments are bordering both sides of the Jordan Valley.

## 2.4 Stratigraphy

### 2.4.1 Overview

This work uses the stratigraphical taxonomy of the National Resources Authority (NRA) Amman, Jordan, which is based on the scheme of Masri (1963) and the Quennel Group (1951) (Tab. 2.1). The test area is dominated by sedimentary rocks of Upper Cretaceous Age (Albian to Maastrichtian), mainly limestones, dolomites and marls of the Ajloun and Belqa Groups, which are underlain by sandstones of the Kurnub Group of Lower Cretaceous age, with outcrops on fault zones along the Wadi Shueib structure (Mikbel & Zacher, 1981; Salameh, 1980; Bender, 1968a). The Ajloun Group consists of approximately 350 - 400 m thick interbedded limestones, marly limestones and dolomitic limestones.

Tab. 2.1: Stratigraphy in the Wadi Shueib catchment area (modified after Powell, 1989). The numbers (Z1, ..., B2) indicate the common used shortcuts for the geological units.

Period	Epoch	Quennel Group (1951)	Masri (1963)	Bender (1974)		Brief description	Thickness	
Upper Cretaceous	Campanian	Belqa	Amman al Hisa	Phosphorite	B2	Phosphorite & silicified limestone	~??m	
	Santonian			Silicified limestone	B1	Massive chalk & marlstone, fossiliferous	~10m	
	Coniasian		Wadi Um Ghudran					
	Turonian	Ajlun	Wadi as Sir	Massive limestone	A7	Thinlayered dolomite or massive grey limestone, fossiliferous. To the top more Chertlayers.	~130m	
			Wadi Shu'ayb	Echinoidal limestone	A5,6	White crystalline limestone and Ammonites (A6), and thinlayered limestone and marlstone (A5)	~30m	
			Hummar		A4	Massive grey, sometimes yellowish limestone, often crystalline and cavernous	~45m	
			Cenomanian	Fuheis	Nodular limestone	A3	Thinlayered, soft white limestone	~70m
				Na'ur		A1,2	Massive hard grey limestone + chertlayers (A2), and grey marlstone (A1)	~110m
	Lower Cretaceous	Albian	Kurnub	Subeihi	Varicoloured sandstone	K2	Multicoloured sandstone	~250m
		Abtian		Aardo	White massive sandstone	K1	White, yellow massive sandstone (does not occur in study area)	
Neocomian		<i>Angular unconformity</i>						
Jurassic		Zarqa	Azab		Z2	Does not occur in study area	~??m	
Triassic			Ma'in	Zarqa	Z1	Does not occur in study area		
Permian								

The Belqa Group includes a sequence of mainly limestones, intercalated with thick-bedded chert but also chalk, marls, silicified limestones and phosphatic horizons. Tab. 2.1 summarizes the stratigraphical units in the test area mapped by various authors.

#### 2.4.1.1 Kurnub Group

The Kurnub Sandstone in the test area consists mainly of cross-bedded massive bodies of porous pink, red to violet, but also yellow, brown and white quartz arenite. Glauconitic sandstone is often present. Particle size is coarse to medium sand fraction, usually only loosely cemented

(Kuntz, 2003). In the upper layers carbonate cementation is evident and particle sizes become finer. After Powell, 1989, the thickness of the Kurnub Sandstone in the test area is approximately 250 m. In general, in northern Jordan the Kurnub Sandstone consists of very fine to coarse-grained, partly carbonaceous sandstones with intercalations of sandy dolomite, dolomitic limestones, siltstone and shale (Margane et al., 2002).

The terrigenous sediments of the Kurnub Group of Neocomian to Albanian age (Flexer, 2001; Andrews, 1992) lies with a marked unconformity on Lower Palaeozoic, Permian, Triassic and Jurassic strata (Andrews, 1992). The Kurnub Sandstones were deposited in a braided to meandering river environment with possible shallow marine environment (Andrews, 1992).

### 2.4.2 Ajloun Group

The thickness of the Ajloun Group in the test area is approximately 390 m (Powell, 1989). The Ajloun Group consists of an alternate bedding of massive limestones and marly, limestones with thin clay and marl layers, that can be identified morphologically by their gentle slopes forming a significant contrast to the prominent hard limestones (Fig. 2.7).

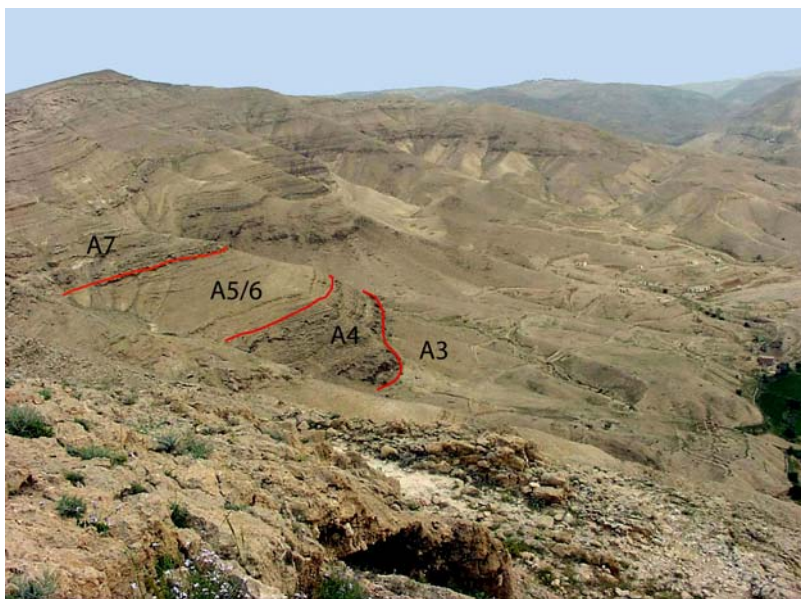


Fig. 2.7: Sequence of the Ajloun Group and indicated boundaries of the A3, A5/6 and A7 formations, (image width: 600 m photograph taken 11.09.2002).

#### Na'ur Formation (A1-A2)

The Naur Limestone Formation was deposited between Late Albian to Early Cenomanian and shows a sequence of glauconitic sandstone and dolomitic sand-, siltstone at its base (Moh'd, 1998). Basal carbonates appear as beds of limestone and dolomite with interbedded marly, sandy facies predominantly in the lower parts of the section (A1). The upper part (A2) of this formation consists of alternating limestone and marl overlain by marl interbedded with thin layers of marly limestone. The top of the formation is marked by dolomitic limestones with chert nodules. The total thickness of the Naur Formation (A1-2) in the test area is approximately 110

meters. The deposition environment of the formation was tidal and lagoonal to open-marine (Shawabkeh, 2001).

### **Fuheis Formation (A3)**

The Middle Cenomanian Fuhays Formation with an approximate thickness of 70 m consists of sequences of marlstone, limestone and dolomitic limestone which are often marly and grade upwards to calcareous clay (Moh'd, 1998). The marlstone facies is medium thick bedded, soft or hard and at some places nodular. Limestone facies is mostly thin bedded and occasionally fossiliferous.

### **Hummar Formation (A4)**

The Hummar Formation consists of about 45 m thick often karstified limestones, dolomitic limestones and dolomites of Upper Cenomanian age, forming partly massive, prominent cliffs. The limestones are medium to thick bedded, partly nodulated with some marly interbeds (Makhlouf, 1996). The dolomites occur as hard bedded layers associated with chert nodules. Within the Hummar Formation massive cliff horizons are common (Fig. 2.8). The Hummar Formation was deposited in a tidal sedimentation environment, with limestones being deposited in subtidal regime, dolomites within intertidal conditions (Moh'd, 1998).



Fig. 2.8: Cavernous Hummar Formation showing prominent, massive cliffs in the upper part (image width: ~ 25m, photograph taken 02.05.2005).

### **Wadi Shu'ayb Formation (A5/A6)**

The Cenomanian to early Turonian Wadi Shu'ayb Formation is mainly composed of marly limestone, chalky marlstone and calcareous siltstone. The Shu'ayb Formation is in general significantly softer than the massive limestones formations above and below, thus forming usually well observable gentle slopes, forming a clearly visible morphological contrast. The Formation thickness in the test area is approximately 30 m. The sedimentation environment was formed by an open marine to subtidal regime (Moh'd, 1998).

### **Wadi as Sir Formation (A7)**

The Wadi as Sir Formation is forming the major part of the rock outcrops in the test area and consists of bedded massive limestones, dolomitic limestones and dolomites with chert bands, chalky limestone and marls deposited under full marine to subtidal conditions (Shawabkeh, 2001). The middle member is believed to have been deposited in a shoal to reef environment (Moh'd, 1998). Chert nodules or lenses are present mainly in the upper and middle part forming sometimes continuous layers. The formation thickness is about 130 to 150 meters.

#### **2.4.2.1 Belqa Group**

The name Belqa Group was firstly introduced by Quennel (1951) and forms a sequence of predominantly limestones and chalks showing partly high amounts of chert and phosphorite. The Belqa Group is represented in the test area by its basal parts including the Wadi Umm Ghudran Formation and the Amman Silicified Limestone Formation. The term Amman Silicified Limestone Formation was used by El-Hiyari (1985) and by the National Resources Authority (NRA) Amman for the equivalent of the middle part of the "Amman al Hisa" Formation named by Masri (1963) (Tab. 2.1).

#### **Wadi Umm Ghudran (B1)**

The Wadi Um Ghudran Formation, assigned to Coniacian and Santonian age overlays disconformably the Wadi as Sir Formation containing thin to massive white chalk and marls, with occasional beds of limestone that were deposited in a moderately deep-water pelagic environment (Shawabkeh, 2001). Due to its softness the formation was locally eroded completely or shows a thin sequence up to 20 m in the test area.

#### **Amman Silicified Limestone (B2)**

The Amman Silicified Limestone Formation of Coniacian to Santonian age is up to 50 m thick and consists of thick bedded, often massive limestone, dolomite, silicified dolomite and limestone and phosphate. The depositional environment is described by Moh'd (1998) as shallow marine with occasional changes to continental conditions, evidenced by the presence of silcrete as parts of chert.

## **2.5 Tectonics**

The SW border of the test area is situated at the transition zone from the Jordan Rift Valley to the eastern highlands. The uplift of the Jordan Rift shoulders affected all previous structures of the bordering high lands (Horowitz, 2001). Thus, the structures in the area are related to the Dead Sea Transform and therefore considered as one of the rift-side catchments, affected directly by the Jordan Rift Valley.

The test area is dominated by normal faults of variable throws and trends and by several anticlines and synclines (Fig. 2.11, Fig. 2.12). Partly, the fault displacement can be clearly indicated by the movements of the prominent massive limestone cliffs in the test area (Fig. 2.10). The prevailing fault directions are NW-SE and NNE-SSW, in the northern part with downthrow to the E in the southern part with downthrow to the W. The vertical fault motion is taken up by the

main faults but the horizontal displacement, connected with the Dead Sea transform, occurs decentralized on many joint-planes (Prof. Elias Salameh, Geology Department, University of Jordan, Amman, *personal communication*, 2003).

The general trend of anticlines and synclines axes is NE-SW. The dominating structural element in the eastern part of the test area is the *Wadi Shueib structure*, a fold belt of approximately 25 km length and 1 - 4 km width, which extends from the S to NE direction south of Salt (Mikbel & Zacher, 1981) and continues north into the *Suweilih structure* described by Salameh (1980), ending approximately between the cities of Jerash and Zarqa (Fig. 2.9). Several former studies of the structure exist that use different names: *Salt Flexure* (Burdon, 1959), *Suweilih structure* (Bender, 1974; Wiesmann, 1969). Due to the fact that the structure is running parallel to the Wadi Shueib valley over a long distance, Mikbel & Zacher (1981) introduced the name *Wadi Shueib structure* which was later adopted by the National Resources Authority (NRA) for the official geological maps.

Within the *Wadi Shueib structure* there exist several tightly folded synclines and anticlines. Beside the larger scaled folds which possess widths of some hundreds of metres up to kilometres, a multiplicity of minor folds is presented in the test area, which possess widths of only few meters. Westwards of the wadi channel of the Wadi Shueib itself, the layers show a gently dipping of 0° up to 15° towards the Jordan Rift Valley.

Major folds are characterised by large interlimb angles, symmetric nature and amplitudes of some hundreds of metres. This western part of the mapping area is strongly fractured by numerous faults. After Mikbel & Zacher (1981) the folding of the *Wadi Shueib structure* is supposed to be the result of ESE-WNW acting compressional forces. The compression occurred as a consequence of the northward directed movements and the rotation of the Arabian Plate (chapt. 2.3). Wiesemann (1969) considered the formation of the "Shuna-Suweilih-fault" (= Wadi Shueib structure) to be a deflection of the Dead Sea transform into an older fault direction.

The structural evolution of the test area can be summarized in two different stages (Mikbel & Zacher, 1981). During Late Cretaceous times, some of the NNE trending folds were composed as part of the Syrian Arc System. These folds indicate ESE trending compressional forces and originate from the accumulation of horizontal stress in the Arabian plate when it was overthrust over the subducted Thetys ocean. After this folding phase NS trending faults were formed in Palaeocene up to Miocene times that are associated with the main Dead Sea Transform (Moh'd et al., 1998) when extension occurred along the Transform and thus parallel normal faulting occurred due to compressional stress in the northern Arabian plate.

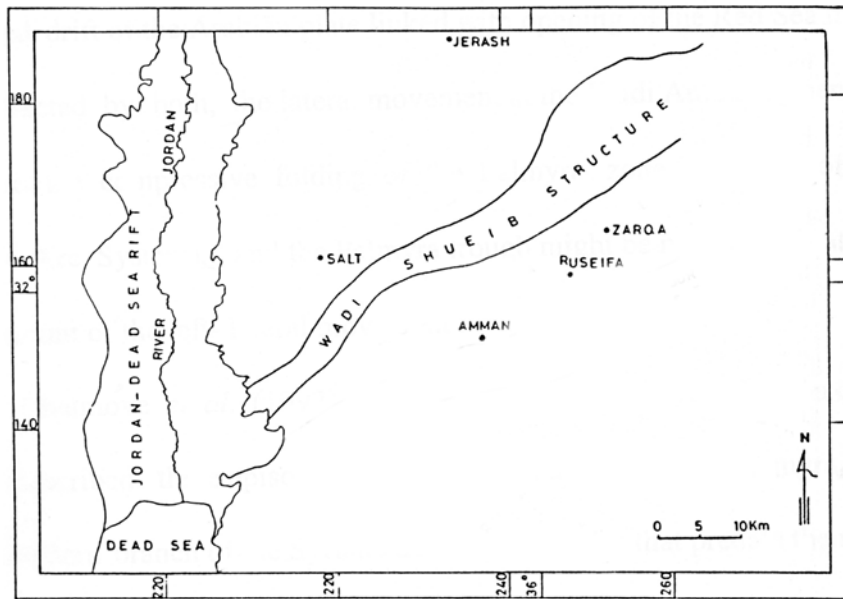


Fig. 2.9: Location of the Wadi Shueib Structure (modified after Qassem, 1997).



Fig. 2.10: Normal fault; showing a dip-slip displacement of approximately 50 m of the massive limestones of the Hummar Formation (photograph taken 03.05.2005).

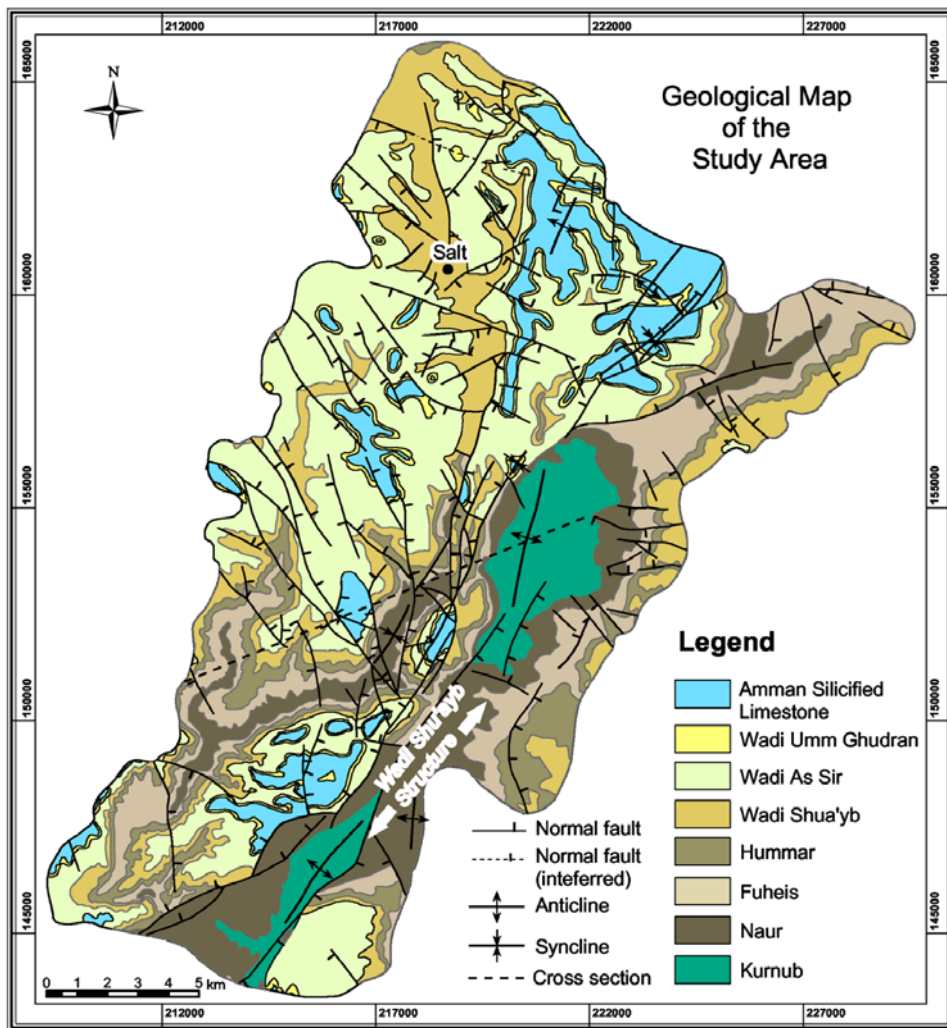


Fig. 2.11: Geological Map of the test area (modified after Shawabkeh, 2001; Moh'd & Muneizel, 1998; MacDonald & Partners, 1963; Sawarieh & Barjous, 1993).

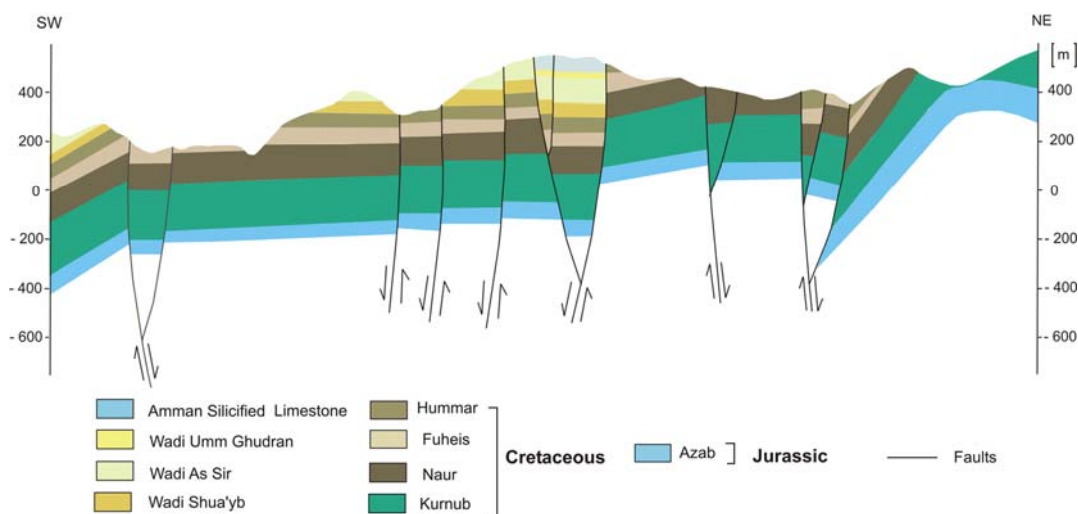


Fig. 2.12: Geological cross section of the test area (modified after Shawabkeh, 2001). The location of the cross section is indicated in Fig. 2.11.

## **2.6 Hydrogeology**

### **2.6.1 Hydrogeological situation**

The test area is dominated by interstratifications of karstic limestones, marls and dolomites of the Upper Cretaceous Ajloun Group and lower part of the Belqa Group. Big parts of the test area are intensively jointed and cut by faults. The joints are often enlarged by corrosion.

Two main aquifer complexes can be considered: the Lower and the Upper Cretaceous Aquifer Complex. The Lower Aquifer Complex is only represented by a small outcrop of the coloured sandstones of the Kurnub Group along the Wadi Shueib structure. No significant springs emerge from the Lower Aquifer Complex in the test area consequently the Lower Aquifer Complex is of minor importance for water supply.

The Upper Cretaceous Aquifer Complex includes the complete sequence of the Ajloun Group (Tab. 2.1). Three aquifer systems within the Ajloun Group are relevant in the test area: the Naur Aquifer (A1/2), the Hummar Aquifer (A4), and the Wadi Es-Sir Aquifer (A7). The single aquifer systems of the Upper Cretaceous Aquifer Complex are interbedded between the Fuhays (A3) and the Shueib (A5/6) Formations, which are composed of interlaid thin layers of marls, dolomitic thinly bedded limestones or siltstones, acting more or less as leaking aquitards. However, especially in tectonic compressive areas within the test area, where the Fuhays and Shueib Formations are strongly vertically jointed and fractured, the overlaying aquifer systems are hydraulically connected through fractures and fault zones.

The aquifer systems are drained by several springs that are partly used for drinking water supply. A few wells were drilled in the test area around Salt and near Shunat Nimrin penetrating the Hummar (A4) and Naur (A1/2) aquifer. Most of these wells are abandoned, sealed and no longer used for drinking water supply due to high concentration of nitrates (Ta'any, 1992).

### **2.6.2 Karstification**

The limestones of the Naur Aquifer (A1/2) are partly karstified, featuring only caves and few surface karst microforms such as small karren. In general, the Naur Limestones form a moderately developed karst aquifer with interstratified layers of marl and marly limestone and approximate thickness of 110 meters. Within the Hummar Aquifer (A4) massive cliff horizons exist that favour angular cave formation (Fig. 2.8). Dissolution features along joints and bedding planes are common. Despite its small thickness of approximately 45 m, the Hummar Aquifer forms an important aquifer in the test area. The Wadi Es-Sir Limestone forms a well developed 130 to 150 m thick karst aquifer. The high to very high degree of karstification of the partly very pure, micritic limestones results in caves, distinct karst features such as karren and a "blocky" appearance of the landscape with large boulders (Fig. 2.13). However, the uppermost Wadi Es-Sir Aquifer often faces contamination problems due to its typical karst aquifer characteristics of high flow velocities, fast hydraulic reactions, short residence times and therefore a poor contaminant retention potential, therefore if possible water from the underlying Hummar Aquifer is favoured for drinking water supply. The limestones are only partly covered by shallow soils. The occurrence of sparse forest canopy dominated by pines and oak trees is not restricted to the



existence of continuous soil cover. Even though the slopes are often steep (20 - 30°), there is almost no surface runoff, the biggest part of the runoff is infiltrating fast in the underground.



Fig. 2.13: Wadi Sir Formation showing typical microkarst relief, cave systems and a “blocky” appearance of the landscape (photographs taken 03.05.2003).

Dominant distinctive *surface* karst landforms such as big karst depressions, dolines or poljes are missing in the test area. The existing karst features in the test area are limited to karren, caves, conduits and enlarged fractures, solution cavities and solutional microforms. An earlier phase of karstification occurred at the Turonian-Senonian boundary (Flexer, 2001), due to a global eustatic fall leading to the vadose-karstic dissolution of top of the then youngest carbonatic formations and to a regional unconformity. The cave formation within the Ajloun group is related to times with a state of water saturation in which slow laminar motion along bedding plains and joints created interconnecting patterns of tiny tubes (Jennings, 1985).

Since a close relationship between the hydrologic regime, the climate zone and the existence of karstified rocks is expected (Semmel, 1973), new karst features are poorly developed under today’s (semi-)arid climatic conditions with water shortage, also due to missing vegetation and thus little soil carbon dioxide (Jennings, 1985). Furthermore, high evaporation rates render low precipitation even less effective. Under (semi-)arid climate, the depth of the karst forms become more shallow due to the fact that in the course of high seasonal precipitation events high surface flows grow within a short time period and limits the contact action and time of the limestones with the water that contains high amounts of carbon acid and therefore a low pH value (Semmel, 1973). Sparse or missing vegetation and thin or absent soil cover prevent the surface runoff from infiltrating and reduce the absorptive capacity for water.

For the development of *subterranean* karst forms especially in semi-arid regions there is often the input and subsurface inflow from remote areas with higher precipitation rates needed.

### 2.6.3 Springs and surface waters

The test area is drained by a dense wadi stream net whereas the Wadi Shueib course acts as a receiving stream for the entire area and discharges in the Wadi Shueib dam reservoir in the southwestern part of the test area.

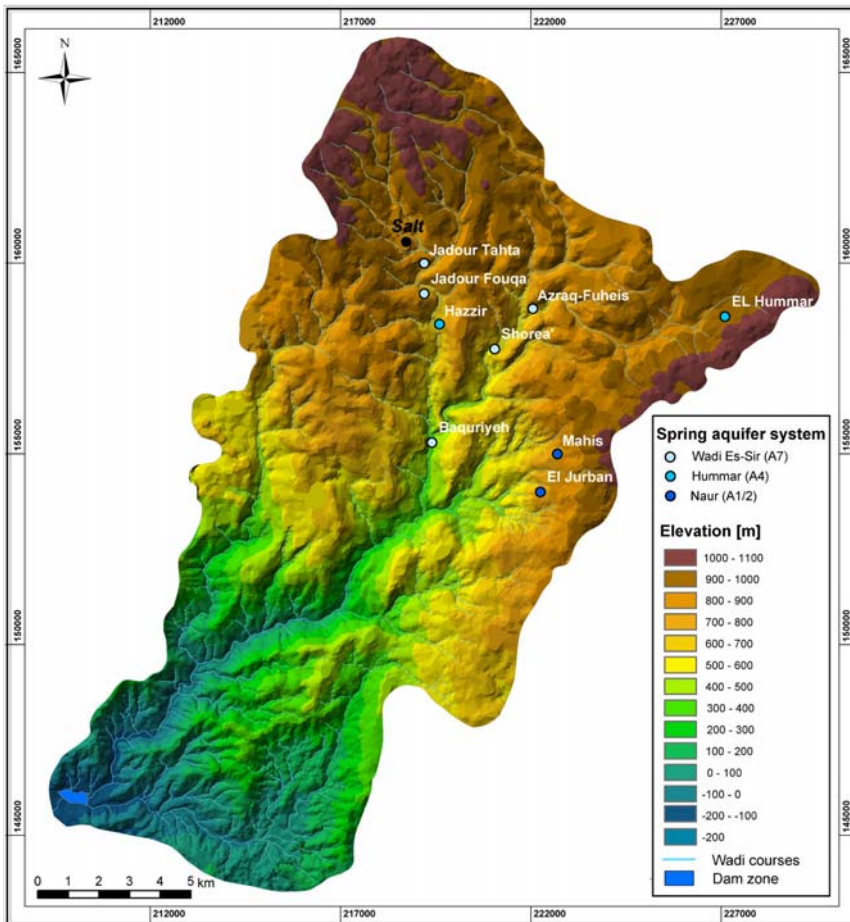


Fig. 2.14: Location and aquifer system of the main springs in the test area and the wadi courses on top of a DEM (spatial resolution 15 m).

Several springs emerge from the aquifers and are described in detail by Ta'any (1992). The main springs in the test area and the dense wadi network are displayed in Fig. 2.14. Only the three most significant and biggest springs, the Baqouriyeh, the Azraq-Fuheis and the Hazzir spring, are described in the following sections regarding their characteristics and hydrochemistry. Baqouriyeh and Azraq-Fuheis springs discharge from the Wadi Sir Formation (A7), the Hazzir spring discharges from the Hummar unit (A4). These springs provide the major drinking water supply of the main villages in the test area. The coordinates and discharge amounts of these springs are indicated in Tab. 2.2.

The **Baqouriyeh spring** is located in a highly fractured faulted area within the Wadi Sir Formation discharging at the contact to the lower permeable Shueib Formation (A5/6) from enlarged cavities. The groundwater flow is directed from the outcropping recharge zone of the

The drainage path of the surface runoff follows the topography in NE-SW direction and the underground flow follows mainly the dipping of strata of the Naur, Hummar and Wadi Sir aquifers separated by the lower permeability interstratifications of the Fuheis and Shueib Formations. However, the thickness of the Fuheis unit is about 70 m, the Shueib unit is only 30 m. The faults that run across the test area show displacements ranging from several tenner m up to more than 100 m allowing hydraulic flow and contact between the bordering aquifers (Fig. 2.12).

Several springs emerge from the aquifers and are described in detail by Ta'any (1992). The main

Wadi Sir Formation north and northeast of the spring. The spring shows turbidity after six hours to one day after heavy rainfall events.

The **Azraq-Fuheis spring** discharges at the contact of hard massive limestones to thin layers of marly limestone within the Wadi Sir Formation. The groundwater flow is directed from the higher located outcrops of the Wadi Sir and Amman Silicified Limestone near Fuheis in the SE towards NW. Periodically the spring is influenced by two sources of contamination: cement waste water of the Fuheis Jordan cement factory and waste water from the pumping station of the Wadi Azraq located in Fuheis, both located southeast of the spring. In wintertime strong rainfall results in flooding of the sewer system and overflow of the interposed catchment basin of the pumping station. As a consequence thereof, waste water infiltrates into the underground, penetrates the Wadi Es-Sir Limestones and contaminates the Azraq Fuheis spring, making the spring unusable for up to three months of the year.

The **Hazzir spring** is a fault spring discharging within the Shueib Formation. The spring is fed by water ascending at a fault zone from the Hummar Formation (A4) (Ta'any, 1992). The spring shows a relatively constant discharge amount not affected directly by heavy rainfall. It is assumed that the spring water originates deep in the aquifer since the discharging spring water is relatively cool during summer and relatively warm during winter.

Tab. 2.2: Location and discharge of the major springs in the test area

Name	Location (Palestine Grid)		Aquifer	Discharge (m <sup>3</sup> /h)		
	E [m]	N [m]		Max	Min	Aver
Baqouriyeh	155.300	219.400	A7	860	61	350
Azraq-Fuheis	158.810	222.050	A7	583	50	252.
Hazzir	158.400	219.600	A4	332	10.1	83.9

Treated wastewater effluents from Salt treatment plant flow in the Wadi Shueib course and are collected together with the winter flash floods in the Wadi Shueib Dam reservoir at the southwestern part of the test area. The dam water is used for agricultural purposes and for recharging the groundwater of Shunat Nimrin area (Ta'any, 1992).

#### 2.6.4 Hydrochemistry and microbiology

Detailed water analysis from all existing springs in the Wadi Shueib, based on samples between 1972 and 1990 are given in the work of Ta'any 1992. Since then, some springs ran dry or were captured.

Current spring analysis from 2002-2004 were kindly provided by Prof. Dr. Salameh from the Geological Department, University of Amman, Jordan. The hydrochemical parameters of the three main springs are presented in Tab. 2.3 and Tab. 2.4.

With the exception of nitrate, which exceeds in all samples of the Hazzir spring the permission level of 50 mg/l of the Jordanian Standards of drinking water (No.286, 1990), the main hydrochemical springs parameters fulfil the Jordanian regulations.

Elevated phosphate concentrations in all three springs indicate an input of anthropogenic wastewater or fertilizer. After Kölle (2003) phosphate concentrations higher than 100 µg/l can be considered as pollution indicator. Organic waste, excrements or waste water can have a direct impact on the phosphate concentrations in the ground water (Kölle, 2003).

Tab. 2.3: Results of hydrochemical analysis of the major cations and anions in the three major springs of the test area (source: Analysis of the Geological Department, University of Amman).

Spring	Date	pH	E.C us/cm	Temp C°	Ca 2+ meq/l	Mg 2+ meq/l	Na + meq/l	K + meq/l	Cl <sup>-</sup> meq/l	SO <sub>4</sub> <sup>2-</sup> meq/l	HCO <sup>3-</sup> meq/l	NO <sup>3-</sup> meq/l	PO <sub>4</sub> <sup>3-</sup> meq/l
Baqouriyeh	21.07.02	7,27	611	21,5	2,83	1,52	2,06	0,10	1,36	0,43	4,32	0,50	
Baqouriyeh	19.01.03	7,55	626	18,7	3,57	1,65	1,50	0,10	1,33	0,71	4,09	0,58	
Baqouriyeh	16.03.03	7,04	587	18,4	3,90	1,37	0,60	0,07	1,20	0,62	3,42	0,60	
Baqouriyeh	30.06.03	7,86	550	19,0	3,81	1,27	0,73	0,05	1,22	0,57	3,43	0,48	
Baqouriyeh	13.08.03	7,43	587	20,5	3,68	1,64	0,78	0,05	1,25	0,53	3,86	0,46	
Baqouriyeh	16.11.03	7,00	622	19,3	5,04	0,59	0,86	0,07	1,38	0,69	3,86	0,60	
Baqouriyeh	20.01.04	7,33	626	19,3	4,18	1,42	0,86	0,07	1,42	0,54	3,89	0,56	
Baqouriyeh	08.03.04	7,43	622	18,8	3,88	2,00	0,60	0,07	1,47	0,77	3,58	0,52	0.09
Baqouriyeh	19.04.04	7,15	646	19,2									0.13
Baqouriyeh	03.08.04	7,43	622	18,8									
Azraq-Fuheis	21.07.02	7,49	500	23,3	2,58	1,38	1,20	0,02	0,88	0,12	4,03	0,30	
Azraq-Fuheis	19.01.03	7,80	485	17,6	3,21	1,19	0,52	0,02	0,80	0,23	3,50	0,46	
Azraq-Fuheis	16.03.03	7,32	482	20,0	3,42	1,27	0,43	0,00	0,83	0,42	3,35	0,49	
Azraq-Fuheis	30.06.03	7,42	494	22,3	3,51	0,97	0,52	0,02	0,92	0,29	3,33	0,45	
Azraq-Fuheis	13.08.03	7,23	508	20,5	3,59	0,97	0,65	0,00	0,99	0,30	3,44	0,44	
Azraq-Fuheis	16.11.03	7,76	514	19,9	3,39	1,56	0,60	0,02	0,92	0,78	3,42	0,36	
Azraq-Fuheis	20.01.04	7,13	520	19,0	3,18	1,52	0,60	0,02	1,02	0,20	3,52	0,48	
Azraq-Fuheis	08.03.04	7,19	514	14,4	3,58	1,60	0,65	0,00	1,48	0,55	3,31	0,40	0.09
Azraq-Fuheis	19.04.04	7,48	523	19,1									0.12
Azraq-Fuheis	03.08.04	7,19	514	14,4									
Hazzir	21.07.02	7,17	814	20,4	4,58	0,91	2,32	0,30	1,63	0,69	4,75	1,09	
Hazzir	19.01.03	7,50	830	16,6	4,22	1,74	1,52	0,30	1,74	0,36	4,67	1,07	
Hazzir	16.03.03	6,97	739	17,7	4,20	2,05	0,86	0,17	1,60	0,51	3,97	1,02	
Hazzir	30.06.03	7,87	778	20,1	4,49	1,56	1,41	0,23	1,45	0,86	4,21	1,07	
Hazzir	13.08.03	7,12	780	20,0	4,46	1,65	1,19	0,25	1,71	0,42	4,28	1,00	
Hazzir	16.11.03	6,92	845	18,5	5,04	1,56	1,30	0,25	1,84	0,91	4,30	1,35	
Hazzir	20.01.04	7,54	826	17,6	4,78	1,99	1,30	0,25	1,87	0,81	4,33	1,10	
Hazzir	08.03.04	6,95	802	18,1	4,68	2,39	0,95	0,23	1,79	0,61	4,57	1,05	0.13
Hazzir	19.04.04	7,15	840	17,8									0.16
Hazzir	03.08.04	6,95	802	18,1									

The analysis results show no significant amounts of heavy metals, all concentrations are lower than the thresholds of the Jordanian Standard for Drinking Water (Tab. 2.4).

Tab. 2.4: Results of hydrochemical analysis heavy metals in the three major springs of the test area (source: Analysis of the Geological Department, University of Amman).

Spring	Date	Cu ppm	Zn ppm	Cr ppm	Fe ppm	Mn ppm	Sr ppm	Pb ppm	Cd ppm
Baqouriyeh	20.01.2004	0.006	0.090	0.005	0.15	0.004	0.86	less 0.01	less 0.01
Azraq-Fuheis	20.01.2004	0.003	0.040	0.006	0.12	0.002	1.25	less 0.01	less 0.01
Hazzir	20.01.2004	0.004	0.040	0.005	0.09	0.001	0.67	less 0.01	less 0.01

The results of the microbiological analysis are listed in Tab. 2.5. For comparison sample results from 1991 described by Ta'any (1992) are also shown. There are high amounts of total coliforms

in the spring analyses from 1991 and 2004. In the analysis from 1991 there is also a certain amount of faecal coliforms. Faecal coliforms usually live in human or animal intestinal tracts, and their presence in drinking water is a strong indicator for recent sewage or animal waste contamination. However, in the samples of 2004 no faecal coliforms could be detected, indicating that the coliforms are not of faecal origin. It is not surprising to find a high amount of total coliforms because waste water treatment plant bypasses, combined sewer overflows and storm water runoff during high stream flow can contribute to a significant amount of contamination to the groundwater in the test area. Francis et al. (2000) found a statistically significant relationship between land use and total coliforms detections. Higher concentrations of total coliforms were found among the agricultural land use areas, and a greater percentage of total coliforms detections were found in well samples with septic systems on the property.

The high amount of faecal coliforms in a Azraq-Fuheis spring sample from May 1991 supports the above described observation that there is a periodically input of contamination sources in the spring mainly by infiltrating waste water.

Tab. 2.5: Microbiological analysis of the three main springs in the test area.

<i>Spring</i>	<i>Date</i>	<i>pH</i>	<i>E.C us/cm</i>	<i>Temp C°</i>	<i>Feacal Coliforms 1/10 ml</i>	<i>Total Coliforms 1/ 10 ml</i>
Baggurieh	19.04.2004	7.15	646	19.2	0	377000
Baggurieh	03.08.2004	7.43	622	18.8	0	127000
Baggurieh	19.03.1991				4	21
Baggurieh	26.05.1991				43	460
AzraqFuheis	19.04.2004	7.48	523	19.1	0	381000
AzraqFuheis	03.08.2004	7.19	514	14.4	0	148000
AzraqFuheis	19.03.1991				< 3	150
AzraqFuheis	26.05.1991				> 2400	> 2400
Hazzir	19.04.2004	7.15	840	17.8	0	147000
Hazzir	03.08.2004	6.95	802	18.1	0	146000
Hazzir	19.03.1991				< 3	< 3
Hazzir	26.05.1991				< 3	< 3



### **3 THEORETICAL ASPECTS OF GROUNDWATER VULNERABILITY, HAZARDS AND RISK INTENSITY**

#### **3.1 Groundwater vulnerability**

##### **3.1.1 Basics concepts in groundwater vulnerability**

The concept of groundwater vulnerability is based on the assumption that the physical environment provides natural protection to groundwater against contaminants resulting from human impacts entering the subsurface environment (Vrba & Zaporozec, 1994).

The intrinsic vulnerability of groundwater to contaminants is the sensitivity of the geological sequence independently of the nature of the contaminants which depends on the geological and hydrogeological characteristics of the geological sequence (Zwahlen et al., 2004). The term specific vulnerability takes into account a particular contaminant or a group of contaminants in addition to the intrinsic vulnerability of the area. In the present study solely the intrinsic vulnerability is considered.

Fundamental concepts and the different approaches of groundwater vulnerability have been previously described in various studies and therefore are not discussed in detail within this thesis (Zwahlen et al., 2004; Daly et al., 2002; Goldscheider, 2002; Gogu & Dassargue, 2001; Magiera, 2000; Doerflinger & Zwahlen, 1998; Hölting et al., 1995; Rosen, 1994; Vrba & Zaporozec, 1994; Aller et al., 1987; Foster, 1987). The PI-method (Goldscheider et al., 2000), that was used in this study is described in the following section in more detail.

##### **3.1.2 The PI Method**

The PI-method, originally developed for European karstic areas, is based on two main factors: the P-factor and the I-factor. The P-factor (protective cover factor) considers the effectiveness of the overlying layers including the properties of the geological materials between the groundwater table and the earth surface. Factors influencing the effectiveness of the overlying layers comprise:

- the thickness and eFC of the topsoil,
- the recharge rate per year,
- the thickness and grain size distribution of the subsoil,
- the lithology and degree of fracturing of the rocks.

The I-factor (infiltration conditions) indicates the degree of bypassing of the protective functions by lateral surface and subsurface flow (Goldscheider et al., 2000). It takes into consideration the infiltration conditions such as

- the dominant flow process,
- the flow concentration of the surface water depending on the slope,

- the hydraulic conductivity of the soils,
- the depth to the low permeability layers,
- the land cover conditions,
- the existence of sinking streams, swallow (sink-)holes and the discharge direction in the test area.

The protective effectiveness (P-factor) of the rock cover above the aquifer is determined by a point-counting system. The final vulnerability map is calculated by multiplying the thematic maps of the P-factor and the I-factor leading to the PI-factor that indicates the groundwater vulnerability. The higher the PI factor, the higher is the protective function and hence the lower is the vulnerability of the uppermost aquifer. The vulnerability of the test area is discussed in chapter 7.

### 3.1.3 Existing groundwater vulnerability maps in Jordan

Within the project cooperation "Groundwater Resources of northern Jordan" (Project No. 89.2105.8) between the Bundesanstalt für Geowissenschaften und Rohstoffe (BGR, Federal Institute for Geosciences and Natural Resources) and the Ministry of Water and Irrigation (MWI) the following studies, dealing with groundwater vulnerability mapping in Jordan, were accomplished: Margane et al. (1999, 1997), Hijazi et al. (1999). These studies used the GLA method developed by the German Geologischen Landesamt (GLA, State Geological Surveys) and the BGR published by Hölting et al. (1995).

Al Farajat (2002) studied the vulnerability in the region of Aqaba using the DRASTIC index (Aller et al, 1987). Tadros (2001) studied the vulnerability in a test area in the most northern part of the Amman-Zarqa-Basin, not following any existing vulnerability approach, but taking into account several parameters such as water depths, groundwater flow direction, infiltration rate.

## 3.2 Groundwater hazards

Groundwater hazards are defined by the COST Action 620 (Zwahlen et al., 2004) as potential sources of contamination resulting from human activities taking place mainly at the land surface (De Ketelaere et al., 2004). For hazard evaluation and classification it is essential to define the quantity and the toxicity of the substances which can be released. Hazards can be classified by their duration of disposal, their geometry, the type of human activity or the nature of the contaminants (De Ketelaere et al., 2004). According to their geometrical features, hazards can be differentiated in punctiform (e.g. septic tanks), linear (e.g. streets) and polygonal (e.g. agricultural area), strongly depending on the mapping scale.

Numerous human activities have negative effects on the environment and the groundwater resources, thus, it is impossible to include all these variants in a hazard map. Hence, the hazard map can only incorporate the main impacts which are based on the production, transport, storage, utilization and disposal of harmful substances. The release of the contaminants occurs



over several temporal scales, ranging from an instantaneous event (accident spill) over weeks to months (fertilisers).

The harmfulness of different hazard types is expressed as hazard index (HI). The HI is determined through a weighting, ranking and reduction scheme. In a first step the location, the type according to the hazard inventory list of the COST ACTION 620 and the size of the hazard are displayed in an unclassified hazard map. In a second step a classified hazard map is generated showing the degree of harmfulness for the groundwater expressed as hazard index that was calculated as a result of the weighting, ranking and reduction factor. On the classified hazard map, each hazard type of the unclassified hazard map with its predefined HI is assigned to one of five hazard level classes symbolised by five colours (blue for low hazard level to red for very high hazard level).

The hazard inventory of the COST ACTION 620 follows three levels for the determination of the weighting factor. In the first level (level I) hazards are classified into three main categories which are based on the land use: agricultural activities, infrastructural development and industrial activities (Tab. 3.1).

Tab. 3.1: Three levels of hazard classification. The example of municipal waste shows the level III hazard type classification (modified after De Ketelaere et al., 2004).

Number	Level I Categories of Hazards	Level II Subcategories of Hazards	Level III Hazard Type	Weighting Value
1	<i>Infrastructural development</i>		...	
1.1		Waste water		
1.2		<b>Municipal waste</b> →	Garbage dump	40
1.3		Fuels	Waste loading station	40
1.4		Transport / traffic	Sanitary landfill	50
1.5		Recreational facilities	Spoils depository	35
1.6		Diverse hazards	Sludge from treatment plants	35
			...	

Then the three main categories are further subdivided based on additional criteria (level II in Tab. 3.1), which distinguish between hazards according to the main source of possible groundwater contamination (solid or liquid contaminants) or else refer to types of industrial or agricultural activities with their corresponding spectrum of possible pollutants. In a last step, further subdivision of the subcategories is made, indicating all possible existing types of hazards within each subcategory (level III in Tab. 3.1), leading to the weighting value of each hazard. The classified hazard map of the test site is shown in chapter 8.

### **3.3 Groundwater risk intensity**

Guidelines for the assessment of the risk intensity are given by Hötzl et al. (2004) for the COST Action 620 (Zwahlen et al., 2004). Groundwater protection schemes are usually based on the concepts of contamination risk and risk management (Adams & Forster, 1992; Daly & Warren, 1998). Daly et al. (2004) define risk with regard to groundwater as a possible contamination resulting from a hazardous event, defined as the likelihood or expected frequency of a specific adverse consequence on groundwater. Risk is not intended as absolute measure but as means of relative measure or comparison. In a first approach risk assessment identifies the existing for potential hazards and exposures pathways of groundwater contamination taking into account the likelihood of an impact, the intensity of a potential impact and the vulnerability of the groundwater. However, this kind of assessment, described by Hötzl (2004) as “risk intensity” and quantified by the Risk Intensity Index (RII) doesn’t specify the damage for the groundwater and the resulting consequences according to the general risk evaluation. The latter are determined by the Risk Sensitivity Index (RSI), which depends on the amount and toxicity of the contaminants in relation to the groundwater storage capacity, flow rate as well as on the economic and ecological importance of the affected groundwater.

In this study only the risk intensity was investigated. For the risk intensity assessment and to maximise the possibilities for a sustainable groundwater management the COST Action 620 guidelines suggest to combine the hazard map with the groundwater vulnerability map, using the interaction between the surface contamination load and the aquifer pollution vulnerability at the location of concern. The risk intensity map reflects potential groundwater contamination by human activities, showing that the highest risk of contamination exists where a dangerous hazard is located in zones which are characterized by highly vulnerable aquifers. The risk intensity map of the test area is discussed in chapter 9.

## 4 THEORETICAL ASPECTS OF REMOTE SENSING

### 4.1 Physical principles of remote sensing

Lillesand & Kiefer (2000) define remote sensing “as the science and art of obtaining information about an object, area or phenomena through the analysis of data acquired by a device that is not in contact with the object, area, or phenomenon under investigation”.

The sensors used to acquire the remote sensing data record the variations in the way surface features reflect and emit electromagnetic energy (Lillesand & Kiefer, 2004), travelling at the speed of light in a harmonic wave pattern (Sabins, 1997), penetrating media (air, water) as well as the vacuum (space). All matters at temperatures above absolute zero continuously emits electromagnetic radiation. Laws of physics state that the higher the energy is the shorter are the wavelengths and the higher the temperature of the matter the higher is the emitted energy.

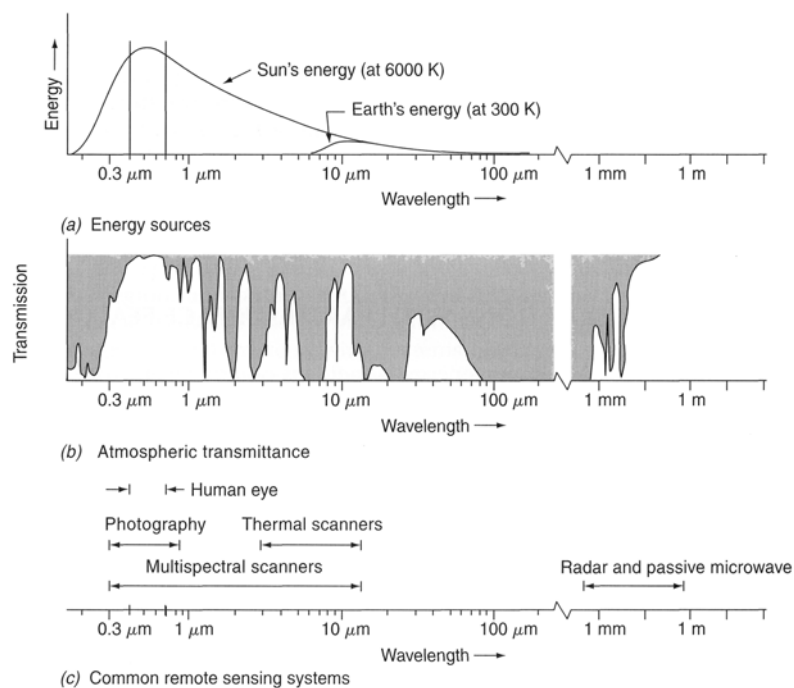


Fig. 4.1: Spectral characteristics of (a) energy sources, (b) atmospheric transmittance, and (c) common remote sensing systems (Lillesand & Kiefer, 2004).

including visible light (VIS), near infrared (NIR), short wave infrared (SWIR), thermal infrared (THIR) and microwaves (Fig. 4.1c).

When electromagnetic energy is incident on any given earth surface feature, three fundamental energy interactions are possible: reflection, absorption and transmission (Lillesand & Kiefer, 2004). The proportions of energy interactions will vary for different earth features, depending on their material type and condition allowing to distinguish different surface features in an image.

Due to the wavelength dependency even within a given feature type, the proportion of reflected, absorbed and transmitted energy varies for different wavelengths. These interactions influence the information content of the spectral values acquired by the sensors. As shown in Fig. 4.2

The emission is characterised by spectral signals showing various wavelengths depending on the physical characteristics of the matter. Electromagnetic waves are often categorized by their wavelength location within the electromagnetic spectrum. After Bähr & Vögtle (1998) the usefulness of the electromagnetic spectrum for remote sensing applications is described by the wavelength and the atmospheric transmittance (atmospheric windows) (Fig. 4.1b). Within the wide range of the electro-magnetic spectrum common remote sensing systems use comparatively few and narrow bands

spectral characteristics allow for a differentiation of given feature types (soil, vegetation, water) based on their spectral reflectance curves, showing the reflectance [%] of surface feature types within a given spectral range.

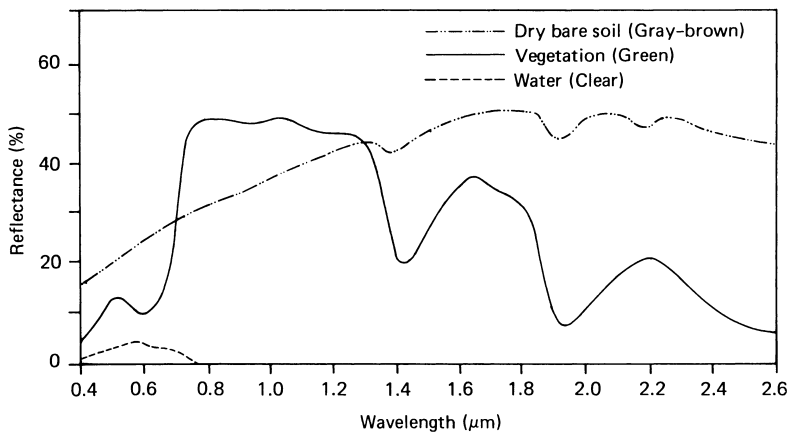


Fig. 4.2: Typical spectral reflectance curves for vegetation, soil, and water (Lillesand & Kiefer, 2004).

After Bähr & Vögtle (1998) the information content of satellite images depends on the acquisition time, the area, the range and position of the spectral bands within the electromagnetic spectrum and the spectral reflection. The analysis of the raw satellite image information can be accomplished either by visual or digital image interpretation. The visual study of remote sensing imagery involves

several basic characteristics of features displayed on an image such as: shape, size, pattern, tone (or hue), texture, shadows, site, association, resolution (Olson, 1960). Whereas pattern is produced by the spatial arrangement of visible discernible objects, association is the relation to neighbouring objects and texture is the arrangement and frequency of tonal variations in the image.

## 4.2 LANDSAT ETM<sup>+</sup>

There are many moderate and high spatial resolution satellites existing. LANDSAT and SPOT are the most well-known due to their historical long term use and widespread availability (Lillesand & Kiefer, 2004). As LANDSAT ETM<sup>+</sup> data is used in this work (chapt. 5, methodology and data sets) the LANDSAT satellite is described in detail in the following section.

The LANDSAT 7 Enhanced Thematic Mapper Plus (ETM<sup>+</sup>) is a NASA earth resource satellite that acquires multispectral images within a wide range of the electromagnetic spectrum, including seven bands from the visible to the thermal infrared with varying wavelengths and one panchromatic band. Depending on its range of wavelengths, each band shows special characteristics (Tab. 4.1). The Worldwide Reference System (WRS) allows inquiry about LANDSAT images by path and row number. WRS paths are sequential east-to-west satellite track identifiers and rows identify the latitude of the image centre.

The LANDSAT ETM<sup>+</sup> sensor was launched on board of NASA's LANDSAT 7 spacecraft in April 1999 in a sun-synchronous orbit in 705 km altitude, capturing scenes in N-S descending mode and crossing the equator between 10.00 and 10.15 AM (local winter time). The Landsat ETM<sup>+</sup> is a whiskbroom imaging system, which employs a bi-directional scan mirror assembly (SMA) to sweep the detector's line of sight in west-to-east and east-to-west directions across track.

The multispectral passive ETM<sup>+</sup> sensor records electromagnetic radiation in multiple regions of the electromagnetic spectrum, which is reflected or emitted from the earth's surface (Lillesand & Kiefer, 2004) unlike active remote sensing methods that provide their own source of electromagnetic radiation (e.g. RADAR) to illuminate the terrain (Sabins, 1997). The incoming energy is separated into several spectral components that are sensed independently. The electric signals generated by each of the detectors of the multispectral scanner are amplified by the system's electronics and recorded by a multichannel tape recorder.

For each detector the intensity of the electronic signal of the instantaneous field of view (IFOV) – that is expressed as the cone angle within which incident energy is focused on the detector results in a single digital number (DN) that is represented as pixel by its grey value. Due to the finite storage capacity, a digital number is stored with a finite number of bits (binary digits). The number of bits determines the radiometric resolution of an image. The radiometric resolution of the LANDSAT ETM<sup>+</sup> imagery is 8-bit, resulting in digital numbers ranging from 0 to 255 (2<sup>8</sup>).

For results at scales between 1:50,000 and 1: 500,000 the choice of LANDSAT ETM<sup>+</sup> imagery data appears to be suitable because of the combination of extensive geographical coverage of the area of interest, wide spectral range, good vegetation discrimination, good data availability and a relative cost-efficiency compared to conventional data collection.

Tab. 4.1: Spectral bands of the LANDSAT ETM+ sensor (grey: band not used in this work).

	<b>Band</b>	<b>Spectral range [μm]</b>	<b>Spatial resolution [m]</b>	<b>Characteristics (after Bähr, 1985)</b>
1	visible blue	0.45 – 0.52	30	Coastal water application, soil/vegetation differentiation
2	visible green	0.52 – 0.60	30	Maximum of green reflectance of vegetation, vegetation vigour
3	visible red	0.63 – 0.69	30	Minimum of green reflectance, vigour and biomass content,
4	near infrared	0.76 – 0.90	30	Maximum of Chlorophyll reflectance, vegetation vigour, complete absorption of water
5	mid infrared	1.55 – 1.75	30	Vegetation and soil moisture indicator
6	thermal infrared	10.40 – 12.50	60	Thermal imaging or mapping e.g. for geological information
7	mid infrared	2.08 – 2.35	30	Discrimination of mineral and rock types
8	panchromatic	0.52 – 0.90	15	Higher spatial resolution, used for data fusion

Depending on the level of detail in the desired results, one potential disadvantage of LANDSAT ETM<sup>+</sup> imagery can be the spatial resolution of 30 m (multispectral bands) or 15 m (panchromatic band). Further details on the sensor and image characteristics, the LANDSAT 7 spacecraft, and the LANDSAT project objectives can be found in NASA (2002).

### 4.3 Satellite image classification

The most commonly used method to derive information from satellite imagery is the implementation of a classification. The purpose of multispectral digital image classification is to produce thematic maps where each pixel is assigned on the basis of spectral response to a particular theme (Gupta, 2003). The methods of image classification are largely based on the principles of pattern recognition. A pattern may be defined as a meaningful regularity in the data, that can be identified during the classification process. The process of image classification involves conversion of satellite spectral data, according to the DN-values, into different classes or themes of interest (e.g. rock, water, crops). There are two basic approaches of image classification: *unsupervised* and *supervised*.

The *unsupervised classification*, also called cluster analysis, first groups the pixels according to their DN-value to several spectral classes. This clustering method uses spectral distances and iteratively classifies the pixels, redefines the criteria for each class and classifies again, so that the spectral distance pattern in the data gradually merge. The spectral distance between the candidate pixel and each cluster mean is calculated. The pixel is assigned to the cluster whose mean is closest (Sabins, 1996).

The Iterative Self Organizing Data Analysis (ISODATA) algorithm is a common method for performing unsupervised classifications used by many image analysing software packages. The ISODATA algorithm randomly selects spectral cluster means in the multidimensional input data space. Next, each pixel is then grouped into a certain spectral cluster based on the minimization of a distance function between this particular pixel and the cluster means. After each iteration, the total number of which is provided by the user, the cluster means are updated, and clusters are possibly split or merged, depending on the size and spread of the data points in the clusters. The user interacts at the beginning of the procedure by specifying the minimum, maximum and desired number of spectral classes to be generated, the maximum number of iterations to be carried out and a maximum percentage of unchanged pixels that has to be reached between two a posteriori iterations leading to the convergence of the algorithm. After the unsupervised classification it is the users responsibility to attach meaning to the resulting classes (Jensen, 1996), merge or disregard them. Thus, unsupervised classification is not completely free from the users intervention, it does not depend upon a priori knowledge of the test area (Gupta, 2003).

In a *supervised classification*, first representative samples of different ground-cover types or classes of interest in the image have to be located. These classes of interest are called training areas. The training areas are selected based on the analyst's familiarity with the area and knowledge of the actual groundcover types. Training areas should be both representative, internal homogenous and completely including all spectral classes constituting each information class to be discriminated by the classifier (Lillesand & Kiefer, 2004). For obtaining as accurate results as possible an adequate number of training areas for each information class is needed. For practical use Lillesand & Kiefer (2004) recommend for the amount of pixels per training area per class the minimum target value of  $10n$  to  $100n$  where  $n$  is the number of spectral bands used. However, the amount of pixels used should be adapted to the situation and complexity of the test area.

The DN-values of the pixels in all spectral bands representing these training areas are then used to generate some statistical parameters, training data statistics or signatures, depending on the classification algorithm used (Gupta, 2003). In the classification stage, each pixel in the *input* image data is sorted into the land cover class it most closely resembles. In the output stage, the category label assigned to each pixel during the classification process is then recorded in the corresponding cell of the interpreted *output* image as individual land cover type. It is important to consider, that the pixels within each class do not have a single, repeated spectral value, but illustrate the variability of the spectral properties found within each cover class. These clouds of points represent multidimensional descriptions of the spectral response patterns of each category of cover type to be interpreted (Lillesand & Kiefer, 2004).

For the optimal number of land cover classes a combined approach involving both supervised and unsupervised classification methods is generally the best.

#### 4.4 Normalized Difference Vegetation Index (NDVI)

Since the 1960s scientists have extracted and modelled various vegetation biophysical variables such as vegetation indices using remote sensing data (Clarke, 2000). There are more than 20 vegetation indices in use, whereof the Normalized Difference Vegetation Index (NDVI) is widely adopted and applied to LANDSAT imagery.

The Normalized Difference Vegetation Index (NDVI) is used to qualify and quantify the vegetation cover. The NDVI is a dimensionless measure of vegetation vigour and density computed from multispectral data and was developed by Rouse et al. (1974) using the equation (4.1) below

$$NDVI = \left( \frac{NIR - VIS(RED)}{NIR + VIS(RED)} \right) \quad (4.0)$$

The magnitude of NDVI is related to the level of photosynthetic activity in the observed vegetation (Kidwell, 1997). The NDVI is calculated by dividing the difference of near infrared (NIR) and visible reflectance (VIS) red band by the total reflectance.

Vegetated areas generally yield high values for the NDVI because of their relatively high near-infrared reflectance and low visible (red) reflectance. Plant chlorophyll (green pigment) absorbs incoming radiation in the visible band (red), while the internal leaf structure and water content are responsible for a very high reflectance in the near infrared region of the spectrum. Rock and bare soil areas have similar reflectance values in the two bands, resulting in an NDVI near zero (Lillesand & Kiefer, 2000; Sabins, 1997). As the amount of green vegetation increases in a pixel, NDVI increases to nearly 1.

NDVI is often correlated to a variety of vegetation characteristics that include quantity, productivity, biomass etc. It has to be taken into account that NDVI is not linearly related with the actual vegetation cover on the ground (Kidwell, 1997). So, twice as high NDVI does not mean twice as much vegetation cover on the ground. A reduction in the NDVI of a crop can indicate poor soil, poor drainage, lack of nutrients, disease, fungal infections or water stress.

## 4.5 Orthophotos

Orthophotos are orthographic photographs that do not contain the scale, tilt and relief distortions characterising aerial photographs (Lillesand & Kiefer, 2004). After Hildebrandt (1996) an orthophoto is a differential distorted aerial photograph and therefore converted from the central perspective projection to the orthographic projection.

Before the aerial photograph information can be interpreted and extracted in a way that is useful for a GIS or further processing, the photographs must be orthorectified to remove distortion from the image. To convert an aerial photograph in an orthophoto, each image pixel is processed through photogrammetric equations using ground control points, camera calibration and orientation parameters, and a digital terrain model. The result is an orthorectified image in which distortions and displacements are removed, allowing distances, areas and angles to be precisely measured and allowing for a more complex spatial analysis. Orthophotos have one scale, even in varying terrain, and they show the terrain in actual detail.

With the introduction of computer-based, softcopy photogrammetric mapping and GIS systems, that operate in a desktop computing environment and are able to manipulate both vector and raster data, the demand for images in raster format and the combination of orthophotos and GIS has increased sharply (Welch & Jordan, 1996). Digital orthophotos can be considered as base maps, that can be used to extract features, to update existing coverages for land use/cover and infrastructure and assess changes in the landscape caused by construction or environmental phenomena (Welch & Jordan, 1996). The construction of digital orthophotos on desktop systems has to be considered as state-of-the-art and provides an important tool for visualizing information that is not available on topographic maps (Krupnik, 2003).



## **5 REMOTE SENSING IN HYDRO(GEO)LOGY, GROUNDWATER VULNERABILITY AND HAZARD MAPPING**

### **5.1 Introduction**

In the field of hydro(geo)logy remote sensing techniques are often applied. Over the last few years, with the emerge of the GIS and a wider availability of digital data, together with the continuously decreasing cost in computer power, several computationally intensive distributed process-orientated models have been developed that integrate information derived by remote sensing data such as the Systeme Hydrologique Europeen (SHE) model (Abbott et al., 1986), the TOPMODEL (Beven et al., 1984; Beven & Kirkby, 1979) or TerrainLab (Chen et al., 2005).

Remote sensing imagery provides spatial information about the processes of the land phase of the hydrological cycle whereas land cover maps are the basis of hydrologic response units for modelling units. For an understanding of the hydrology of areas with little available data, a better insight into the distribution of the physical characteristics of the catchments is provided by image processing techniques. Some of the new measurement methods can give at least to some extent reliable areal totals or averages of hydrologic variables such as precipitation, evapotranspiration and soil moisture (Jackson, 2002; Belz, 2000; Meijerink, 2000; Su, 1996; Ahmed, 1995; Engman & Gurney, 1991; Waters et al., 1990; Farnsworth et al., 1984).

Most of the information for groundwater derived from remote sensing data is obtained by qualitative reasoning and semi-quantitative approaches. The information derived from remote sensing imagery is often of surrogate nature and has to be merged with geohydrological data to become meaningful (Meijerink, 2000). Within the last two decades numerous studies were accomplished within the field of hydrogeology focusing mainly on groundwater assessment, exploration, groundwater recharge, soil moisture and water management (Meijerink, 2000; Sander, 1996; Engman & Chauhan, 1995; Teeuw, 1995; Farnsworth et al., 1984). Since passive remote sensing only observes the surface of the earth, it is important to establish a link between the surface observations and the groundwater phenomena (Jackson, 2002).

An overview of the use of remote sensing data types, remote sensing techniques for hydrology, hydrogeology and water management is given in (Fig. 5.1). The following chapter briefly summarises the state-of-the-art knowledge of the possible use of remote sensing data for hydrogeological applications.

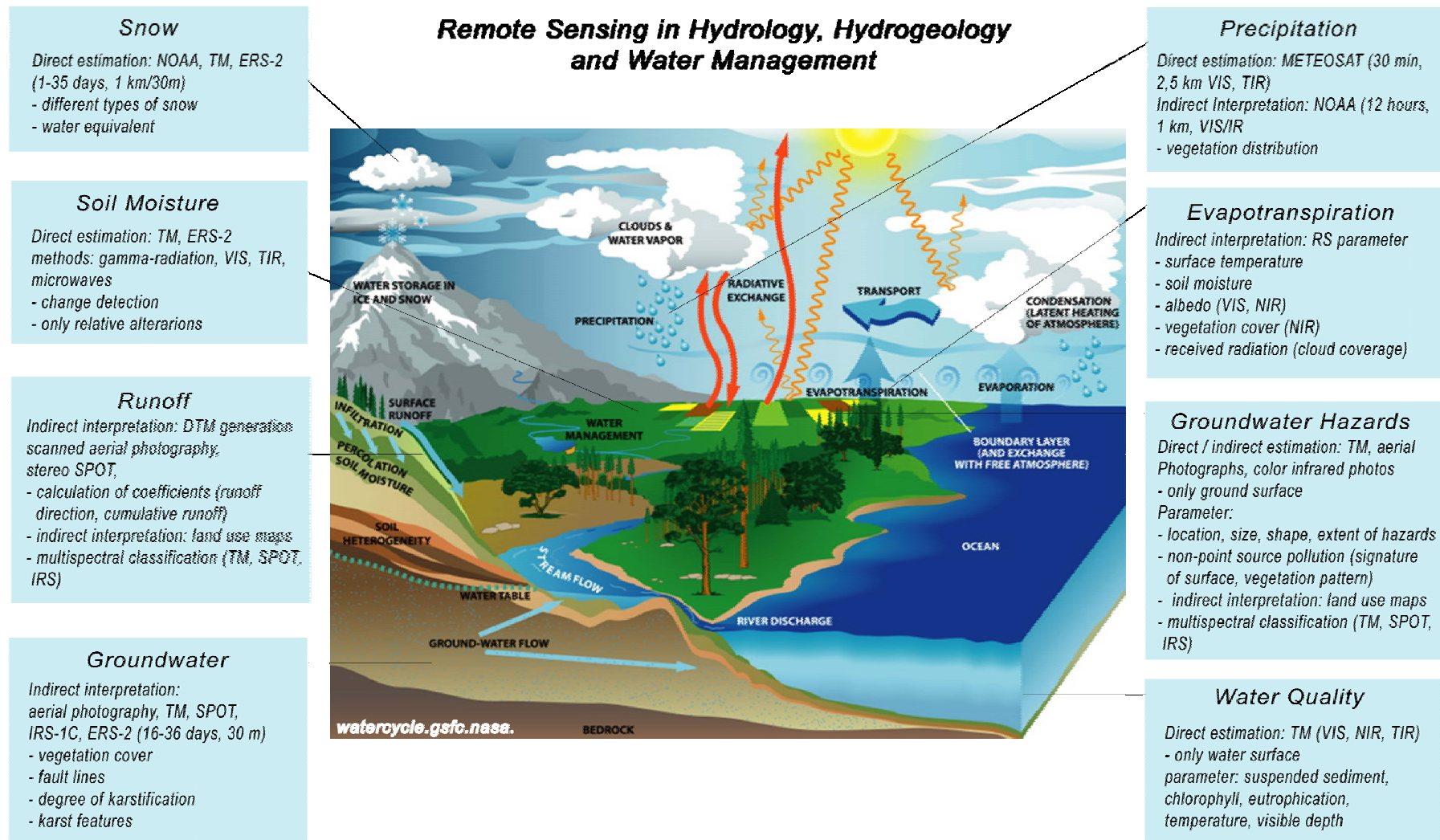


Fig. 5.1: Applications of remote sensing in hydrology, hydrogeology and groundwater management (text modified and supplemented after Hochschild, 1998, image: NASA.)

## **5.2 Applications in the field of hydrogeology**

### **5.2.1 Degree of karstification**

For karst landscapes, the surface characteristics are expressed as solution morphology on a regional scale. Because of the spatial resolution, on LANDSAT ETM<sup>+</sup> images karst forms smaller than the spatial resolution (e.g. karren, small dolines) cannot be distinguished. Only the larger solution and fracture-controlled structures (dolines, dry valleys) can be recognized. Thus, the advantage of using LANDSAT ETM<sup>+</sup> imagery is not the identification or the recognition of individual small-scale karst features, such as karren, but the assessment of the karstification (karst pattern and texture) at regional scales.

The following studies focus on karst morphology and the related hydrology using LANDSAT TM data: Kazemi (2003), Kaufmann et al. (1986), Parcharidis et al. (1998). However, Parcharidis et al. (1998) realized that it is very difficult to detect and recognize structures related to small-karstic phenomena, the work of Kaufmann et al. (1986) is limited to the detection of submarine springs using the thermal band of the LANDSAT TM data. The work of Kazemi (2003) focuses on filter operations and visual extractions of karst related features such as lineaments from remote sensing data and their correlations with hydrologic behaviour of the karst.

The use of orthophotos for the differentiation of different karstification levels is discussed in chapter 6.4).

### **5.2.2 Evaporation and evapotranspiration**

Atmospheric parameters which affect the evapotranspiration including surface temperature, surface soil moisture, surface albedo, vegetative cover and incoming solar radiation often cannot directly be gained by remote sensing (Engman & Gurney, 1991). The calculation of the crop evapotranspiration is usually done by definition of the crop stages and assigning a crop coefficient to each stage for each crop (Doorenbos & Pruitt, 1977). Furthermore the evaporation of the conveyance has to be added (Meijerink, 2000; Meneti, 2000). Dezetter et al. (2003) use remote sensing data to characterise the vegetation dynamics and the associated water flux for the assessment of the real evapotranspiration.

### **5.2.3 Recharge**

For the calculation of recharge many qualitative and semi-quantitative approaches exist (Lubczynski & Gurwin, 2005; Brunner et al., 2004; Saraf et al., 2004; Jackson, 2002). Qualitative approaches use visual interpretation of remotely sensed images whereas the geomorphology can be used for delineation of the various soils or overburden units. After segmentation of the terrain in physiographic units where each segment has a set of geomorphologic soil properties and vegetation types, transfer functions are needed to convert meteorological and terrain data into quantitative values of recharge (Meijerink, 2000). The conversion of the data is often difficult. Estimated values of similar areas can be taken from literature but in most cases are site-specific and therefore will not fit in a reliable way; on the other hand direct field measurements can be made.

The different land cover types, the geological situation and other relevant information derived from multispectral image classification, orthophotos etc. can be used in a semi-quantitative approach, whereby a water balance of the upper zone is calculated (Meijerink, 2000; Houston, 1982; Rodier, 1975). Ben-Dor et al. (2004) investigated the infiltration rates in semi-arid soils in Israel using airborne hyperspectral technology. The study links a developed spectral parameter based on the soil reflectance information and rain simulator treatments for the assessment of soil infiltration affected by the soil crust.

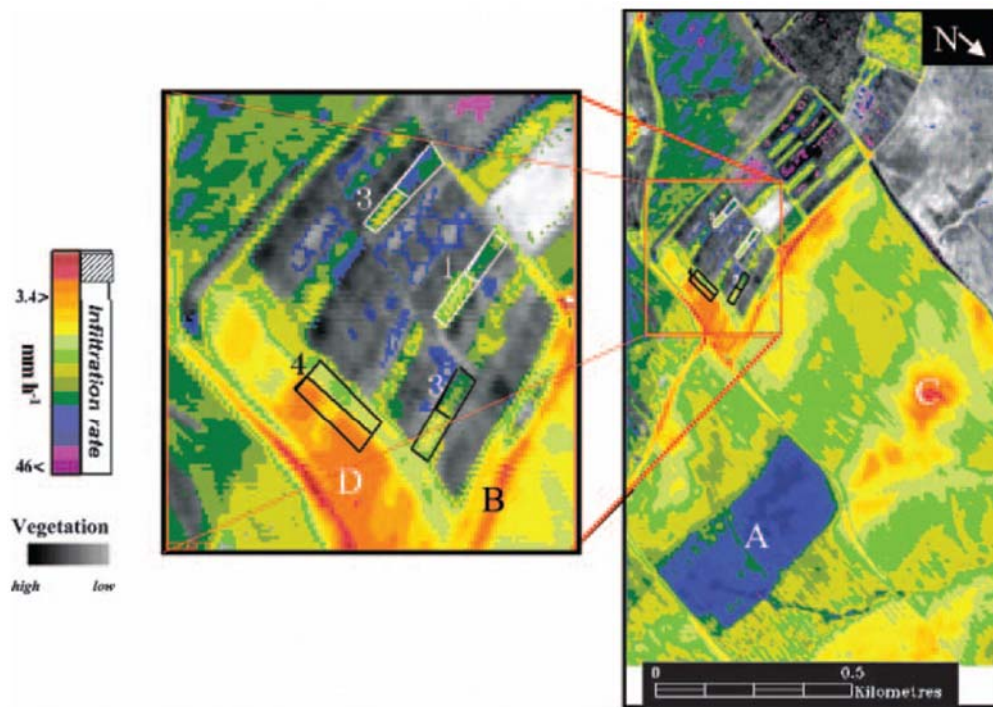


Fig. 5.2: Infiltration rate image of research area, as generated on the basis of soil reflectance information. A low infiltration rate area is marked as A on the image, high infiltration areas are marked as B,C, D (Ben-Dor et al. 2004).

Jackson (2002) describes active and passive remote sensing techniques (such as microwaves techniques) that provide information on soil moisture and water-balance models that link and transfer these observations to the recharge.

#### 5.2.4 Groundwater explorations

Remote sensing data allow effective mapping of features that favourable the groundwater occurrence (Alsdorf & Lettenmaier, 2003; Robinson, 2002; Sander, 1996). Aquifer features can be observed using visible and infrared satellite aircraft imagery. In some cases it is not possible to identify direct indicators for groundwater, features associated with recharge zones such as rivers, canals, lakes or features associated with discharge zones such as springs, soil moisture and anomalous vegetation. Then indirect indicators have to be used to assess groundwater characteristics such as topographic features, surface gradient, type of rock, regional structural features, soil characteristics, vegetation, soil moisture, drainage density, fracture systems or

hydrogeological surface features such as sinkholes, alluvial fans and fault zones which provide valuable information for groundwater assessment.

The major studies dealing with the assessment and exploration of groundwater follow the principle that groundwater occurrence is also controlled by structural features in the bedrock, that can be identified as lineaments on remotely sensed images. Several studies with different approaches and varying degrees of success (Sander, 1996) exist (Ahmed, 1996; Boeckh, 1992; Greenbaum, 1992; Waters et al., 1990; Zall & Russell, 1979; Lattman & Pariek, 1964).

For the assessment of groundwater under (semi)-arid climate several studies exist focusing on lineament analysis, land cover mapping or Normalized Vegetation Difference Index (NDVI) calculation, including passive and active remote sensing systems (Baumgartner et al., 1997; Baban, 1997; Gupta et al., 1997; Koch & Mather, 1997; Singhroy & Momani, 1996; Waynakh, 1995; Teeuw, 1995; Tauer & Humborg, 1992).

In groundwater studies in Ghana lineaments could be identified by linear anomalies of lush vegetation, which were observable on dry-season imageries (Sander, 1996). Assuming that vegetation anomalies represent water availability due to the presence of transmissive fracture zones, such features can be important for further well targeting. Hereby, it should be taken into consideration that the value of lineaments for successful well siting is more likely to be associated with the increased confidence that the mapped feature truly represents a transmissive geological structure, rather than with an assessment of the size of the feature identified. Because of the varied nature of lineaments Carruthers et al. (1993) suggest to prove the hydraulic significance of a lineament by drilling and well testing.

### **5.2.5 Groundwater table**

Changes in depth to water table can be inferred through examination of vegetation changes information derived from satellite imagery (Hoffmann, 2005). Image interpretations are used to locate areas where the groundwater table is probably low. This can be identified on the images by an effect on vegetation, relative soil moisture, land cover and land use or in details of the drainage system. The appearance of groundwater at or near the surface is caused by either the intersection of topographic depressions and a static phreatic groundwater level or by a discharge zone of a groundwater flow system. The reconstruction of the groundwater surface is a manual operation, unless so many data points are available that one of the interpolation methods can be meaningfully employed. Furthermore, it is often difficult to recognize features directly related to the groundwater especially in cultivated areas (Meijerink, 2000).

Nature surface water bodies such as streams, lakes, springs, lakes and wetlands interact with groundwater bodies in nearly all landscapes (Winter, 1999). In upland areas it is often not possible to clearly interpret if the shallow groundwater table is perched and possibly seasonal or whether it is the surface of the coherent groundwater body. Merging of image interpretations with hydrogeological field data can produce more reliable results.

Groundwater leakage and upwelling in coastal seas as well as karst springs and the related karst features can be detected on thermal imagery by the thermal contrast that exists at sea surface between upwelling groundwater with low density and surrounding sea water with higher density (Kaufmann et al., 1986).

## 5.2.6 Conclusions and discussion

Groundwater assessment using remote sensing imagery can be useful in areas where groundwater recharge zones are associated directly with fault zones or joint systems. The existing quantitative approaches for groundwater recharge often do not possess negligible sources of inaccuracy such as spatial variation of horizontal and vertical soil hydraulic parameters or the root parameters. Meijerink (2000) assumes that it is very difficult to determine a reliable value of the potential evaporation, because of the varying results when comparing data from evaporations pans with calculated values. Often remote sensing data is combined with groundwater models, one-dimensional unsaturated flow models and energy balances (Lubczynski & Gurwin, 2005).

## 5.3 Applications for groundwater vulnerability and hazard mapping

### 5.3.1 Overview

The application of remote sensing techniques in groundwater vulnerability and hazard assessment is a powerful tool to enhance the accuracy and actuality of the land use and land cover data and to fill lacks in topographic information of an area. Following a brief summary of existing approaches using remote sensing techniques for groundwater vulnerability and hazard mapping applications a detailed description of the use of remote sensing data as applied within this study is given in chapter 6.

### 5.3.2 Groundwater vulnerability and remote sensing

Groundwater vulnerability studies that are limited to the use of land use data based on satellite images were accomplished by Al-Adamat et al., (2003), Bressan & Dos Anjos (2003), Magiera (2002), whereas the usage of remote sensing data for vulnerability assessment is often proposed theoretically without going in detail or presenting practical applications and solutions (Spiteri, 2004; Margane, 2002).

### 5.3.3 Groundwater hazards and remote sensing

To date, no attempts to implement the hazard guidelines and mapping procedure of the Cost Action 620 (De Ketelaere et al., 2004) for the assessment of groundwater hazards on the basis of remote sensing imagery exist. However, there are several studies dealing with the assessment of groundwater hazards including the monitoring of water quality, waste water effluence, non point source pollution, hazardous waste observation sites using remote sensing data (Schultz & Engman, 2000; Kjeldsen et al., 1998; Dekker et al., 1995; Engman & Gurney, 1991; Finkbeiner & O'Tool, 1985; Farrell, 1985; Svoma & Pysek, 1983).

At this point, it should be mentioned that the main difference between the Cost Action 620 hazard inventory and existing approaches for hazard assessment is the fact that the Cost Action 620 hazard maps are limited to *potential* hazards that pose a *potential* polluting threat and can have a *potential* impact on groundwater. The other approaches of hazard mapping assess *existing*

hazards that have *already* contaminated the environment in some way, showing visible or measurable consequences on water quality or changes in vegetation patterns and growth of plants.

Farrell (1985) evaluated the use of colour infrared photographs for the identification of onsite wastewater soil absorption systems. Svoma (1985) studied the use of colour and colour infrared aerial photographs for changes in vegetation for detecting groundwater pollution by industrial fertilizers, oil leaks and natural gas leaks on actual emergencies and on experimental sites. Aerial photographs using special film and filters for sensing reflected ultraviolet radiation were used for mapping of oil spills on surface water bodies, thermal infrared for detection of seepage from leach fields and underground storage tanks and low frequency airborne electromagnetic methods (AEM) were applied for the detection of variations in groundwater salinity and deeper brine contaminated aquifers (Ellyett and Pratt, 1975).

Agricultural Non Point Source pollution models that estimate nitrogen, phosphorus and chemical oxygen demand concentration in runoff and assess agricultural impact on surface water quality were accomplished by Mattikalli & Engman (2000). The Non Point Source pollution inputs are based on spatially varying controlling parameters including land cover, land use, soils and topography. Modelling Non Point Source pollution of urban areas using manipulated land use data and an empirical urban water quality model was done by Kim & Ventura (1993). Other Non Point Source pollution studies using remote sensing data were done by Jakubauskas et al. (1992), Schechter (1976), OKI (1975).

#### **5.3.4 Discussion**

Most studies of groundwater hazard assessment produce qualitative or semi-quantitative results; often remote sensing imagery is only used as an indirect means to assess the required parameters. The usage of the data is often limited to special site-specific conditions in a relatively small area, special plant species, and special hydrogeological situations such as the existence of a shallow groundwater table where the roots of plants have contact with the contaminated groundwater.

Often the results or specific applications cannot be transferred to other areas. For example, in the case of a thick unsaturated zone of a karstic aquifer, the plants are independent from the groundwater level, the roots are not in contact with the contaminated water and can not be used as an indicator for groundwater contamination. Often the applications inherit high sources of error due to the fact that plant diseases can have also other reasons than e.g. waste water adsorption (Farrell, 1985).





## 6 DATA SETS AND METHODOLOGY

### 6.1 Introduction

In this chapter the data processing of the remote sensing imagery, auxiliary GIS data and the methodology applied for the soil investigations is described including the results of the respective data processing steps and applied methodology. An overview of the main data types and processing steps of the present study is displayed in the flowchart in Fig. 6.1.

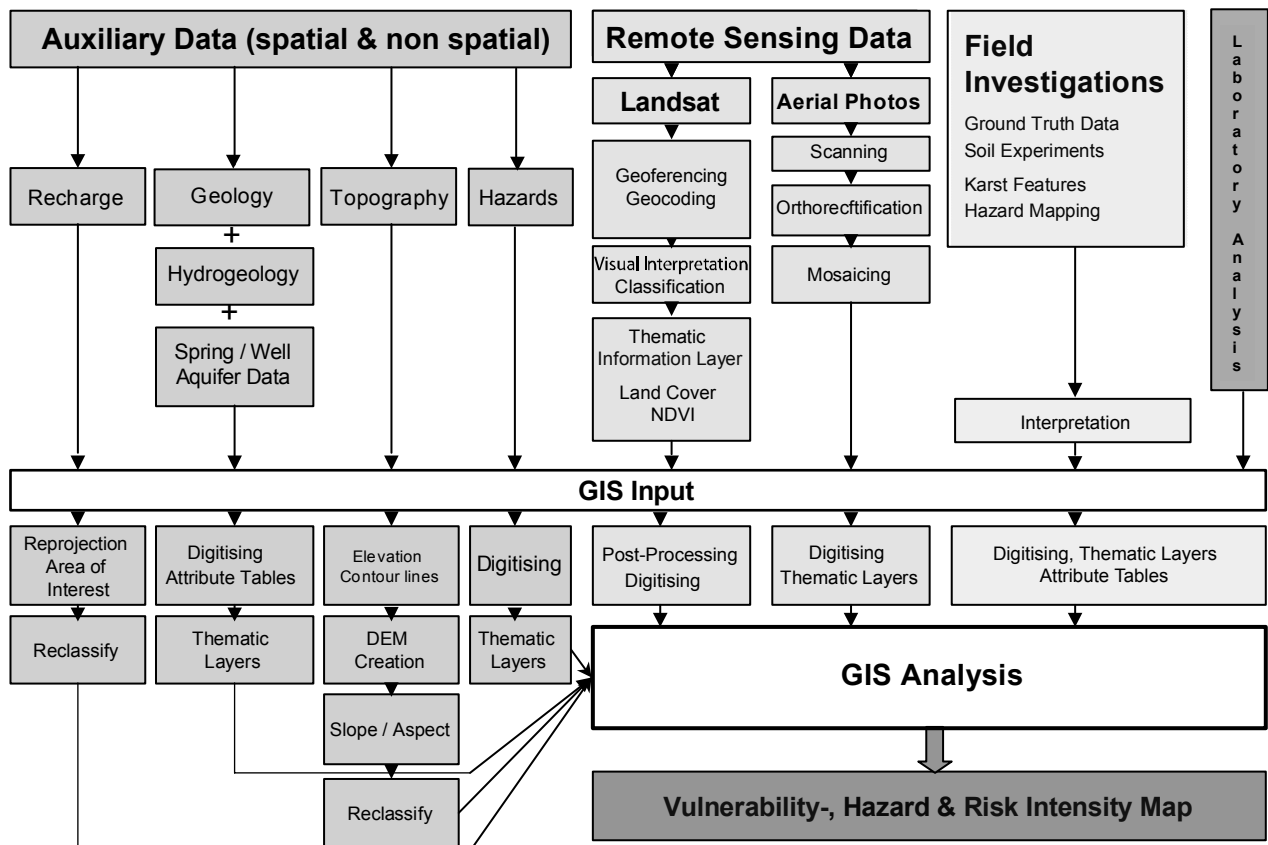


Fig. 6.1: Processing steps and data types of the present study.

Landsat ETM<sup>+</sup> image data acquired at the 21<sup>st</sup> of May 2001, analogue aerial b/w photographs from 16<sup>th</sup> of October 1992 (scale: 1:30,000) and digital colour aerial photographs from 23<sup>th</sup> of September 2000 (scale 1:10,000) were processed with the software *Geomatica 9.0* from *PCI Geomatics™* and post-processed with *ArcGIS 8.3®* from *ESRI*. The remote sensing data processing included data pre-processing, classification of the satellite images and aerial photographs and post-processing steps such as on-screen digitising. For the orthorectification process of the remote sensing imagery, area-wide GPS data were acquired, ground control points (GCPs) and reference data (ground truth) were collected for the delineation of the trainings sites for the supervised classification. For the satellite image, the aerial photographs and all other data generated or modified with *ArcGIS* the projection parameters displayed in (Tab. 6.1) were used.

Existing spatial and non spatial data was collected, supplemented by field investigations or laboratory analysis and digitised with ArcGIS. GPS data were acquired with the *etrex summit* GPS from GARMIN.

Tab. 6.1: Projection parameters of the used remote sensing images and thematic data layers.

<b>Projection parameters</b>	
Projection type	<b>Cassini</b>
Ellipsoid	<b>Clarke 1880</b>
Longitude of projection centre	<b>35° 12' 02.749"</b>
Latitude of projection centre	<b>31° 44' 02.749"</b>
False Easting	<b>170251.555</b>
False Northing	<b>126867.909</b>

## **6.2 LANDSAT ETM<sup>+</sup> data**

### **6.2.1 Pre-processing**

The pre-processing included georeferencing, geocoding and linear contrast stretching of the image. Georeferencing was done by selecting ground control points spread over the whole Landsat ETM<sup>+</sup> subscene, using Nearest Neighbour (NN) resampling of the uncorrected image. The rectification process of the Landsat ETM<sup>+</sup> started before the first GPS field campaign in the test area could be accomplished, therefore no GPS data could be used for determining the ground control points for the geometric correction of the Landsat ETM<sup>+</sup> image. The geometric correction of the raw Landsat ETM<sup>+</sup> image was based on 20 ground control points (GCPs) taken from 1:25,000 topographic maps from 1963 from the Royal Jordanian Geographic Center (RJGC) and resulted in an overall RMS error for x = 0.8 pixels and y= 0.74 pixels, with a maximum error for x = 2 pixels and y = 1.88 pixels.

The errors result from partly incorrect topographic maps being out of date and from not always clearly identifiable GCPs on the topographic maps and the image. The GCPs were usually taken at cultural features such as road intersections. However in the southern part of the test area it was often difficult to find distinctive features. One disadvantage of the NN resampling is the fact that the DN of the closest pixel in the input image is taken disregard of a slight offset up to one-half pixel. The advantage of NN resampling is that the original input pixel values are not changed.

### **6.2.2 Pan-sharpening**

For pan-sharpening the LANDSAT ETM<sup>+</sup> image the Intensity-Hue-Saturation (IHS) technique was applied. The IHS transformation is a fusion procedure for merging a panchromatic with a three-colour RGB imagery in the IHS colour space (Carper et al., 1990; Kraus, 1990; Albertz, 1991). Digital images are typically displayed as additive colour composites using the three

primary colours: red, green, blue (RGB). In addition to the RGB system, the Intensity-Hue-Saturation (IHS) system is another well-known colour system (Bähr & Vögtle, 1996). “Intensity” relates to the total brightness of a colour. “Hue” refers to the dominant average wavelength of light contributing to a colour. “Saturation” specifies the purity of a colour relative to grey (Carper et al., 1990). The transformation was applied to the image using a hexcone model. The aim of the IHS transformation was to merge the 15 m resolution panchromatic band with the 30 m resolution multispectral bands image to get a higher spatial resolution of the image data.

The higher resolution panchromatic data was displayed as the intensity component, the lower resolution multispectral data was displayed as hue and saturation components. The result is a composite image having the spatial resolution of the 15m panchromatic data and the colour characteristics of the original 30 m multispectral data. The disadvantage of the IHS transformation is that it allows only three bands to be applied.

### 6.2.3 Normalized Difference Vegetation Index (NDVI)

The NDVI was calculated to investigate if the results of this index could also be used as direct or indirect input for some parameters of the vulnerability and hazard assessment such as the occurrence, location and extent of agricultural areas. The NDVI was calculated based on the LANDSAT ETM<sup>+</sup> data using a modified equation of Rouse et al. (1974) (chap. 4.4):

$$NDVI = \left( \left( \frac{NIR - VIS}{NIR + VIS} \right) + 1 \right) \cdot 127 \quad (6.1)$$

Due to the normalization, the values for the NDVI the values in the original formula developed by Rouse et al. (1974) range from 1.0 to -1.0. In this study the original formula was scaled to theoretically data ranges between 0-255 by adding 1 (grey range between 0 and 2) and multiplying the results with 127. Using the modified formula (6.3) the resulting values range between 1 and 186.

#### 6.2.3.1 Results

The seasonal pseudo-colour coded NDVI of the LANDSAT ETM<sup>+</sup> image from the 21st of May 2001 after importing and reclassification in ArcGIS, is shown in (Fig. 6.8). The NDVI values were divided into four classes according to the “cover condition”, intensity and situation of vegetation observed and mapped during field survey in the test area and compared to the existing digital colour high-resolution orthophotos (Tab. 6.2). Characteristic examples for the NDVI cover classes are shown in Fig. 6.2. Although some procedures exist to develop automated threshold selection based on local minima detection, the threshold selection was based on the comparison of the ground truth data collected during the field survey. The selected NDVI classes have been verified by visual analysis. Crops and orchards with excellent vigour and density are represented as dense agriculture, also partly pine and oak trees. It could not be avoided that also the forest areas had to be included in this class, because of similar NDVI values.

Tab. 6.2: Vegetation classes according to specific NDVI value ranges.

Vegetation class	NDVI value	Fig. 6.2
<b>No vegetation or little vegetation</b> bad lands, urban areas, quarry areas, water bodies	1 - 115	(a)
<b>Grass / bushes</b>	115 - 122	(b)
<b>Mixed land use</b> orchards / agriculture	122 - 127	(c)
<b>Dense agriculture/ forest</b>	127 - 186	(d)



Photograph taken 06.05.2003, width ~ 150m



Photograph taken 02.05.2003, width ~ 50m



Photograph taken 28.05.2003, width ~ 80 m



Photograph taken 28.05.2003, width ~ 50m

Fig. 6.2: Characteristic examples of the NDVI cover classes. Type a) is dominating on elevations below sea level in bad lands with sparse soil and vegetation cover, quarries and urban areas. Type b) is dominating in elevations above sea level above limestones with patchy soil cover or mature yellow or harvested crops. Type c) is dominating in areas with agricultural fields with green crops, orchards, oaks and pine trees with intervals of several meters between the trees. Type d) is dominating over dense orchards and pine or oak trees, in the majority of cases located close to a wadi course or well irrigated agricultural fields.

The highest NDVI class in the test area is dominated by the dense wadi vegetation and the forest areas. In the test area in April and May agricultural fields and therefore irrigated fields are having their peak plant growth, showing high NDVI values (chapter 2.2).

The results of the NDVI values strongly correlate with the precipitation amount or applied irrigation practices, the soil situation and stage of maturation of the crops in the test area and in the areas above sea level also with the major wadi courses and therefore the water availability.

### 6.2.3.2 Accuracy assessment and error discussion

The correlation of the classified NDVI with the agricultural areas, orchards and forest areas mapped on the base of the aerial photographs (1:30,000) shows good results (Fig. 6.8): in the lowest NDVI class hardly no agriculture, orchards and forest exist on the thematic orthophotos layers. In the second lowest class few crop fields exist but hardly no orchard or forest areas. In the NDVI class mixed land use many crop fields, orchards and forest areas exist. The highest NDVI class is dominated in the test area by dense agricultural areas including crops, orchards and forest areas (Fig. 6.8). For the accuracy assessment of the NDVI 48 GPS acquired points were compared with the delineated NDVI classes and resulted in an agreement of 85.4 % (Appendix 4). Some errors occurred due to the fact, that the stage of growth was not considered and temporal differences between ground truth and date of scene overpass by satellite exists and therefore for example some green wheat fields, recorded during the GPS campaign, were probably dry or already harvested in May 2001 and therefore missclassified as no or little vegetation. Forest were only classified properly if the distance between the trees was not too big and the crowns were close together.

Some other errors occurred due to the following reasons:

- the influence of the atmosphere has also an effect on the NDVI values which means that the outcome of NDVI values is restricted to a limited range,
- in the test area it was not possible to distinguish between dense wadi vegetation and the oak and pine forest, however this would have been useful for the subsequent vulnerability and hazard assessment and implies a certain degree of error,
- in the study only one LANDSAT ETM<sup>+</sup> image was used. Compared to the use of multitemporal images this can cause limitations or lead to possible error sources: in one single NDVI image, mature crops can be confused with no or little vegetated zones,
- using only one image allows just a qualitative assessment about high and low vegetated areas to the time when the image was acquired, marking clearly the areas below and above sea level by a clearly visible change in the NDVI values, but does not allow for qualitative and quantitative assessment of the vegetation cover classes crops, orchards, pines and oaks. In a single NDVI image, barren fields are indistinguishable from temporarily fallow, healthy fields (Wallace et al., 1993),
- according to the studies of Lenney et al. (1996) agricultural fields have high NDVI values during periods of peak growth as well as low NDVI values following harvesting, during the early stage of growth, and while fallow.

- Orchards or perennials have continuously high NDVI values. In the test area agricultural fields and therefore irrigated fields are having their peak plant growth in April and Mai, showing then high NDVI values. All potential agricultural areas are cultivated in spring, there are many small and isolated fields existing, often smaller than 30 m x 30 m. The mapped control areas showed that at the date of the LANDSAT ETM+ data acquisition at the end of May many fields have been harvested, or yellow and mature and therefore give only a low NDVI value.

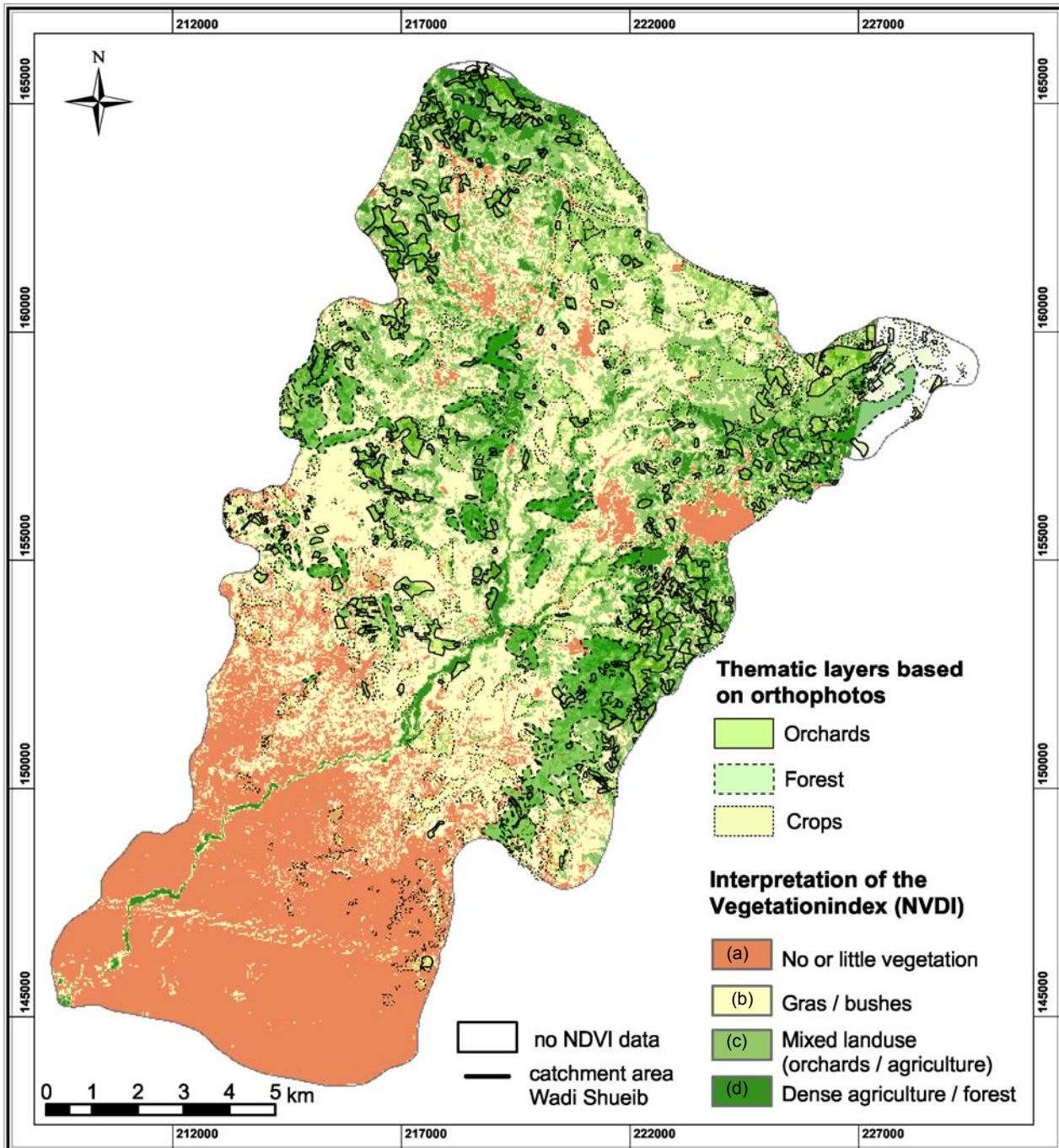


Fig. 6.8: NDVI classes pseudo-colour coded, after reclassification of the vegetation index results in ArcGIS, overlaid by the thematic orthophoto layers orchards, forest, crops (see chapter 6.3).

The benefit of the vulnerability assessment could have been to distinguish between crops and orchards and pines and oaks areas according to the NDVI values and use the results for the infiltration and soil conditions. For the hazard assessment the amount of fertilisers could have been assessed based on the NDVI results.

## 6.2.4 Unsupervised classification

### 6.2.4.1 Classification process

For the unsupervised classification of the scene the ISODATA algorithm was chosen. The main goal of the unsupervised classification was to assess the spectral content of the Landsat ETM<sup>+</sup> image, to make a preliminary interpretation prior to conduct a supervised classification procedure and to get an idea about the possible amount and separability of the classes.

Using the unsupervised classification parameterisation given in Tab. 6.3, the application of the ISODATA clustering for the clipped subset of the LANDSAT ETM<sup>+</sup> image resulted in 49 spectral clusters. The clusters were merged to 11 spectral classes, defined by visual inspection of the false colour composite of the LANDSAT ETM<sup>+</sup> image, using the accorded topographic maps sheets, the panchromatic aerial photographs, digital colour photographs (for section of the area), and results from a first field survey. The collection of GPS-acquired ground truth data and detailed fieldwork was performed in a later stage as preparation for the supervised classification.

Tab. 6.3: Parameterisation (given in PCI Geomatics terminology) for the ISODATA clustering algorithm.

ISODATA parameter	Value
Min. clusters	40
Max. clusters	50
Desired clusters	45
Max. iterations	35
Movement threshold	0.01
Min. threshold	1
Standard deviation	9
Lumping threshold	4
Max. lump pairs	5

### 6.2.4.2 Results

The result of the unsupervised classification determines the spectrally separable classes of the image. The classified data were compared with reference data of the test area and the 49 spectral classes were merged to 11 possible land cover classes. The result of the unsupervised classification with the interpretation of the spectral classes is shown in Fig. 6.3 and the relative frequency in area percent of each land cover class in Fig. 6.4. According to the interpreted results, the dominating land cover class is represented by limestones and spectral classes assigned to mixed land use.

Analysing results one is in general confronted with the disadvantage of unsupervised classifications, namely that heterogeneous pixels are not clearly assigned to the informational classes and that there can be some problems of matching the clusters of the spectral classes to the informational classes. Thus, the spectral class assigned to the informational class *urban* (not dense) contains pixels in the northwestern and northeastern part that could be clearly identified as urban area, whereas in the southern part some pixels of the same class exist within range land areas where theoretically no urban areas exist.

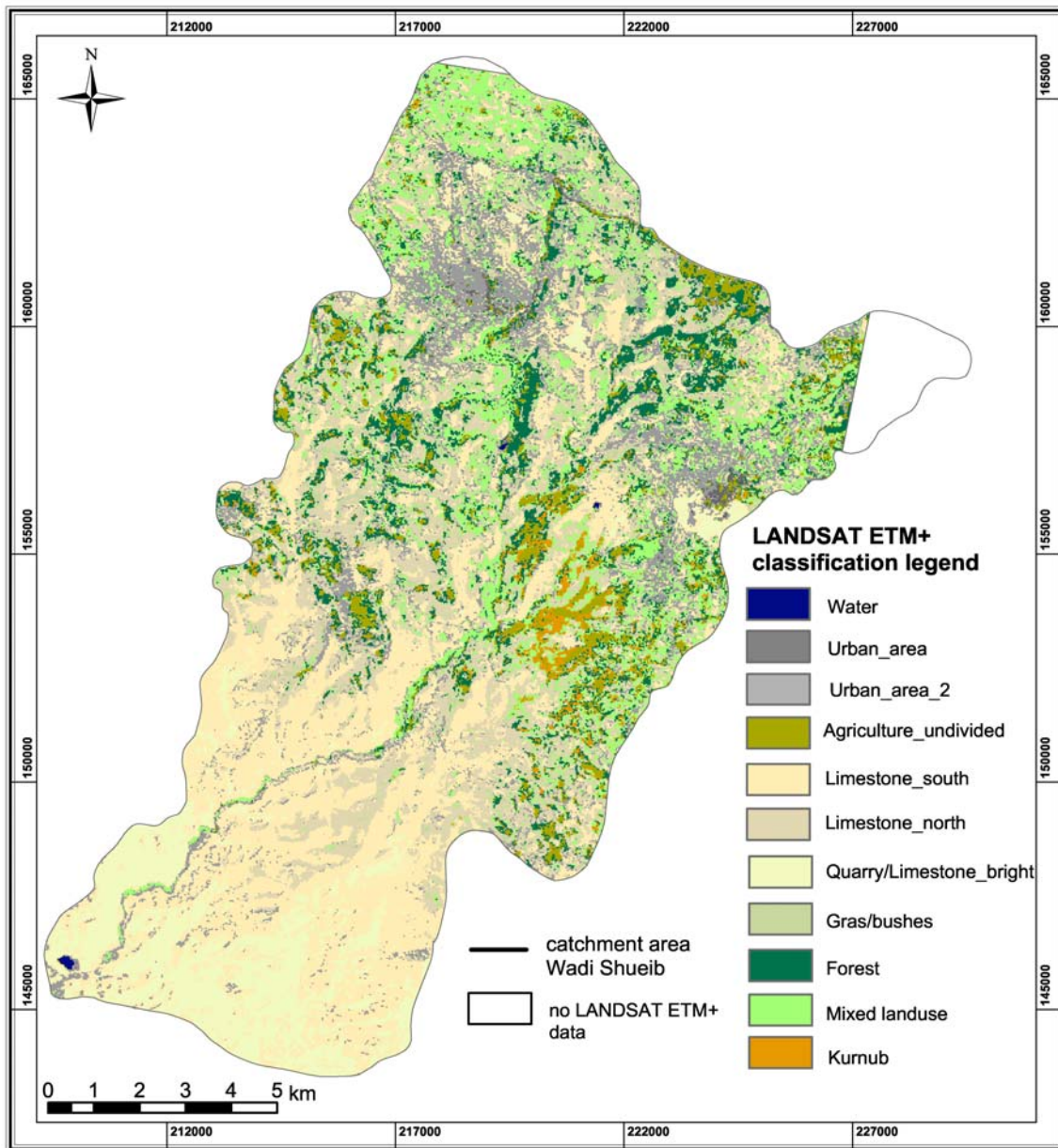


Fig. 6.3: Unsupervised classification result of the LANDSAT ETM+ data of the test area.

At the time when the unsupervised classification was performed no complete data set was available that could have been used as a reference classification assumed to be accurate enough for a reliable quantitative accuracy assessment. The collecting of ground truth data



through field work GPS and detailed field work was performed in a later stage as preparation for the supervised classification.

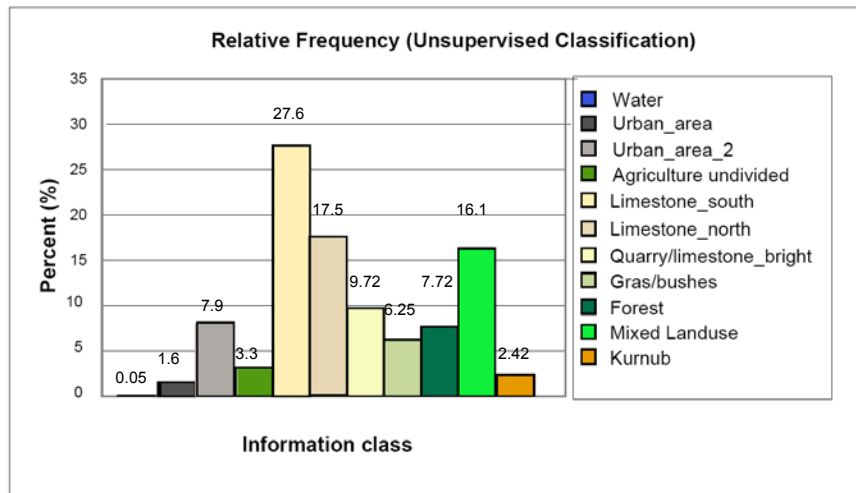


Fig. 6.4: Class area percentage of the unsupervised classification of the LANDSAT ETM<sup>+</sup> data.

## 6.2.5 Supervised classification

### 6.2.5.1 Determination of the training sites

The ground truth data collected by field survey was used partly for the delineation of training sites for a supervised classification and for the evaluation of the classification results.

The determination and amount of the training sites were based on the results of the unsupervised classification and on the informational classes requirements for a later use for the groundwater vulnerability and hazard approach. The field survey for the training areas was accomplished between 25<sup>th</sup> of April and 30<sup>th</sup> of May 2003. The main land cover, soil and vegetation types were already known from former field surveys.

For the fieldwork in Jordan the satellite image print was separated into nine sectors in A4 format and overlaid by transparent paper where the training areas, towns, street intersections for orientation were mapped. Coordinates from suitable areas on the satellite image were taken from topographic maps and later located and verified in the test area using GPS. Furthermore some areas clearly distinguishable from neighbouring areas were directly mapped in the test area. For each potential training site a form was filled in, indicating details of several parameters such as location, size, elevation, slope, aspect, land cover, vegetation type, and vegetation cover.

### 6.2.5.2 Description of the training sites

The supervised classification was applied using 12 informational classes in total. It was not needed for the vulnerability assessment but also not possible to distinguish between crops, pasture types and orchards, due to the high degree of heterogeneity of the land cover and due to the fact that most of the crop and orchard fields are very small (often below the cell resolution of the multispectral bands of 900 m<sup>2</sup>) or often intermixed with each other, leading to a high amount of mixed pixels and uncertainty. Furthermore the farmers in the test area use crop rotations or

crop combinations, therefore it could not be assured that the existing crop types on the image from 2001 represent the vegetation during the acquisition of the training sites in the year 2003.

It was also considered to classify the formations of the single aquifers within the Ajloun Group but since the different limestones are partly covered by soil and vegetation and are spectrally very similar this was not possible. Often the litho logy changes in a small scale within several tens of meter due to steep valley flanks. The classification of different limestone types is in general a problem due to their spectral similarity. This spectral differentiation is even reduced due to partly presence of duricrusts in the test area. The calcareous duricrust cover the rugged topography developed on the limestones and over soils. The duricrust formation involved the recrystallization of original calcite in the parent limestones, the introduction of additional calcite either from above or below. Differences in the thickness of the crusts are attributed to differences in the climate under which they formed, and differences in their degree of development are attributed to differences in their age (Chapman, 1974). Calcareous duricrust is recognized widely as an indicator of semi-arid climate, and under certain circumstances, it provides evidence of climatic changes.

Through ground check the following twelve categories represented by several training sites were determined:

- Water
- Urban area (dense)
- Urban area 2 (not dense)
- Agricultural areas (undivided)
- Limestone (S exposed)
- Limestone (N exposed)
- Quarry/ limestone bright
- Grass/ bushes/ range land
- Forest (pine/ oak)
- Mixed land use
- Kurnub 2 (S exposed)
- Kurnub 3 (N exposed)

Due to the fact, that just one bigger water body at the dam in the south-western part of the test area exists and two smaller artificial water reservoirs that can be easily distinguished and clearly separated, the class *water* is not described as training area in the following.

**Urban area (dense)**

Especially the dense urban areas can clearly be distinguished from the surrounding vegetated areas or rocks. The class dense urban area consists of buildings standing closely together with almost no open space or vegetation between the walls. It comprises sealed areas in the major small towns, small settlements, or main streets.

Photograph taken 03.05.2003

**Urban area 2 (not dense)**

Corresponds to "Urban areas (dense)", but considers the less dense built-up zones, including urban areas with a varying amount of vegetation or rock outcrops between single houses.

Photograph taken 03.05.2003

**Agricultural areas (undivided)**

Clearly separable, intensively used agricultural fields can be found in plane areas over medium to thick soil layers, several parcels are connected to each other. Crops and orchards, mainly olive and lemon trees are cultivated. Crop rotation is applied.

Photograph taken 02.05.2003

**Limestone S / N**

The limestone is subdivided in S and N exposed limestones, due to different spectral reflection values. Above the limestones thin to patchy soils with sparse or no vegetation are existing. Over steep gradients the bare rocks crop out. In general, less soil and vegetation coverage is characterising this class.

Photograph taken 30.04.2003



### **Quarry / limestone bright**

This class comprises quarry areas where no soil cover exists and limestone in the south below the sea level where soil and vegetation and soil development are very limited or not present.

Photograph taken 30.04.2003



### **Grass / bushes**

Defines the areas over limestones where patchy soils, grass, shrubs and bushes in a varying cover degree exist.

Often grass or bushes grow on accumulated soil, filling the joint and karstified fissures of the limestone, forming mixed pixels of vegetation and limestone.

Photograph taken 02.05.2003



### **Forest (pine / oak)**

In the test area two types of forest are existing: oak and pine forest. The two forest types are combined in one class since a further differentiation for the later vulnerability assessment is not necessary.

Photograph taken 28.05.2003



### **Mixed land use**

These areas consists of several, often irregularly shaped small parcels. Due to the different vegetation types (crops, orchards), a very inhomogeneous pattern exists. The single areas used for agriculture are very small, producing a high amount of mixed pixels. The boundaries of the parcel are not clear or become indistinct with the surrounding area. A clear separation is not possible.

Photograph taken 28.05.2003



### Kurnub 2 / 3 (S / N exposed)

The Kurnub Sandstone areas were subdivided in S and N. If only patchy or almost no soil cover and vegetation exist, the Kurnub Sandstone can be spectrally clearly separated from the limestone, due to its reddish colour.



Photograph taken 06.05.2003

Often the spectral signatures are not significant enough to distinguish between agriculture plants and wild growing bushes. Often wild olive trees that are not treated with fertilisers grow in the surroundings of agricultural olive fields that are treated with fertilisers and chicken dung. This is an important point to consider for the hazard mapping. For this reason for the supervised classification the informational classes *mixed land use* and *agriculture undivided* were chosen. *Agriculture undivided* is applied to classify the small size of the single parcels of lands where a differentiation between orchards and crops can not be applied precisely enough. *Mixed land use* consists of several, often irregularly shaped small parcels that show due to different vegetation types (agriculture, bushes) a very inhomogeneous pattern. A clear separation is not always possible or the single areas used for agriculture are very small (< 200 m<sup>2</sup>). The boundaries of the parcels are often not clear or become indistinct with the surrounding areas.

The spectral differences of the training areas in each used channel can be estimated by observing the mean grey values (Fig. 6.5).

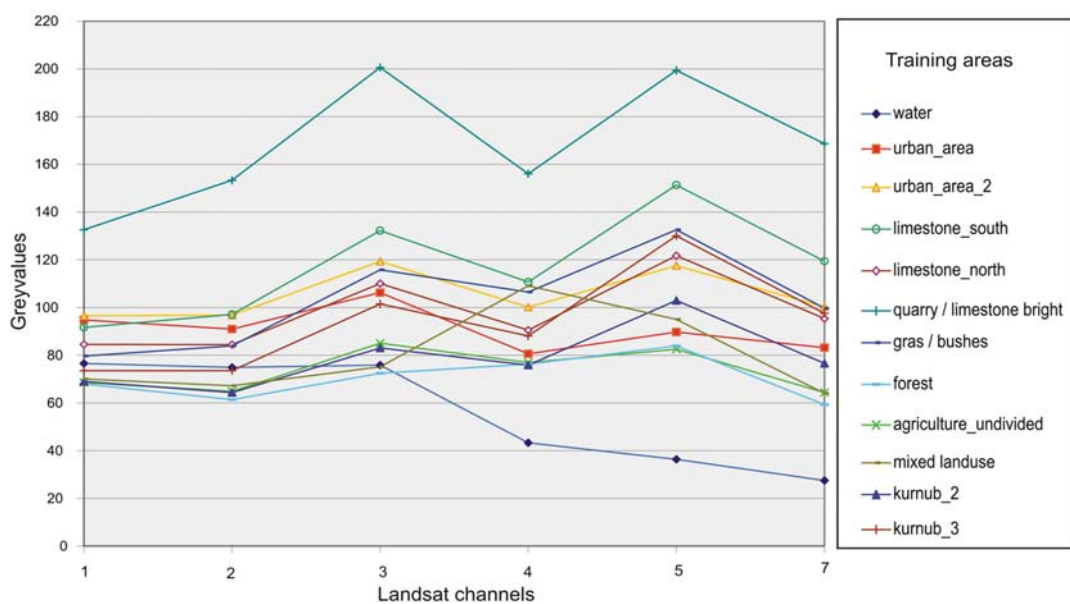


Fig. 6.5: Mean grey values of the training areas of the used bands of the LANDSAT ETM<sup>+</sup> image.

These signatures were used to classify all pixels in the scene. See Appendix 2 for the mean grey values of each training site for all bands used and the standard deviations. With exception of class quarry / limestone bright the mean grey values differ within a small range in all spectral classes for band 1 and 2. Especially within the classes agriculture, mixed vegetation, forest and Kurnub 2 the range of the grey values is very narrow. The mean grey values of band 3,4, shows a larger variability. Band 5 and 7 shows the largest variability and a wide range of the grey values. The supervised classification was applied using the Maximum Likelihood algorithm without null classes taking in total 12 informational classes using band 1-5 and 7. The thermal band was not included since the spatial resolution of 60 m was not suitable for the mapping purposes.

### **6.2.5.3 Results**

The main goal of the supervised classification of the LANDSAT ETM<sup>+</sup> image was to estimate the land cover. The results of the supervised classification are shown in Fig. 6.6. Limestone outcrops form the major land cover of the test area (Fig. 6.7). The limestone is covered to a varying degree with no or thin soil layers and no to little vegetative cover. Especially in the areas below sea level in the southwestern part of the study area with low precipitation rates and steep relief, the development of soil and vegetation cover is limited or even not present. Therefore the naked to little overgrown limestones are distinguishable from areas above sea level where soil layers in varying thickness and partly abundantly covered with vegetation exist and cover the limestone partly to a high degree.

For a later determination of the groundwater vulnerability and the groundwater hazards it was important to get information of the extent and distribution of the different land cover types e.g. for a more accurate assessment of the infiltration conditions and of the existence of area-wide possible non-point hazard distributions caused by the use of fertilisers.

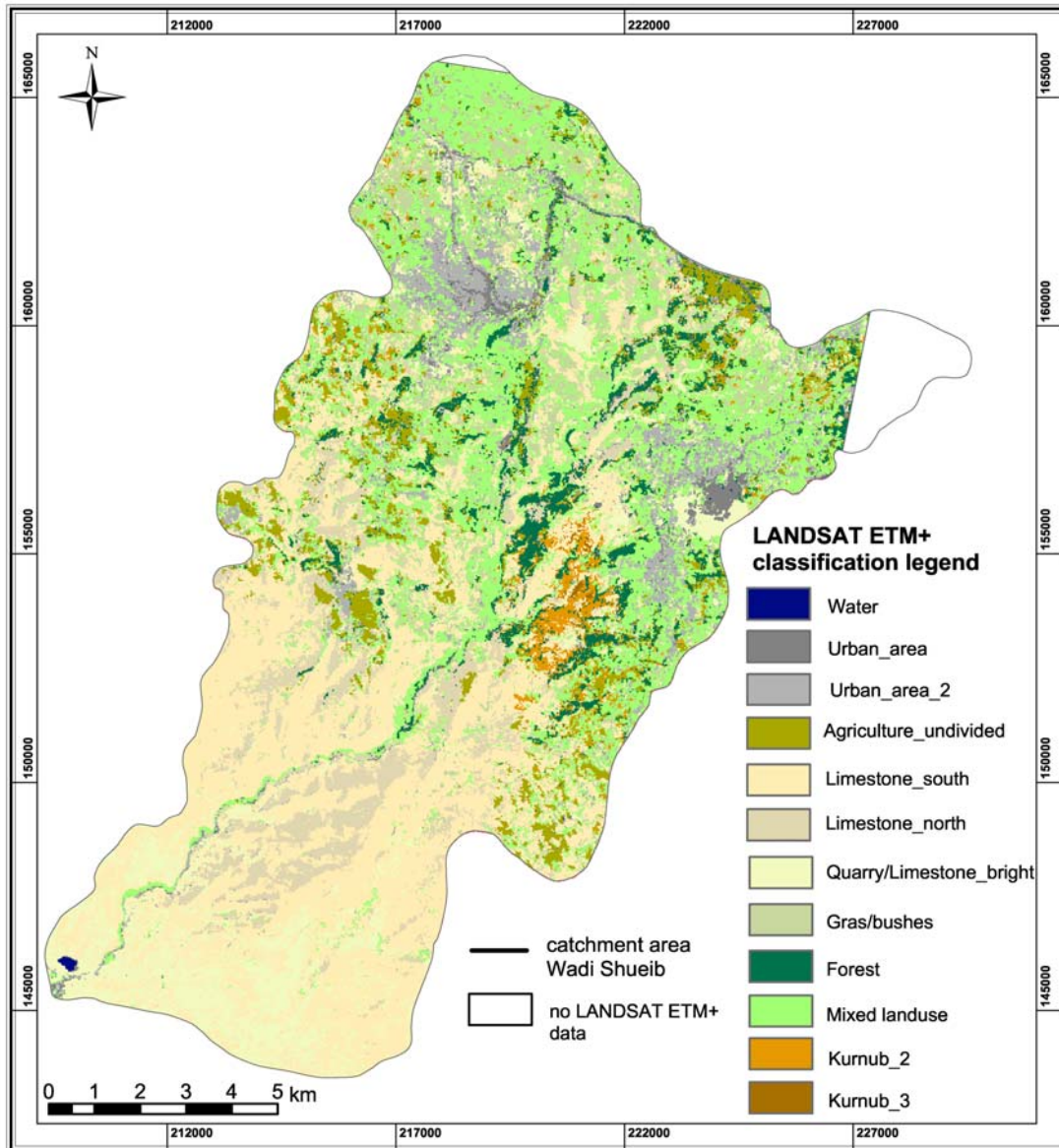


Fig. 6.6: Supervised classification results of the LANDSAT ETM<sup>+</sup> data of the test area.

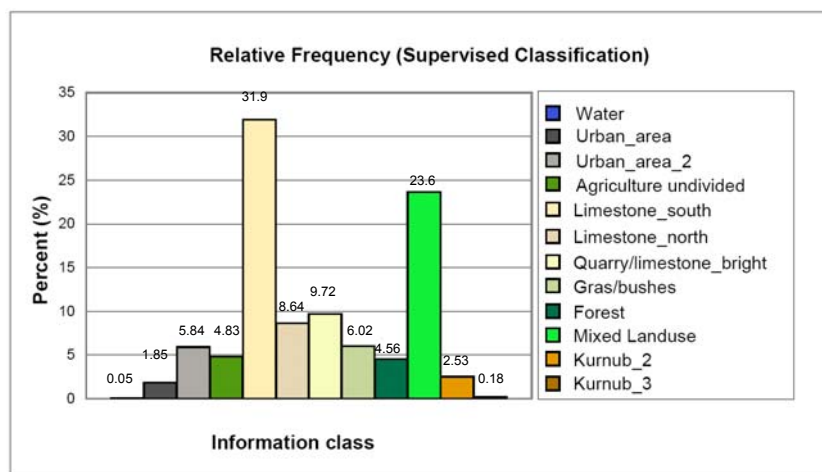


Fig. 6.7: Class area percentage of the supervised classification of the LANDSAT ETM<sup>+</sup> data.

### 6.2.5.4 Accuracy assessment

The evaluation of the classification results of the LANDSAT ETM<sup>+</sup> image was accomplished using the separability of the single spectral classes, the confusions matrix (error matrix) and 48 GPS acquired groundtruth points.

#### Signature separability

The separability was calculated with the Bhattacharya distance (bd) measure which calculates distances based upon class means and covariance matrices (Richards, 1986). The bd is calculated as real values between zero and two. Separation between signatures is characterized as good when  $1.9 < bd < 2.0$ , poor when  $1.0 < bd < 1.9$ , and very poor when  $0.0 < bd < 1.0$ . The average separability of 1.989 shows that the majority of the classes are clearly separable. The values listed in Tab. 6.4 show the separability of each spectral signature.

Tab. 6.4: Separability of the spectral classes using Bhattacharya distance.

Average Separability: 1.9895 Maximum Separability: 2.0000 Minimum Separability: 1.6491												
		1	2	3	4	5	6	7	8	9	10	11
1	Water											
2	Urban_1	1.9999										
3	Urban_2	2.0000	1.9467									
4	Agriculture ud	2.0000	1.9995	2.0000								
5	Limestone S	2.0000	2.0000	1.9999	1.9999							
6	Limestone N	2.0000	1.9998	1.9999	1.9999	1.9435						
7	Quarry / LS	2.0000	1.9999	1.9999	2.0000	1.9856	1.9999					
8	Bushes /Grass	2.0000	2.0000	1.9999	2.0000	1.9971	1.9999	1.9997				
9	Forest	2.0000	2.0000	1.9994	2.0000	1.9805	1.9999	1.9999	2.0000			
10	Mixed land use	2.0000	1.9999	1.9996	1.9999	1.9930	1.9987	1.9999	1.9819	1.9999		
11	Kurnub_2	2.0000	1.9998	2.0000	1.9990	1.9938	1.9999	1.9999	1.9997	<b>1.6492</b>	1.9996	
12	Kurnub_3	2.0000	2.0000	2.0000	2.0000	1.9855	1.9999	1.9999	1.9999	1.9993	1.9999	<b>1.7315</b>

Only two values are smaller than 1.9, the value between the Kurnub shadow areas and the forest areas is 1.64917 and the value between Kurnub 2 and Kurnub 3 is 1.73151 (bold numbers in Tab. 6.4). For classes having these low values a separability is difficult. However, similar spectral classes showing low separability can be merged (e.g. Kurnub 2 and Kurnub 3). For the forest and Kurnub 2 class the choice of alternative training sites did not improve the results, therefore the obtained results were taken as basis for the further work.

#### Confusions matrix

One of the most common means of expressing classification accuracy is the preparation of a classification error matrix (Lillesand & Kiefer, 2004). Error matrices compare on a category-by-category basis the relationship between known reference data (ground truth, training areas) and the corresponding results of an automated classification. The error matrix is prepared to determine how well a classification has categorized a representative subset of pixels used in the training process of a supervised classification. The matrix lists the known cover types used for



training (training areas) in columns versus the pixels actually classified into each land cover category by the classifier shown in the rows (Tab. 6.5).

Tab. 6.5: Confusions matrix of the supervised classification of the LANDSAT ETM<sup>+</sup> data.

		<i>Overall accuracy = 97.52 %</i>											<i>Average Accuracy: 97.66 %</i>	
		<i>Kappa Coefficient = 0.9731</i>												
	Class	1	2	3	4	5	6	7	8	9	10	11	12	Total
1	Water	<b>100.00</b>	0.00	0.00	0.00	0.00	0.00	0.00	0.00	0.00	0.00	0.00	0.00	100
2	Urban_1	0.00	<b>99.60</b>	<b>0.40</b>	0.00	0.00	0.00	0.00	0.00	0.00	0.00	0.00	0.00	100
3	Urban_2	0.00	0.00	<b>100.00</b>	0.00	0.00	0.00	0.00	0.00	0.00	0.00	0.00	0.00	100
4	Agriculture ud	0.00	0.00	0.00	<b>100.00</b>	0.00	0.00	0.00	0.00	0.00	0.00	0.00	0.00	100
5	Limestone S	0.00	0.00	0.00	0.00	<b>99.50</b>	0.00	0.00	0.00	0.00	<b>0.50</b>	0.00	0.00	100
6	Limestone N	0.00	0.00	0.00	0.00	<b>0.73</b>	<b>99.27</b>	0.00	0.00	0.00	0.00	0.00	0.00	100
7	Quarry LS	0.00	0.00	0.00	0.00	<b>0.99</b>	0.00	<b>99.01</b>	0.00	0.00	0.00	0.00	0.00	100
8	Bushes /Grass	0.00	0.00	0.00	0.00	<b>0.90</b>	0.00	0.00	<b>99.10</b>	0.00	0.00	0.00	0.00	100
9	Forest	0.00	0.00	0.00	<b>2.32</b>	0.00	0.00	0.00	0.00	<b>96.25</b>	0.00	<b>1.43</b>	0.00	100
10	Mixed land use	0.00	0.00	0.00	0.00	0.00	0.00	0.00	0.00	0.00	<b>100.00</b>	0.00	0.00	100
11	Kurnub_2	0.00	0.00	0.00	0.00	<b>4.11</b>	0.00	0.00	0.00	<b>6.51</b>	0.00	<b>88.18</b>	<b>1.20</b>	100
12	Kurnub_3	0.00	0.00	0.00	0.00	<b>6.03</b>	0.00	0.00	0.00	0.00	0.00	<b>3.02</b>	<b>90.95</b>	100
	Total	100.00	99.60	100.40	102.32	112.26	99.27	99.01	99.10	102.76	100.50	92.63	92.15	

Statistic measures and characteristics about the classification can be obtained from the confusions matrix. The confusions matrix is used for the study of classifications errors of omission (exclusion) and commission (inclusion). All pixels that are classified into the proper informational class are located along the major diagonal of the error matrix (bold italic numbers in Tab. 6.5). All nondiagonal numbers (>0) of the matrix represent errors of omission (exclusion) or commission (inclusion). The omission errors are found in nondiagonal row elements. Commissions errors are found in nondiagonal column elements.

The **overall accuracy** is computed by dividing the total number of correctly classified pixels of a object class by the total number of reference pixels of the training areas (Lillesand & Kiefer, 2004). The **average accuracy** is the average of the accuracies obtained for each class. The error matrix in Tab. 6.5 indicates an overall accuracy of 97.52% and an average accuracy of 97.66 %.

It should be understood that these values are just statistical value showing how well the statistics extracted from the training areas can be used to categorize each informational class. The high percentage of the overall and average accuracy in the error matrix means that the chosen training areas are homogenous, the informational classes are spectrally separable and that the classification procedure worked well (Lillesand & Kiefer, 2004). Furthermore the overall accuracy provides no exact information about the classification accuracy of individual informational classes. Misclassifications caused by spectral similarity are not considered, therefore random matching can occur.

In contrast to the overall accuracy the **Kappa coefficient** takes into account not only the correct classified pixels, but also the single categories and the misclassification within the categories (Campbell, 1996). After Lillesand & Kiefer (2000) "The Kappa statistics is a measure of the difference between the actual agreement (true agreement) between reference data and an

automated classifier and the change agreement between reference data and a random classifier.” Conceptually,  $\kappa$  can be defined as:

$$\kappa = \frac{\text{observed accuracy} - \text{change agreement}}{1 - \text{change agreement}} \quad (6.2)$$

In the ideal case true agreement approaches 1 and change agreement approaches 0, Kappa approaches 1. After Cohen (1960) the Kappa statistics is computed as:

$$\kappa = \frac{N \sum_{i=1}^r \chi_{ii} - \sum_{i=1}^r (\chi_{i+} \times \chi_{+i})}{N^2 - \sum_{i=1}^r (\chi_{i+} \times \chi_{+i})} \quad (6.3)$$

Where

- $r$  = number of rows on the confusions matrix
- $\chi_{ii}$  = the number of observations in row  $i$  and column  $i$  (on the major diagonal)
- $\chi_{i+}$  = total observations in row  $i$  (shown as marginal total to right of the matrix)
- $\chi_{+i}$  = total observations in column  $i$  (shown as marginal total at bottom of the matrix)

The obtained Kappa value for the supervised classification in the test area is 0.97.

For the classification accuracy of the individual informational classes 48 **groundtruth points** of representative, uniform land cover, different from the training areas were acquired and compared with the informational classes obtained during the supervised classification. Their comparison with the classification result showed an agreement of 75 % (see Appendix 3). Misclassifications occurred between *mixed land use* and *agriculture undivided*, because in some areas both classes show similar spectral reflectance due to similar vegetation characteristics. Some shady *north exponated limestones* were classified into the *forest class*. Several misclassification occurred between the classes *grass/bushes* and *limestone north/south exponated* due to the high variability of the pixel's spectral composite depending on the cover degree of the *grass/bushes* and their dry up degree. Some misclassifications occurred between the *Kurnub 2 / 3* classes and the *limestone north/south* classes due to the fact that the limestones sometimes tend to be slightly reddish and then show similar spectral signature as the Kurnub Sandstone.

### 6.2.5.5 Error discussion

Possible errors in supervised classification results can occur due to the following reasons:

- a big portion of the land surfaces appears relatively inhomogeneous,
- each landscape unit or land cover type is formed by a complex mosaic of different structures,

- especially under arid but also under the existing semi-arid conditions in the test area an area-wide soil or vegetation cover is missing and results in a high variability of the land cover degree and thus in a high variability of the spectral composite of the pixels,
- the different degree of irrigation or aridity of the plants leads to spectral differences of the “same” informational classes,
- most of the crops and orchards fields are very small (often equal or even smaller than the area of the 30 m x 30 m ground cell of the spectral information of the LANDSAT ETM<sup>+</sup> data) or often intermix with each other, leading to a high amount of mixed pixels and uncertainty. Mixed pixels present a difficult problem for the image classification, since their characteristics are not representative of any single land cover type and therefore can not assigned clearly to an informational class and cause uncertainties in the applied classifications algorithms (Lillesand & Kiefer, 2004). Within this study no spectral mixture analysis or fuzzy classification was applied to deal with the classification of the mixed pixels,
- some errors occurred due to the fact that the stage of growth was not considered; a temporal difference between ground truth collection and date of scene overpass by satellite exists and therefore for example some green wheat fields recorded during the GPS campaign from 25th of April and 30th of May 2003 were probably dry or already harvested in May 2001.

### **6.2.6 Comparison of the unsupervised and supervised classification results**

There exists a certain degree of agreement between the land cover assigned to the spectral classes of the unsupervised classification and the informational classes of the supervised classification. The supervised classification usually works more accurate since it takes advantage of the information of multivariate spreads of each class. The key and the most challenging task for the supervised classification is to pick truly representative training samples. The trained samples are required not only to represent the mean vectors but also the spreads for each class. Otherwise, one might get too many unknown classes.

Since supervised classification used reference data to classify the image, it gave better and more homogenous results than the unsupervised classification. In general the informational classes could be acquired more precisely during the supervised classification. In particular, accuracies of the land cover classes *urban area 2* and *mixed land use* proved to be problematic. The unsupervised classification results showed in the southwestern part some pixels of the class *urban area* within limestone areas (range land) where theoretically no urban areas exist. Within the supervised classification this informational classes could be represented better and more accurately thus these classification errors could be reduced to a minimum.

## **6.3 Analogues black and white photographs (1:30,000)**

### **6.3.1 Introduction**

Concerning the relatively small size of the test area and compared to the intension to asses also the degree of karstification and individual fields the usage of high resolution aerial photographs seems to be more efficient than medium resolution satellite data.

Due to security constraints of the Jordanian government and limitations of the project budget the purchase of aerial photographs was restricted to monochromatic analogue photographs with a scale of 1:30,000 and a film format of 23 cm by 23 cm (Wild RMK Top 15 camera) from September/ October 1992. Only for a small part of the test area some digital aerial photographs (scale 1,10,000) from September 2000 were made available.

The black and white paper prints showed a wide range in quality. As a security measure of the Jordanian government all military places and royal houses where erased by the Royal Jordanian Center with a razor blade, leaving white spots on the paper prints. The test area require 18 overlapping photographs (approximately 60 % overlap and 20 % sidelap) to be completely covered.

### **6.3.2 Preparatory work**

The photographs were scanned at a resolution of 16 lp/mm (800 dots per inch (dpi)) with an office A3 flat bed scanner corresponding to a ground cell size of 0.9 m. The resolution of 800 dpi was chosen as a reasonable compromise between needed disk space and required details or information of each photograph and according to the quality of original images. The use of a photogrammetric precision scanner would have been advantageous, however, these scanners are very expensive and were not made available. The aerial photographs had to be scanned completely including the fiducial marks and the data strip at the edges and corners recorded during the exposure. Fiducial marks are small targets on the body of metric cameras. Their positions relative to the camera body are calibrated. Thus, they define the image coordinate system; in that system, the position of the projection centre is known.

During the scanning process on some photographs the brightness and the contrast was adjusted. To assure that the image brightness values of the orthophotos reflect the source imagery as close as possible, this enhancement was limited to a minimum. However, some changes in brightness values may also occur during the scanning and later rectification process.

### **6.3.3 Orthorectification and Mosaicking**

To covert an aerial photograph in an orthophoto, each image pixel is processed through photogrammetric equations using ground control points, camera calibration and orientation parameters, and a digital terrain model. The use of a bundle adjustment provides for simultaneous mathematical treatment of photo coordinate measurements and ground control measurements, as well as treating the exterior orientation parameters of each photo in the block as unknowns (Lillesand & Kiefer, 2004). The bundle adjustment is used to perform the exterior orientation calculations while considering all of the project photos.

Ground control points (GCPs) are used in the block bundle adjustment to establish a geometric relationship among the images in a project, the sensor model and the ground. Tie points (TPs) are used to create geometric harmony among the images in a project so they are positioned correctly relative to one another.

The *Orthoengine* modul of *Geomatica 9.0* uses for the orthorectification process a rigorous math model based on the geometry of a frame camera. This model can compensate for the effects of varying terrain and for distortions inherent to the camera, such as the distortion of the lens, the focal length, the perspective effects, and the camera's position and orientation. The computed math model calculates the camera's position and orientation at the time when the image was taken.

A minimum of four up to a maximum of eleven ground control points (GCPs) using GPS data were collected for each photograph for the orthorectification process (Fig. 6.8). Due to the extreme relief in the test area, partly high distortion or deformation caused by the rectification process and several high residual errors occurred.

The digital orthophoto accuracy is expressed as RMS error that compares the sample coordinates in the orthophoto to their ground coordinates. Due to the extreme relief in the test area, partly high distortion or deformation caused by the rectification process and abnormal high residual errors occurred. The mean x RMS error was 7.15 m, the mean y RMS error was 7.98 m. The partly large error was attributed to the absence of distinct features as suitable GCPs, the inaccurate topographic base maps and the DEM digitised from contour lines (chapter 6.7.2) and finally to the geometric accuracy of the GPS itself.

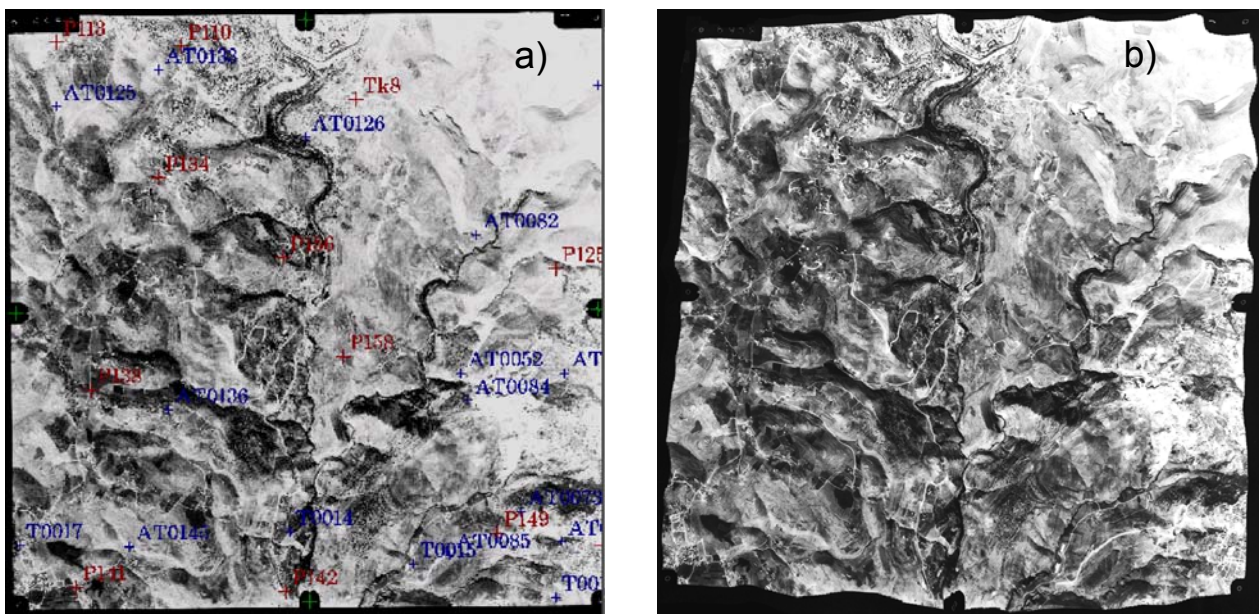


Fig. 6.8: a) Aerial photograph with displayed Ground Control Points (P) and collected Tie points, partly manual (Tk) and automatically collected (AT). b) Orthophoto derived after rectification process of the aerial photograph.

After the orthorectification process all orthophotos were merged to a mosaic covering the whole test area. For the automatic mosaicking process the best results were received using no

automatic colour balance but a minimum differences outline selection method for the overlapping areas. Extreme tonal variations within single images, lack of intensity towards the edges or radiometric roll-off in the original analogue photographs prevented the creation of a mosaic uniform in tone over the whole test area.

### 6.3.3.1 Error discussion

After Krupnik (2003) the apparent simplicity that is reflected in the current availability of orthophoto generation software packages is rather misleading. The geometric accuracy of the orthophotos depends mainly on two factors: the accuracy of the DEM and the accuracy of the exterior orientation parameters. The accuracy of the exterior orientation again depends on four factors. Besides the accuracy of the control and tie point measurements on the image, the distribution of tie points over the model, the accuracy of ground control points over the model and the distribution of ground control points over the model is important.

In addition, the accuracy of the transformation parameters between photo and image coordinate system, which is affected by the accuracy of the fiducial measurement and by the fiducial configuration (Krupnik, 2003) is influencing the geometric accuracy of the orthophotos.

The accuracy of the geometric correction varied with the quality of the DEM, the distribution of the GCPs and the partly excessive relief in the area. Image distortions along streets or fields increased especially near the edges of the orthophotos (Fig. 6.9). Since aerial photographs show a perspective projection on a horizontal plane, only the middle parts are area accurate. It was not possible to compensate for the extreme tonal differences within the images and between adjacent images, the specular reflectors of the very bright limestone quarries and the missing data at the areas of the royal palaces. The orthophotos were overlaid by scanned topographic maps for visual inspection of their geometric accuracies. Hereby the problem was that all existing digital map information is based on the scanned and rectified topographic maps, which could in turn contain errors due to their own scanning and rectification procedure.

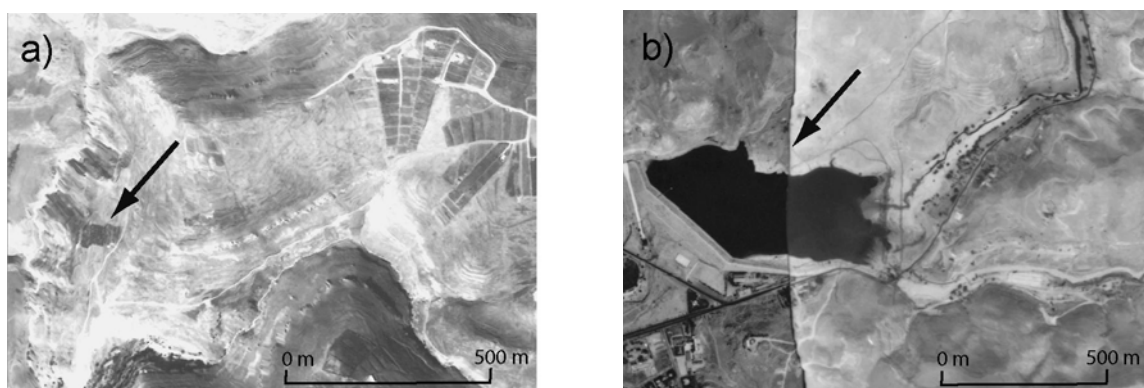


Fig. 6.9: Orthophoto defects in the test area: a) heavy distortions lead to a curved border of an originally straight acre boundary, b) tonal differences between two orthophotos.

It should be mentioned here again that, due to political constraints in Jordan and budget reasons of the project more recent photographs could not be made available. It is obvious that one main advantage compared to topographic map information is the up-to-dateness of orthophotos which

was in this case not warranted, due to the fact that the images are 13 years old. However, the main information derived from the orthophotos and used for the vulnerability and hazard assessment such as the crops-, orchards-, forest areas and drainage density remained more or less time-invariant during the last decades. Whereas thematic layers concerning for example the urbanisation, infrastructure or excavation sites result in some errors in the hazard inventory list due to developments within the last decade and therefore were mapped if possible based on the LANDSAT ETM<sup>+</sup> data.

#### **6.3.4 Post-processing and analysing**

The mosaic was loaded in ArcGIS for post-processing and analysis. The orthophoto mosaic was used for digitising vector information producing the following thematic maps (Fig. 6.10):

- Infrastructure
- Urbanization
- Crops
- Orchards
- Forest
- Drainage pattern

The resulting thematic maps were taken as inputs for the soil, land use and infiltration conditions for groundwater vulnerability and for hazard mapping. However, the spatial resolution did not allow for mapping distinctive features or pattern such as the degree of karstification or jointing.

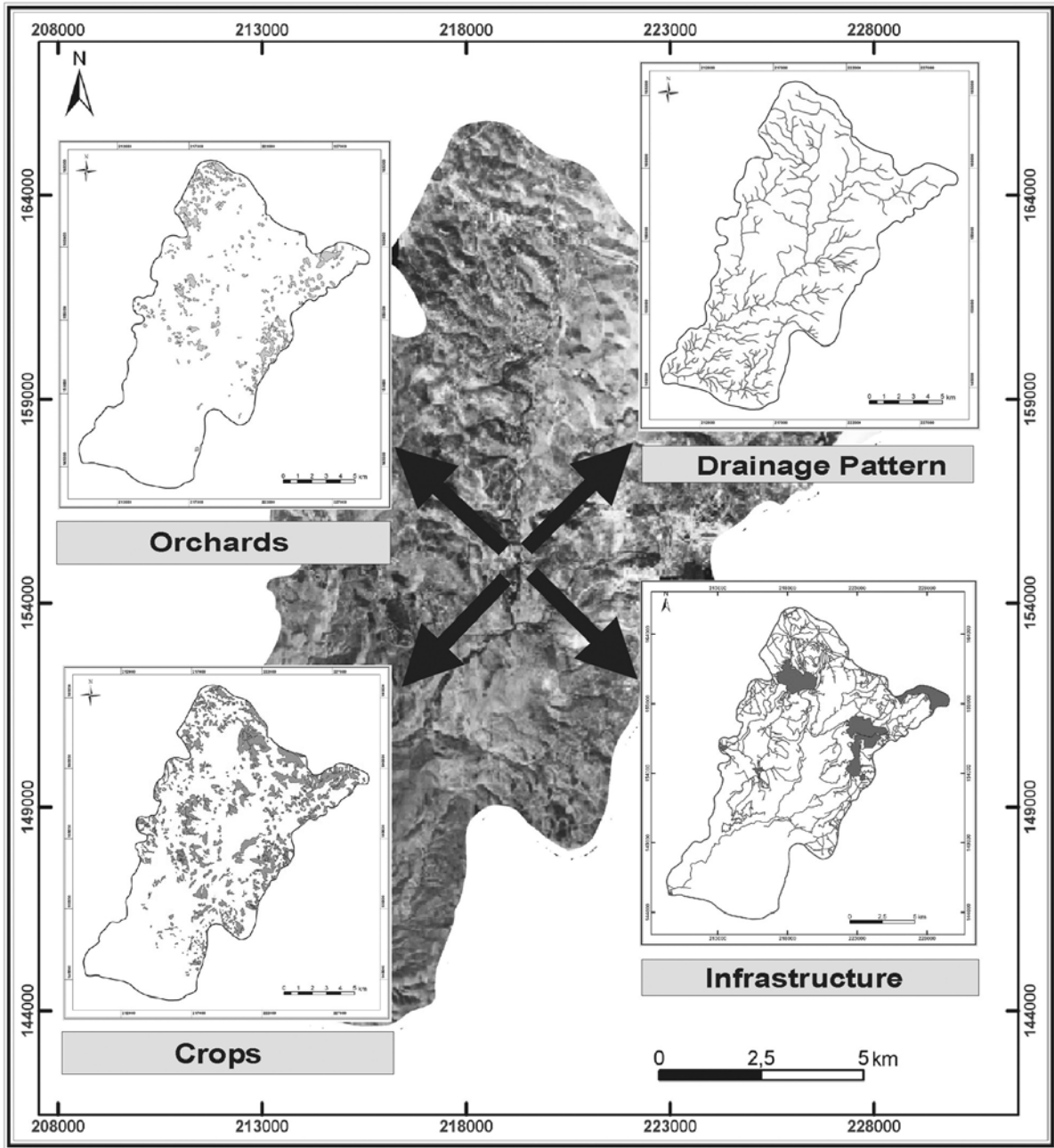


Fig. 6.10: Examples of thematic maps derived by on-screen digitising the orthophoto-mosaic of the black & white aerial photographs 1:30,000.



## 6.4 Digital colour photographs

### 6.4.1 Introduction

For a part of the test area (about 50 km<sup>2</sup>) colour digital aerial photographs (Camera type: Wild 15/4 UAG-S, No 13280) with the scale 1:10,000 acquired in September 2000 were made available. The colour negatives were scanned the by Royal Jordanian Geographic Center in Amman with a photogrammetric precision scanner with resolution a of 20 µm resulting in a ground pixel resolution of 0.20 m.

### 6.4.2 Orthorectification

The GCPs were collected from the orthophotos based on the 1:30,000 panchromatic aerial photographs. The mean x RMS error was 4.86 m, the mean y RMS error was 7.93 m. The large error was attributed to the fact that the GCP were adopted from the rectified panchromatic orthophotos with an inherent error and partly high distortion and deformation caused by the rectification process. However, this geometric accuracy loss was accepted since it was more important that the two orthophoto datasets and mosaics match with each other. After generating the orthophotos they were mosaicked.

### 6.4.3 Post-processing and analysis

#### 6.4.3.1 Visual Interpretation

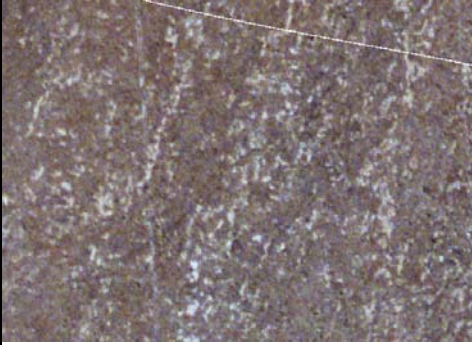

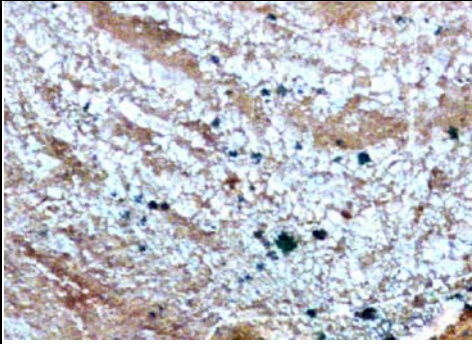
The degree of karstification / fracturing of the aquifers in the test area (Naur, Hummar, Wadi Sir Formations, chap. 2.4) was assessed based on GPS acquired reference points with a known degree of karstification / fracturing of the limestone outcrops that were compared with the texture they produce on the orthophotos. The karstified areas were delineated based on their specific texture taking into account the description for the individual karst levels given in the vulnerability approach of Goldscheider (2002) supplemented by own descriptions (Tab. 6.7).

Tab. 6.6: Degree of karstification / fracturing (F) used for the calculation of the vulnerability after the PI-method, Goldscheider (2002).

Fracturing	F
non-jointed	25.0
slightly jointed	4.0
moderately jointed, slightly karstified or karst features completely sealed	1.0
moderate karstic or karst features mostly sealed	0.5
strongly fractured or strongly karstified and not sealed	0.3
Epikarst strongly developed, not sealed	0.0
not known	1.0

Tab. 6.7 shows examples of the three distinguished karst / fracture classes and their descriptions. The levels *non-jointed*, *slightly jointed* and *not known* are not existing in the test area and are therefore not considered in the interpretation key (Tab. 6.6). The karstification mapping results were transferred to the whole test area, whereas the mapped dominating karst level of each individual limestone formation was assumed to exist area wide in this specific formation. For the geological layers that overlay the aquifers (Fuheis-, Shueib Formation, chapt. 2.4) in the test area a moderately jointed, slightly karstified degree was assessed area-wide.

Tab. 6.7: Interpretation key used for the classification of the three levels of karstification following the PI-method after Goldscheider (2002).

<b>Interpretation key for the degree of fracturing / karstification</b>			
<b>F</b>	<b>Examples on the orthophotos</b>	<b>Description of fracturing/ karstification (after Goldscheider, 2002)</b>	<b>Additional description</b>
<b>0.5</b>	 <p>image section ~ 60 m</p>	moderately karstic or karst features mostly sealed	limestones are partly covered by soils, surface texture is smoother due to little distinctive dissolution features like karren or widened fractures
<b>0.3</b>	 <p>image section ~ 70 m</p>	strongly fractured or strongly karstified and not sealed	abrupt changes of tonal variations between the limestones and the dissolution features or fractures that are filled with soil producing a rougher surface texture, partly sparse soil cover
<b>0.1</b>	 <p>image section ~ 50 m</p>	epikarst, strongly developed, not sealed	blocky appearance of the limestones due to intensive fracturing and karstification, partly very rough texture due to dense karst pattern, soil cover is often missing

It is obvious that the results of on-screen digitising while applying the interpretation key is influenced to a certain degree by a subjective choice of the author. But in regard of the desired qualitative final result it is considered appropriate.

To reduce the size of the images for the visual interpretation, the geotiff format of the scanned aerial photographs was compressed to *ecw* format developed by Earth Resource Mapping ([www.ermapper.com](http://www.ermapper.com)). The *ecw* (Enhanced Compressed Wavelet) format uses mathematical wavelet transformations to store image data, allowing a great reduction of the file size (about 1:30) whereas the amount of data loss is relatively small and georeferencing information is retained. The thematic layer of the karstification was imported to ArcGIS and overlaid by geological information to compare the degree of karstification of the single aquifers.

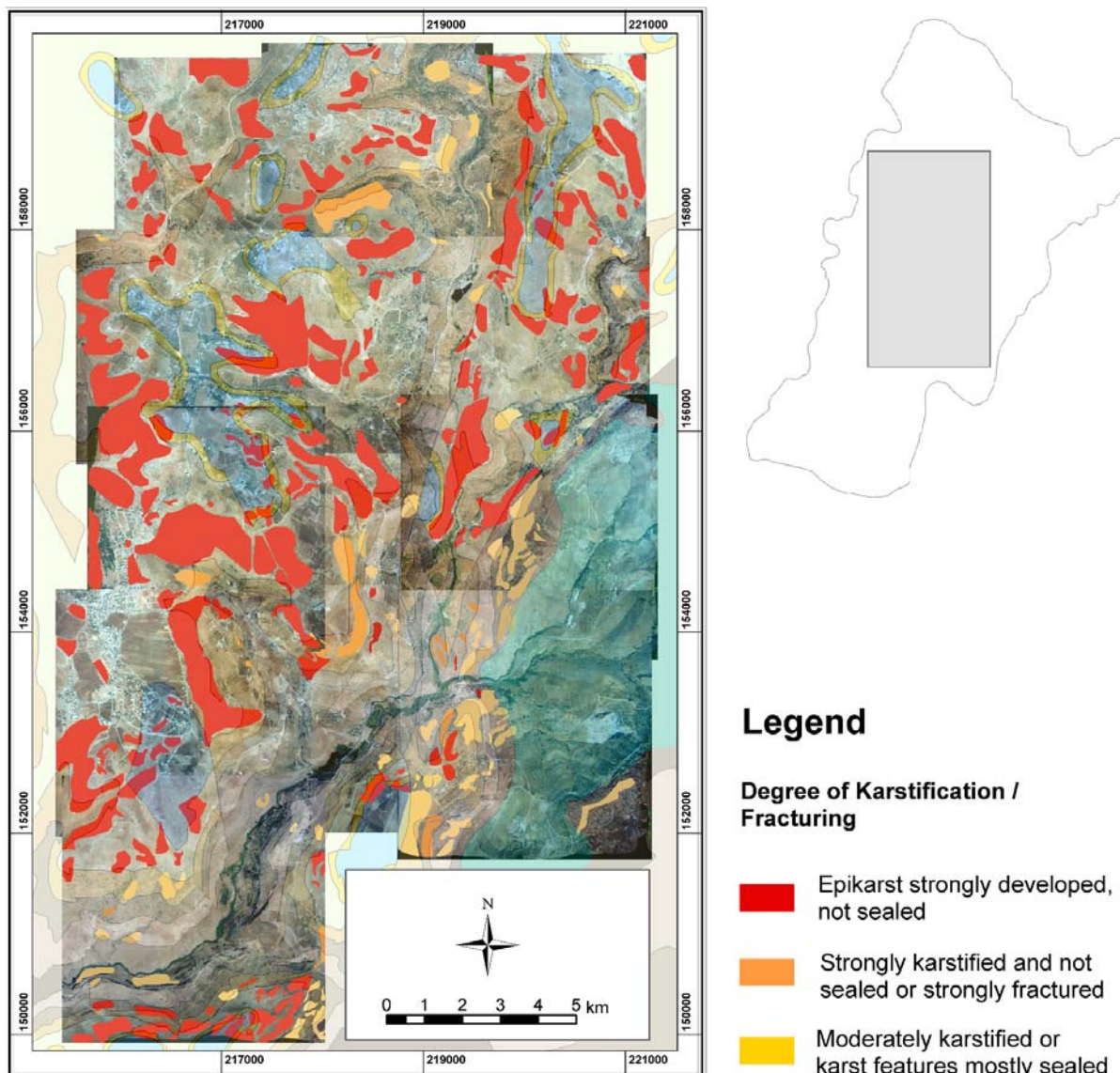


Fig. 6.11: Digital orthophotos (1:10,000) overlaid by the geology (70 % transparent) and digitised thematic layer showing three levels of karstification. The grey box indicates the coverage of the digital colour orthophotos in the study area.

The visual interpretation results clearly indicate the existence of a generally high degree of karstification (Epikarst strongly developed not sealed) above massive limestone (A7 aquifer). The Hummar formation (A4) is mainly strongly karstified, whereas the Naur Formation (A1/A2) is predominately moderately karstified.

### 6.4.3.2 Supervised classification results

With the 3 band orthophoto mosaic the usefulness of an supervised classification was tested to distinguish the main land cover classes. The classification result is shown in Fig. 6.12. The spectral resolution of the images is limited to the visible wavelength hence a vegetation discrimination in orchards, forest and crop based on the spectral signatures was impossible. Besides the images were taken in September when the crop fields have already been harvested. Yohay & Kadmon (1998) realised that there are several difficulties resulting from the application of computerized methods to analyse vegetation data from aerial photographs. A separability of the soil of fallow fields and the thin soil cover between the outcropping limestones was also not possible. Due to the fact that almost all the houses are made out of limestone from the region or concrete and have no silhouetted roofs, some misclassifications between houses/ urban areas and outcropping limestone occurred. A high amount of misclassifications occurred between dark or umbrageous orchard or forest areas and street informational class (Fig. 6.12). Chicken farms could not be separated from normal apartment houses. Due to the high amount of misclassifications, the result of the supervised classification was not used as input for the groundwater vulnerability and hazard assessment.

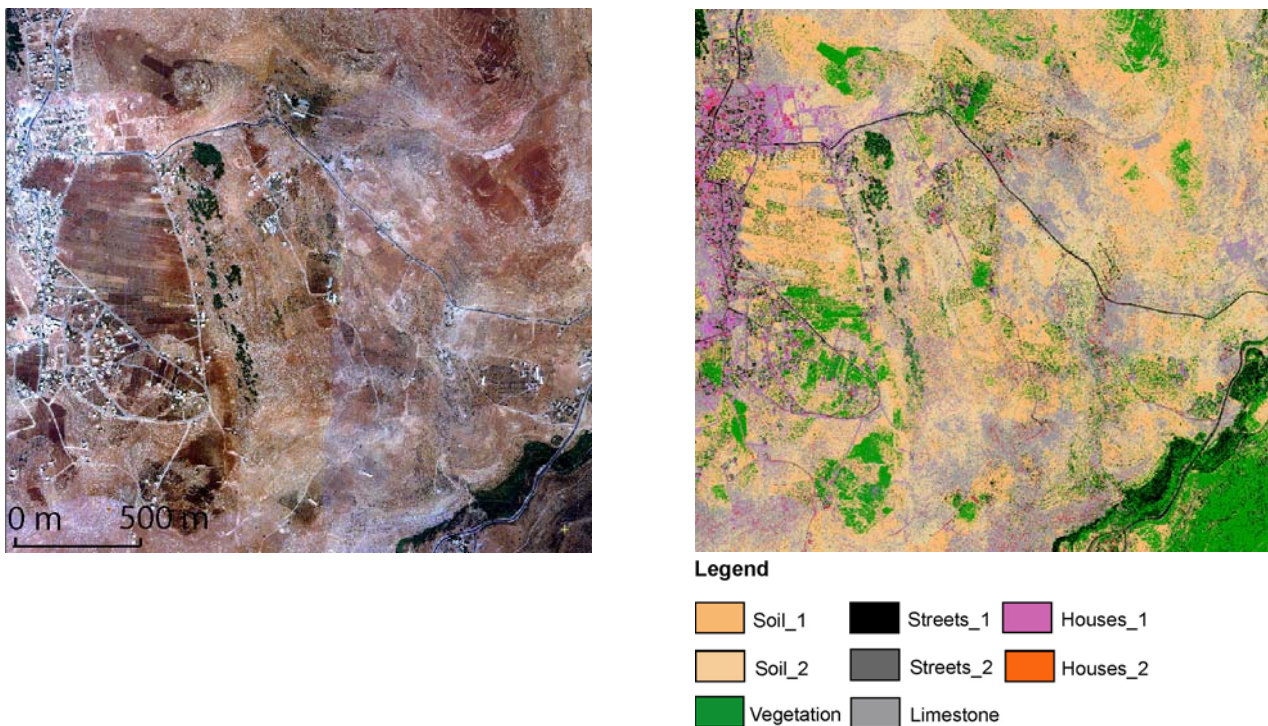


Fig. 6.12: Section of the automatic supervised classification result of the digital aerial colour photographs after merging of informational classes.

Chander et al. (2004) agree that a supervised classification based upon three colour bands is inadequate for more than 3 classes. He recommends to use additional data layers such as a texture layer (based on laser scanning) to consider not simply the colour characteristics but also the spatial variability of the signal response. Additional data layers or segmentation algorithms can be included in classification schemes as used by the *eCognition*<sup>®</sup> software from *Definiens Imagine*<sup>®</sup>. The classification process is based on fuzzy logic, to allow the integration of a broad spectrum of different object features such as spectral values, shape, texture for classification. For instance, using an object-oriented approach in the test area, an algorithm could be applied that separates the chicken farms by their length-width ratio from the spectral similar apartment houses. However, using object-orientated software was beyond the scope of this thesis, therefore finally the digital orthophotos were solely used for visual classification of the karst degree and location of hazards. For better classification results and a better separation between the land use types the usage of infrared aerial photographs would have been useful.

## 6.5 LANDSAT ETM<sup>+</sup> image contra orthophotos

### 6.5.1 Comparison of the agriculture areas

For the comparison of the thematic layers concerning the agricultural areas gained by on-screen digitising based on the b/w orthophotos and by supervised classification of the LANDSAT ETM<sup>+</sup>, the thematic layers were first overlaid within ArcGIS for a visual interpretation (Fig. 6.13).

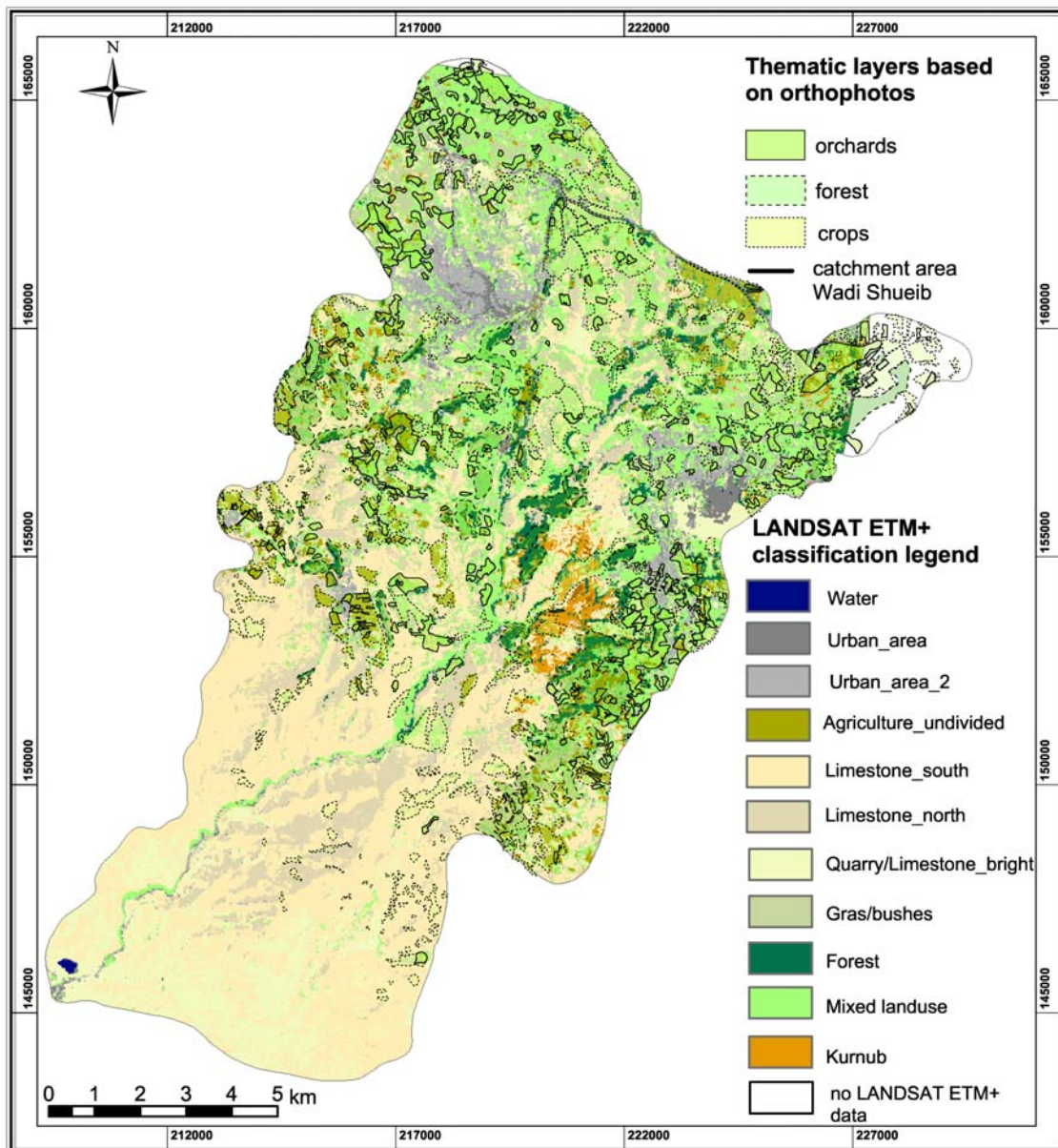


Fig. 6.13: Supervised classification results of the LANDSAT ETM<sup>+</sup> data overlaid by the thematic maps of the orthophotos generated within ArcGIS.

For the comparison of the percentage of the specific agricultural areas the thematic layers of the *orchards* and *crops* of the orthophotos were merged to one thematic layer named *agriculture*. The two informational classes of the supervised classification results of the LANDSAT ETM<sup>+</sup> image *mixed land use* and *agriculture undivided* were combined to one thematic layer named

*agriculture mixed*. The classes *mixed land use* and *dense agriculture/forest* of the NDVI were merged to the class *NDVI agriculture* (Tab. 6.8).

The direct comparison of the visual interpretation results of the b/w orthophotos with the LANDSAT ETM<sup>+</sup> automatic classification results proved to be problematic due to the following reasons: for the thematic layers of the b/w orthophotos *crops* and *orchards* the visible fields were digitised. Due to the partly bad quality of the b/w orthophotos, the high distortions the extreme tonal differences not all agricultural areas could be identified and digitised. In the layers *agriculture mixed* and *NDVI agriculture* an inherent error exists, due to the fact that the layers contain a certain amount of non-agricultural areas, that was not possible to separate during the supervised classification and the NDVI classification process (see chapter 5.4.4 and 5.4.5). The area percentages of the layers *agriculture*, *agriculture mixed* and *NDVI agriculture* are indicated in Tab. 6.8. The results mirror the above described possible errors: the smallest percentage of agricultural area exists in the thematic orthophoto layers. The thematic layers based on the LANDSAT ETM<sup>+</sup> image show a higher percentage of “agriculture” areas.

The colour digital aerial photographs were used for inspecting these additionally classified areas. The additionally classified areas of the *agriculture mixed* class of the supervised classification comprise mainly the land cover classes oak / pine forest, grass and bushes, wild olives, but partly also agricultural areas that could not be delineated on the orthophotos.

Tab. 6.8: Comparison of the percentages of agricultural areas in the study area based on the information derived from different remote sensing data sources and processing steps.

Name of merged layer	Data source and processing	Name of source layer	Percentage of classified agriculture area [%]
agriculture	panchromatic orthophotos on-screen digitising	crops orchards	17.1
agriculture mixed	LANDSAT ETM <sup>+</sup> supervised classification	agriculture undivided mixed land use	28.4
NDVI agriculture	LANDSAT ETM <sup>+</sup> vegetation index (NDVI)	mixed land use dense agriculture / forest	29.6

## 6.5.2 Conclusions

Regarding the relative small size of the test area, the orthophotos have one major advantage: the higher spatial resolution that allows for a delineation of small and individual agricultural areas, woodlands, detached houses and the street network. For instance, on the LANDSAT ETM<sup>+</sup> image the delineation of the streets was limited to the four-lane highway in the northern part of the test area, smaller roads could not be recognized but are important for the hazard mapping. For further processing as well as the assessment of groundwater vulnerability and hazards the orthophotos were taken wherever possible. The results of the thematic layers of information derived by the orthophotos is more suitable and accurate. Even if few agriculture fields could not be mapped the results of the information derived from the orthophotos mirror more precisely the situation in the test area than the supervised classification results of LANDSAT ETM<sup>+</sup> data.

## **6.6 Soil investigations**

### **6.6.1 Overview**

Within this thesis detailed soil investigations were conducted. The aim of this soil investigations was to estimate the soils protective potential against contamination for the groundwater and to obtain parameters needed for the vulnerability assessment such as thickness and effective field capacity of the soils. For this purpose first a soil map, scaled 1:50,000, was drafted based on the Jordanian Soil Atlas (National Soil Map Project, Ministry of Agriculture, 1994) and field investigations. For the soil map the soil classification the US soil taxonomy (USDA, 1993) of the Jordan Soil Atlas has been translated into the World Reference Base (WRB) of soil resources (Food and agriculture organisation of the United Nations (FAO), 1998). The WRB is a sophisticated international system for soil correlation, adopted by the International Union of Soil Sciences (IUSS) in 1998 (Kuntz, 2003). For the parts of the test area that have not been mapped already by the National Soil Map Project, the soils were mapped accordingly to the WRB.

Secondly, at representative locations soil samples were taken, infiltration tests (Infiltrometer) and soil coring were accomplished (Werz et al., 2005). The following chemical parameters were analysed: pH, cation exchange capacity (CEC), particle size distribution, bulk density, pore volume, effective field capacity (eFC).

#### **6.6.1.1 Soil map**

The soil map shows polygons with specific soil map units (Fig. 6.14). Most map units are associations (Soil Survey Manual, USDA, 1993) of reference soil groups, usually with one or no inclusion. Inclusions are smaller undistinguishable areas within the mapped boundaries of the soil units that are covered by soils, not fitting into the typical setting and are indicated in the soil map units as an error (in area percent) (Tab. 6.9). Following the WRB of soil resources the predominated reference soil groups are distinguished by the presence (or absence) of specific diagnostic horizons, properties and/or materials (e.g. vertisols, cambisols). A limited number of 'qualifiers' with unique definitions, describe individual soil units within the reference soil groups (e.g. lithic, chromic). Some parameters of the soil groups (e.g. average thickness, soil occurrence) in the Jordanian Soil Atlas have been modified by Kuntz (2003) to mirror the test area more precisely (Tab. 6.9). The soil map was used as a base map to identify different map units, which then were examined in more detail at profile or soil locations (Fig. 6.14).



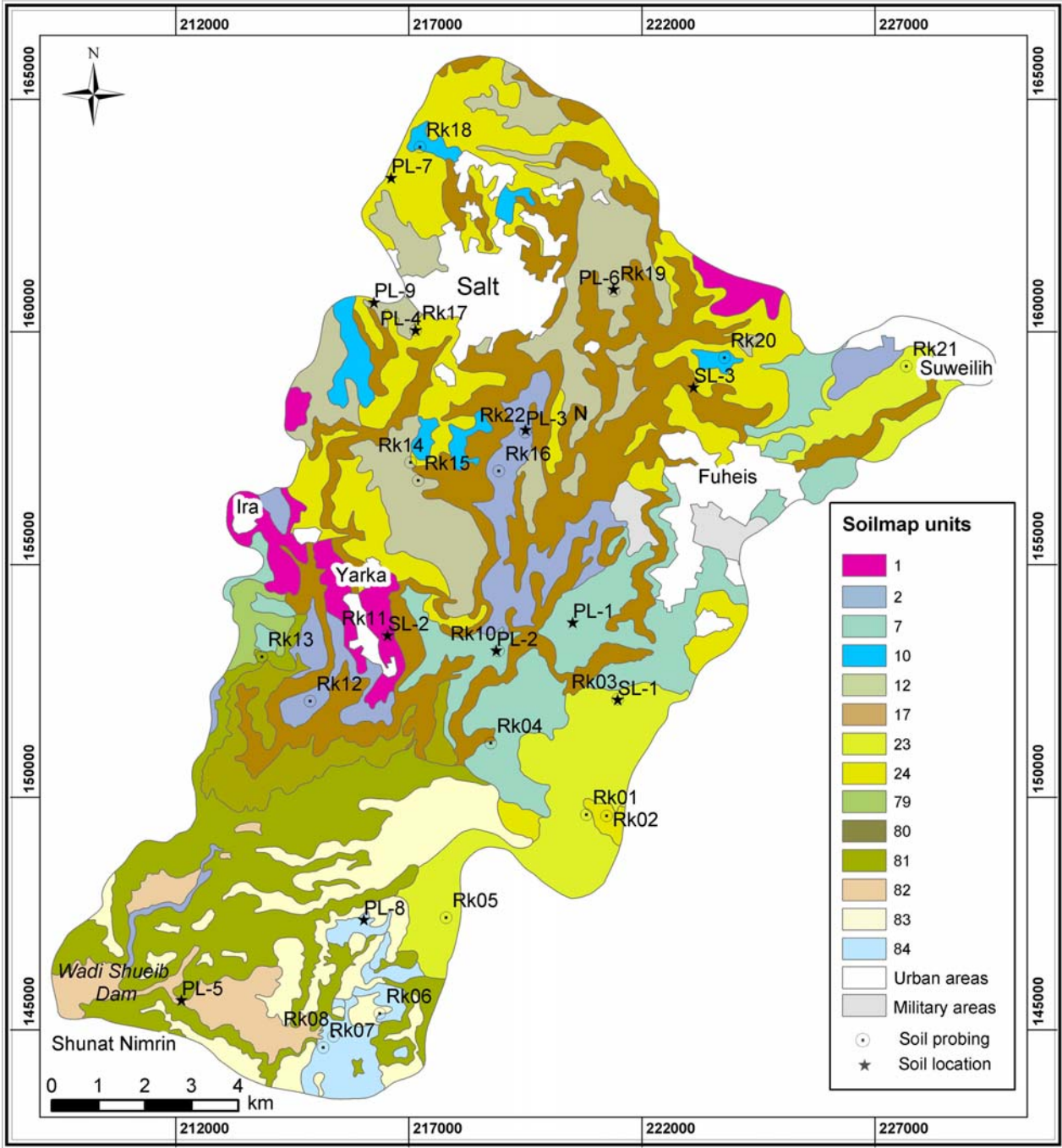


Fig. 6.14: Soil map of the test area including soil coring and soil locations (Werz et al., 2006).

Tab. 6.9: Soil map units in the test area based on reference soil types and added qualifiers of the WRB (modified after Kuntz, 2003).

**Soil map unit 1**

Area [km /%]	5.8km / 2.9%
Elevation & Slope	300-670 / 0-8%
Thickness	100-170cm
Predominant Soils	Chromic Vertisol 55% Vertic Cambisol 30%
Error	Rendzic Leptosol 15%
Associated Location	SL-2

**Soil map unit 7**

Area [km /%]	17.3km / 8.7%
Elevation & Slope	400-1150 / 0-25%
Thickness	70-150cm
Predominant Soils	Chromic Cambisol 60% Vertic Cambisol 20%
Error	Rendzic Leptosol 20%
Associated Location	PL-1 / PL-2

**Soil map unit 12**

Area [km /%]	17.9km / 9.1%
Elevation & Slope	700-1050 / 9-25%
Thickness	60-120cm
Predominant Soils	Chromic Cambisol 50% Calcaric Cambisol 30%
Error	Dystric Leptosol 20%
Associated Location	PL-6 / PL-4

**Soil map unit 23**

Area [km /%]	15.6km / 7.9%
Elevation & Slope	600-1100 / 9-16%
Thickness	30-70cm
Predominant Soils	Dystric Leptosol Rendzic 35% Chromic Cambisol 30%
Error	
Associated Location	SL-1

**Soil map unit 79**

Area [km /%]	1.3km / 0.7%
Elevation & Slope	400-600 / 0-40%
Thickness	30-80cm
Predominant Soils	Aridic Cambisols 70%
Error	Lithic Leptosols 30%
Associated Location	

**Soil map unit 81**

Area [km /%]	22.7km / 11.5%
Elevation & Slope	-300-300 / 9-100%
Thickness	10-50cm
Predominant Soils	Aridic Cambisol 50% Aridic Calcisol 50%
Error	-
Associated Location	

**Soil map unit 83**

Area [km /%]	12.6km / 6.4%
Elevation & Slope	-100-500 / 0-18%
Thickness	10-80cm
Predominant Soils	Yermic Calcisol 60% Lithic Leptosol 30%
Error	Calcaric Cambisol 10%
Associated Location	Smp1 / Smp4

**Soil map unit 2**

Area [km /%]	9.5km / 4.8%
Elevation & Slope	300-960 / 5-40%
Thickness	100-175cm
Predominant Soils	Calcaric Cambisol 65% Chromic Cambisol 35%
Error	-
Associated Location	PL-3 N

**Soil map unit 10**

Area [km /%]	3.1km / 1.6%
Elevation & Slope	450-1100 / 5-16%
Thickness	60-110cm
Predominant Soils	Chromic Cambisol 70% Leptosols 30%
Error	
Associated Location	(Rks 20)

**Soil map unit 17**

Area [km /%]	35.6km / 18.0%
Elevation & Slope	400-1000m / 26-60%
Thickness	20-60cm
Predominant Soils	Mollic Leptosol Dystric 30%
Error	Chromic Cambisols 20%
Associated Location	SL-3

**Soil map unit 24**

Area [km /%]	24.8km / 12.5%
Elevation & Slope	450-1100 / 9-16%
Thickness	10-40cm
Predominant Soils	Lithic Leptosols Mollic 50%
Error	Chromic Cambisols 20%
Associated Location	PL-7 / PL-9

**Soil map unit 80**

Area [km /%]	5.2km / 2.6%
Elevation & Slope	0-300 / 5-40%
Thickness	60-110cm
Predominant Soils	Aridic Cambisols 40% Aridic Calcisols 60%
Error	-
Associated Location	

**Soil map unit 82**

Area [km /%]	5.4km / 2.7%
Elevation & Slope	-300-300 / 0-26%
Thickness	10-80cm
Predominant Soils	Lithic Leptosol Yermic 30%
Error	Ochric Cambisol 30%
Associated Location	PL-5

**Soil map unit 84**

Area [km /%]	3.9km / 2.0%
Elevation & Slope	0-300 / 6-20%
Thickness	40-120cm
Predominant Soils	Takyric Calcisol Aridic 30% 40%
Error	Leptosols 30%
Associated Location	PL-8

The dominating soil units in the test area are soil unit 17 (18 %), 24 (12.5 %) and unit 81 (11.5 %). Soil map unit 17 comprises mainly *Leptosols* which are mineral soils whose formation was conditioned by the physiography of the terrain. They are formed in the test area on steep to very steep hill slopes. Surfaces are usually very stony and rock outcrops often cover large areas. Soil development is restricted to the spaces between greater boulders or small local depressions. The land cover is mostly grass, forest or occasionally olive trees.



Fig. 6.15: Lithic Leptosol fills and seals karst cavity. (Photograph taken May 2003.)

Soil map unit 24 includes very thin, often *lithic Leptosols* which are characterised by a depth of the underlying source hard rock of about 10 cm or less. Some deeper patches fill karst features such as solution channels, cavities or fissures in the underlying limestones and can act as a seal (Fig. 6.15). On these soils only grass occurs, occasionally some trees. Soil map unit 81 comprises *aridic* soils, which are common soils under arid conditions, on very steep escarpments or hill slopes in the lower elevations of the test area. These soils have a large coarse fraction of stones and

loamy fine material. Grass grows sparsely on these slopes. The soil polygons on the soil map pretend an area-wide soil cover and soil thickness though in reality the limestones are often only barely covered with soil and consequently the characteristic karstic limestones are widely exposed in the test area. Calcisols are mineral soils whose formation was conducted by the semi-arid climate. Due to the high relief in the test area, a high degree of spatial heterogeneity of the thickness and soil type occur within small distances (Werz et al., 2005).

### 6.6.1.2 Methods of soil investigation

The soil locations that were analysed are displayed on the soil map in Fig. 6.14. The locations were named with the prefix “PL” if a vertical soil profile already existed, for example near a construction site, all other sampled locations were labelled with the prefix “SL”. In Fig. 6.16 the location where ram probing was done are indicated as soil probing.

For the assessment of the soils several parameters were analysed in the field as well as in the laboratory, employing the following measurement techniques: soil coring, infiltrometer test, particle size distribution, soil-pH, natural water content, cation exchange capacity and suction power measurements. Tab. 6.10 gives an overview of the analysed parameters, the applied

methods and a short overview of the main results or remarks. Appendix 1 gives an example of a data form sheet filled in for all soil locations that were investigated in the test area.

Tab. 6.10: Analysed soil parameters and implemented soil tests in the test area. For detailed descriptions of the individual tests refer to Kuntz, 2003.

Test	Method / Material	Parameter
<b>Infiltrometer Test</b>	Double ring Infiltrometer DIN 19682-7	Infiltration rate/ hydraulic conductivity
<b>Particle size distribution</b>	DIN 18123 Seelheim ( 1880)	Granulometric parameters Hydraulic conductivity
<b>Ram probing with core extraction</b>	Gasoline Breaker (Wacker model BH23) DIN 4022	Soil thickness, vertical variation
<b>Soil pH</b>	WTW 330-i portable pH-meter DIN ISO 10390	Assessment of possible role of pH value for heavy metal mobility
<b>Potential Cation Exchange Capacity (CEC)</b>	Methylene-Blue Adsorption ("HALO-Method")	Evaluation of the retention potential of the soils for water pollutants
<b>Suction power / effective Field Capacity (eFC)</b>	Van Genuchten's model	Indicator for the residence time of infiltration water in the soil
<b>X-ray Diffractometry</b>	Diffractometer (Siemens D-500)	Clay mineral content

All profile and soil location samples were analysed with X-ray diffractometry (Siemens D-500) to get an impression of the clay mineral content. Certain minerals produce certain peaks at defined angles. The diffractometer in the laboratories of the Department of Applied Geology in Karlsruhe uses a Cu-K $\alpha$  source (40 KV, 30 mA) with a wavelength of  $\lambda=1.5406 \text{ \AA}$ . All samples were analysed from angles of  $1^\circ < 2\theta < 65$ .

### 6.6.1.3 Results

Two types of hydraulic conductivity values were obtained. Infiltration rates (m/s) were obtained by field experiments using the Infiltrometer. K-values were obtained in the laboratory by particle size distribution and application of indirect approximation methods using formulas that relates the k-value to particle size, particle size distribution and porosity.

#### Infiltration rates

The majority of the infiltration rates in the test area range between  $1,4 \times 10^{-5}$  and  $3.3 \times 10^{-6}$  m/s (Tab. 6.12). Compared with typical standard infiltration rates for specific soil textures shown in Tab. 6.11, the major sample results would indicate sandy soil, even if the results of the application of the DIN 4022 (German Institute for Norms, 1987) indicate mainly silt components in the soils of the test area. Accordingly, the measured infiltration rates seem too be to high in

general. The increased infiltration rates might be due to the following reasons: the effects of macropores and the high skeleton content in the soils, or the fact that the required penetration depth of the Infiltrometer of 5-10 cm following the DIN 19682-7 (Deutsches Institut für Normung, German Institute for Norms, 1997), was not reached at most locations.

Tab. 6.11: Typical saturated infiltration rates for specific soil textures.

Soil	Typical Saturated Infiltration Rates* [mm/hr]
Sand	200
Loamy sand	50
Sandy loam	25
Loam	12.7
Silt loam	6.3
Sandy clay loam	3.8
Clay loam and silty clay loam	2.3
Clay	1.3

\*Source: Texas Council of Governments, 2003

Tab. 6.12: Saturated infiltration rates in the test area.

Location	Saturated Infiltration Rates [after DIN]	
	[mm/hr]	[m/s]
PL_1	199	$2.8 \times 10^{-6}$
PL-2	252	$7.0 \times 10^{-5}$
PL-3 N	180	$5.0 \times 10^{-5}$
PL-4	180	$5.0 \times 10^{-5}$
PL-5	12	$3.3 \times 10^{-6}$
PL-6	119	$3.3 \times 10^{-5}$
PL-9 (& PL-7)	241	$6.7 \times 10^{-5}$
SL-1	47	$1.3 \times 10^{-5}$
SL-3	202	$5.6 \times 10^{-5}$

### Hydraulic conductivity (k)

The k values were calculated from the granulometric curves of the sieving analysis after Seelheim (1880) (Fig. 6.16). For the interpretation of the results it has to be considered that the unconformity coefficients in all samples were higher than 5, which is normally a criteria that has to be fulfilled for the formula of Seelheim (Fig. 6.17). The k values show a wide range within five order of magnitudes. The soil samples of the locations with very low k values show a characteristic high amount of clay minerals. The soils at the locations with the highest k value (PL-5) are very heterogeneous, dominated by gravel and sand. The k-values obtained by using the granulometric curves seems to mirror the situation in the test area more realistic than infiltration rate hydraulic conductivities.

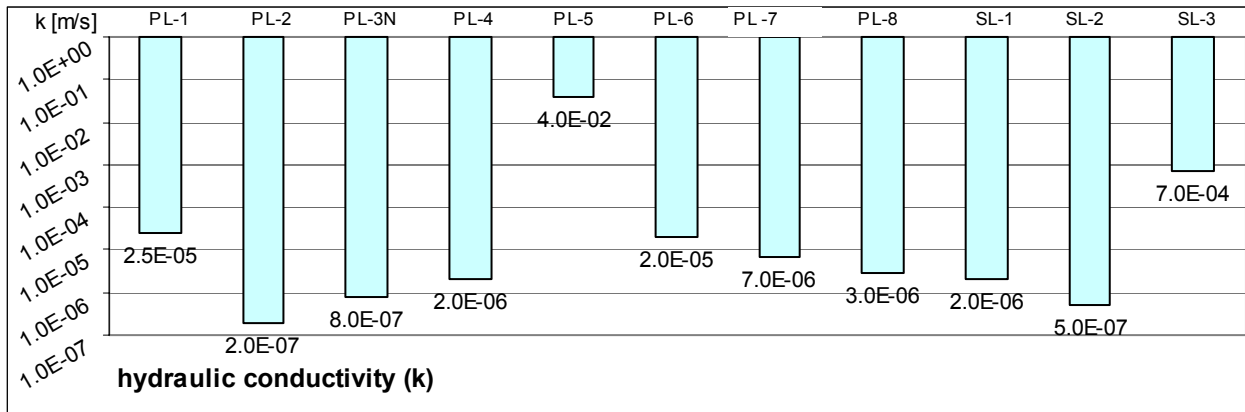


Fig. 6.16: Hydraulic conductivities of representative soil locations (modified after Werz et al., 2006).

### Granulometric parameters

The granulometric parameters of the unconformity coefficient indicate that all soils are unconform to very unconform (DIN 4022, Deutsches Institut für Normung, German Institute for Norms, 1987) (Fig. 6.17). This high degree of unconformity is mainly due to the high skeleton content in the soils.

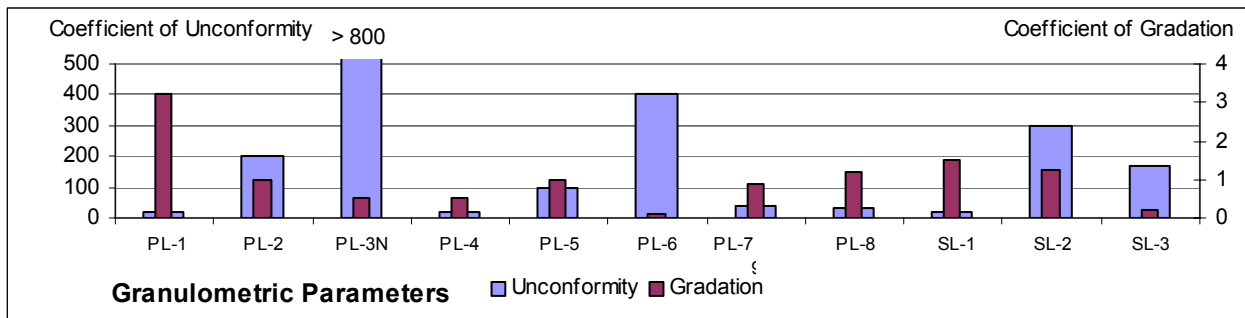


Fig. 6.17: Granulometric parameters: unconformity and gradation of representative soil locations (modified after Werz et al., 2006).

### Soil thickness

The measured soil thickness at representative locations varies over a wide range from 0.35 m or less to more than 3.0 m, mainly due to the topographically complex landscape characterized by a steep relief (Fig. 6.18). The soil thickness results seem to pretend a generally high soil thickness in the test area which is misleading since in the major parts shallow soils or patchy soil cover exist. In fact the results mirror the choice of the locations for soil coring and field experiments. The soil coring was conducted mainly in agricultural areas with deep and continuous soil cover.

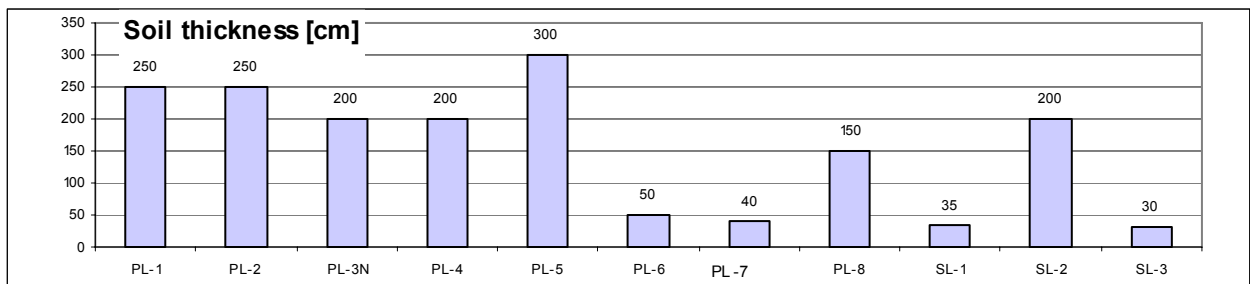


Fig. 6.18: Soil thickness of representative soil locations (modified after Werz et al., 2006).

### Cation exchange capacity (CEC)

With one exception, all CEC values range between approximately 12 to 33 meq/100 g, the majority of the values range between 20 to 31 meq/100 g (Fig. 6.19). After AG BODEN (1994) this corresponds to a high to very high CEC and indicates a high clay fraction. The results of the X-ray diffractometry confirm the high clay fraction.

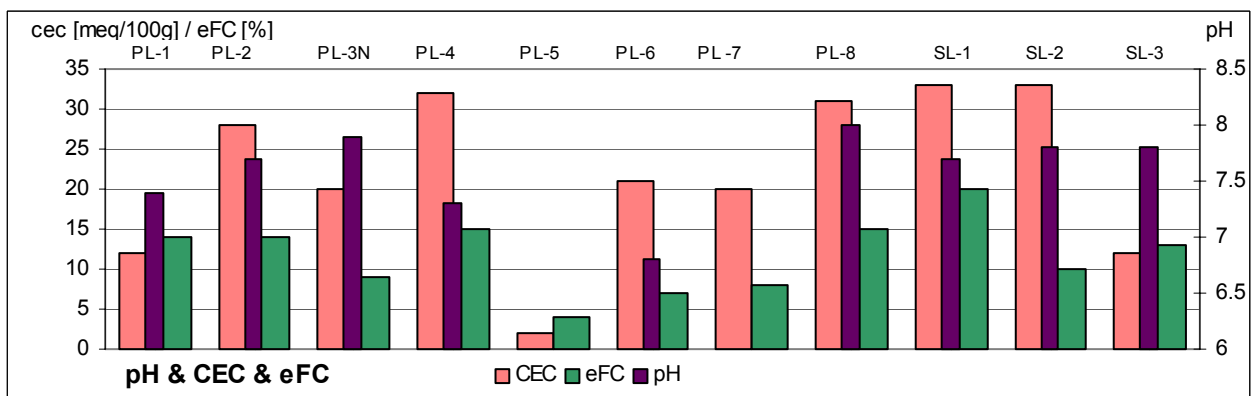


Fig. 6.19: CEC, eFC and pH values of representative soil locations (modified after Werz et al. 2006).

### pH-value

Alkali pH values dominates in the soils in the test area and range from pH 6,7 to pH 8,1 and are caused by the high content of calcium carbonate in the soils (Fig. 6.19). The high calcium carbonate contents in the soils are of lithogenous origin, related to the underlying limestone parent material.

### Effective field capacity (eFC)

The majority of the soils shows a medium eFC, with values ranging from 4 to 21 % (equivalent 40 to 210 mm) AG BODEN (1994) (Fig. 6.19). For some locations the eFC could not be measured. To fill in these data-vacancies and to be able to verify the measured values, the eFC values were estimated according to the "Bodenkundliche Kartieranleitung" (AG Boden, 1996). For this purpose all samples were "translated" into the according nomenclature (AG Boden, table 26), and a bulk density class was assigned according to table 19. Therefore the fine-soil including only particle size fractions below 2mm was adopted from the measured granulometric curves and converted to 100%. Effective field capacity was then estimated using table 56 (AG Boden, 1996). The final values were calculated by taking the coarse particle fraction (skeletal content) into

account (Kuntz, 2003). According to AG Boden (AG Boden, 1996, pp.295) the estimated values were multiplied with the factor:  $(100 - \text{Skeletal content [\%]}) / 100$ .

### **X-ray diffractometry**

The main minerals in the soil samples of the test area are quartz, calcite, dolomite, and swelling clay minerals such as montmorillonite and other smectites. X-ray diffractometry results show that high intensities in the  $2\theta$  area from  $1^\circ$  to  $15^\circ$  are common in all samples and indicate comparatively high amounts of clay minerals. The swelling clay minerals such as montmorillonite and other smectites can be clearly identified by their distinctive, broad and asymmetric diffraction peaks around  $14\text{\AA}$  to  $15\text{\AA}$  ( $4,5^\circ$ - $6^\circ$   $2\theta$ ). Only samples from the very top soils such as PL-5 lack these minerals, due to leaching and relocation into deeper soil horizons (Kuntz, 2003). The X-ray diffractograms show clear peaks for quartz at  $4,2\text{\AA}$  and  $3,3\text{\AA}$  in any sample. Soils developed above Kurnub Sandstone (PL-1) or on Amman Silicified Limestone (PL-6) show very high quartz contents, compared to soils above softer units such as the Fuheis Formation (PL-3N).

#### **6.6.1.4 Discussion**

The soil map and the results of the soil investigations are intended to give qualitative information about the protective potential of the soil cover against hazards posing a threat to the groundwater. The idea behind the protective potential of soil is in general, that contaminants travelling through the soil undergo mechanical, physico-chemical and microbial processes (soil-pollutant interaction mechanism) reducing the load, summarized as "natural attenuation" (Yong et al., 2003; Brady et al., 1997; Knorr, 1997; Lewandowski, 1997). These processes are enhanced by the assimilative capability of soils, the various reactive processes in soils and are dependant on the soil type itself, on the residence time of the infiltrated water which in turn is controlled by the thickness of the soil layer, its permeability and the amount of infiltration water. A significant factor in the development of the natural attenuation capacity of soils comes from the composition of the soil and the immediate environment, i.e. the soil-water system as a geoenvironmental feature (Yong et al., 2003). The composition of soils in the test area is a precondition for a high ability to naturally attenuate contaminants and pollutants.

The pH values of soils strongly influences what chemical processes will occur in the subsurface environment. The mainly alkali pH values of the soils in the test area in the range of pH 6,7 to 8,1 originating from the high carbonate contents due to the mainly limestone parent material, reduces the mobility of the heavy metals to a minimum and enables a deposition of the heavy metals within the soils. Furthermore the high carbonate content of the soils leads to a permanent buffering of the pH value, and facilitates that the pH value stays in neutral or alkali environment keeping down the mobility of the heavy metals.

The high CEC favours the pollutants cations to be exchanged and fixed in the soils, since the CEC is the sum of exchangeable cations that material can bind at a specific pH (Scheffer & Schachtschabel, 1989). A high CEC, caused by a high clay and organic matter content, enhance the retention of cations such as  $\text{Al}^{3+}$ ,  $\text{Fe}^{2+}$ ,  $\text{Ca}^{2+}$ ,  $\text{Mg}^{2+}$ ,  $\text{NH}_4^+$  and heavy metals. The cations can be binded either by physical adsorption, due to unsatisfied charges of the soil particles, or by chemical adsorption including chemical bonding between atoms.



The eFC is commonly used as an indicator for the residence time of the water in the soil and is needed as additional attribute for the groundwater vulnerability map. The high amount of carbonates and swellable clay minerals provide the soils with a high pollutant retention potential since the clay minerals on one side enables physical adsorption of heavy metals and on the other side enable ionic exchange between alkali/ alkali earth elements (Scheffer & Schachtschabel, 1989).

## **6.7 Additional spatial and non-spatial data**

### **6.7.1 Data layers generated with ArcGIS**

Due to the fact that remote sensing imagery could not provide all information necessary for this study, field investigations, GPS data, elevation information, topographic maps, hydrogeological and hydrological data and hazard characteristics had to be included and combined with the information derived from remote sensing imagery. Therefore within this work several point, line and polygon data layers (“shapefiles”) and raster layers (“grids”) were generated within ArcGIS and used additionally for the generation of the vulnerability, hazard, and risk intensity maps. The most important thematic maps that are not included as figures in this work are listed in Appendix 5. Attribute tables were assigned to the thematic layers including specific relevant data for the generation of the vulnerability, hazard, and risk intensity maps. Within ArcGIS several operators (tools) were used such as conversion, transformation and calculation tools to create new data layers.

### **6.7.2 Digital Terrain Model (DTM)**

A DEM of the test area was generated within ArcGIS from digitised contour lines with an elevation interval of 20 m, based on 1:50,000 topographic maps digitised wadi courses and known geodetic points at hill tops. From the vector data an elevation grid with a cell size of 15 m was interpolated using the *topogrid* command (Fig. 2.14). The wadi streams in the test area were used as break lines indicating local minima, the geodetic heights indicate local maxima. The interpolation method of ArcGIS 8.3 is based on Hutchinson & Dowling (1991), using an iterative finite interpolation technique. It is optimised to have the computational efficiency of “local” interpolation methods (e.g. inverse distance weighted interpolation) without losing the surface continuity of global interpolation methods such as krigging and splines. The used technique in the *topogrid* command is a discretised thin plate spline technique (Wahba, 1990), where the roughness penalty was modified to allow the fitted DEM to follow abrupt changes in terrain such as streams or ridges. The DEM mirrors the steep relief in the test area. However, to what extent contours and resulting DEMs reflect the actual morphology is generally difficult to evaluate (Carrara et al., 1997).



## 7 GROUNDWATER VULNERABILITY IN THE TEST AREA

The groundwater vulnerability map was generated based on information deriving from the processed remote sensing image and the orthophotos, on data from soil investigations and field data including existing hydrogeological and hydrological data, on the DEM, and on geological maps. For the assessment of the groundwater vulnerability the PI-method after Goldscheider (2002) was applied. Due to the small scale heterogeneity of the land cover, the thematic vector layers deriving through the analysis of the orthophotos are more detailed and suitable to represent the land cover in the test area than the results deriving from the classification of the LANDSAT ETM<sup>+</sup> data. Therefore the usage of the thematic orthophoto layers was favoured whenever possible.

### 7.1 Protective cover (P-factor)

The protective factor effectiveness determined by the total protective function ( $P_{TS}$ ) was calculated based on the scheme displayed in Fig. 7.1

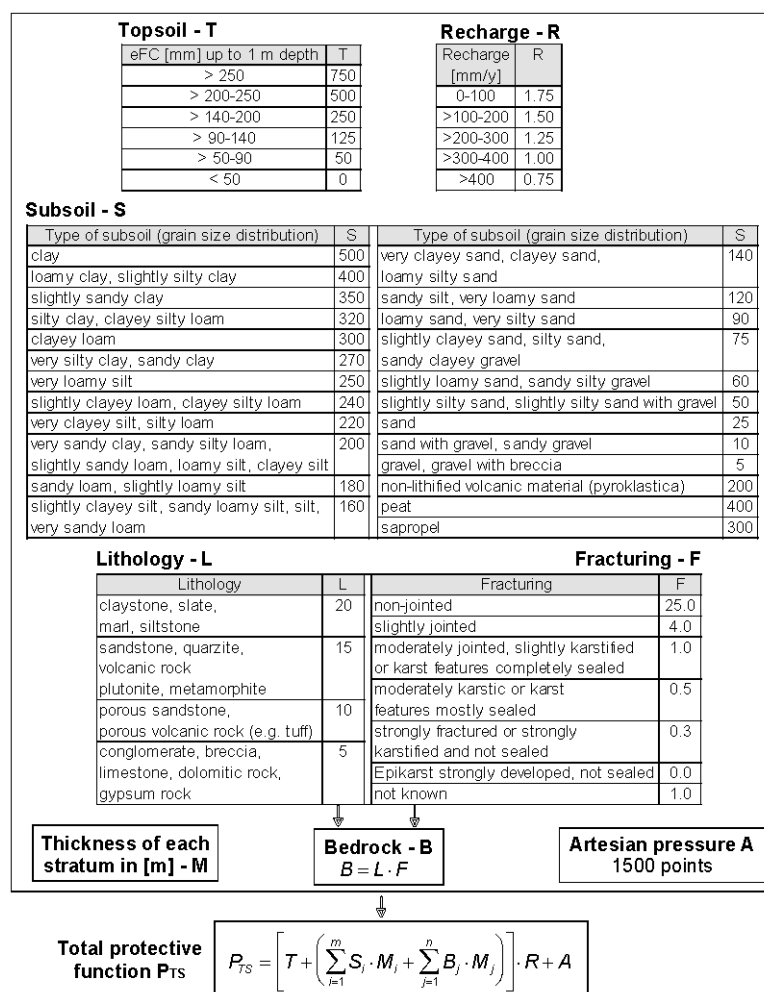


Fig. 7.1: Determination of the P-factor (Goldscheider, 2002).

For the topsoil layer the thematic orthophoto layers of the crops and orchards were merged to one agriculture layer and combined with the individual measured or estimated effective field capacities (eFC) of the soils (chapter 6.6.3). Depending on the eFC, protection points for the topsoil (T) were assigned (Fig. 7.1). Field investigations showed that off site the agricultural areas very often just patchy thin soil cover exists with bare rock outcrops in between. To avoid a overestimation of the soils' protective capacity the soils were assumed as area-wide and assigned with a T value within agricultural land, the areas outside were taken as zero.

The estimation on the recharge volume (R) in the test area is based on the precipitation modelling results of Orthofer (2001) (Fig. 7.2), considering that only approximately 12 % of the precipitation is available for groundwater recharge in the test area (Ta'any, 1992). For the precipitation modelling a response model with several variables such as the respective location, the regional valley-ridge system and the large-scale climatic conditions were used. The influence of the variables were quantified using multiple regression functions with measurement data from monitoring sites and explanatory variables. Due to the fact that the PI-method was developed for European karst areas the indicated recharge range was defined for moderate climatic conditions. Hence, the recharge range mirrors not the typical situation in (semi-)arid Mediterranean climate zones and uses recharge amounts for the calculations that are in general too high. In the test area the lowest possible R value is assigned area-wide since the recharge amount is less than 100 mm/year.

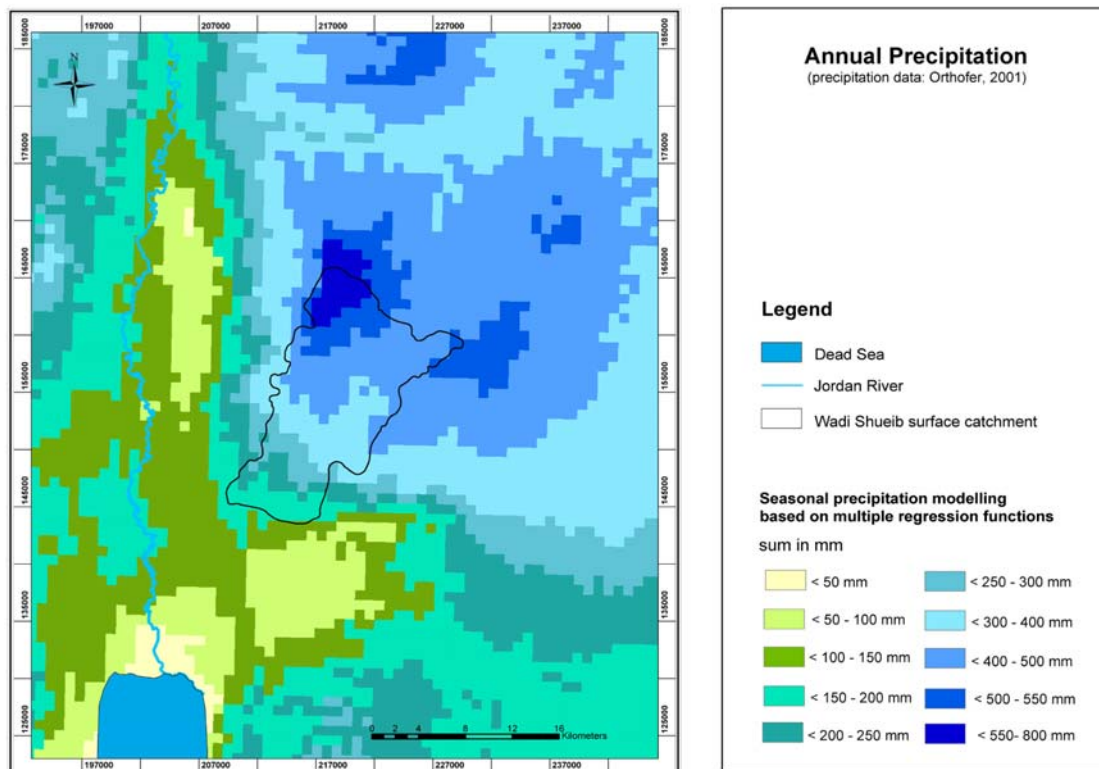


Fig. 7.2: Annual precipitation in the test area and surroundings based on modelling results from Orthofer (2001). Cell size 850 m.

According to Al-Daher (1989) very limited and small subsoil deposits (wadi floor deposits) exist beneath the Wadi Shueib course, but these are of no significance for the protective function of the groundwater and therefore not considered as a special layer as indicated for the determination of the P-factor (Fig. 7.1).

The lithology is based on existing geological maps and studies of Ta'any (1992). The degree of karstification was determined using the results of the visual interpretation of the high-resolution digital orthophotos (chapter 5.6.3.1) that were extrapolated to the whole test area and compared with observations made during field work. The lithology comprises the lithology and fracturing / degree of karstification of the rocks that overlay the specific uppermost aquifer and the lithology and karstification of the unsaturated zone of the specific uppermost aquifer expressed as "bedrock factor" B.

The thickness of the unsaturated zone of the karstified aquifers was estimated if available based on well data (provided by the Ministry of Water and Irrigation (MWI), Amman). Most of the wells are concentrated in two clusters in the area of Salt in the north (four wells) and near the Wadi Shueib dam in the south (four wells). In other parts of the test area the thickness of the unsaturated zones had to be estimated using the topography and the elevation of the discharging springs. Due to the lack of information a constant formation thickness and constant depth to the groundwater table within the aquifer units were assumed for the unsaturated zones, even if there could exist some local changes within the aquifers due to the complex tectonic situation. An average thickness of 60 m was estimated for the unsaturated zone of the Naur aquifer, 50 m respectively 75 m regarding the Hummar and Wadi Sir aquifer. The total protective function  $P_{TS}$  of the overlying layers is then calculated after the formula indicated in Fig. 7.1.

## 7.2 Infiltration conditions (I-factor)

The determination of the I-factor (infiltration conditions, degree of bypassing) is based on several calculation steps displayed in Fig. 7.3. First the dominant flow process in the test area was assessed based on hydraulic conductivity (k) values of the soils and the depth to the low permeability layers. For k values of the soils the calculated values from the granulometric curves of the soil samples were taken (chapter 6.3.5). The depth to the low permeability layers were determined based on the soil thickness indicated in the soil map, adjusted with extrapolations from locations with known soil thickness to locations with similar conditions. The explanation of the flow process types code (Type A - F) is given in Fig. 7.4. To estimate the frequent Hortonian overland flow (Type F) over paved surfaces (settlements), the urban areas delineated by the supervised LANDSAT ETM<sup>+</sup> classification were extracted and combined with the soil map. The dominating flow process is infiltration mainly over the highly karstified limestones.

For the calculation of the I'-factor the PI-method distinguishes between two types of vegetation cover that are relevant for the infiltration conditions: forest and field (meadow, pasture) areas and combine them with the slope. Under moderate European climate conditions woodland's infiltration is enhanced because of the characteristics of the forest soil (loose organic material, abundant macro pores) and due to the reduction of the precipitation intensity through interception. Agricultural areas often enhance surface runoff due to the soils' characteristics

(clayey, loamy soils) such as increased compaction caused by farming. In the test area no woodland comparable to a typical European forest exists. Oak and pine tree forests grow directly over more or less karstified limestone, hardly any soil cover is present. In most cases patchy soil fills the surface karst cavities.

1<sup>st</sup> Step: Determination of the dominant flow process

		Depth to low permeability layer		
		< 30 cm	30-100 cm	> 100 cm
Saturated hydraulic conductivity [m/s]	> 10 <sup>-4</sup>	Type D	Type C	Type A
	> 10 <sup>-5</sup> -10 <sup>-4</sup>		Type B	
	> 10 <sup>-6</sup> -10 <sup>-5</sup>	Type E		
	< 10 <sup>-6</sup>	Type F		

2<sup>nd</sup> Step: Determination of the I'-factor

Forest				
dominant flow process		Slope		
		< 3.5 %	3.5 - 27 %	> 27 %
infiltration	Type A	1.0	1.0	1.0
subsurface flow	Type B	1.0	0.8	0.6
	Type C	1.0	0.6	0.6
surface flow	Type D	0.8	0.6	0.4
	Type E	1.0	0.6	0.4
	Type F	0.8	0.4	0.2

Field/Meadow/Pature				
dominant flow process		Slope		
		< 3.5 %	3.5 - 27 %	> 27 %
infiltration	Type A	1.0	1.0	0.8
subsurface flow	Type B	1.0	0.6	0.4
	Type C	1.0	0.4	0.2
surface flow	Type D	0.6	0.4	0.2
	Type E	0.8	0.4	0.2
	Type F	0.6	0.2	0.0

3<sup>rd</sup> Step: Determination of the I-factor

Surface Catchment Map		I' factor					
		0.0	0.2	0.4	0.6	0.8	1.0
a	swallow hole, sinking stream and 10 m buffer	0.0	0.0	0.0	0.0	0.0	0.0
b	100 m buffer on both sides of sinking stream	0.0	0.2	0.4	0.6	0.8	1.0
c	catchment of sinking stream	0.2	0.4	0.6	0.8	1.0	1.0
d	area discharging inside karst area	0.4	0.6	0.8	1.0	1.0	1.0
e	area discharging out of the karst area	1.0	1.0	1.0	1.0	1.0	1.0

I-map

Fig. 7.3: Determination of the I-factor (Goldscheider, 2002).

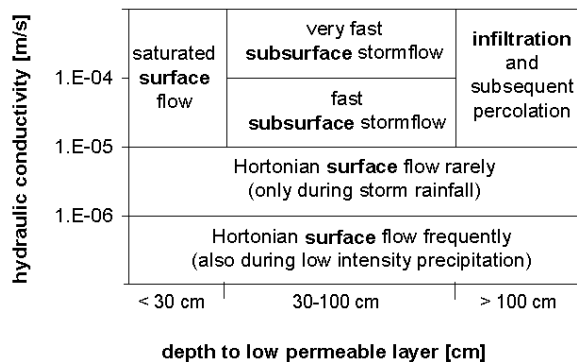


Fig. 7.4: Determination of the dominant flow process (after Goldscheider, 2002).

Therefore, the forest areas were not considered as separate vegetation cover with specifically assigned values as normally intended by the PI-method but just the I'-factor values for field (meadow, pasture) areas were used for the determination of the overall I'-factor (Fig. 7.4). For the calculation of the I'-factor the dominant flow process layer was merged with the slope layer. The slope was calculated within ArcGIS based on the DEM, then converted from slope degree to slope percent and resampled to the three slope classes provided by the PI-method (Fig. 7.3).

Concerning generation of the surface catchment types (Fig. 7.3), no swallow holes or sinking streams could be detected during fieldwork, though deep wadis could be considered as potentially more vulnerable zones because they are often deeply incised into the aquifer and the depth to the groundwater table is less. Many wadis follow the direction of faults and indicate higher permeable zones. Thus, it could be possible that contaminants infiltrate relatively easy through the wadi bed into the aquifer as part of the surface runoff. Further investigations should be conducted to assess whether zones under the wadi beds are more permeable and possibly lead to direct and fast infiltration of contaminated water into the aquifer.

The I-factor map is shown in Fig. 7.5b. For the determination of the final I-factor only the surface catchment values for "areas discharging inside karst area" were taken into account.

### 7.3 Results

For the final vulnerability map the thematic layers of the P-factor and the I-factor are multiplied resulting in the PI-factor. The results show the spatial distribution of the natural protection of the respectively uppermost aquifer system in the test area. Two levels of the protective function dominate: a moderate protective function (yellow colour) and a very low protective function (red colour) (Fig. 7.5a). The areas with a low protective function match with the outcrops of mainly bare karstified limestones and dolomites with well-developed karst features and only patchy soil cover. A high protective function exists in the area of the outcrop of the Kurnub Sandstone, due to the thickness of the unsaturated zone and the type of lithology leading to higher protection points. The class "very high protective function" does not exist in the test area. In general, the contribution of the topsoil to the protective function of the aquifer is very small. For more than 80 % of the area a topsoil value (T) of zero is assigned, indicating that no protective potential of the soils exist at this locations (Fig. 7.7).

The I-map includes the whole range of bypass probabilities, from very low to very high (Fig. 7.5). It is dominated by a very low degree of bypassing of the protective function (blue colour), and a low degree of bypassing (green colour). The areas with a very low degree of bypassing are mainly existing in the test area over bare karst where the dominant flow process is infiltration. Areas with high degree of bypassing exist on steep wadi flanks with fast surface flow, due to small hydraulic conductivities, no or shallow soils and limited infiltration possibilities.

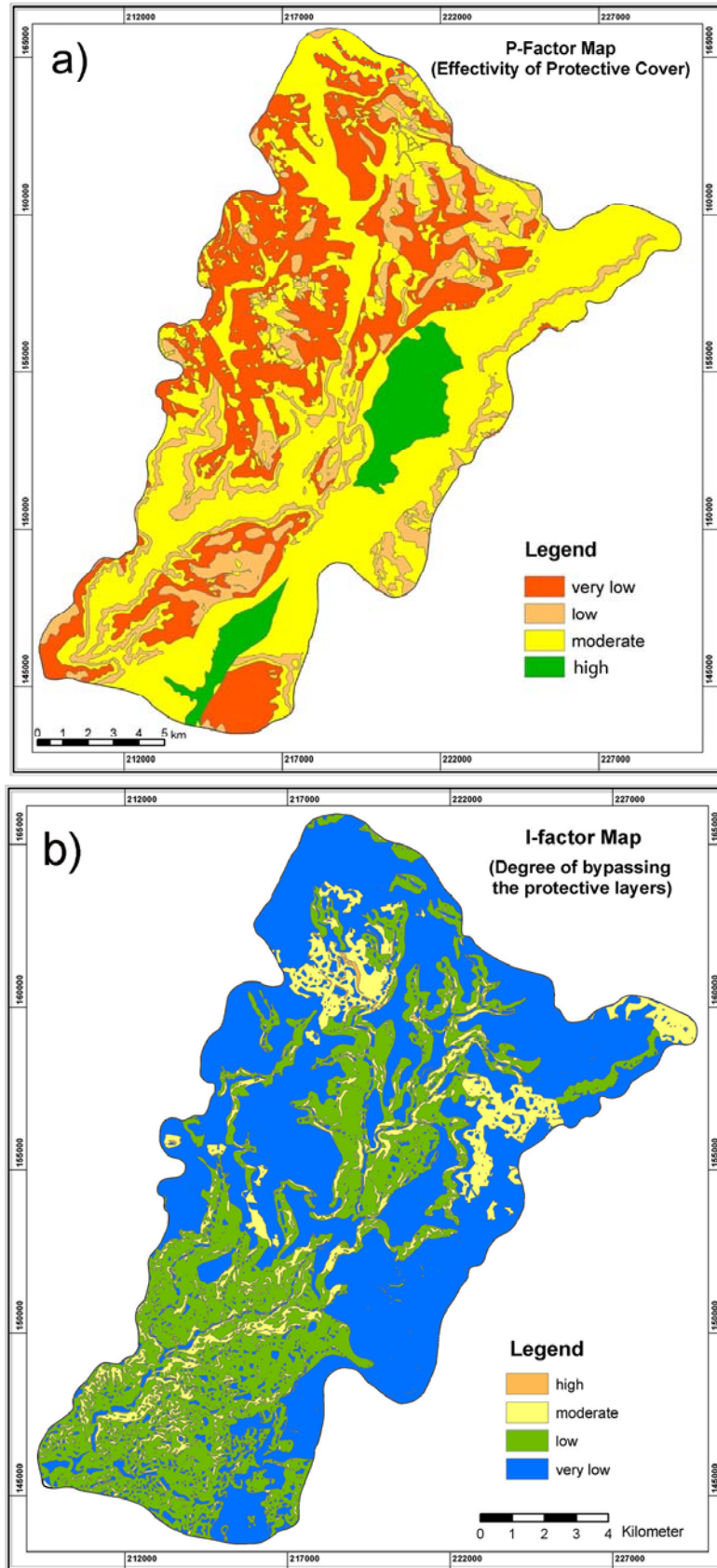


Fig. 7.5: a) P-Factor map showing the protective cover effectiveness, b) I-Factor map showing the infiltration conditions expressed as degree of bypassing.



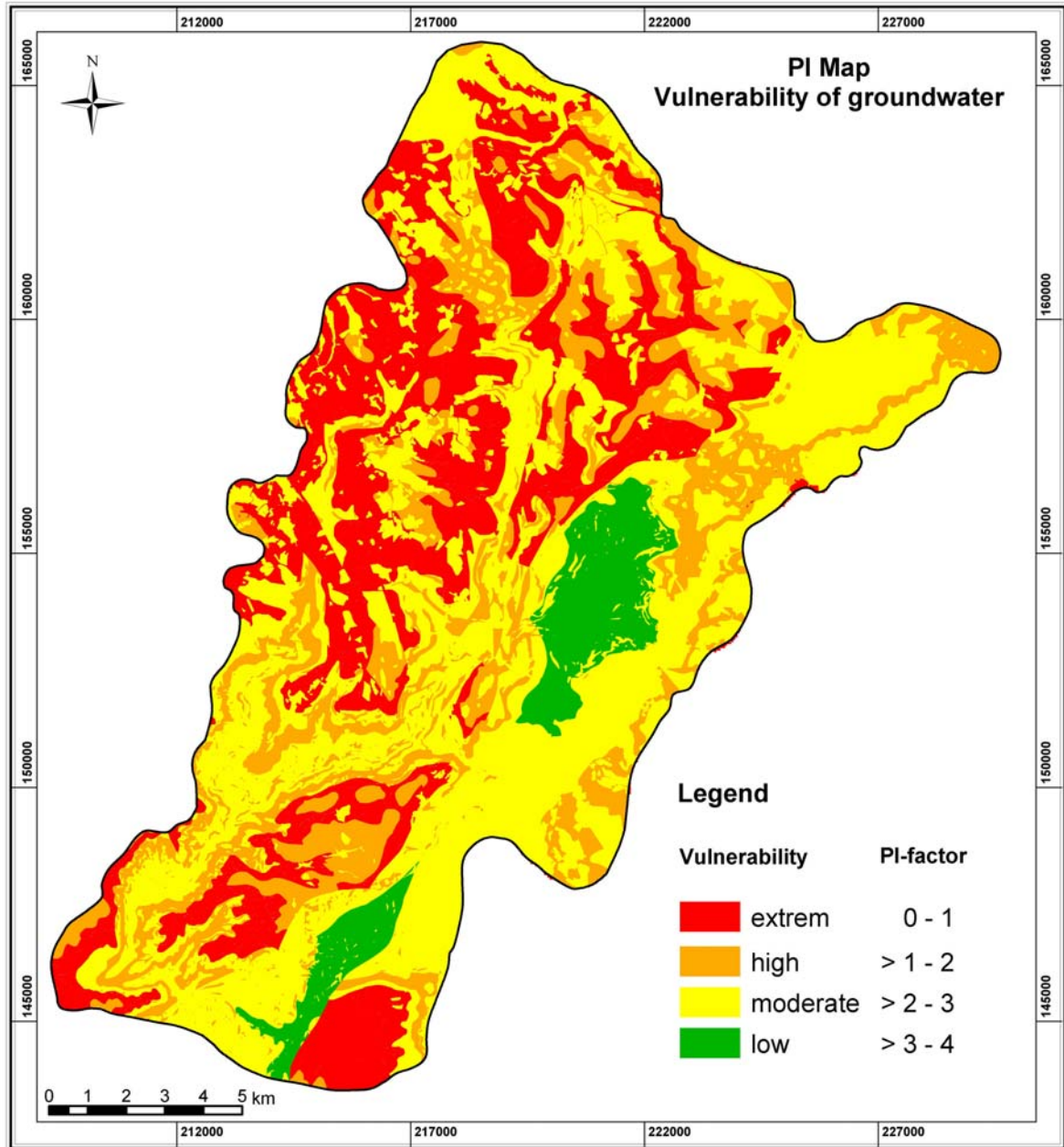


Fig. 7.6: Groundwater vulnerability map of the test area.

Tab. 7.1: Legend of vulnerability, P-factor and I-factor map (after Goldschneider, 2002).

vulnerability map		P-map		I-map	
vulnerability of groundwater		protective function of overlying layers		degree of bypassing	
description	$\pi$ -factor	description	P-factor	description	I-factor
extreme	0-1	very low	1	very high	0.0-0.2
high	>1-2	low	2	high	0.4
moderate	>2-3	moderate	3	moderate	0.6
low	>3-4	high	4	low	0.8
very low	>4-5	very high	5	very low	1.0

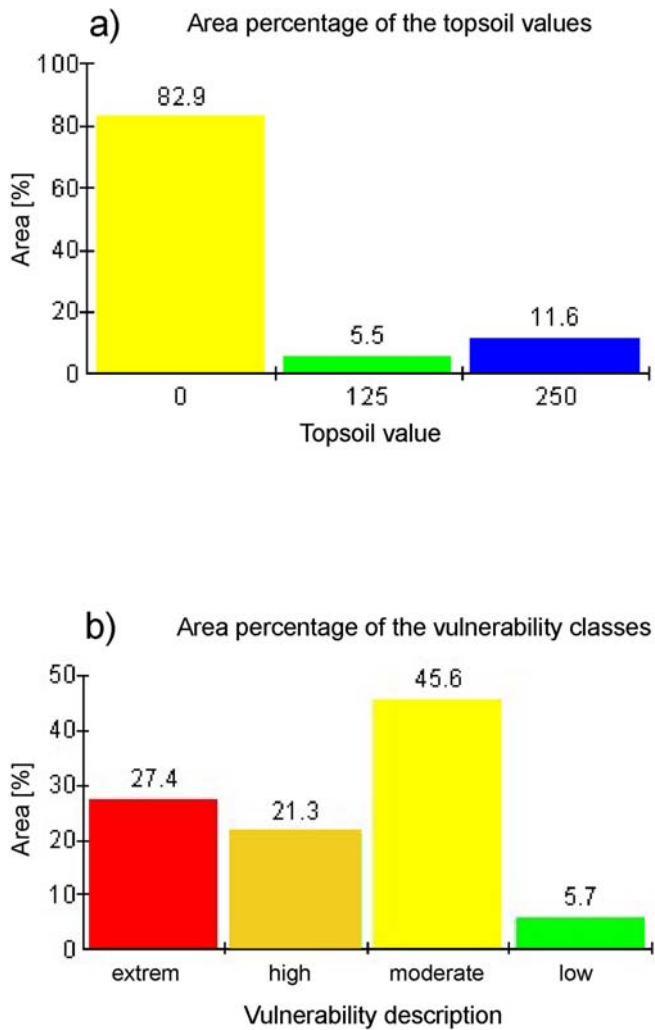


Fig. 7.7: a) Area percentage of the assigned topsoil values for the protective cover; b) area percentage of the existing vulnerability classes.

The areas with a very high degree of bypassing (orange colour) are limited to steep slopes favouring surface flow with missing soil cover leading to a fast surface or subsurface flow.

For the final PI-factor and the degree of vulnerability the P-factor and I-factor are multiplied. Consequently, the resulting map shows the spatial distribution of the intrinsic vulnerability and the natural protection of the uppermost aquifer. The PI-factor is subdivided into five vulnerability description classes. By combining the P-map with the I-map mainly parts with moderate protective function are affected and are assigned in the final vulnerability map to highly vulnerable areas, due to a high bypass probability.

The class “very low vulnerability” is not present (Fig. 7.6). In 45.6 % of the test area a moderate vulnerability dominates (Fig. 7.7b). About one third of the area shows a high vulnerability, due to different reasons: many outcrops of naked or barely covered highly karstified rocks exist and steep slopes favour a bypassing of the protective function of the overlying layers. A main factor is the poor degree of soil coverage. 82.9 % of the test area are missing a continuous soil cover that can function as effective protective layer against contaminants (Fig. 7.7 b).

## 7.4 Error discussion

Assessing the groundwater vulnerability of an area, one is often confronted with a general lack of data concerning the geological or hydrogeological information and specific characteristics such as formation thickness, groundwater table or hydraulic characteristics of the fault zones. Especially in a tectonically complex area such as the test area where groundwater observation wells are rare, abandoned or missing, several parameters needed for the vulnerability assessment have to be assessed or transferred from regions with a similar lithology.

Also the fact that the PI-method was developed originally for European conditions should be taken into account while examining the mapping results. The general assumption that forest cover favours infiltration, whereas agricultural areas are more likely to produce surface runoff (Goldscheider, 2002) can not be applied in the test area, due to the different characteristics of the forest and soil characteristics under (semi-)arid conditions. The recharge range of the PI-method does not mirror the climatic situation of (semi-) arid Mediterranean climate zones and thus does not differentiate recharge amounts below 100 mm/a. For a vulnerability method application in dry climates the considered recharge amounts should be smaller and contain finer gradings.

Concerning the slope classification in  $< 3.5\%$ ,  $> 3.5\%$  and  $< 27\%$  and  $> 27\%$  of the PI-method it should be considered that in the test area at the steep valley slopes terracing practice for olive trees is commonly used to reduce surface runoff and soil erosion. In the PI method steep slopes are given low ratings. This assumption is based on the fact that surface contaminants deposited on sites having steep slopes will tend to runoff rather than stand long enough to infiltrate (Aller et al., 1987). Terracing, of course, dramatically alters slope, converting a formerly steep slope to a nearly flat area. Most topographic maps and accordingly DEMs based on this topographic maps rarely depict terracing (Merchant, 1994). Though the rating of the slope angle ought to be adjusted upwards to account for terracing.



## 8 GROUNDWATER HAZARDS IN THE TEST AREA

### 8.1 Introduction

The hazards in the test area were evaluated at a scale of 1:50,000 using the guidelines of the COST Action 620 (De Ketelaere et al., 2004) based on fieldwork (Storz, 2004) and the thematic layers derived from classified remote sensing data (Werz et al., 2005). The two main objectives can be summarised to

- test the applicability of a hazard mapping approach developed in Europe with European standards in a less-developed country like Jordan with different standards in environmental policy
- and to investigate the applicability of remote sensing imagery for hazard mapping.

The main hazard sources to be expected in the test area are shown in Fig. 8.1. Nitrate concentrations of more than 100 mg/l in many highly cultivated areas and more than 200 mg/l in some urban zones in Jordan indicate that groundwater is already polluted to an alarming extent (Salameh, 1996). In the test area in many spring samples high concentrations of microbiological contaminants exist (Ta'any 1992) and most of the wells in the test area were abandoned and sealed, due to high concentrations of nitrates. Besides non-point source pollution of the agricultural areas many potential point source pollutions such as leaking septic tanks, illegal waste dump, or chicken farms exist.

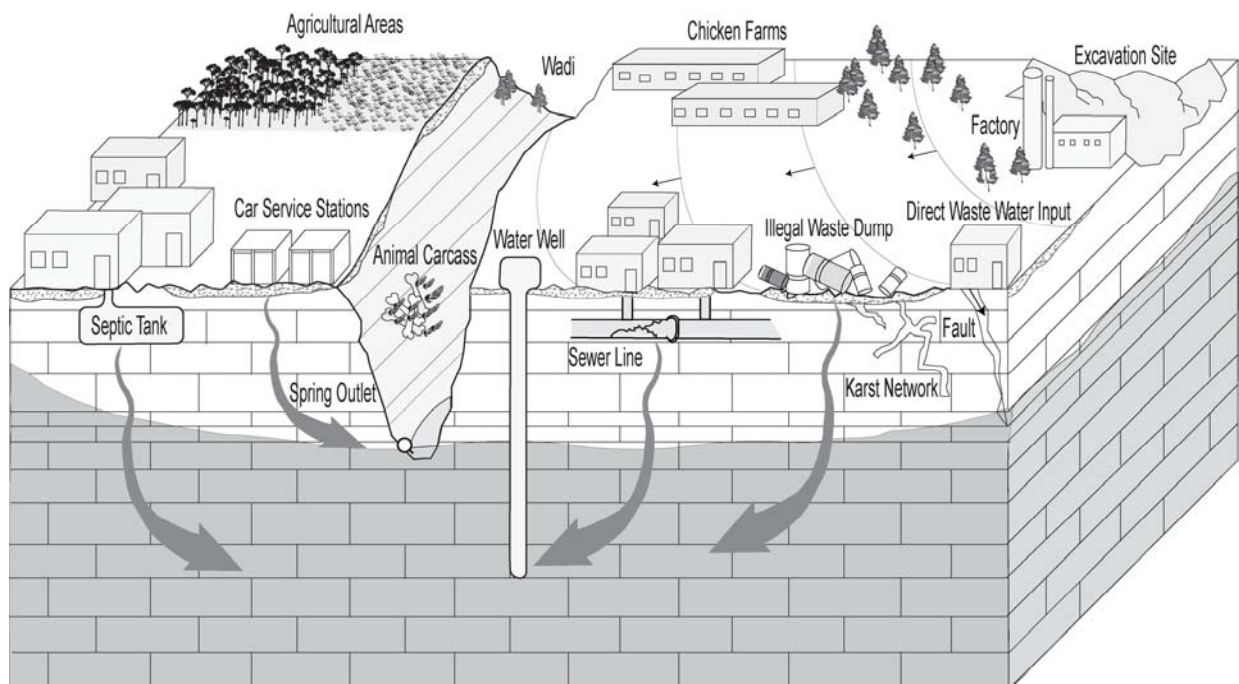


Fig. 8.1: Schematic illustration of the main hazards in the test area (Werz & Hötzl., 2005).

In the test area the prevalent industrial businesses are rather small firms and garages such as car service stations, car washing stations and locksmitheries, operating in small garages and represent most of the point hazards. In general, the garages possess a standardised size of 7 m x 4 m. Unpaved floors allow the infiltration of waste water or waste oil. The spatial distribution of the garages is hard to determine. In the village of Salt, the industrial areas have no connection to the waste water treatment plant (Storz, 2004).

## 8.2 Compilation of the hazard map

For the unclassified hazard map location, size and extent of the following hazards were derived by using thematic layers gained by the interpretation of the orthophotos and the LANDSAT ETM<sup>+</sup> image:

- agricultural areas (crops, orchards),
- excavation sites,
- street network,
- urbanisation,
- waste water treatment plants,
- Jordan cement factory,
- animal barn (chicken farms)
- and detached houses (Werz & Hötzl, 2005).

The hazards that could not be mapped using remote sensing data were mapped by fieldwork using a GPS. In the test area, in addition to the hazard types urbanisation, detached houses, agricultural areas and streets, 351 individual hazards were identified.

Due to the special situation and the character of the test area in Jordan, the approach of De Ketelaere et al. (2004) had to be modified in various aspects of data evaluation, estimation and representation (Werz et al., 2006). Not all detected hazard types that were mapped in the test area were considered by the COST ACTION 620 hazard list that was initially developed according to European standards. Therefore, the list had to be adjusted accordingly. Additional hazard types include: car brush stations, car service stations, locksmitheries, car wash stations, building business and pumping stations (Werz et al., 2006).

### 8.2.1 COST ACTION 620 Weighting value

For the weighting value (H) the toxicity and the properties of the hazards regarding mobility and solubility were taken into account, and a relative, non-measurable value defined by the COST Action 620 hazard inventory list (De Ketelaere et al., 2004) was assigned. The weighting value ranges between 0, indicating non harmful substances at all, and 100, indicating places with very

harmful substances such as nuclear waste sites. For handling the wide range of different degrees of harmfulness the scale should be interpreted in a logarithmic scale rather than linear.

Fig. 8.2 gives an overview of the hazard types, the assigned weighting value and their number of occurrence in the test area. A low weighting factor is assigned to hazards with a low degree of harmfulness, e.g. greenhouses (weighting factor = 20), high weighting values are assigned to hazards that have a high degree of harmfulness, e.g. urban areas without sewer system (weighting factor = 70).

Fig. 8.2: Hazard types, weighting value (H) and number of occurrence of the hazard types in the test area; n.n. indicates that there are no numbers for the hazards are existing.

Hazard type	Weighting value (H)	Number	Hazard type	Weighting value	Number
Animal Barn	30	20	Hospital	35	2
Building Business	40	4	Intensive Agricultural Area	30	4
Car Brush & Car Service Station	45	99	Locksmithery	35	50
Car Washing Station	40	14	Manure Heap	45	26
Chemical Industry	65	5	Military Area	35	7
Detached Houses	45	n.n.	Parking Space	35	6
Excavation Site	25	6	Pumping Station	65	1
Factory Farm	30	35	Sport Area	25	2
Filling Station	60	11	Stock Pile of raw material	60	1
Food Production	45	2	Streets	40	n.n.
Garbage Dump / Municipal Waste	40/35	9	Transformer Station	30	1
Graveyard	25	27	Urban Area With/without sewer system	35/70	n.n.
Greenhouse	20	11	Waste Water Treatment Plant	35	2

For streets, additional considerations according to pollution dispersal had to be made. Harmful substances, which are caused by traffic, do not only affect the ground directly under streets. The generated contaminants are partly spread onto adjacent roadsides, condensed in the surrounding areas or washed out of the unsecured roads onto the ground beyond the roads. Besides that, the influence on the groundwater decreases with longer distance to the traffic routes and with greater depth (Golwer, 1995). To represent this additional sphere of influence, a buffer zone of ten meters at each side was placed around the streets.

### 8.2.2 COST ACTION 620 Ranking ( $Q_N$ ) and Reduction factor( $R_f$ )

For ranking hazards of the same hazard type and thus weighting values that differs from the average degree of harmfulness, the weighting value can be raised or reduced by the ranking factor ( $Q_N$ ). The ranking factor ( $Q_N$ ) is adjusted by many parameters, which are for example the size, the presence of waste oil or scrap, manure, visible leakage of polluting liquids or the mode of funeral. In order to maintain a balance with the average weighting values, the ranking factor should change the weighting values only slightly and therefore range between 0.8 and 1.2 (De Ketelaere et al., 2004).

The proposed application of the ranking factor ( $Q_N$ ) for the urbanisation was impracticable in this case. The hazard inventory list distinguishes between two urbanisation weighting values: 35 for urbanisation possessing leaking sewer pipes and sewer systems and 70 for urbanisation without sewer system. These values represent a wide range that cannot be covered using the ranking factor. In the test area it was impossible to get exact information about the number of houses that are connected to the sewer system and that are using septic tanks. The sole information that was available in the test area was a percentage value per village of the unconnected houses (Storz, 2004). Therefore the ratio of connected houses in respect to all houses in total was used to adjust the hazard weighting value between 35 and 70 (Tab. 8.1). Consequently, five different weighting values were assigned to the urbanisation areas. No further ranking factor was applied subsequently.

Tab. 8.1: Evaluated hazard index of the urbanisation in relation to the percentage of connected houses to the sewer system (modified after Storz, 2004).

Location of villages	Connected houses [in %]	Hazard index
Mahis	90 - 100	35
Fuheis	90	38
Suweilih	60	49
Salt	50	53
Houses outside villages	0	70

The reduction factor ( $R_f$ ) is another possibility to modify the weighting values.  $R_f$  is used, if information about status, maintenance, age, security measurements etc. exist, including the probability that a hazard release might take place (De Ketelaere et al., 2004). For the estimation of this parameter many factors have to be evaluated and all circumstances, which can reduce the degree of harmfulness, have to be considered. The reduction factor ( $R_f$ ) range theoretically from 0 up to 1 (De Ketelaere et al. (2004). This factor should be understood as negative exponential term. If no information is known, then  $R_f = 1$ . If there is useful information concerning the reduction of the likelihood that a contamination event occurs,  $R_f$  values  $< 1$  up to 0 can be used.

In the test area it was impossible to get the necessary information about the protective devices, management of companies or installation of filter systems and own waste water treatment plants. Only in two cases a reduction process was performed (Storz, 2004). One car service station that is equipped with a safety gully for the waste water and a filling station that provides a safety channel for the waste water were each assigned a  $R_f = 0.8$ . To all other hazards a reduction



factor of 1 was assigned as appointed by De Ketelaere et al. (2004), indicating that there are no reasons known to reduce the likelihood of an impact to the groundwater.

## **8.3 Results**

### **8.3.1 Unclassified hazard map**

In the test area twenty-seven different hazard types were evaluated. The dominating hazard types in the test area are small industries, agricultural and municipal hazard point source contaminations that are caused for example by manure heaps and filling stations or oil pumps (Werz & Hötzl, 2005). Industrial hazards form the majority in the test area, followed by the agricultural hazards and the municipal hazards. Fig. 8.4 gives an overview of the distribution of the amounts of the single hazard types within the three hazards categories industrial, municipal, agricultural. However, it has to be taken into account that the highest area percentage of hazards in the test area exists within the agricultural and urban polygonal hazards.

The unclassified hazard map displays the existing hazard types, their location and size (Fig. 8.3) by the use of special graphic symbols or signatures delineated by De Ketelaere et al. (2004). The dominating types are businesses of small industry.

The test area shows big differences in the development and grade of urbanisation and can be subdivided into a highly urbanised northern part with a well developed infrastructure, a settlement of certain industrial plants and a variety of agricultural activities and into an almost deserted southern part which is dominated by agricultural land use with no infrastructural facilities. On this account, the distribution of hazards, their size as well as the occurrence of different types vary strongly and mirror the differences between the northern and southern part.

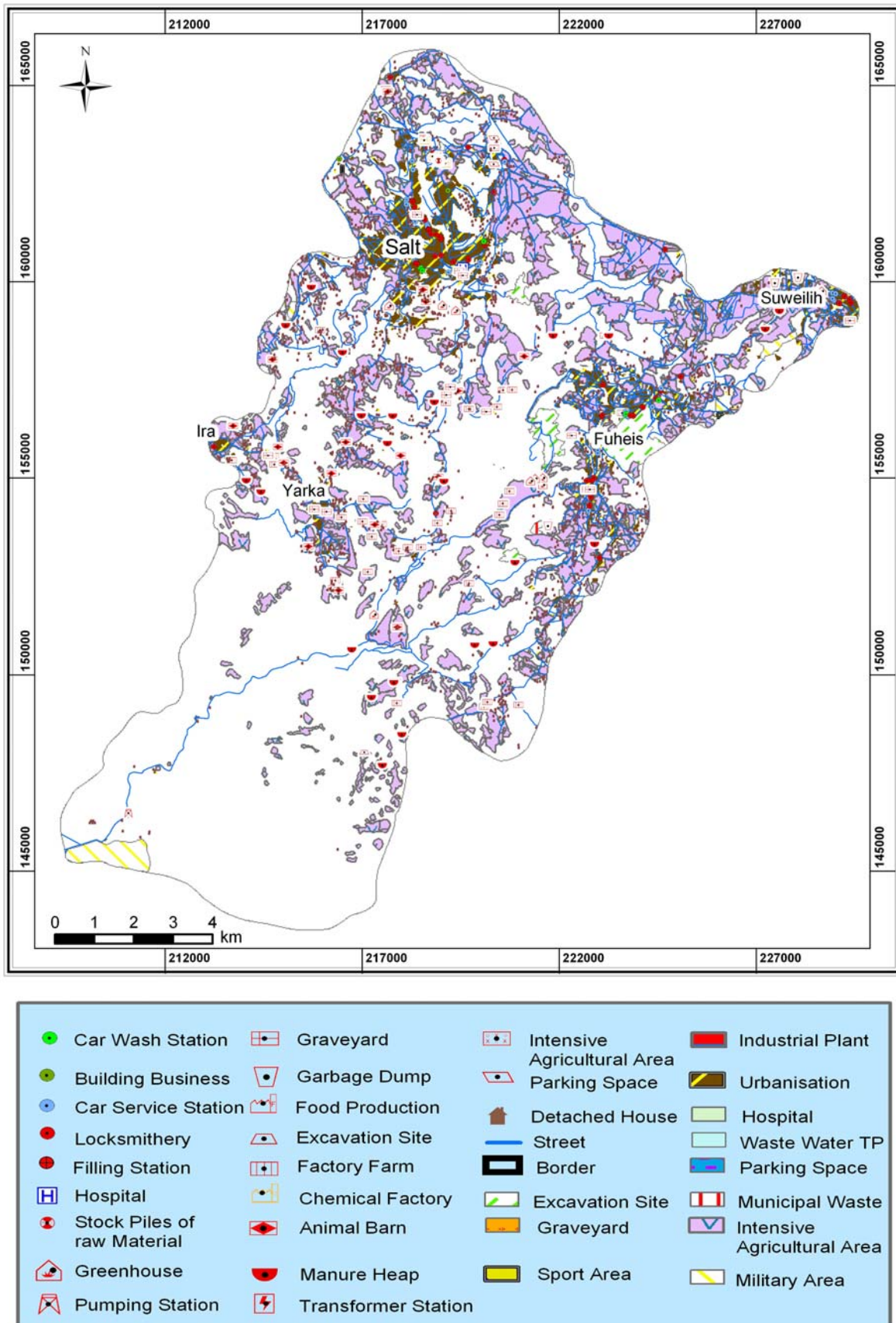


Fig. 8.3: Unclassified hazard map of the test area (modified after Storz, 2004).

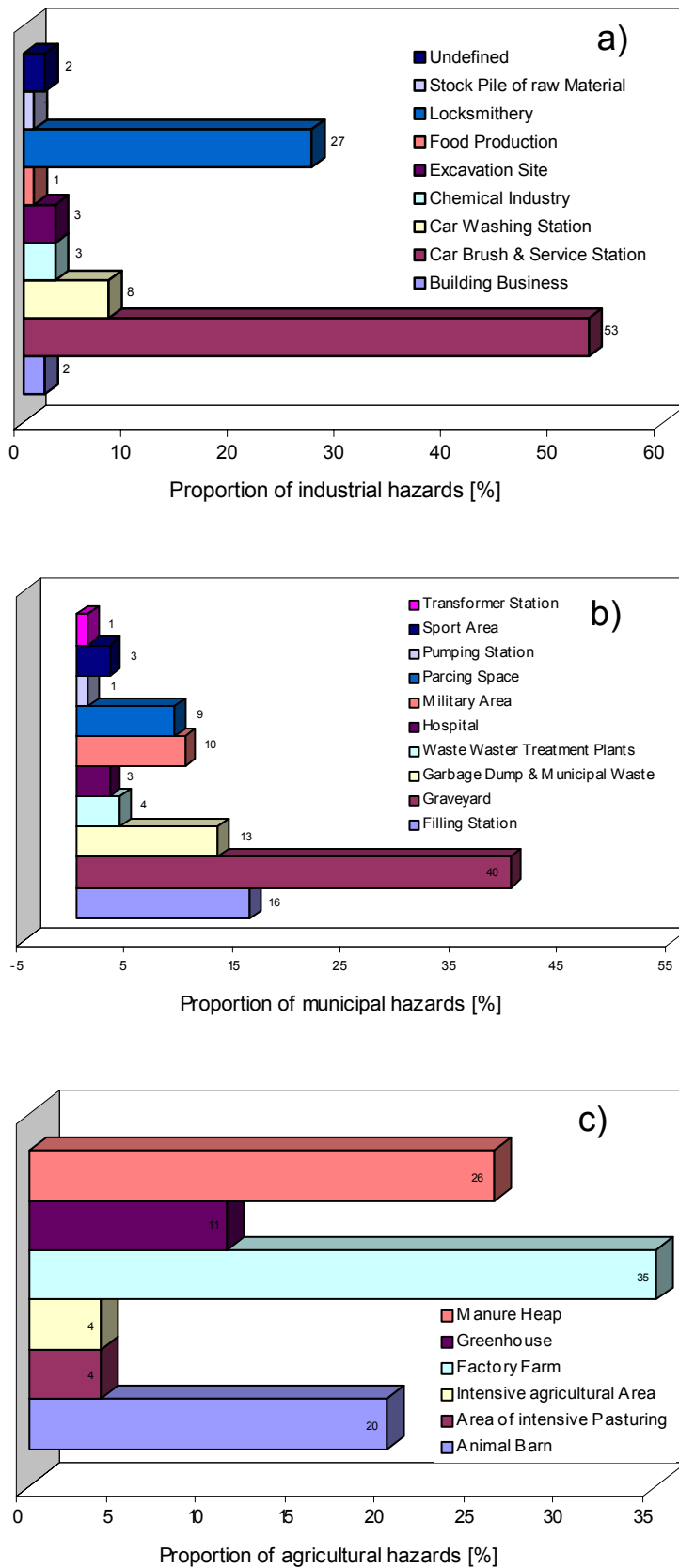


Fig. 8.4: Occurrence of a) industrial hazards, b) municipal hazards, c) agricultural hazards.

## Classified hazard map

The classified hazard map shows the hazard index (HI) that was calculated from the weighting value, ranking factor and reduction factor after the following formula (Fig. 8.5):

$$HI = H \cdot Q_N \cdot R_f \quad (8.1)$$

HI:	Hazard Index
H:	Weighting Factor
$Q_N$ :	Ranking Factor
$R_f$ :	Reduction Factor

For the classified hazard map the vector map of unclassified hazards was converted into raster data with a chosen cell size of 25 m x 25 m. The chosen raster cell size is big enough that individual point hazards can still be identified on the 1:50,000 map and small enough that point hazards are not displayed on a too large area.

The hazard index (HI) represents the degree of harmfulness for any hazard to the groundwater. The hazard index values are classified in five classes and are expressed as hazard level ranging from *no* or *very low* to *very high*. The highest hazard index exists in the urban areas of the villages and arises from the calculation and addition of two or more hazard types within a chosen raster cell size of 225 m<sup>2</sup> (25 m x 25 m). An example for very high hazard index in the test area is the existence of a filling station with unpaved floor over an urbanised area within one raster cell. Significant hazards are situated in the villages. As indicated by the blue colour (Tab. 8.2), to the majority of the test area no or a very low hazard level is assigned. Over 80 % percent of the area are classified to the lowest hazard index class showing no or accordingly a very low hazard level. Less than 1 % shows a high to very high hazard level. This is also due to the fact that the major parts in the S are neither populated nor used for agricultural purposes.

It is obvious that, due to the classification system, within the blue area the existence of very low hazardous substances cannot be distinguished from areas where no hazards at all are existing. Coexistent hazards within one cell which can coexist in reality, such as a locksmithery over urbanised area, are added or ranked up, hazards which exclude each other, such as a factory farm over an intensive agricultural area, were valued with the respectively highest weighting value. The Cost Action 620 does not specify how to calculate two or more superimposed hazard types within one raster cell. According to the Cost Action 620 the weighting scale should be considered as a kind of logarithmic to take into account the wide range of different hazard types. By addition of the weighting values of superimposed hazards such as a leaking oil pump over a leaking sewage system in the underground, values would occur that exceed the highest possible weighting value of 100 (assigned to nuclear waste sites). This means that this areas would be overrated compared to the others. A modified calculation method is suggested by Junker (2004), that divides the original weighting values by 10, to reduce the weighting scale from 10 to 100 to 1 to 10, and then from the logarithm to the basis two:

$$HI_{mod} = 2^{HI/10} \quad (8.2)$$

The application of this formula would lead to possible values from 1 to 1024 expressing more clearly the range of hazards.

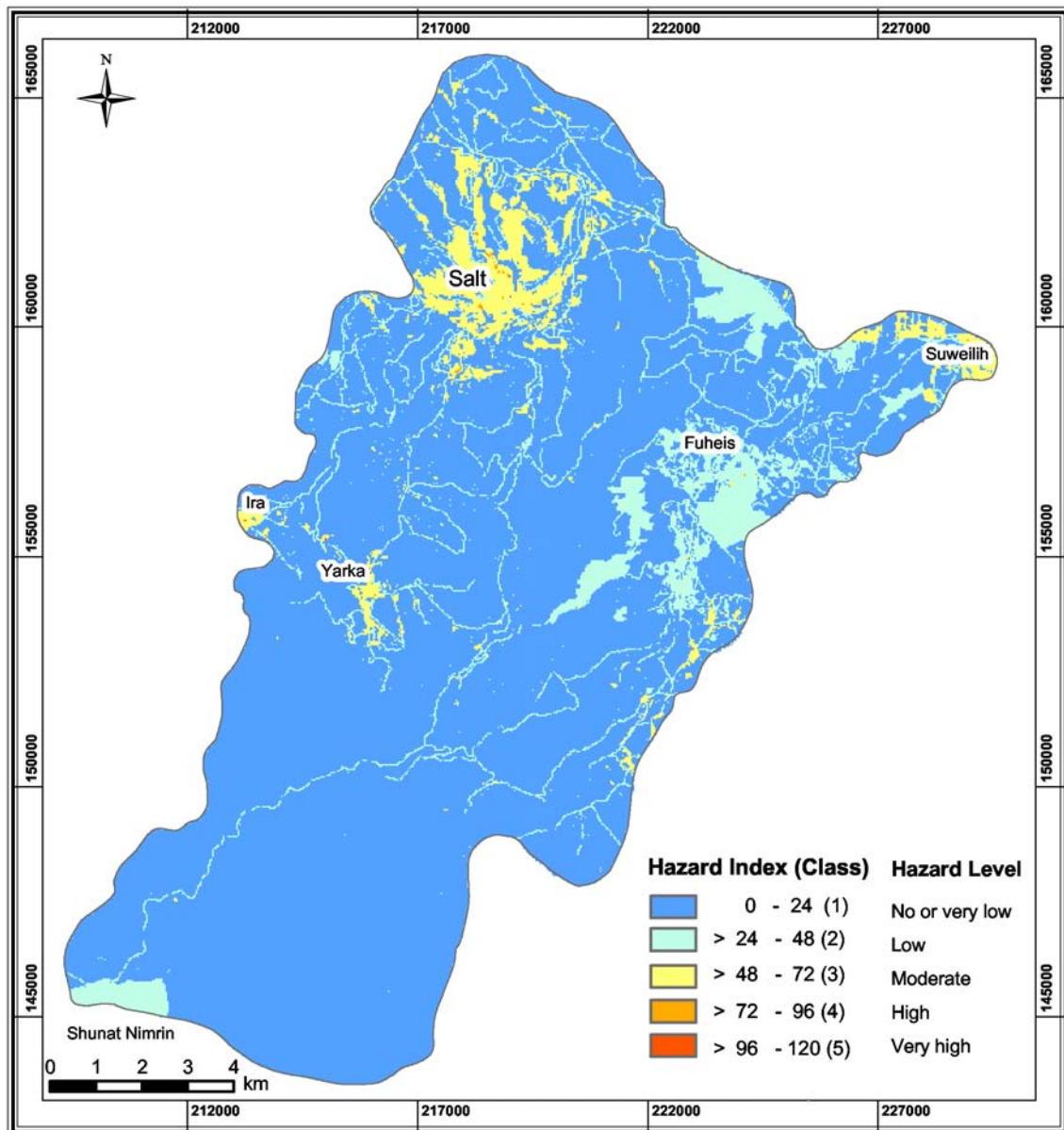


Fig. 8.5: Classified Hazard map of the test area (modified after Storz, 2004).

Tab. 8.2: Distribution and proportion of the hazard index (HI) classes in the test area.

Hazard Index	Hazard Index Class	Hazard Level	Colour	Area Percent (%)
0 - 24	1	No or very low	Blue	82.432
25 - 48	2	Low	Green	12.574
49 - 72	3	Moderate	Yellow	4.939
73 - 96	4	High	Orange	0.042
97 - 120	5	Very high	Red	0.013

## 8.4 Error discussion & conclusions

Caused by missing environmental awareness areas along the streets, the wadis and urban areas are often polluted with domestic waste, agricultural garbage such as chicken carcasses, and building debris. Waste oil is often not disposed in a special way, but simply discharged to the ground. Therefore, in many cases garbage could not be mapped as singular hazards as suggested by the De Ketelaere et al. (2004) and compared to the European standard, therefore the weighting value of urbanisation seems to be too low in general.

Unlike in Germany, in Jordan no regulations for the handling of substances hazardous to water and registers with the relevant businesses exist (“Verordnungen zum Umgang mit wassergefährdenden Stoffen und über Fachbetriebe”). In Germany within given time periods, name and address of all firms as well as the types and amount of substances hazardous to groundwater are recorded and updated. The Trade Supervisory Office in Germany also provides databases with all office master data (“Betriebs-Stammdaten”), furthermore at the environmental agencies there is a land register existing indicating all known contaminated sites or abandoned hazardous sites.

In Jordan there is lack of information in respect of the potential groundwater hazards. Lists of number, type, location, and the size of industrial firms were not existing or available from public offices or ministries. The fact that data about the state and age of plants is missing can be considered as normal in areas comparable with the test area in Jordan. Precise and reliable information concerning infrastructural installations, such as waste water, sewer systems or utilisation ratio of streets, or the amount and nature of fertilizers or number of livestock in agriculture, is often difficult to obtain (Storz, 2004).

The resolution and data display of the unclassified hazard map is problematic in places where several hazards coexists within neighbouring raster cells. Storz (2004) applied partly transparency to the point hazard symbols and added a small black point to indicate the “exact” location of the hazard that is hidden under the sizeable symbols. Within the chosen raster scale of 25 x 25 m, one was often confronted with the case that within the ground resolution area of the cell two or more small point hazards exist that both had to be added or the value of the more dangerous hazard type was taken.

The test area is considered as a weakly developed area of Jordan, the major difficulty is based on the lack of information as well as the problems in the data evaluation. Besides the inspection of the area, interviewing inhabitants and employees of companies and municipalities, the analysis of orthophotos and satellite images was an important tool for data evaluation (Werz et al., 2006). In general, the agriculturally dominated sections of the test area are affected only by a small or no degree of harmfulness. Significant hazards are only located in the industrialized areas of Salt, Fuheis, Mahis and Suweilih. In the test area the prevalent industrial companies are rather small firms and garages such as car service stations.



Fig. 8.6: Leaking oil pump in the test area causing a significant point hazard.

In respect to potential groundwater contamination, these facilities are problematic because of their unpaved floors, in which waste oil can infiltrate. Leaking oil pumps are also a common point hazard (Fig. 8.6). One of the prevalent problems that occurred following the hazard mapping arose from the lack of information concerning the connection of settlements with a communal waste water system, therefore the weighting values were adjusted in relation to the percentage of connected houses.

In the test area there is a call for action, demanding to improve the environmental situation based on the hazard map, including for example the abandonment of the illegal waste dump or the connecting of all households to waste water treatment plants.

## 8.5 Applicability of the COST Action 620 in the test area

The main aim of the hazard inventory of the COST Action 620 is to cover all various hazards that are considered relevant for groundwater and to allow, through a reasonable subdivision, the mapping, evaluation and assessment of the hazards in an economically feasible and practical manner (De Ketelaere et al., 2004).

Since the COST Action 620 hazard and risk mapping approach was developed from scientists of several European countries it cannot take into account any country-specific characteristics. Therefore the hazard mapping instructions are rather general and unspecific. Although several hazards could be located using the remote sensing imagery, the mapping of the individual hazards required intensive fieldwork. In the test area with a size of nearly 200 km<sup>2</sup> it is impossible to map all hazard types within a realistic time frame. One main point is that even a very detailed elaboration just represents the current situation and the type of hazards or the corresponding degree of harmfulness may partly change in the future due to infrastructural or industrial development. Such an up-to-date inventory can then be used for an hazard map showing the ad hoc status. However, an updated inventory of all hazardous sites and an assessment of the

hazards posed from existing human activities is necessary for all national environmental objectives for surface water, groundwater and ecosystems and groundwater protection schemes.

Due to the intension of the COST Action 620 that the hazard maps should be clear and easy to understand, and no “overclassification” in too many hazard classes occurs, the COST Action 620 hazard methodology and its different hazard types cannot encompass every existing single hazard type. Therefore the missing hazard types had to be adopted to the COST Action 620 list such as car brush stations, car service stations, locksmitheries, car wash stations, building business and pumping stations.

After the weighting, ranking and reduction procedure several mapped hazards such as excavations sites, greenhouses or graveyards were assigned to a hazard index lower 24 and therefore belong to the lowest hazard class. In the classified hazard map these hazards cannot be distinguished from the areas where no hazards exist since all areas with a hazard index between 0 and 24 are displayed in blue. In industrial zones with a high density of different hazards, the different hazard type symbols’ overlay reduce the recognisability and limit the use of the unclassified hazard map. In this case it would be better to assign a polygonal hazard symbol to the industrial areas and display only special hazards with a significant hazard index such as fuel stations with an individual point symbol. Of course, also more detailed maps in a larger scale for areas with hazard concentration can be generated.

After mapping all potential hazard types in a large and time consuming undertaking, it can not be assured that the mapped and classified hazards are actually relevant for the groundwater, since mostly insufficient information about the state of the hazard types was available. The hazard map of the test area shows the risk of groundwater pollution of each hazard in relation. The hazard weighting value, ranking and reduction factor represents a more or less arbitrarily ascertained value within a relative assessment scheme that is not directly measurable or allows to compare the different hazard types among each other. The ranking factor is difficult to define and to give meaningful reasons for the chosen value between the 0.8 and 1.2. Often the use of the ranking factor proved to have no influence on the final hazard index value.

The finally assessed hazard indices mirror to a several degree the subjectivity of the author, based in an ideal case to his profound scientific experience, indicating a simplified classification scheme of the harmfulness of each hazard based on many assumptions and interpretations, due to fact that often important data are missing.

However, even if there are some constraints for the applicability of the COST Action 620 hazard guidelines in the test area, from a groundwater protection point and groundwater management point of view, it is very important to have precise information where potential hazard are located, and where in an area a hazardous event may occur. Even if some hazard types had to be added to the COST Action 620 hazard inventory list to represent the situation in the test area, it was relatively easy to assign the existing individual hazards to the associated hazard type of the inventory list. Due to the limited amount of hazard types the resulting unclassified hazard map is quite simple and easy to read and understand, compared to hazard inventories from some environmental agencies that provide lists in which several thousands of specific branches of different hazard activities are listed. This simplicity of the hazard maps is indispensable if the maps shall serve as efficient tool in planning and decision-making processes for planners,



consultants and stakeholders for both national and local entities as an integral component of environmental impact studies (De Ketelaere et al., 2004) . Even though there are few industrial activities and a very low hazard level prevails in the test area, there are some “hot spot” of contamination existing that produce, combined with the groundwater vulnerability at this places a high to very high risk intensity for the groundwater. Therefore, the hazard map in combination with the groundwater vulnerability map is very useful for carrying out a risk intensity assessment to be aware of and reduce existing hazards and to avoid further contamination of the groundwater.



## 9 GROUNDWATER RISK INTENSITY IN THE TEST AREA

### 9.1 Introduction

Following the guidelines of the COST Action 620 (De Ketelaere et al., 2004), the hazard map was combined in a next step with the groundwater vulnerability map to produce a risk intensity map. The risk intensity map reflects the probability of groundwater to be actually contaminated by human activities, showing that the highest risk of contamination exists where a dangerous hazard is located in zones which are characterized by highly vulnerable aquifers. The groundwater vulnerability and hazard map shows clearly the vulnerable areas and the potential “hot spots” of contamination in the test area and supplies information for urban management, decisions and planning aspects for a variety of applications.

The risk intensity map is based on the risk intensity index (RII) that is calculated by simply multiplying the reciprocal value of the hazard indices (HI) of the classified hazard map with the PI-factor ( $\pi$ ) of the groundwater vulnerability using formula (9.1) provided by Hötzl et al. (2004):

$$RII = \frac{1}{HI} \cdot \Pi \quad (9.1)$$

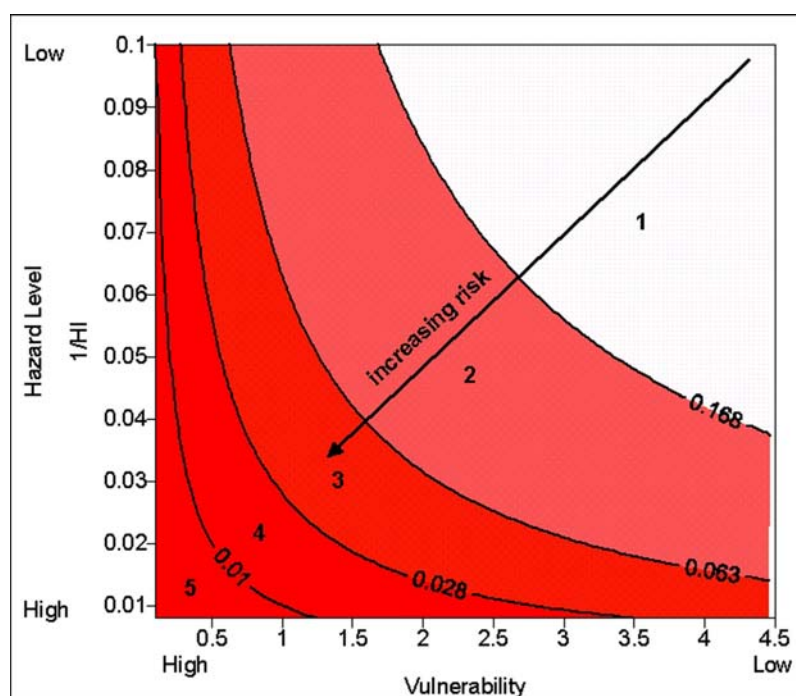


Fig. 9.1: Diagram of risk intensity index calculated after equation (9.1). Five classes were assigned to build risk classes (after Hötzl et al., 2004).

The reciprocal value of the hazard index is used, due to the fact that the hazard index and the PI-factor are tending in the opposite direction with higher risk (Hötzl et al., 2004).

Fig. 9.1 displays the diagram of the risk intensity index and the classification of the levels, showing an increasing risk depending on the vulnerability factors and the hazard levels.

The application of the formula (9.1) has the disadvantage that the inputs are the predefined classes of the vulnerability and risk intensity map and not the single calculated hazard indices that would allow for infinitely variable risk values.

## 9.2 Results

Even if the major parts of the test area are assigned to a very low risk intensity, in the villages and their surroundings differences in risk intensity distributions showing moderate to high risks are present. The map clearly shows that in the urban areas of Salt, Fuheis, Yarka and Ira the highest risk intensity occurs, since concentrations of different hazard types, assigned to a high hazard index, are located over karstified limestone with patchy soil cover (low protective cover effectiveness) showing a high vulnerability (Werz & Hötzl, 2005).

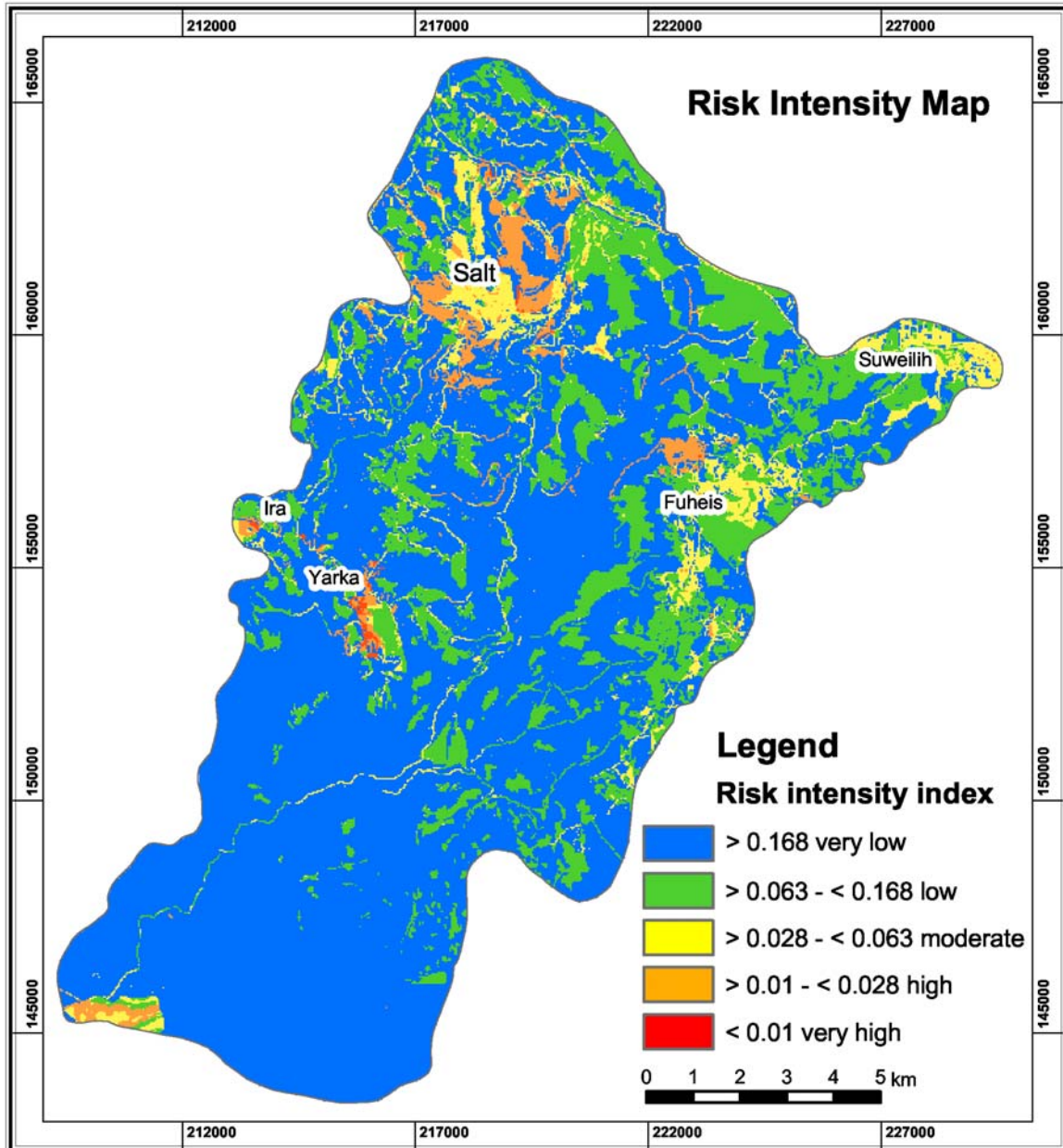


Fig. 9.2: Risk intensity map of the test area (Werz & Hötzl, 2005).

At some places where the hazard map shows no or only a slight variations of the hazard index the variations in the risk intensity level are mainly due to the vulnerability that varies significantly in some parts. Thus, N of Fuheis, where the hazard index is low but the vulnerability is partly

extreme, a high risk intensity index is assigned to this locations. The low risk intensity areas are dominated by agricultural areas that were delineated in the unclassified hazard map but were not anymore visible in the classified hazard map since they were classified in the no or very low hazard index class. But, in the risk intensity map they are visible again due to the fact that the areas are characterised by a moderate vulnerability resulting in a low hazard index and therefore can be distinguished from the background showing a very low risk intensity index.

Very high risk intensity exists in Yarka, Ira and its surroundings where animal barns, urban areas without connection to waste water systems, graveyards, factory farms and car service stations are located directly over the highly to very highly karstified Wadi Sir aquifer (A7) (Fig. 9.2). Fig. 9.1 point out that the calculated risk intensity index can be very high if the vulnerability is high even if the hazard index is low. The risk intensity map shows that the problematic areas with relatively high risk levels are located in the middle and northern part, where the risk areas are concentrated in the urban and agricultural areas.

Regarding the results of the risk intensity map one has to keep in mind that unlike to the groundwater vulnerability map that is quasi valid timelessly due to the fixed natural hydrogeological and hydrological setting, the risk intensity map can change if the classified hazard map changes, due to modification in the hazards that can be potentially released.

### 9.3 Use of the risk intensity map for groundwater management

The results of the risk intensity map indicate problem areas where effort should be made to reduce existing hazards and to prevent or minimize the probability of a contamination event and its consequences by implementing special actions. Thus, the mapping results can help decision makers to understand the interactions between surface water, groundwater, and the environmental system. In the test area implemented actions should include for instance land use practices directing developments towards lower contamination release, connection of detached houses to the sewer system, or at least the furnishing of all septic tanks with suitable security measurements such as sealing concrete walls. Since outcropping karstified limestones are dominating in the test site, direct waste deposition and wastewater injection in the karst pipes or widened joints of the limestones, or the disposal of animal carcass in wadi beds or karst forms should be definitively prevented.

Groundwater monitoring networks should be implemented including the analysis of groundwater samples (including also samples from the sealed wells) for microbiological parameters and identify the sources of the coliform bacteria (septic tanks, leaking sewer systems, injection of waste water, animal barns). Expanded groundwater monitoring for nonpoint-source pollution such as pesticides, herbicides and phosphates should be done. Since microbiological contamination and water quality are also dependant on time that water transporting potential hazards needs to reach the groundwater table, the transit time of the water in the unsaturated zone of the karst aquifers should be investigated in a next step, for instance, based on tracer test results, isotope analysis or transport model results. To increase the awareness for the Jordanian people how their activities can pose a threat to groundwater information should be distributed on a local level.

Daly et al. (2004) pointed out, that for further application, and particularly with regard to risk management, a complex risk assessment including not only risk intensity but additional risk *sensitivity* assessment is necessary. The risk sensitivity of an area depicts “the sensitivity of the groundwater against a certain impact under consideration of the economical and ecological value of the resource”, including the damage that results in the reduction in value of the target. The sensitivity assessment includes flow conditions (flow quantity, flow velocity, flow direction) and important sensitivity parameters such as the attenuation rate, the biodegradation or the chemical milieu of the water in the aquifer itself (Zwahlen et al., 2004). The inclusion of dynamic processes can be achieved by the use of transport models. Scholles (1997) emphasised that uncertainties that are typically associated with calculations of the economical and ecological value of groundwater allow only a certain classification of the groundwater body, according to more or less qualitative subdivision on the basis of recent or further utilisation of the groundwater that is taken as basis for the risk assessment. However, due to the severe freshwater shortage in Jordan, in general all existing freshwater resources, also the small freshwater reservoir in the test area, are important and economical and ecological valuable.

## 10 USEFULNESS OF REMOTE SENSING DATA FOR GROUNDWATER RISK INTENSITY MAPPING

### 10.1 Overview

To enable a useful, effective and common implementation of groundwater vulnerability, hazard and risk intensity maps it should be possible to generate them relatively fast, cheap and up-to-date, therefore the use of remote sensing imagery can be a very helpful tool for parts of the mapping process. Within this study it was tested how many information, that can be used for groundwater vulnerability and hazard mapping, can be derived from a LANDSAT ETM<sup>+</sup> image and orthophotos applying different data extraction.

Regarding groundwater vulnerability, remote sensing data can play mainly the role of allocation or supplementation of missing topographic map information and, if possible, of lithological or surface structural features (fractures, faults, karst). For the hazard assessment remote sensing data proved to be very useful for the unclassified hazard map indicating location, size, extension of hazards such as agricultural areas (crops, orchards), excavation sites, street network, urbanisation, waste water treatment plants, animal barns (chicken farms) and detached houses.

Tab. 10.1: Thematic layers used for the groundwater vulnerability (dark grey shaded) and hazard assessment (light grey shaded) based on information from remote sensing imagery.

Thematic layer	Data source	Data extraction	Usage
Crops, orchards	Orthophotos (1:30,000)	Digitising (ArcGIS)	Topsoil layer, P-factor
Degree of karstification	Orthophotos (1:10,000)	Digitising (Geomatics)	Karst layer, P-factor
Urban areas (paved surfaces)	LANDSAT ETM <sup>+</sup>	Supervised classification	Dominant Flow Process, I-factor
Crops, orchards, forest	Orthophotos (1: 30,000)	Digitising (ArcGIS)	Unclassified hazard map
Cement factory	Orthophotos (1:30,000) LANDSAT ETM <sup>+</sup>	Digitising (ArcGIS) Visual Interpretation	Unclassified hazard map
Chicken farms	Orthophotos (1:30,000) LANDSAT ETM <sup>+</sup>	Digitising (ArcGIS) Visual Interpretation	Unclassified hazard map
Detached houses	Orthophotos (30,000)	Digitising (ArcGIS)	Unclassified hazard map
Excavation sites	Orthophotos (1:30,000) LANDSAT ETM <sup>+</sup>	Digitising (ArcGIS) Visual Interpretation	Unclassified hazard map
Street network	Orthophotos (30,000)	Digitising (ArcGIS)	Unclassified hazard map
Urbanisation	Orthophotos (1:30,000) LANDSAT ETM <sup>+</sup>	Digitising (ArcGIS) Supervised classification	Unclassified hazard map
Waste water treatment plant	Orthophotos (1:30,000) LANDSAT ETM <sup>+</sup>	Digitising (ArcGIS) Visual Interpretation	Unclassified hazard map

In some cases the type of industrial firm or type of hazard could be classified directly on the images. An overview of the thematic layers used for the vulnerability and hazards assessment derived from the LANDSAT ETM<sup>+</sup> image and the orthophotos is shown in Tab. 10.1. The main difference between geological and topographic maps compared to satellite imagery classification results is that land cover and land use information derived from this images gives transient up-to-date information which is partly seasonal variable. Land cover and land use information is valuable basic information for the calculation of the infiltration conditions and dominant flow process, or the amount of fertilisers used.

## 10.2 Lessons learned

### Remote sensing imagery

The scope of the multilateral GIJP project, within which this study was performed, can be considered as typical for the situation in many developing countries. The problems to be handled concerning the groundwater vulnerability and protection of the freshwater resources affect mostly regional areas with sparse or insufficient database. The combination of processed remote sensing data, GPS information, field survey and collateral data for an integrated use in a GIS has been proved to be successful for the generation of a risk intensity map for the test area in Jordan.

However, the remote sensing imagery that was made available for this study was to some extent suboptimal. The analogue black & white aerial photographs were thirteen years old. The analogues photographs had a very bad quality and were manipulated to erase the royal houses and military installations. Current digital aerial photographs were just made available for a section of the test area and not for a whole area coverage. Since sovereignty over the airspace is controlled on a regional level, normally it is impossible to buy aerial photographs elsewhere than the in the respective countries. Even though support was provided by the Amman University and other project partners in Jordan the buying of the aerial photographs proved to be very difficult. The process of searching and ordering aerial photographs was very time consuming due to the security measurements and political constrains that exist in Jordan. During the second stay in Jordan only the black-and white aerial photographs could have been made available. During the third stay it was allowed to buy digital aerial photographs, limited to section of the test area.

The speed at which the digital image processing of the LANDSAT ETM<sup>+</sup> could produce thematic maps was much faster than the processing of the panchromatic orthophotos in GIS by on-screen digitising of different thematic layers. It was very time consuming to digitise the small crops and orchards fields of the test area. Furthermore it is in general more expensive to acquire aerial photographs covering the complete test area for mapping purposes since more images and subsequently more GPS points and fieldwork is needed. One main advantage of the LANDSAT data is the worldwide availability of most recent ETM<sup>+</sup> imagery, whereas aerial photographs are often limited in actuality and coverage or in some countries are not made available, due to political or security reasons. For the last years relatively recent satellite images (up to 2002) such as LANDSAT or ASTER imagery can be downloaded for free for example from the homepage of the *Global Landcover Facility: Earth Science Data Interface ESDI*:  
<http://glcfapp.umiacs.umd.edu:8080/esdi/index.jsp>



In the era of permanently increasing disc space the memory requirements of remote sensing data files seem to become less important but the RAM size on personal computers often still limits a stable working e.g. with large orthophotos in ArcGIS. Whereas the LANDSAT ETM<sup>+</sup> subscene needed relatively small disk space (about 6 MB) one uncompressed scanned colour aerial photograph had a size of about 500 MB. In this regard it is important to find a compromise between tolerable file sizes and spatial resolution of remote sensing data.

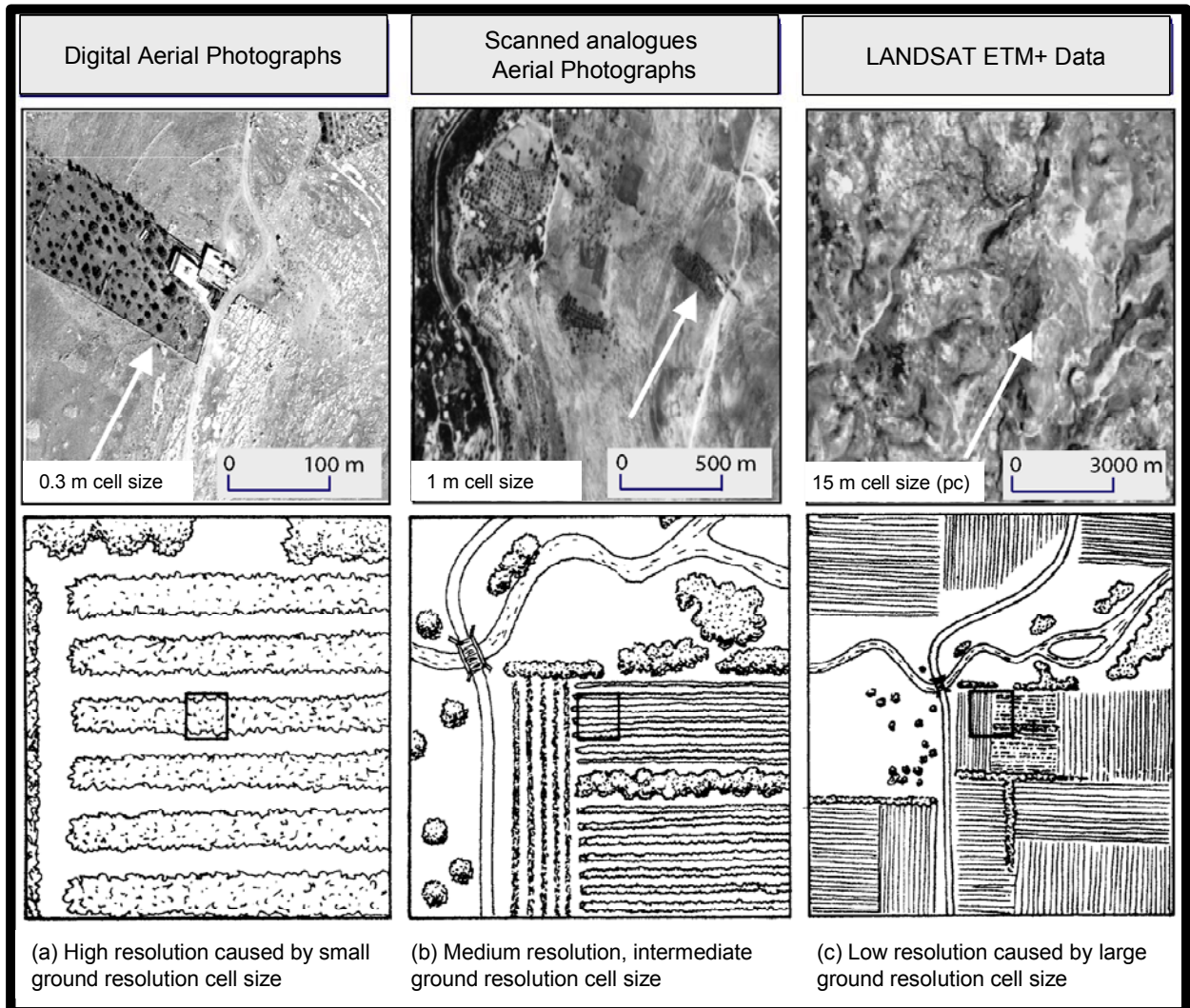


Fig. 10.1: Effect of ground resolution cell size of different remote sensing images used in this work (illustration modified after Lillesand & Kiefer, 2000).

The use of current LANDSAT ETM<sup>+</sup> data appears to be a suitable combination of extensive geographical coverage of the area of interest, wide spectral range, good vegetation discrimination, good data availability and a relative cost-efficiency compared to conventional data collection. The current LANDSAT ETM<sup>+</sup> image provided a good general survey of the land cover conditions and allowed generalised and up-to-date statements. The LANDSAT ETM<sup>+</sup> data for the test area provided six bands of the electromagnetic spectrum (the thermal band was not considered) from visible light to (near) infrared wavelengths, whereas the aerial photographs

were limited to one broad swath across the visible part of the spectrum. The LANDSAT ETM<sup>+</sup> data gave a good general and current overview of the test area.

The risk intensity map of the test site was based on the groundwater vulnerability and hazard maps mapped and printed at scale 1:50,000. At this scales, only a general overview of the hazards and their location and thus the risk intensity can be given. Usually, risk intensity mapping with a scale between 1:50,000 and 1:100,000 are used for general maps. However, for decision-making purposes or since parts of the test area show a high concentration of hazards such as the urban areas, for the hazard map and for the risk intensity map detailed maps at larger mapping scale (1:10,000 up to 1:1,000) are recommended.

Concerning the remote sensing data used and the relatively small size of the test area (185 km<sup>2</sup>) the major advantage of the aerial photographs over the LANDSAT ETM<sup>+</sup> data is the higher spatial resolution (an order of an magnitude better: less than one meter versus 15 m/ 30 m). These higher spatial resolution allowed the interpretation of small features such as karst forms, small and individual agricultural areas and woodlands, street networks and the detection of detached houses. For instance with the LANDSAT ETM<sup>+</sup>, the delineation of the streets was limited to the four-lane highway in the northern part of the test area; smaller roads could not be recognized. The effects of the ground resolution cell size of the three remote sensing data sets used in the test area is shown in Fig. 10.1.

Another important point to be considered is the scale of the mapping results. There is no image scale that is suitable for all mapping purposes. For topographic mapping Albertz (1991) uses for the image scale the following rule of thumb

$$M_b = 250 \cdot \sqrt{M_k} \quad (10.1)$$

where the image scale number  $M_b$  is equivalent to the root of the desired mapping scale number  $M_k$  times 250:

In some studies LANDSAT data are used for scales of 1:50,000 but in general LANDSAT data is used for mapping results with a scale of 1:100,000 or even smaller. The geometric accuracy of the LANDSAT image for mapping scales of 1:50,000 as applied for the test area is unsatisfying and not detailed enough, and thus the use of the LANDSAT ETM<sup>+</sup> data seems to be at the limit of use. Aerial photographs (scale 1:30,000) are normally used for mapping results of a scale between 1:20,000 up to 1:40,000 and aerial photographs with a scale of 1:10,000 are used for accordingly large scale mapping results. For geological or geosciences mapping purposes image scales of 1:20,000 or 1:30,000 are generally used (Albertz, 1991). All facts considered, the use of orthophotos is more useful, detailed and reasonable for the test area than the LANDSAT ETM<sup>+</sup> data. Consequently, whenever possible the data extraction results of the orthophotos were favoured compared to the LANDSAT ETM<sup>+</sup> data results.

### **Groundwater-Vulnerability**

Regarding the groundwater vulnerability assessment one important fact has to be kept in mind: several parameters used for the groundwater vulnerability assessment are based on information

beneath the earth's surface, namely the subsurface (e.g. unsaturated zone) and the underground (e.g. aquifer characteristics, thickness of geological units) that cannot be provided or replaced directly by the processed remote sensing data. This is due to the fact, that passive sensors have no ground penetrating capabilities and that some needed parameters solely can be obtained by other field or laboratory measurements. Sometimes, second-order or indirect indicators and significant variables that describe the physical geography and can influence the hydro(geo)logical processes can be derived from remote sensing imagery. They allow for a qualitative assessment of hydrogeological characteristics of an area such as topographic features, rock types, regional structural features, weathering and karstification, vegetation, soil moisture, drainage density, or special geological features such as sinkholes, alluvial fans, buried channels and faults.

### **Groundwater hazards**

Concerning the hazard mapping, it is obvious that the detection of hazard types by remote sensing is only possible if the hazards exhibit distinct characteristics that can be recognised on the images by their special spectral signatures, or special tone, texture, pattern, shape, size or associated characteristics. Chicken farms, green houses and agricultural areas are easy to identify, due to their shape, tone and texture or surrounding context, whereas it is impossible to classify car wash stations within urban areas because they are often included in the basement of blocks of flats. Consequently remote sensing techniques can be helpful if interpretation keys are existing, if objects can be clearly delineated or if the spectral signatures of the hazard types allow a classification. Especially within dense urbanisation centres information e.g. about the location of small businesses could solely be mapped by intensive field work or rarely by information from competent authorities. Detached houses could be mapped using the orthophotos, however, it was often not possible to distinguish inhabited detached houses from simple garages by orthophoto interpretation.

It is important to consider that there are special characteristics of the hazard types needed for the ranking and reduction procedure for the hazard index (HI) that only in exceptional cases can be assessed by remote sensing data. In most cases additional information is needed, for example data about the age, the security measurements and productivity or the amount of fertilisers used for agricultural purposes. However, in the study area often exactly these data were not made available and had to be assessed.

### **Uncertainty**

The process of deriving information from remote sensing data always inherits to some degree uncertainty regarding the results produced. The inability to perfectly co-register remotely sensed image data sets may substantially limit the ability to accurately monitor major land cover changes and so limit scientific understanding of environmental processes and changes (Foody & Atkinson, 2003). Especially for thematic maps, the larger is the mapping scale, the more the accuracy of the resulting map decreases. A second factor concerns the nature and quality of the remote sensing imagery and auxiliary data inputs such as field data. The better the quality and accuracy of the auxiliary data, the higher will be the accuracy of the resulting thematic maps.

**Closing comment**

In summary, the combination of LANDSAT ETM<sup>+</sup> imagery and aerial photographs combined with additional data in a GIS has shown a high potential to provide reasonably accurate information, enhancing topographical and other thematic information for groundwater risk intensity mapping. However, remote sensing data will never be a stand-alone technique, able to replace conventional data acquisition needed for groundwater vulnerability mapping and groundwater hazard mapping in order to assess the risk intensity.

## 11 RECOMMENDATIONS

### 11.1 Choice of the remote sensing data

Scale restricts type, quantity, and quality of data (Star & Estes, 1990), thus the appropriate map scale must fit to the level of detail required in the project. The choice of the remote sensing data that is used is dependant on the desired scale for the risk intensity maps. Therefore different remote sensing data type and sensors have to be considered dependent if the resulting maps should show a general overview or provide site-specific details for planning and groundwater management strategies. In the case of a desired risk intensity mapping scale of 1:50,000 in a relatively small area of interest and a high spatial heterogeneity of the land cover such as the presented test area, the use of orthophotos with a higher spatial resolution and accuracy should be favoured. In the case of bigger areas of interest, for example areas larger than 5000 km<sup>2</sup> showing a more homogenous land cover such as the flat areas in the Jordan Valley, and desired mapping results of 1:100,000 but also detailed maps of the “hot spot” in critical areas, a hierarchical approach is recommended. In a hierarchical approach phenomena at an intermediate scale are investigated and information regarding potential critical areas is used for further investigations at a lower scale with high or very high spatial resolution data, that could be used for 1:10,000 detail maps. High resolution satellite data can be provided for example by the IKONOS and Quick Bird satellite sensors that guarantee highly accurate, commercial multispectral imagery. IKONOS data have a spatial resolution of 1 m in the panchromatic band and of 4 m in the multispectral band. Quick Bird has a spatial resolution of 0.61 m in the panchromatic band and of 2.44 m in the multispectral band. However, it should be mentioned that IKONOS and Quick Bird data are still relatively expensive compared to LANDSAT data and aerial photographs. For very detailed maps of 1:5,000 up to 1:1,000 high quality digital aerial photographs with corresponding scales should be favoured.

### 11.2 Choice of the image analysing software

The results show that the integrated use of GIS and remote sensing technique is a powerful tool for the assessment of the groundwater risk intensity. The large amount of information derived from digital images offers new opportunities for vulnerability and hazard assessment, particularly those parameters related to land use, vegetation coverage, urbanisation and infrastructure make this approach valuable for the evaluation, of endangered groundwater bodies.

One approach to improve the classification results of the LANDSAT ETM<sup>+</sup> would be the use of ancillary data that can be integrated if an object-orientated software programme is used for the image analysis such as *eCognition*<sup>®</sup> from *Definions*. Beyond purely spectral information *eCognition* is able to take into account special characteristics of the features (shape, texture) by using additional algorithms, relevant attributes or relational or contextual information that improves the classification by enabling classification schemes that are not solely based on the spectral features of the remote sensing data. Class-related tools allow an evaluation of relation, for instance embedding or distance, of an image object to a specific class in the neighbourhood.

### **11.3 Validation of the results**

A validation of the risk intensity results is needed. Tracer tests have to be carried out in the test area to prove the hydraulic connection between “hot spots” of contaminations at the ground surface and the aquifer. The results could prove an assumed path that a specific contamination load will take, help to define a mean transit time of contamination transport of the potential hazards to determine the underground flow paths and to delineate the catchment areas of the drinking water springs, to get information about the mechanisms of contamination transport, and to evaluate the risk potentially resulting from existing hazards. For example, for the estimation of the vertical percolation velocity in the unsaturated zone of the Wadi Sir Aquifer (A7), a tracer at the Azraq-Fuheis spring could be helpful. The springs is discharging at the bottom of a small wadi of the lower parts of the Wadi Sir Formation which has a thickness of about 10m. To avoid as far a possible lateral movement of the tracer, the tracer could be distributed directly E of the spring on the mountain ridge. So far it was not possible to get a permission to carry out tracer tests in the test area, due to the fact that some of the main springs supply the royal houses with water.

Contamination transport models such as three-dimensional variable-density ground-water flow and solute-transport simulators should be used to verify and validate the results of the risk intensity maps. There exist special models that are able to quantify the fast and slow infiltration conditions in karst systems such as double porosity models (Maloszewski et al., 1998; Jeannin & Sauter, 1998) or even triple porosity models with matrix, fractures and conduits (Maloszewski et al., 2002) or a conduit system in a continuum model (Liedl & Sauter, 1998). The extensive database such as the soil characteristics that was generated for the test area can be a valuable model input. However, detailed information about the underground flow characteristics that are important for transport models are missing so far and only can be estimated or translated from other similar regions in Jordan.

### **11.4 Delineation of groundwater protection zones**

With the results of tracer tests, groundwater protection zones should be established following for example the German guidelines for the establishment of water protection areas including individual protection zones (DVGW, 1995). The establishment of protection zones for the springs in the test area could primarily help to reduce the microbiological contamination existing in several springs, by implementing a microbiological 50 days protection area. At least for the major springs that are used for drinking water supply for many people in the test area groundwater protection zones and protection concepts should be implemented.

### **11.5 Groundwater management in the test area**

Several water related problems exist in countries with water scarcity. In general there is lack of understanding how integrated approaches to water resources development and management works caused by the matter of education concerning environmental knowledge and awareness.. Often it is impossible to find a balance between water supply and demand. Missing protection and management strategies lead to a continuous mining and pollution of the groundwater

resources. Activities carried out in the test area that causes a negative impact to local groundwater systems include agriculture, industrialization and urbanization.

Regarding the spring sample analysis of the test area (Ta'any, 1992; Salameh, 2005) the main problems seem to be the microbiological inputs (coliforms) and partly elevated phosphate concentrations, indicating an influence of organic waste, excrements or waste water. The microbiological pollution hot spots in the test area seem to be the septic tanks that are often constructed within the karstified aquifer itself, and often lack paved walls. Waste water treatment plant bypasses, combined sewer overflows, and storm water runoff during high stream flow can contribute to a significant amount of contamination of the groundwater. Economic incentives are required for the industry and water utilities to invest in adequate wastewater treatment and recycling and to increase the amount of connected households to the wastewater system, stop illegal waste dump or direct waste water input in the test area.

For a sustainable groundwater management in the test area studies should be accomplished about the groundwater occurrence and aquifer properties, including water well records, aquifer and pumping tests. A problem concerning the monitoring is the fact that only a few wells exist in the test area, which are nearly all closed and sealed. Due to the complex tectonic situations and the dense fault network, the hydrogeological situation in the centre parts of the test area is not known in detail. Also the role of the faults concerning their permeable or impermeable characteristics could only be assessed.

In the test area as well as in the whole country of Jordan, there is a need for improved monitoring of the groundwater. Groundwater management strategies should be initiated where problems are evident, regardless of data limitations, including protection of the groundwater aquifers from pollution and application of rehabilitation techniques. Public awareness campaigns and community participation towards preserving groundwater from pollution and depletion should be initialised and enforced.

In urban areas exists an urgent demand for a more integrated approach to the management of groundwater and wastewater interactions and for the interaction between public and private systems. This approach should also include the empowerment of people at the local level to manage and protect their groundwater and water resources. Strategic initiatives that enhance the awareness of decision makers and the public of the importance of groundwater resources should be implemented and point out the significance of the emerging problems and the practical responses available to address such problems.

There is a demand for the development of a combination of technical, economic, social, and institutional approaches for groundwater management in Jordan that also reflects the local conditions. Technology transfer, capacity building, and research development must take place to transfer this knowledge on to the practical field level of restoring and re-establishing old practices of water use and water management.

The delineation of country wide groundwater risk intensity maps can be the first step to assess the status and risk of groundwater and consequently the results can be used as a basis for groundwater management strategies.





## 12 REFERENCES

- Abbott, M.B., Bathurst, J.C., Cunge, J.A., O'Connell, P.E. & Rasmussen, J. (1986): An introduction to the European System - Systeme Hydrologique Europeen, "SHE", 2. Structure of a physically-based, distributed modelling system.- *Journal of Hydrology*, 87: 61-77.
- Abed, A.M. (1984): Emergence of Wadi Mujib (Central Jordan) during Lower Cenomanian time and its regional tectonic implications.- In: Dixon, J.E. & Robertson, A.H.F. (eds) (1984): *The Geological Evolution of the Mediterranean*.- Blackwell & Scientific Publications, London, 213-216.
- Abu Shams, I. (2004): Regional Cooperation for Developing Non-Conventional Water Resources.- *Proceedings of the 2<sup>nd</sup> Israeli-Palestinian-International Conference on Water for Life in the Middle East*, Antalya 10-14 Oct. 2004, 131-133.
- Adams, B. & Foster S.S.D. (1992): Land-surface zoning for groundwater protection.- *Water and Environmental Management Journal*, 6: 312-320.
- AG Boden (1994): *Bodenkundliche Kartieranleitung*.- Hannover, 392 p.
- Ahmed, M. (1996): Lineaments as Groundwater Exploration Guides in Hard-Rock Terranes of Arid Regions.- *Canadian Journal of Remote Sensing*, 22(1): 180-191.
- Ahmed, N.U. (1995): Estimating soil moisture from 6.6 GHz dual polarization, and/or satellite derived vegetation index.- *International Journal of Remote Sensing*, 16: 687-708.
- Al-Adamat, R.A.N., Foster, I.D.L. & Baban, S.M.J. (2003): Groundwater vulnerability and risk mapping for the Basaltic aquifer of the Azraq basin of Jordan using GIS, Remote sensing and DRASTIC.- *Applied Geography*, 23: 303-324.
- Al-Farajat, M. (2001): *Hydrogeo-Eco-Systems in Aqaba/Jordan Coasts and Region; Natural Settings, Impacts of Land Use, Spatial Vulnerability to Pollution and Sustainable Management*.- *Forschungsergebnisse aus dem Bereich Hydrogeologie und Umwelt*, 30, 220 p.
- Albertz, J. (1991): *Grundlagen der Interpretation von Luft- und Satellitenbildern*.- Wissenschaftliche Buchgesellschaft, Darmstadt, 204 p.
- Al-Daher, N. (1989): *Soil erosion susceptibility survey and evaluation: the example of Wadi Shueib Basin, Jordan*.- Master thesis University of Amman (unpublished), 125 p.
- Al-Hadidi, L., & Abdel-Nabi, F. (2004): *Wastewater Management and Reuse in Jordan*.- *Proceedings of the 2nd Israeli-Palestinian-International Conference on Water for Life in the Middle East*, Antalya 10-14 Oct. 2004, 166-180.
- Al-Kharabsheh-Atef, A. (1999): Influence of long-term overpumping on groundwater quality at Dhuleil Basin, Jordan.- *Forschungsergebnisse aus dem Bereich Hydrogeologie und Umwelt*, 18: 2.1-2.10.
- Aller, L., Bennet, T., Lehr, J.H., Petty, R.J. & Hackett, G. (1987): *DRASTIC: a standardized system for evaluating ground water pollution potential using hydrogeological settings*.- U.S. Environmental Protection Agency, Oklahoma, 266 p.
- Alsdorf, D.E. & Lettenmaier, D.P. (2003): Tracking fresh water from space.- *Science*, 301:1491-1494.
- Andrews, I.J. (1991): *Paleozoic lithostratigraphy in the subsurface of Jordan*.- *Subsurface Geology Bulletin No.2*, NRA, Geology Directorate, Amman, 67p.

- Baban, S.M.J. (1997): Potential application of satellite remote sensing (SRS) and GIS in maximizing the use of water resources in the Middle East: examining Iraq as a case study.- In: Baumgartner, M.F., Schultz, G.A. & Johnson, A.I. (eds) (1997): Remote Sensing and Geoinformation Systems for Design and Operation of Water Resources Systems.- IAHS Publication, 242: 17-23.
- Bähr, H.-P. & Vögtle, T. (eds) (1998): Digitale Bildverarbeitung: Anwendung in Photogrammetrie, Kartographie und Fernerkundung.- Wichmann Verlag, Heidelberg, 345 p.
- Bähr, H.-P. (eds) (1985): Digitale Bildverarbeitung: Anwendung in Photogrammetrie und Fernerkundung.- Wichmann Verlag, Karlsruhe, 282 p.
- Baumgartner, M.F., Schultz, G.A. & Johnson, A.I. (eds) (1997): Remote Sensing and Geoinformation Systems for Design and Operation of Water Resources Systems.- IAHS Publication 242, IAHS Press, Wallingford, 255 p.
- Bayer, H.-J., El-Isa, Z., Hötzl, H., Mechie, J., Prodehl, C. & Saffarini, G. (1989): Large tectonic and lithospheric structures of the Red Sea region.- *Journal of African Earth Sciences*, 8: 565-587.
- Bayer, H.J. (1988): Wadi Araba und Jordantal. Ein tektonischer Graben und zugleich Blattverschiebung?.- *Natur und Museum*, 188 (2): 33-45.
- Bayer, H.J., Hötzl, H., Jado, A.R., Roscher, B. & Voggenreiter W. (1988): Sedimentary and structural evolution of the northwest Arabian Red Sea margin.- *Tectonophysics*, 153: 137-151.
- Belz, S. (2000): Nutzung von LANDSAT Thematic Mapper Daten zur Ermittlung hydrologischer Parameter.- *Mitteilungen des Institutes für Wasserwirtschaft und Kulturtechnik der Universität Karlsruhe (TH), Theodor Rehbock-Wasserbaulaboratorium*, 206, 153 p.
- Bender, F. (1982): On the Evolution of the Wadi Araba – Jordan Rift.- In: *Geologisches Jahrbuch*, C45: 1-20.
- Bender, F. (1974). *Geology of Jordan. Contribution of the Regional Geology of the Earth.- Gebrüder Bornträger, Berlin*, 196 p.
- Bender, F. (1968): *Geologie von Jordanien.- Gebrüder Bornträger, Berlin*, 196 p.
- Ben-Dor, E., Goldschleger, N., Braun, O., Kindel, B., Goetz, A.F.H., Bonfil, D., Margalit, N., Binaymini, Y., Karnieli, A. & Agassi, M. (2004): Monitoring infiltration rates in semi-arid soils using airborne hyperspectral technology.- *International Journal of Remote Sensing*, 25: 2607-2624.
- Beven, K. & Kirkby, M. (1979): A physically based, variable contributing area model of basin hydrology.- *Bulletin of Hydrologic Sciences*, 24: 43-69.
- Beven, K.J., Kirkby, M.J., Schofield, N. & Togg, A.F. (1984): Testing a Physically-Based Flood Forecasting Model (TOPMODEL) for three U.K. Catchments.- *Journal of Hydrology*, 69: 119-143.
- Boeckh, E. (1992): An exploration strategy for higher-yield boreholes in the West African crystalline basement.- In: Wright E.P. & Burgess W.G. (eds) (1992): *Hydrogeology of crystalline basements aquifers in Africa.- Geological Society Special Publication*, 66: 87-100.
- Böhlke, J.-K. (2002): Groundwater recharge and agricultural contamination.- *Hydrogeological Journal*, 10: 153-179.
- Brady, P. V., Borns, D.J. & Brady, M. V. (1997): *Natural Attenuation: CERCLA, RBCAs, and the Future of Environmental Remediation.- Lewis Publishers, New York*, 172 p.

- Bressan, M.A. & Dos Anjos, C.E. (2003): Techniques of remote sensing applied to the environmental analysis of part of an aquifer located in the Sao Jose dos Campos Region sp, Brazil.- *Environmental Monitoring and Assessment*, 84(1-2): 99-109.
- Brunner, P., Bauer, P., Eugster, M. & Kinzelbach, W. (2004): Using remote sensing to regionalize local precipitation recharge rates obtained from the Chloride Method.- *Journal of Hydrology*, 294 (4): 241-250.
- Burdon, D.J. (1959): *Geology of Jordan*.- Benham & Co. Ltd., Colchester, 82 p.
- Campbell, J.B. (1996): *Introduction to Remote Sensing*.- Guilford Publications, New York, 622 p.
- Carper, W., Lillesand, T. & Kiefer, R. (1990): The use of Intensity-Hue-Saturation transformations for merging SPOT panchromatic and multispectral image data.- *Photogrammetric Engineering and Remote Sensing*, 56 (4): 459-467.
- Carrara, A., Bitelli, G. & Carla, R. (1997): Comparison of techniques for generating digital terrain models from contour lines.- *International Journal of Geographical Information Science*, 11(5): 451-473.
- Carruthers, R.M., Greenbaum, D., Jackson, P.D., Mtetwa, S., Peart, R.J. & Shedlock, S.L. (1993): *Geological and Geophysical Characterisation of Lineaments in south-east Zimbabwe and Implications for Groundwater Exploration*.- British Geological Survey, NERC, Technical Report WC/93/7.
- Chandler, J.H., Rice, S. & Church M. (2004): Colour aerial photography for riverbed classification.- *Proceedings of the 20th International Society for Photogrammetry and Remote Sensing (ISPRS) Congress, Istanbul July 2004*, 120-125.
- Chapman, R. W. (1974): Calcareous Duricrust in Al-Hasa, Saudi Arabia.- *Geological Society of America Bulletin*, 85(1):119–130.
- Chebaane, M., El-Naser, H., Fitch, J., Hijazi, A. & Jabbarin, A. (2004): Participatory groundwater management in Jordan: Development and analysis of options.- *Hydrogeological Journal*, 12(1): 14-32.
- Chen, J.M., Chen, X., Ju, W. & Geng, X. (2005): A remote sensing driven distributed hydrological model: mapping evapotranspiration in a forested watershed.- *Journal of Hydrology*, 305:15-39.
- Clarke, K.C. (2000): *Remote Sensing of the environment*.- John R. Jensen, London, 528 p.
- Cochran, J.R. (1983): A model for development of the Red Sea.- *American Association of Petroleum Geologists Bulletin*, 67: 41-69.
- Cohen, J. (1960). A coefficient of agreement for nominal scales.- *Educational and Psychological Measurement*, 20: 37-46.
- Coleman, R.G. (1984): The Red Sea: A small ocean basin formed by continental extension and sea floor spreading.- *27th International Geological Congress*, 23: 93-121.
- CORE LAB (1987): *Azraq Basin Study*.- Report for the National Resources Authority, Amman, (unpublished), 80 p.
- Daly, D. & Warren, W. (1998): Mapping groundwater vulnerability- the Irish perspective.- In: Robins, N. (ed.) (1998): *Groundwater pollution, aquifer recharge and vulnerability*.- Geological Society London, Special Publication, 130: 179-190.
- Daly, D., Dassargues, A., Drew, D., Dunne, S., Goldscheider, N., Neale, S., Popescu, I.C. & Zwahlen, F. (2002): Main concepts of the European Approach for (karst) groundwater vulnerability assessment and mapping.- *Hydrogeological Journal*, 10(2): 340-345.

- Daly, D., Hötzl, H., & De Ketelaere, D. (2004): Risk Assessment- Risk Definition.- In: Zwahlen F. (ed) (2004): COST Action 620- Vulnerability and Risk Mapping for the Protection of Carbonate (Karst) Aquifers.- Final Report, 106-107, Public European Communities, Luxembourg.
- De Ketelaere, D., Hötzl H., Neukum, C., Civita, M., & Sappa, G. (2004) Hazard Analysis and Mapping.- In: Zwahlen F. (ed) (2004): COST Action 620- Vulnerability and Risk Mapping for the Protection of Carbonate (Karst) Aquifers.- Final Report, 86-105, Public European Communities, Luxembourg.
- Dekker, A.G., Malthus, T.J. & Hoogenboom, H.J. (1995): The remote sensing of inland water quality.- In: Danson, F.M. & Plummer S.E. (eds) (1995): Advances in Environmental Remote Sensing.- John Wiley and Sons, Chichester, 150 p.
- Dewey, J.F., Pitman, W.C, Ryan, W.B.F & Bonin, J. (1973): Plate tectonics and the evolution of the Alpine System.- Geological Society of America bulletin, 84: 3137-3180.
- Dezetter, A., Delclaux, F., Leconte, J., Servat, E., Mahe, G. & Paturel, J.E. (2003): Prise en compte de la Végétation à l'aide de données NOAA AVHRR dans la modélisation pluie debit en Afrique de l'Ouest.- In: Servat E., Najem W., Leduc C. & Shakeel A. (eds.) (2003): Hydrology of Mediterranean and Semiarid Regions.- IAHS Publication, 278: 144-150.
- Doerflinger, N. & Zwahlen F. (1998): Practical guide, groundwater vulnerability mapping in karstic regions (EPIK).- Swiss Agency for the Environment, Forests and Landscape (SAEFL), Bern, 56 p.
- Doorenbos, J. & Pruitt, W.O. (1977): Guidelines for Predicting Water Requirements.- FAQ Irrigation and Drainage Paper 24, Rome, 144 p.
- Dottridge, J. & Abu-Nizar, J. (1999): Groundwater resources and quality in northeastern Jordan; safe yield and sustainability.- Applied Geography, 19 (4): 313-323.
- Eisbacher, G.H. (1996): Einführung in die Tektonik.- Enke, Stuttgart, 400 p.
- El-Hiyari, M. (1985): The geology of Jabal Al Mutarammil - Map sheet No. 3252III.- Bulletin No.1, National Resources Authority, Amman, 51 p.
- Ellyett, C.D. & Pratt, D.A. (1975): A Review of the Potential Applications of Remote Sensing Techniques to Hydrogeological Studies in Australia.- Australian Water Resources Council Technical Paper No. 13, Australian Governmental Publishing Service, Canberra, 147 p.
- Engman, E.T & Gurney, R.J. (1991): Remote Sensing in hydrology.- Chapman and Hall, London, 225 p.
- Engman, E.T. & Chauhan, N. (1995): Status of Microwave Soil Moisture Measurements with Remote Sensing.- Remote Sensing of Environment, 51:189-198.
- ERDAS (1999): ERDAS Field Guide.- Atlanta, 306 p.
- Farnsworth, R.K., Barret, E.C. & Dhanju, M.S. (1984): Application of remote sensing to hydrology including groundwater.- IHP-II Project A. 1.5; UNESCO, France, 200 p.
- Farrell, S.O. (1985): Evaluation of Colour Infrared Aerial Surveys of Wastewater Soil Absorption Systems.- EPA/600/2-85/039 (NTIS PB85-189074), 43 p.
- Finkbeiner, M. & O'Tool, M.M. (1985): Application of Aerial Photography in Assessing Environmental Hazards and Monitoring Cleanup Operations at Hazardous Waste Sites.- In: Proceeding of the 6th National Conference on Management of Uncontrolled Hazardous Waste Sites, Hazardous Materials, Oct. 1984, Washington D.C., 116-124.
- Flexer, A. (2001): The pre-Neogene geology of the Near-East.- In: Horowitz, A. (ed) (2001): The Jordan Rift Valley.- Balkema Publishers, Tokyo, 720 p.

- Flexer, A. & Honigstein, A. (1984): The Senonian succession in Israel- lithostratigraphy, biostratigraphy and sea level changes.- *Cretaceous Research*, 5: 303-312.
- Flexer, A. (1971): Late cretaceous palaeogeography of northern Israel and its significance for the Levant geology.- *Journal of Paleogeography, Palaeoclimatology, Palaeoecology*, 10: 293-316.
- Flexer, A. (1968): Stratigraphy and facies development of the Mount Scopus Group in Israel and adjacent countries. *Israel Journal of Earth Science*, 17: 85-114.
- Food and agriculture organisation (FAO) of the United Nations (1998): World reference base for soil resources.- *World Soil Resources Report 84*, Rome, 88 p.
- Foody, G.M. & Atkinson, P.M. (2002): *Uncertainty in Remote Sensing and GIS*.- Wiley, Southampton, 307 p.
- Fournier, R.A., Edwards, G., & Eldridge, N.R. (1995): A Catalogue of potential spatial discriminators for high spatial resolution digital images of individual crowns.- *Canadian Journal of Remote Sensing*, 21: 285-298.
- Foster, S.S.D. (1987): Fundamental concepts in aquifer vulnerability, pollution risk and protection strategy.- In: Duijvenbooden, W. van & Waegeningh, H.G. van (eds) (1987): TNO Committee on Hydrological Research, The Hague. Vulnerability of soil and groundwater to pollutants.- *Proceedings and Information*, 38: 69-86.
- Francis, D.S., Helsel, D.R. & Nell, R.A. (2000): Occurrence and distribution of Microbiological Indicators in Groundwater and Streamwater.- *Water Environmental Research*, 72: 152-161.
- Fraser, R.S., Bahethi, O.P. & Al-Abbas, A.H. (1977): The effect of the atmosphere on the classification of satellite observation to identify surface features.- *Remote Sensing and Environment*, 6: 229-249.
- Garfunkel, Z. & Ben-Avraham, Z. (1996): The structure of the Dead Sea basin. - *Tectonophysics*, 80: 1-26.
- Garfunkel, Z., Zak, I. & Freud, R. (1981): Active Faulting in the Dead Sea rift.- *Tectonophysics*, 266: 155-176.
- Gogu, R.C. & Dassargue, A. (2001): Intrinsic vulnerability maps of a karstic aquifer as obtained by five different assessment techniques: comparison and comments.- *Proceedings of the 7th Conference on limestone, hydrology and fissured media*, Besançon Sept. 20 - 22, 2001, 161-166.
- Goldscheider, N. (2002): *Hydrogeology and Vulnerability of Karst Systems, Examples from the Northern Alps and the Swabian Alb*.- Schriftenreihe Angewandte Geologie Karlsruhe, Karlsruhe, 68:I-XXI 1-236.
- Goldscheider, N., Klute, M., Sturm, S. & Hötzl, H. (2000): The PI method – a GIS based approach to mapping groundwater vulnerability with special considerations of karst aquifers.- *Zeitschrift für Angewandte Geologie*, 46 (3): 157-166.
- Golwer, A. (1995): Traffic routes and their groundwater risk.- *Eclogae Geologicae Helvetiae*, 88 (2): 403-419.
- Greenbaum, D. (1992): Structural Influences on the occurrence of groundwater in SE Zimbabwe. - In: Wright E.P. & Burgess W.G- (eds) (1992): *Hydrogeology of crystalline basement aquifers in Africa*.- Geological Society Special Publication, 66: 77-85.
- Gupta, K.K., Deelstra, J. & Sharma, K.D. (1997): Estimation of water harvesting potential for a semiarid area using GIS and remote sensing.- In: Baumgartner, M.F., Schultz, G.A., Johnson,

- A.I. (eds) (1997): Remote Sensing and Geoinformation Systems for Design and Operation of Water Resources Systems.- IAHS Publication 242: 53-63.
- Gupta, R.P. (2003): Remote sensing geology.- Springer, New York, 655 p.
- Hall, J., Krasheninnikov, V.A., Hirsch, F., Benjamini C. & Flexur, A. (2005): Geological Framework of the Levant. Volume II: The Levantine Basin and Israel.- Historical Productions-Hall, Jerusalem, 815 p.
- Hardisty, P.E., Hunt, R., Nachasi, N., Garabieyh, A., Berjawi, Y. & Taha, M. (2004): Water and nutrient -recycling seepage treatment for small communities in the Jordan Valley.- Proceedings of the 2nd Israeli-Palestinian-International Conference on Water for Life in the Middle East, Antalya Oct. 10-14, 2004, 50-53.
- Hijazi, H., Hobler, M., Rayyan, M. & Subah, A. (1999): Groundwater Resources of Northern Jordan, Special Report No. 4: Mapping of Groundwater Vulnerability and Hazards to Groundwater in the Area South of Amman.- BGR & WAJ, Technical Cooperation Project Advisory Services to the Water Authority of Jordan, BGR archive no. 112708, 57 p.
- Hildebrandt, G. (1996): Fernerkundung und Luftbildmessung für Forstwirtschaft, Vegetationskartierung und Landschaftsökologie.- Wichmann Verlag, Karlsruhe, 676 p.
- Hirsch, F. (1984): The Arabian sub-plate during Mesozoic.- In: Dixon, J.E. & Robertson, A.H.F. (eds) (1984): The Geological Evolution of the Mediterranean. The Geological Society, Blackwell & Scientific Publications, London, 836 p.
- Hochschild, V. (1998): Einsatz der Fernerkundung für die hydrologische Systemanalyse im südlichen Afrika.- In: Zeitschrift für Photogrammetrie und Fernerkundung, Karlsruhe, 4: 98-107.
- Hoffman, J. (2005): The future of satellite remote sensing in hydrogeology.- Hydrogeology Journal, 13: 247-250.
- Holopainen, M. & Wang, G. (1998): The calibration of digitised aerial photographs for forest stratification.- International Journal of Remote sensing, 19(4): 677-696.
- Horowitz, A. (2001): The Jordan Rift Valley.- Balkema Publishers, Tokyo, 729 p.
- Hölting, B., Haertle, T., Hohberger, K.H., Nachtigall, K.H., Villinger, E., Weinzierl, W. & Wrobel, J.P.: (1995) Konzept zur Ermittlung der Schutzfunktion der Grundwasser-überdeckung.- Geologisches Jahrbuch, C63: 5-24.
- Hötzl, H., Delporte, C., Liesch, T., Malik, P., Neukum, C., & Svasta J. (2004): Risk mapping.- In: Zwahlen F. (ed) (2004): COST Action 620- Vulnerability and Risk Mapping for the Protection of Carbonate (Karst) Aquifers.- Final Report, 113-121, Public European Communities, Luxembourg.
- Hötzl, H., Delporte, C., Liesch, T., Malik, P., Neukum, C., & Svasta J. (2004): Risk Assessment Concept.- In: Zwahlen F. (ed) (2004): COST Action 620- Vulnerability and Risk Mapping for the Protection of Carbonate (Karst) Aquifers.- Final Report, 108-113, Public European Communities, Luxembourg.
- Houston, J.F.T. (1982): Rainfall and Recharge to a Dolomitic Aquifer at Kabwe, Zambia.- Journal of Hydrology, 59: 173-187.
- Husseini, M.I. & Husseini, S.I. (1990): Origin of the Infra-Cambrian salt basins of the Middle East.- In: Brooks, J. (ed.) (1990): Classic Petroleum Provinces. Geological Society Special Publication, 50: 279-292.

- Husseini, M.I. (1992): Upper Palaeozoic tectono-sedimentary evolution of the Arabian and adjoining plates.- *Journal of the Geological Society, London*, 149: 419-429.
- Hutchinson, M. F. & Dowling, T. I. (1991): A Continental Hydrological Assessment of a New Grid-Based Digital Elevation Model of Australia.- *Hydrological Processes*, 5: 45-58.
- Jiries, A. (1999): Hydrochemistry of springs and groundwater as affected by human Activities / Karak area, Jordan.- *Forschungsergebnisse aus dem Bereich Hydrogeologie und Umwelt*, 18: 180-188.
- Jackson, T.J. (2002): Remote sensing of soil moisture: Implications for groundwater recharge.- *Hydrogeological Journal*, 10: 40-51.
- Jakubauskas, M.E., Whistler J.L., Dillworth, M.E. & Martinko, E.A. (1992): Classifying remotely sensed data for use in an agricultural non-point pollution model.- *Journal of Soil and Water Conservation*, 47(2): 179-183.
- Japan International Cooperation Agency (JICA), Ministry of Water (MWI), Hashemite Kingdom of Jordan (1995): The study on Brackish Groundwater Desalination in Jordan, Main Report.- Yachiyo Engineering Co. Ltd., Mitsui Mineral Development Engineering Co. Ltd., Tokyo.
- Jeannin, P.Y., Sauter, M. (1998): Analysis of karst hydrodynamic behaviour using a global approach: a review.- *Bulletin d'Hydrogéologie, Centre d'Hydrogéologie, Université de Neuchâtel*, 16: 31-48.
- Jennings, J.N. (1985); *Karst Geomorphology*.- Basil Blackwell, Oxford and New York, 293 p.
- Jensen, J.R. (1996): *Introductory digital image processing*.- Prentice-Hall, Englewood Cliffs, New Jersey, 318 p.
- Junker, A. (2004): *GIS-gestützte Hazardkartierung im Raum Rastatt*.- Master Thesis University of Karlsruhe, Karlsruhe (unpublished), 100 p.
- Jordanian Standards of drinking water (2001): Open Files, No. 286.- Jordanian Institute of standards and Metrology. Amman, 15 p.
- Kashai, E.L. & Crocker, P.F. (1987): Structural geometry and evolution of the Dead Sea - Jordan Rift system as deduced from new subsurface data.- *Tectonophysics*, 141: 33-60.
- Katawa, Y., Ohtani, A., Kusaka, T. & Ueno, S. (1990): Classification accuracy for the MOS-1 MESSR data before and after the atmospheric correction.- *Geoscience and Remote Sensing*, 28: 755-760.
- Kaufmann, H., Reichert, B., & Hötzl, H. (1986): Hydrogeological Research in Peloponnesian Karst Area by Support and Completion of LANDSAT Thematic Data.- *Proceedings of the IGARSS' 86 Symposium, Zürich, Sept. 8-11 1986, Ref. ESA SP-254, ESA Publications Division*, 437-441.
- Kazemi, R. (2003): *Reconnaissance of karst hydrology in the Lar catchment, Iran using Remote Sensing and GIS*.- Master thesis Institute for Geoinformation science and earth observation (ITC), Enschede, (unpublished), 50 p.
- Kidwell, K.B. (1997) *NOAA Global Vegetation Index User's Guide*.- U.S. Department of Commerce NOAA National Environmental Satellite data and Information Service, 85 p.
- Kim, K. & Ventura, S. (1993): Large-scale modelling of urban non-point source pollution using a geographical information system.- *Photogrammetric Engineering and Remote Sensing*, 59(10): 1539-1544.

- Kjeldsen, P., Grundtvig, A., Winther, P. & Andersen, J.S. (1998): Characterization of an old municipal landfill (Grinstead, Denmark) as a groundwater pollution source: landfill history and leachate composition.- *Waste Management and Research*, 16(1): 3-13.
- Knorr, C. (1997): *Mikrobieller Schadstoffabbau*.- Vieweg, Wiesbaden, 466 p.
- Koch, M. & Mather, P.M. (1997): Lineament mapping for groundwater resource assessment: a comparison of digital Synthetic Aperture Radar (SAR) imagery and stereoscopic Large Format Camera (LFC) photographs in the Red Sea Hills, Sudan. – *International Journal of Remote Sensing*, 18(7): 465-1482.
- Kölle, W. (2003): *Wasseranalysen – richtig beurteilt*.- WILEY-VCH Verlag, Weinheim, 315 p.
- Kraus, K. (2004): *Photogrammetrie, Geometrische Informationen aus Photogrammetrie und Laserscannaufnahmen, Band 1*.- Walter De Gruyter, Berlin, 516 p.
- Kraus, K. (1986): *Photogrammetrie, Grundlagen und Standardverfahren, Band 1*.- Ferdinand Dümmler, Bonn, 486 p.
- Kraus, K. (1990): *Fernerkundung. Band 2: Auswertung photographischer und digitaler Bilder*.- Ferdinand Dümmler, Bonn, 310 p.
- Krupnik, A. (2003): Accuracy prediction for ortho-image generation.- *Photogrammetric Record*, 18(101): 41-58.
- Kuntz, D. (2003): *Soils in the Wadi Shueib catchment area and their protective potential for the Groundwater- Salt area*.- Master Thesis University of Karlsruhe, Karlsruhe (unpublished), 161 p.
- Lattman, L.H. & Parizek, R.R. (1964): Relationship between fracture tracers and the occurrence of ground water in carbonate rocks.- *Journal of Hydrology*, 2: 73-91.
- Lenney, M.P., Woodcock, C.E., Collins J.B. & Hamdi, H. (1996): The Status of Agricultural Lands in Egypt: The Use of Multitemporal NDVI Features Derived from LANDSAT TM.- *Remote Sensing of the Environment*, 56: 8-20.
- Lewandowski, J. (1997): *Schadstoffe im Boden*.- Springer, Heidelberg, 339 p.
- Liedl, R. & Sauter, M. (1998): Modelling of aquifer genesis and heat transport in karst systems.- *Bulletin d'Hydrogéologie, Centre d'Hydrogéologie, Université de Neuchâtel* 16:185-200.
- Lillesand, T.M., & Kiefer, R.W. (2004): *Remote Sensing and Image Interpretation*.- John Wiley and Sons, New York, 763 p.
- Lubczynski, M.W. & Gurwin, J. (2005): Integration of various data sources for transient groundwater modelling with spatio-temporally variable fluxes - Sardon study case, Spain.- *Journal of Hydrology*, 306(1-4): 71-96.
- MacDonald, M. & Partners (1963): *Salt – 1:25.000 C.W.A. Geologic Series – Sheet 215/150*.- Jordan office for geological and engineering services, Amman.
- Magiera, P. (2000): Methoden zur Abschätzung der Verschmutzungsempfindlichkeit des Grundwassers.- *Grundwasser*, 3: 103-114.
- Maloszewski, P., Benischke, R., Harum, T. & Zojer, H. (1998): Estimation of solute transport parameters in a karstic aquifer using artificial tracer experiments.- Dillon, P. & Simmers, I. (eds.) (1998): *Shallow Groundwater Systems*.- *International Contributions to Hydrogeology*, 18: 177-190.
- Maloszewski, P., Stichler, W., Zuber, A. & Rank, D. (2002): Identifying the flow systems in a karstic-fissured-porous aquifer, the Schneealpe, Austria, by modelling of environmental O<sup>18</sup> and H<sup>3</sup> isotopes. – *Journal of Hydrology*, 256: 48-59.



- Margane, A., Hobler, M. & Subah, A. (1997): Groundwater Resources of Northern Jordan, Special Report No. 3: Mapping of Groundwater Vulnerability and Hazards to Groundwater in the Irbid Area.- BGR & WAJ, Technical Cooperation Project Advisory Services to the Water Authority of Jordan, BGR archive no. 112708, 50 p.
- Margane, A., Hobler, M., Almomani, M. & Subah, A. (2002): Contributions to the Hydrogeology of Northern and Central Jordan.- *Geologisches Jahrbuch*, C68, 52 p.
- Margane, A., Hobler, M. & Subah, A. (1999): Mapping of Groundwater Vulnerability and Hazards to Groundwater in the Irbid Area, N-Jordan.- *Zeitschrift für Angewandte Geologie*, 45(4): 175-187.
- Masri, M. (1963): Report on the geology of the Amman, Zerqa area.- Central Water Authority, Amman, 1-74.
- Mattikalli, M. N. & Engman, E.T. (2000): Integration of Remotely Sensed Data into Geographical Information systems.- In: Schultz G.A. and Engman T.E. (eds) (2000): *Remote Sensing in Hydrology and Water Management*.- Springer, Berlin, 483 p.
- Meijerink, A.M.J. (2000): Groundwater.- In: Schultz G.A. & Engman E.T. (eds) (2000): *Remote Sensing in Hydrology and Water Management*.- Springer Verlag, Berlin, 483 p.
- Menenti, M. (2000): Evaporation.- In: Schultz G.A. and Engman E.T. (eds) (2000): *Remote Sensing in Hydrology and Water Management*.- Springer Verlag, Berlin, 483 p.
- Merchant, J.W. (1994): GIS-Based Groundwater Pollution Hazard Assessment: A Critical Review of the DRASTIC Model.- *Photogrammetric Engineering and Remote Sensing*, 60(9): 1117-1127.
- Mikbel, S. & Zacher, W. (1981): The Wadi Shueib Structure in Jordan.- *Neues Jahrbuch für Geologie und Paläontologie Monatsheft*, 9: 571-576.
- Ministry of Water and Irrigation (MWI) (2004): National Water Master Plan of Jordan- Water Resources in Jordan-, National Water Master Plan Directorate, Amman, Jordan, 200 p.
- Moh'd, B. & Muneinzel, S. (1998): The geology of Al Salt area, Map sheet No 3154III.- *Bulletin No. 41*, Amman, 67 p.
- NASA, National Aeronautics and Space Administration (2002): LANDSAT 7 Science Data.- *User Handbook* [online].- Available from: [http://www.gsfc.nasa.gov/IAS/handbook/handbook\\_toc.html](http://www.gsfc.nasa.gov/IAS/handbook/handbook_toc.html).
- Neev, D., & Emmerly, K.O. (1967): The Dead Sea; depositional process and environments of evaporates.- *Bulletin Geological Survey of Israel*, 41: 1-147.
- Neev, D., & Hall, J. (1979): Geophysical investigations in the Dead Sea.- *Sedimentary Geology*, 23: 209-238.
- NRA / PCIAC Study Team (1989): Risha Area Jordan: Reconnaissance Basin Analysis.- Unpublished report for the National Resources Authority, Amman, Jordan.
- Ohio-Kentucky-Indian (OKI) Regional Council of Governments (1975): A Method for assessing rural non point sources and its application in water quality management.- *Water Planning Division, WH-554*; Washington, D.C, 20 p.
- Olson, C.E. (1960): Elements of photographic Interpretation Common to Several Sensors.- *Photogrammetric Engineering*, 26(4): 651-656.
- Orthofer, R., Shuval, H., Issac, J., Daoud, R. & Kupferberger, H. (2001): Developing Sustainable Water Management in the Jordan Valley, Final Report.- INCO-DC Contract No ERBIC18CT970161, 64 p.

- Parcharidis, I., Psomiaids, E., & Stamatii, G. (1998): Using LANDSAT TM images to study the karstic phenomenon.- *International Journal of Aerospace survey and earth science, ITC journal*, 2: 118-124.
- Potter, J.F. (1974): Haze and sun angle effects on automatic classification of satellite data-simulation and correction.- *Journal of the Society of Photo-Optical Instrumentation Engineers*, 51:73-83.
- Powell, J.H. (1989): Stratigraphy and sedimentation of the phanerozoic rocks in central and south Jordan: Part B Kurnub, Ajlun and Belqa Groups.- *Geological Mapping Division Bulletin 11B*, Amman, 127 p.
- Qassem, J.M. (1997): Tectonics along the Wadi Shueib structure. Master thesis University of Jordan, Amman (unpublished), 110 p.
- Quennel, A.M. (1959): Tectonics of the Dead Sea rift.- *Proceedings of the 20<sup>th</sup> International Geological Congress, Association African Geological Survey, Mexico*, 385-405.
- Quennel, A.M. (1951): The geology and mineral resources of (former) Transjordan.- *Colonial Geology and Mineral Resource, London*, 2: 85-115.
- Richards, J. (1986): Remote sensing digital image analysis, an introduction.- *Springer, New York*, 281 p.
- Richtlinien für Trinkwasserschutzgebiete (1995): 1. Teil, Schutzgebiete für Grundwasser.- *DVGW-Regelwerk (Deutscher Verein des Gas- und Wasserfachs), Technische Regeln, Arbeitsblatt W 101*.
- Robinson, C.A. (2002): Applications of satellite radar data suggest that the Kharga depression in SW Egypt is a fracture rock aquifer.- *International Journal of Remote Sensing*, 23: 4101-4113.
- Rodier, J.A. (1975): Evaluation de l'écoulement Annuel dans le Sahel Tropical Africain.- *Travaux et Documents de l'O.R.S.T.O.M*, 46, 121p.
- Rosen, L. (1994): A study of DRASTIC methodology with emphasis on Swedish conditions.- *Groundwater*, 32 ( 2): 278-285.
- Rouse, J.W., Haas, R.H., Schell, J.A. & Deering, D.W. (1974): Monitoring Vegetation Systems in the Great Plains with ERST.- *Proceedings of the 3<sup>rd</sup> Earth Resources Technology Satellite-1 Symposium, Greenbelt, Dec. 10-14 1974, NASA SP-351*, 1: 3010-317.
- Sabins, F.F., (1997): Remote Sensing: Principles and Interpretation.- *W.H. Freeman, New York*, 494 p.
- Sander, P. (1996): Groundwater Assessment Using Remote Sensing and GIS in a Rural Groundwater Project in Ghana: Lessons Learned.- *Hydrogeological Journal*, 4(3): 40-49.
- Saraf, A.K., Choudhury, P.R., Roy, B., Sarma, B., Vijay, S., & Choudhury, S. (2004): GIS based surface hydrological modelling in identification of groundwater recharge zones.- *International Journal of Remote Sensing*, 25(24): 5759-5770.
- Sawarieh, A., & Barjous, M. (1993): National Mapping Project.- *Geological Mapping Division, Geological Map of Suwaylih, 3154-II, National Resources Authority, Amman*.
- Schechter, R.N. (1976): Resources inventory using LANDSAT data for area wide water quality planning.- *Proceedings of the Symposium on Machine Processing of Remotely Sensed Data, West Lafayette June 29 - July 1967*, 80-88.
- Scheffer, F., & Schachtschabel, P. (1989): *Lehrbuch der Bodenkunde*.- Ferdinand Enke, Stuttgart, 475 p.

- Scholles, F. (1997): Abschätzen, Einschätzen und Bewerten in der UVP, Weiterentwicklung der Ökologischen Risikoanalyse.- UVP-Spezial Dortmund, 13: 103-118.
- Schultz, G.A. & Engman, T.E. (2000): Remote Sensing in Hydrology and Water Management.- Springer, Berlin, 475 p.
- Seelheim, F. (1880): Methode zur Bestimmung der Durchlässigkeit des Bodens.- Zeitschrift für analytische Chemie, 19: 387-418.
- Shawabkeh, K.F. (2001): Map sheet 3153 IV.- National Resources Authority, Amman.
- Singhroy, V. & Momani M.R. (1996): Mapping Surface characteristics of Aquifers in Jordan from integrated SAR Images.- Proceedings of the 11<sup>th</sup> Thematic Conference and Workshop on Applied Geologic Remote Sensing, Nevada, 27-29 Febr. 1996: 691-699.
- Spiteri, A. (2004): Data collection using remote sensing.- In: Zwahlen F. (ed) (2004): COST Action 620- Vulnerability and Risk Mapping for the Protection of Carbonate (Karst) Aquifers- Final Report, 122-124, Public European Communities, Luxembourg.
- Song, C., Woodcock, C.E., Seto, K.C., Lenney, M.P. & Scott, M.A. (2001) :Classifications and Change Detection Using LANDSAT TM Data: When and How to Correct Atmospheric Effects ?- Remote Sensing and Environment, 75: 230-244.
- Star, J. & Estes, J.(1990): Geographic Information Systems. An Introduction.- Prentice-Hall, New Jersey, 303 p.
- Storz, R. (2004): GIS-based groundwater hazard mapping of the Wadi Shueib catchment area, Jordan.- Master Thesis University of Karlsruhe, Karlsruhe (unpublished), 149 p.
- Su, Z. (1996): Remote Sensing Applied to Hydrology: The Sauer River Basin Study.- In: Schriftenreihe Hydrologie und Wasserwirtschaft Ruhr-Universität Bochum,15, 187 p.
- Svoma, J. & Pyek, A. (1983): Photographic detection of groundwater pollution, Hydrological Journal of Remote Sensing and Remote Data Transmission.- Proceedings of the Hamburg Symposium, August 1983. IAHS Publication No. 145, 230 p.
- Ta'any Rakad A. A. (1992): Hydrological and Hydrochemical Study of the Major Springs in the Wadi Shueib Catchment Area, Master Thesis Yarmouk University, Irbid (unpublished),300 p.
- Tauer, W. & Prinz, D. (1992): Runoff Irrigation in the Sahel Region: Appropriateness and Essential Framework Conditions.- In: Proceedings of the International Conference on Advances in Planning, Design and Management of Irrigation Systems as Related to Sustainable Land Use, Leuven, 14-17 Sept. 1992, 945-953.
- Teeuw, R.M. (1995): Groundwater Exploration using remote sensing and a low-cost geographical information system.- Hydrogeological Journal, 3(3): 21-30.
- Ten Brink, U.S., & Ben-Avraham, Z. (1989) The anatomy of a pull-apart basin: seismic reflection observations of the Dead Sea basin.- Tectonics, 2: 333-350.
- Ten Brink, U.S., Ben-Avraham, Z., Bell, R., Hassouneh, M., Coleman, D., Andreasen, G., Tibor, G., & Coakley, B. (1993) Structure of the Dead Sea pull-apart basin from gravity analysis.- Journal of Geophysical Research, 98: 21877-21894.
- US Department of agriculture (USDA) (1975): „Soil taxonomy – A basic system of soil classification“.- Agriculture handbook #436, SCS, U.S. Government Printing Office, Washington D.C.
- US Department of agriculture (USDA) (1993): Soil Survey Manual, Soil Survey Staff, Natural Resource Conservation Service, Handbook No. 18, U.S. Government Printing Office, Washington D.C.

- Vrba, J. & Zaporozec, A. (eds) (1994): Guidebook on Mapping Groundwater Vulnerability.- International Contributions to Hydrogeology.- Heise, Hannover, 131 p.
- Wahba G. (1990): Spline models for observational data.- Society for Industrial and Applied Mathematics, Philadelphia.
- Wallace, J.F., Campbell, N.A., Wheaton, G.A. & McFarlane, D.J. (1993): Spectral discrimination and mapping of waterlogged cereal crops in western Australia.- International Journal of Remote Sensing, 14(14): 2731-2743.
- Waters, P., Greenbaum, P., Smart, L., & Osmaston, H. (1990): Applications of remote sensing to groundwater hydrology.- Remote Sensing Reviews, 4: 223-264.
- Waynakh, M. (1995): The use of Synthetic Aperture Radar for mapping groundwater recharge zone in Madaba area.- Proceedings of the 1<sup>st</sup> GlobSAR Regional Symposium, Amman 22-26 Apr. 1995, 12 p.
- Welch, R.A. & Jordan, T.R. (1996): Digital Orthophoto Production in a Desktop Environment.- Geomatics Info Magazine, 10(7): 26-27.
- Welch, R.A. & Jordan, T.R. (1996): Using Scanned Air Photographs. In: Maorain S. & Baros S.L. (eds) (1996): Raster Imagery in Geographic Information Systems.- Onward Press, 560 p.
- Werz, H., Hötzl, H., Kuntz, D., Storz, R. (2006): Investigations of soils, groundwater-vulnerability and groundwater hazards in the surface catchment area of the Wadi Shueib.- In: Dead Sea – Jordan Rift Valley Water Resources Management.- Springer, Heidelberg, 490 p (in press).
- Werz, H. & Hötzl, H. (2005): The usefulness of passive remote sensing data for mapping groundwater risk intensity in semi-arid regions.- submitted July, 2004 to Hydrogeological Journal.
- Werz, H. & Hötzl, H. (2004): Groundwater-Vulnerability Mapping and Hazard-Mapping in Semi-Arid Regions using Remote Sensing Data.- Proceedings of the International Conference on Groundwater Vulnerability Assessment and Mapping, Ustron, 16 to 20 June 2004, 143- 145.
- Wiesemann, G. (1969): Zur Tektonik des Gebietes östlich des Grabenabschnittes Totes Meer, Jordantal.- Beiheft zum Geologisches Jahrbuch, 81: 15-247.
- Williams, J. (2001): GIS Processing of Geocoded Satellite Data.- Springer, London, 327 p.
- Winter, T.C. (1999): Relation of streams, lakes, and wetlands to groundwater flow systems.- Hydrogeology Journal, 7: 28–45.
- Yohay, C. & Kadmon, R. (1998): Computerised classification of Mediterranean vegetation using panchromatic aerial photographs.- Journal of Vegetation Science, 9: 445-454.
- Yong, R.N. & Mulligan, C.N. (2003): Natural Attenuation of Contaminants in Soils.- CRC Press, 450 p.
- Zak, I. & Freud, R. (1982): Asymmetry and basin migration in the Dead Sea rift.- Tectonophysics, 80: 27-38.
- Zall, L. & Russell, O. (1979): Ground Water Exploration Programs in Africa.- Satellite Hydrology, American Water Resources Association, 416-425.
- Zieschang, J. (1961): Zur Zulässigen Höchstbelastung eines Brunnens. Zeitschrift für Angewandte Geologie, 7: 580-582.
- Zwahlen F. (ed) (2004): COST Action 620- Vulnerability and Risk Mapping for the Protection of Carbonate (Karst) Aquifers.- Final Report, Public European Communities, Luxembourg, 297 p.

# 13 APPENDIX

Appendix 1: Example of the soil location analysing results for location PL-6 (modified after Kuntz, 2003)

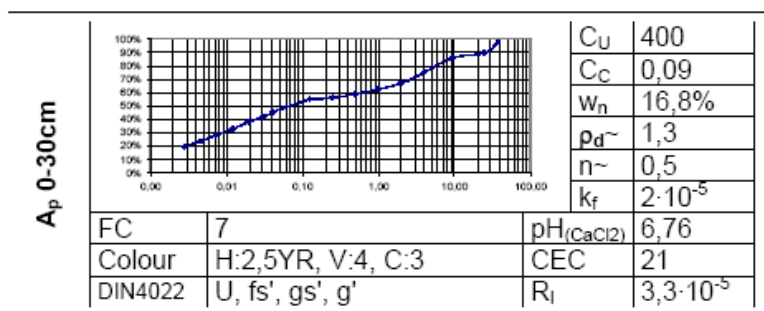
Soil type [WRB]	Leptic Cambisol	Moisture regime	Xeric
Land use	Tilled farmland	Height [m.a.s.l.]	940
Geological formation	Amman silicified limestone	Morphological position	Hilltop
Soil thickness [m]	20-50cm	Coordinates:	221.388 PGE 160.919 PGN

**Description of cover environment represented by location:**

Location PL-6 was chosen to represent soils on hilltops. In general these soils are shallow, although above the hard A7 or B2 formations often still used for agriculture. Thickness rarely surpasses 50cm. Location SL-1 represents a very similar environment. At PL-6 the comparatively low pH is noticeable, together with a low carbonate content a consequence from the silicified parent rock.

Fine material content is surprisingly high, probably increased through farmers removing large boulders and stones from their fields for easier ploughing. Protective potential though is limited due to the typically low depth derived from the morphological position.

**Soil Profile**



**B** 30-50cm, no samples, clay content increased (U,  $\bar{t}$ , s', g')

**mC** 55+cm

(Picture taken a few 100m away from PL-6 & RKS19, therefore horizons different and not correlated to the profile. Image shows  $A_e$  horizon instead of  $A_p$ )

Probed with RKS19.

Granulometric curve of the horizon, with particle size in [mm] on the abscissa and cumulative passing in [%] on the ordinate.

FC	Field Capacity	$pH_{(CaCl_2)}$
Colour	Dry colour of fine soil under daylight (Munsell Hue/Value/Chroma)	CEC
DIN4022	Soil after DIN4022	$R_i$

$C_U$  — Uniformity Coefficient  $C_U = d_{60}/d_{10}$

$C_C$  — Coefficient of Gradation /  $C_C = \frac{d_{30}^2}{d_{10} \cdot d_{60}}$

$w_n$  — Natural water content in weight%

$p_d$  — Dry bulk soil density in  $[g/cm^3]$

$n$  — Void ratio, calculated from bulk density and estimated particle density

$k_f$  — Hydraulic conductivity, calculated after SEELHEIM from granulometric curve:  
 $k_f = d_{50}^2 \cdot 0,00357 [m/s]$

Infiltration rate as measured (chapter 5.3.1.2) in [m/s]

Cation exchange capacity in [meq/100g]. Given is the value measured (chapter 5.3.2.6), which only gives an approximation.

## Appendix 2: Descriptive Statistics: LANDSAT ETM+ image

Water		
Channel	Mean	Standard
1	76.55918	1.54443
2	74.88163	2.35742
3	75.86939	4.96429
4	43.29388	6.29118
5	36.34694	7.63545
7	27.46939	6.26849

Quarry / Limestone bright		
Channel	Mean	Standard
1	132.63054	15.77176
2	153.33169	14.92174
3	200.64368	19.13575
4	156.03448	14.24615
5	199.42857	17.3782
7	168.66667	18.12343

Urban Area		
Channel	Mean	Standard
1	94.77108	6.41533
2	90.95984	7.24599
3	106.22088	8.73134
4	80.58635	7.18611
5	89.71486	8.25418
7	83.13655	9.21396

Gras /Bushes		
Channel	Mean	Standard
1	79.63964	1.85734
2	83.91892	2.58362
3	115.78378	3.68848
4	106.48649	2.18182
5	132.5976	4.9478
7	99.69069	4.30348

Urban Area_2		
Channel	Mean	Standard
1	96.56158	3.51631
2	96.7931	3.91493
3	119.31527	4.93396
4	100.133	4.17323
5	117.51232	5.94006
7	100.27586	5.78539

Forest		
Channel	Mean	Standard
1	67.89643	2.25594
2	61.37857	2.73983
3	72.41607	4.98499
4	76.28571	3.57578
5	83.85893	8.72454
7	59.29643	7.04105

Agriculture Area (undivided)		
Channel	Mean	Standard
1	68.5219	2.17036
2	64.86667	3.50528
3	85.03238	6.03994
4	76.93524	3.32603
5	82.48	6.00746
7	64.37524	4.71696

Kurnub Sandstone_2		
Channel	Mean	Standard
1	68.97945	2.17148
2	64.32363	3.48918
3	83.00856	7.51744
4	75.84932	6.17395
5	102.94349	10.99697
7	76.59932	9.47168

Limestone south		
Channel	Mean	Standard
1	91.64943	5.45445
2	97.10719	7.37911
3	132.22194	9.44213
4	110.72257	7.36364
5	151.33417	9.81021
7	119.43758	7.9024

Kurnub Sandstone_3		
Channel	Mean	Standard
1	73.50754	2.0296
2	73.54271	2.32031
3	101.46734	3.39933
4	88.0603	1.99658
5	130.04523	4.83215
7	97.50251	3.90577

Limestone_north		
Channel	Mean	Standard
1	84.50364	2.36162
2	84.43818	3.65399
3	110.04364	5.49528
4	90.50909	4.07017
5	121.73091	5.98971
7	95.37455	5.39239

Mixed Land Use		
Channel	Mean	Standard
1	70.02643	4.71376
2	67.1674	6.34737
3	75.12775	12.89389
4	109.09692	4.334
5	95.01322	14.04947
7	63.97357	14.64978

Appendix 3: Accuracy assessment of the supervised classification results of the LANDSAT ETM<sup>+</sup> image. 49 GPS acquired groundtruth points are compared with the informational classes of the LANDSAT ETM<sup>+</sup> image.

	<b>code</b>	<b>N</b> <b>(palestine grid)</b>	<b>E</b> <b>(palestine grid)</b>	<b>description</b>	<b>elevation</b> <b>[masl]</b>	<b>geology</b>	<b>groundtruth</b> <b>class</b>	<b>informational</b> <b>class</b>
1	A7	161062,00	218054,00	urban area, not dense, trees between houses	900		3	3
2	A14	159886,00	215740,00	orchards (olive) relatively dense	906	dark red-brown soil	4	4
3	E13	152671,00	218049,00	orchards (mixed) close to wadi course	320		4	10
4	D2	155709,00	214271,00	orchards (olives)	533		4	4
5	D4	155279,00	214036,00	olives and hummus	598		4	4
6	Neu1	159450,00	216903,00	orchards	869		4	4
7	B6	160457,00	221910,00	sparse vegetation, dry grass, brownish	850	wadi sir	5	5
8	E7	153854,00	219854,00	thistles, grass, green to yellow-brownish	450	Kurnub- limestone	5	5
9	E3	156101,00	219599,00	sparse, yellow vegetation	550	massive limestone	5	5
10	G2	150602,00	215299,00	dry, yellow grass, sparse bushes	71	limestone	5	5
11	D6	156279,00	214746,00	dry grass, thistles	558	massive limestone	5	5
12	D14	154226,00	213961,00	graeser, thistles	515	limestone	5	5
13	D17	153567,00	214192,00	grass, thistles	469	limestone	5	5
14	D21	153427,00	214463,00	grass, thistles	427	limestone	5	5
15	I3	147057,00	212159,00	grass, thistles	75		5	5
16	I 10 alt	153002,00	215610,00	dry grass, thistles	513	limestone	5	5
17	B8	158728,00	220039,00	dry grass, single bushes	850	limestone	6	9
18	B5	160837,00	220851,00	between rocks, dry grass, single bushes	860	limestone	6	6
19	B9	160264,00	222047,00	sparse vegetation, dry grass, brownish	760	limestone	6	6
20	E2	155849,00	220062,00	thistles, grass, green to yellow-brownish	552	limestone	6	6
21	A9	160576,00	216206,00	built-up area, limestone debris	954		7	7
22	I10	146739,00	212271,00	grass, thistles	-24		7	7
23	I 27	147649,00	215677,00	small grass, bushes	227	limestone	7	7
24	A2	162742,00	217267,00	yellow grass, single bushes, patchy soil cover	1020	limestone	8	8

code	N (palestine grid)	E (palestine grid)	description	elevation [masl]	geology	groundtruth class	informational class	
25	D5	155979,00	215025,00	grass, thistles	587	limestone	8	6
26	D7	154564,00	216143,00	grass, thistles	660		8	5
27	D10	154151,00	214581,00	grass, thistles	520	limestone	8	5
28	I8	146896,00	212091,00	grass, thistles, debris	57		8	5
29	B3	160924,00	220278,00	dense pine trees	867	wadi sir	9	9
30	F3	150383,00	220364,00	oak forest, yellow grass, bushes	645	massive limestone	9	10
31	F1	150731,00	220678,00	oak forest (tree distance 8-10 m), yellow grass	673	massive limestone	9	6
32	F5	152358,00	222345,00	pinus (3 m)	811	limestone	9	9
33	C5	158747,00	225129,00	orchards homogenous	940		10	10
34	C8	158623,00	224826,00	orchards (mixed)	950	soil (unvegetated)	10	8
35	B4	161213,00	221341,00	wheat, yellow	945		10	10
36	A5	162259,00	216804,00	orchards, separated by stonewalls	1015		10	4
37	A3	162587,00	217414,00	orchards (olives etc)	975		10	10
38	E15	154881,00	220310,00	orchards, bordered by pines, soil (less vegetated)	640		10	10
39	E14	154162,00	219150,00	orchards (mixed), soil (without vegetation)	400		10	10
40	E9	153639,00	218785,00	wheat, yellow	419		10	4
41	E8	154409,00	221768,00	orchards (mixed) sparse grass cover	583	Kurnub, weathered	10	10
42	D1	155631,00	214255,00	wheat	530		10	10
43	D8	154413,00	214748,00	orchards (olives)	488	Terra Rossa	10	10
44	D9	154169,00	214710,00	orchards (olives)	457	Terra Rossa	10	10
45	E16	153530,00	220367,00	orchards (olives), soil cover fresh, no grass	470	Kurnub, weathered,	13	13
46	E11	153606,00	220589,00	thistles, green grass (north exponated), red soil	500		13	13
47	E10	153721,00	220693,00	thistles, small bushes, red soil	460	Kurnub, weathered,	13	13
48	E1	155560,00	220915,00	sparse vegetation	600	Kurnub	13	5



Appendix 4: Accuracy assessment of the NDVI of the LANDSAT ETM<sup>+</sup> image. 49 GPS acquired groundtruth points are compared with the calculated and classified NDVI values.

	<b>code</b>	<b>N (palestine grid)</b>	<b>E (palestine grid)</b>	<b>description</b>	<b>elevation [masl]</b>	<b>geology</b>	<b>NDVI groundtruth</b>	<b>NDVI calculated</b>
1	A9	160576,00	216206,00	built-up area, limestone debris	954		1	1
2	A7	161062,00	218054,00	urban area, not dense, trees between houses	900		1	1
3	D10	154151,00	214581,00	grass, thistles	520	limestone	1	1
4	I3	147057,00	212159,00	grass, thistles	75		1	1
5	I8	146896,00	212091,00	grass, thistles, debris	57		1	1
6	I10	146739,00	212271,00	grass, thistles	-24		1	1
7	I 27	147649,00	215677,00	small grass, bushes	227	limestone	1	1
8	I 10 alt	153002,00	215610,00	dry grass, thistles	513	limestone	1	1
9	B8	158728,00	220039,00	dry grass, single bushes	850	limestone	2	2
10	B5	160837,00	220851,00	between rocks, dry grass, single bushes	860	limestone	2	2
11	B6	160457,00	221910,00	sparse vegetation, dry grass, brownish	850	wadi sir	2	2
12	B9	160264,00	222047,00	sparse vegetation, dry grass, brownish	760	limestone	2	2
13	A14	159886,00	215740,00	orchards (olive) relatively dense	906	dark red-brown soil	2	2
14	A2	162742,00	217267,00	yellow grass, single bushes, patchy soil cover	1020	limestone	2	2
15	F3	150383,00	220364,00	oak forest, yellow grass bushes	645	massive limestone	2	2
16	E11	153606,00	220589,00	thistles, green grass (north exponated), red soil	500		2	2
17	E9	153639,00	218785,00	wheat, yellow	419		2	2
18	E7	153854,00	219854,00	thistles, green to yellow brownish grass	450	Kurnub / limestone	2	2
19	E3	156101,00	219599,00	sparse, yellow vegetation	550	massive limestone	2	3
20	E2	155849,00	220062,00	thistles, green to yellow brownish grass	552	limestone	2	2
21	E1	155560,00	220915,00	sparse vegetation	600	Kurnub	2	2
22	D4	155279,00	214036,00	olives and hummus	598		2	3
23	D6	156279,00	214746,00	dry grass, thistles	558	massive limestone	2	2
24	D5	155979,00	215025,00	grass, thistles	587	limestone	2	2
25	D7	154564,00	216143,00	grass, thistles	660		2	2
26	D14	154226,00	213961,00	grass, thistles	515	limestone	2	2
27	D17	153567,00	214192,00	grass, thistles	469	limestone	2	2

28	D21	153427,00	214463,00	grass, thistles	427	limestone	2	2
29	C5	158747,00	225129,00	orchards homogenous	940		3	4
30	C8	158623,00	224826,00	orchards (mixed)	950	soil (unvegetated)	3	3
31	A5	162259,00	216804,00	orchards, separated by stonewalls	1015		3	3
32	A3	162587,00	217414,00	orchards (olives etc)	975	soil fresh	3	4
33	F1	150731,00	220678,00	oak forest (tree distance 8-10 m), yellow grass	673	massive limestone	3	2
34	E16	153530,00	220367,00	orchards (olives), soil cover fresh no grass	470	Kurnub, weathered,	3	3
35	E15	154881,00	220310,00	orchards, bordered by pines, soil (less vegetated)	640		3	3
36	E10	153721,00	220693,00	thistles, small bushes, red soil	460	Kurnub, weathered,	3	3
37	D1	155631,00	214255,00	wheat	530		3	3
38	D2	155709,00	214271,00	orchards (olives)	533		3	3
39	D8	154413,00	214748,00	orchards (olives)	488	Terra Rossa	3	3
40	D9	154169,00	214710,00	orchards (olives)	457	Terra Rossa	3	3
41	F5	152358,00	222345,00	pinus (3 m)	811	limestone	3	4
42	Neu1	159450,00	216903,00	orchards	869		3	3
43	B4	161213,00	221341,00	wheat, yellow	945		4	4
44	B3	160924,00	220278,00	dense pine trees	867	wadi sir	4	4
45	E14	154162,00	219150,00	orchards (mixed), soil without vegetation	400		4	4
46	E13	152671,00	218049,00	orchards (mixed) close to wadi course	320		4	4
47	E8	154409,00	221768,00	orchards (mixed), patchy grass cover	583	Kurnub, weathered	4	2
48	G2	150602,00	215299,00	dry, yellow grass, sparse bushes	71	limestone	4	1

Appendix 5: Generated thematic GIS layers as intermediated steps of for the final groundwater-vulnerability, hazard- and risk map.

<b>Name of thematic layer</b>	<b>Data type</b>	<b>Data Source</b>	<b>Data extraction</b>	<b>Description of layer</b>	<b>Spatial resolution</b>	<b>Purpose</b>	<b>Included tables</b>
aricu_diss	vector	orthophotos	on-screen digitising	combined agricultural areas (crops, orchards)		groundwater vulnerability, hazard map	
b_nonkarst	vector	scanned geological maps	on-screen digitising	protective cover points of non-karstified layers over aquifer		groundwater vulnerability	lithology, fracturing, thickness,
crops	vector	orthophotos	on-screen digitising	crops		intermediate layer for groundwater vulnerability	
orchards	vector	orthophotos	on-screen digitising	orchards		intermediate layer for groundwater vulnerability	
flowdiss	vector	soil map, field observations	on-screen digitising	estimation of the dominant flow process		intermediate layer dominant flow process type	
geol	vector	scanned geological maps	on-screen digitising	geology of test area		intermediate layer stratigraphy for groundwater vulnerability	
l_strich_dis1	vector	combination of flowdiss with slope conversion and percent	conversion and combination of existing layers	l'-factor		intermediate layer l'-factor values	
l_fact_diss	vector	combination of l_strich_dis1 and surface catchment map	conversion and combination of existing layers	l-factor		groundwater vulnerability	l-factor values
soil map	vector	field investigations and Jordanian soil atlas		soil units		soil cover map	soil unit numbers

Name of thematic layer	Data type	Data Source	Data extraction	Description of layer	Spatial resolution	Purpose	Included tables
b_aqui	vector	scanned geological maps, field observations, orthophotos, well data	conversion and combination of existing layers	protective cover points of the aquifers		groundwater vulnerability	lithology, fracturing/ karstification thickness,
pyear_15clip	vector	modelling results of Orthofer (2001)	clipping and conversion of existing raster layers	annual precipitation	850 m	groundwater vulnerability	precipitation [mm]
soil_eFC_mm	vector	field and laboratory investigations	on-screen digitising	agricultural areas (crops, orchards)		groundwater vulnerability	eFC [mm], topsoil points
streets	vector	orthophotos	on-screen digitising	street net		hazards	
surf_catch	vector	scanned geological maps, field observations	on-screen digitising	surface catchment map		groundwater vulnerability	values for individual zones
topo	vector	scanned topographic maps	on-screen digitising	elevation contour lines		intermediate layer	elevation contour lines values
urban dense wells	vector point	LANDSAT ETM+ Ministry of Water, Amman	on-screen digitising table, plotting in GIS	well characteristics		groundwater vulnerability	water level, formation
tectonics springs	vector point	geological maps, 1:50,000 GPS acquired locations	on-screen digitising table, plotting in GIS	structural features location and type of springs		geological map hydrogeology	type of faults spring characteristics